POSITIONING SENSOR BY COMBINING OPTICAL PROJECTION AND PHOTOGRAMMETRY

by

Benrui Zheng

A dissertation submitted to the faculty of
The University of North Carolina at Charlotte
in partial fulfillment of the requirements
for the degree of Doctor of Philosophy in
Optical Science and Engineering

Charlotte

2014

Approved by:

____
Dr. Brigid A. Mullany

____
Dr. Angela D. Davies

____
Dr. Edward P. Morse

____
Dr. Christopher J. Evans

____
Dr. Shen-En Chen

ABSTRACT

BENRUI ZHENG. Positioning sensor by combining optical projection and
photogrammetry. (Under the direction of DR. BRIGID MULLANY)

Six spatial parameters, (x, y, z) for translation, and pitch, roll, and yaw for rotation, are used to describe the 3-dimensional position and orientation of a rigid body - the 6 degrees of freedom (DOF). The ability to measure these parameters is required in a diverse range of applications including machine tool metrology, robot calibration, motion control, motion analysis, and reconstructive surgery. However, there are limitations associated with the currently available measurement systems. Shortcomings include some of the following: short dynamic range, limited accuracy, line of sight restrictions, and capital cost. The objective of this dissertation was to develop a new metrology system that overcomes line of sight restrictions, reduces system costs, allows large dynamic range and has the potential to provide high measurement accuracy.

The new metrology system proposed in this dissertation is based on a combination of photogrammetry and optical pattern projection. This system has the potential to enable real-time measurement of a small lightweight module’s location. The module generates an optical pattern that is observable on the surrounding walls, and photogrammetry is used to measure the absolute coordinates of features in the projected optical pattern with respect to a defined global coordinate system. By combining these absolute coordinates with the known angular information of the optical projection beams, a minimization algorithm can be used to extract the absolute coordinates and angular orientation of the module itself.

The feasibility of the proposed metrology system was first proved through preliminary experimental tests. By using a module with a 7×7 dot matrix pattern, experimental agreement of 1 to 5 parts in 10^3 was obtained by translating the module over 0.9 m and by rotating it through 60°. The proposed metrology system was modeled through numerical simulations and factors affecting the uncertainty of the measurement were investigated. The simulation results demonstrate that optimum design of the projected pattern gives a lower associated measurement uncertainty than is possible by direct photogrammetric measurement with traditional tie points alone. Based on the simulation results, a few improvements have been made to the proposed metrology systems. These improvements include using a module with larger full view angle and larger number of dots, performing angle calibration for the module, using a virtual camera approach to determine the module location and employing multiple coordinates system for large range rotation measurement. With the new proposed virtual camera approach, experimental agreement at the level of 3 parts in 10^4 was observed for the one dimension translation test. The virtual camera approach is faster than the algorithm and an additional minimization analysis is no longer needed. In addition, the virtual camera approach offers an additional benefit that it is no longer necessary to identify all dots in the pattern and so is more amenable to use in realistic and usually complicated environments. A preliminary rotation test over 120° was conducted by tying three coordinate systems together. It was observed that the absolute values of the angle differences between the measured angle and the encoder reading are smaller than 0.23° for all measurements. It is found that this proposed metrology system has the ability to measure larger angle range (up to 360°) by using multiple coordinate systems. The uncertainty analysis of the proposed system was performed through Monte Carlo simulation and it was demonstrated that the experimental results are consistent with the analysis.

ACKNOWLEDGEMENTS

The work contained in this dissertation would not be possible without my advisors Dr. Angela Davies, Dr. Edward Morse and Dr. Brigid Mullany. I would like to thank Dr. Brigid Mullany, not only for her patience, but also for keeping everything on track and providing recommendations to my dissertation. Dr. Edward Morse has given me tremendous technical advice and guided me into the area of metrology. I would like to thank Dr. Angela Davies, who helped me understand the depths of optical science and guided the fundamentals of this project.

Also, I truly enjoyed working with my lab mates, Kevin E. Bowes, Yue Dong and Yue Zhou. I would like to thank all undergraduate/graduate students in UNCC of who participated in the study of this project, including Charles Borders, Beth Kornarski, Christopher Singer and Christopher Demarco. I am thankful for the help from Eric Browy and Dr. Jonathan Beaman, who helped me on parts design and machining.

I would like to thank the entire Department of Physics and Optical Science, the Center for Precision Metrology (CPM) and the Center for Optoelectronics and Optical Communications (COOC) at UNC Charlotte for their support and excellent resources. Of these people I would like to give my special thanks to Dr. Jimmie Miller for his discussions and suggestions on the experiment and Dr. Christopher Evans, for his extensive knowledge in precision metrology and careful review to my dissertation. I am also grateful to my committee member Dr. Shen-En Chen for agreeing to sit on my committee. In addition, I would like to thank Robert Hudgins, Greg Caskey and Scott Williams for allowing me to use all the wonderful equipment in CPM and COOC.

I am thankful for the funding provided by the Center for Precision Metrology at UNC Charlotte and by the National Science Foundation (NSF) under grant #0928364. Any opinions, findings, and conclusions or recommendations expressed in this dissertation are mine and do not necessarily reflect the views of the NSF.

Lastly, I would like to thank my parents whose love and support sustained me throughout the journey and motivated me to where I am today.

DEDICATION

I would like to dedicate my studies at The University of North Carolina at Charlotte to my parents, Jiaxing Zheng, and Baolan Shao, who have been there through it all and have molded me into the person I have become. Their love and support make this possible.

TABLE OF CONTENTS

LIST OF TABLES

LIST OF FIGURES

LIST OF ABBREVIATIONS

2D	two-dimensional
3D	three-dimensional
AD	distance accuracy
ASME	American Society of Mechanical Engineers
ASPRS	American Society of Photogrammetry and Remote Sensing
CAD	computer-aided design
CCD	charge-coupled device
CMM	coordinate measurement machine
CMOS	complementary-symmetry metal oxide semiconductor
CNC	computer numerical control
CRP	close-range photogrammetry
CT	coded target
DOF	degree of freedom
EOP	exterior orientation parameter
EXIF	exchangeable image file
FC	ferrule connector
FOV	field of view
FVA	full view angle
GPS	Global Positioning System
GNSS	Global Navigation Satellite System
INS	Inertial Navigation System

IOP	interior orientation parameter
JPEG	Joint Photographic Experts Group
JPL	Jet Propulsion Laboratory
LED	light emitting diode
LD	laser diode
LLNL	Lawrence Livermore National Laboratory
LSM	least-squares matching
nm	nanometer
μm	micrometer
mm	millimeter
m	meter
ms	millisecond
mW	milliwatts
NA	numerical aperture
NASA	National Aeronautics and Space Administration
NIST	National Institute of Standards and Technology
PSDs	position sensitive detectors
PSD	power spectral density
RD	distance repeatability
RMS	root mean square
RSS	root-sum-of-squares
SCAAT	single-constraint-at-a-time
SLR	single-lens reflex

SMR	spherically mounted retro-reflector
USB	universal serial bus
UV	ultra-violet

CHAPTER 1: INTRODUCTION

1.1 Motivation

Six spatial parameters, (x, y, z) for translation, and pitch, roll, and yaw for rotation, are used to describe the 3-dimensional (3D) position and orientation of a rigid body - the 6 degrees of freedom (DOF). The ability to measure these parameters is required in a diverse range of applications including machine tool metrology, robot calibration, motion control, motion analysis, and reconstructive surgery. Current 6 DOF measurement techniques include indoor global positioning system (iGPS), inertial sensors (accelerometer based), laser based sensor, computer vision techniques, traditional photogrammetric systems and laser trackers. However, there are limitations associated with the currently available measurement systems. The signal of iGPS may not reach the receiver through a direct line-of-sight, and this may reduce the position accuracy [1, 2]. Six DOF inertial sensors are not suitable for precise measurements because the data processing results in accumulating errors in all six components [3-6]. Utilizing lasers in conjunction with position sensitive detectors (PSDs) can provide excellent position resolution, however the range is limited because the laser cannot deviate from the sensor [5-8]. The computer vision technique has limited measurement accuracy that is on the order of a hundred micrometers [6, 9-14]. Using the photogrammetric method to achieve high precision 6DOF measurements requires line of sight between the object and camera at all times [15-18]. The current laser tracker system is expensive (hundreds of thousands of dollars) and also requires the object to remain within the sensor's line of sight [22, 23].

In this dissertation an unconventional combination of optical pattern projection and photogrammetry is proposed to realize an optical sensor with the ability to measure 6 DOF. It overcomes line of sight restrictions, reduces system costs, allows large dynamic range and has the potential to provide high measurement accuracy.

1.2 Objective of Dissertation

The objective of this dissertation is to develop an inexpensive, non-contact metrology system that enables a large measurement range and has the potential to provide high accuracy measurements. The performance of the proposed metrology system is evaluated and the limitation and capabilities of the system are also explored in this dissertation. The new metrology system overcomes line of sight restrictions between the object and cameras and has the potential to work in realistic manufacturing environments.

Central to the proposed method is the projection of an optical pattern generated by an optical module, which consists of a laser diode and a diffractive element. The optical pattern is generated by passing a laser beam through a diffractive element to produce an array of dots on any surface that intersects the projected diffracted beams. The combination of a laser and a diffractive element is referred to the module. A diffractive element with known design, a laser diode with chosen wavelength and their layout inside the module lead to a defined, known geometric relationship between the diffracted beams and their origin (the module location). Two approaches are proposed to estimate the module location: (1) using an algorithm to determine the module location from the *xyz* coordinates of the laser dot on the wall surface, (2) modeling the module as a virtual pinhole camera so that the module location is determined through the bundle adjustment by using a virtual image associated with the module. Thus only the image of the optical pattern needs to be seen and photogrammetry is used indirectly to determine the position and orientation of the optical sensing module. The basic operating principle of the diffractive element used for the pattern generation makes it possible to treat the module as a virtual pinhole camera. An array of diffracted beams generated by the diffractive element is analogous to the array of chief rays from targets to a camera and this provides the possibility of active triangulation. The active triangulation is the basic principle of the virtual camera approach. The virtual camera approach is faster than the algorithm and an additional minimization analysis is no longer needed. In addition, the virtual camera approach offers an additional benefit that it is no longer necessary to identify all dots in the pattern and so is more amenable to use in realistic and usually complicated environments.

This indirect measurement technique utilizing an optical pattern projection and close-range photogrammetry offers several advantages. Firstly, instead of measuring just one point on the module to determine its location, the projected optical pattern provides a large number of easily identifiable features to contribute to the measurement. System modeling proves that lower measurement uncertainty is achievable through averaging, because photogrammetric measurements of many points in the environment are combined to measure the single location of the module. Secondly, to determine the location of the module it is only necessary to capture images of the projected pattern. The module need not be in the images. This moves the measurement away from the module, and the position of the module can be determined even if a direct line of sight does not exit. As long as a line of sight exists between some part of the optical pattern in the environment and a subset of cameras, it is possible to make a measurement. This facilitates measurements in complicated manufacturing environments or possibly hostile environments such as those with extreme radiation levels (power plants). Further, the geometry of the surface in the environment (the surface that intersects the diffracted beams) needs not be known or be exceptionally simple. Only the absolute *xyz* coordinates of the visible dots of intersection are needed for the minimization algorithm. The angles between the diffracted beams must be known, however, and this means each dot must be traceable to a known diffracted beam. If this becomes difficult, for example, in the case of a complex environmental geometry, identification can be facilitated by using an engineered diffractive element with coded targets designed into the diffracted pattern. This, however, would increase the cost of the system. An alternate method to determine the module location is the virtual camera approach, where the module projecting the optical pattern is itself treated as a virtual pinhole camera. A virtual image of the optical pattern is generated for this virtual camera by knowing the angular characteristics of the optical pattern generated by the module. The module location is determined from the photogrammetric bundle adjustment by determining the location of the virtual camera associated with the virtual image. The additional minimization analysis is no longer needed with the virtual camera approach, and it is no longer necessary to identify all dots in the pattern. Thus the virtual camera model is more sophisticated and more flexible.

Finally, the technique has the potential to provide a favorable combination of a large measurement range (up to tens of meters) with low measurement uncertainty at a low cost. The cost of current system is around \$2000, of which the software costs around \$1000 and the hardware (including cameras, diffraction element, fixtures, etc.) costs around \$1000. Multi-megapixel cameras are continuously reducing in price, and the measurement range can be increased by simply adding extra cameras to increase the area over which the projected dots may be imaged. The cost will increase if a completed system built with such technique is going to be sold on the open market (labor related development cost is included), which is not the scope of this dissertation. Photogrammetric measurements with uncertainties at the same level are possible as long as photographs of the pattern are observable from at least a subset of the cameras. This means the technique can measure very large translations and rotations without a loss in measurement uncertainty. Straight forward applications of the proposed technique include robot calibration by installing the module to the end effector of a robot arm (for certain categories of robots), and head-tracking in a typical virtual reality environment by attaching the module to a human head.

1.3 Dissertation Overview

The dissertation is divided into seven chapters. Chapter 1 discusses the motivation, objective and outline of the dissertation. A literature review of photogrammetry, applications of photogrammetry, and non-contact 6 DOF measurement techniques is given in Chapter 2. Chapter 3 describes the principle of the new metrology system and the factors affecting the photogrammetric measurement. Preliminary translation, rotation tests and robot testing are also discussed in Chapter 3. The underlying aim of Chapter 3 is to show the feasibility of the proposed algorithm based technique. Chapter 4 first investigates the factors affecting the measurement uncertainty through the system modeling. The system modeling provides guidelines to future reduce the measurement uncertainty of the module position. The subsequent improvements to the system are then presented, and angle calibration is discussed in detail. Then the translation test is repeated to verify the success of the discussed improvement. The potential of the proposed method to offer a large dynamic range through the use of multiple coordinate systems is outlined at the end of

Chapter 4. In Chapter 5, an improved method is proposed to estimate the module position by using a virtual camera model and both simulation and experimental tests are performed to validate the virtual camera model. In Chapter 6, a detailed uncertainty analysis is given for the proposed metrology system. Conclusions and future work are discussed in the Chapter 7, which includes the suggestions to enhance measurement capabilities of the proposed metrology system.

CHAPTER 2: LITERATURE REVIEW

Photogrammetry and optical projection are the two critical techniques used in the metrology system proposed in this dissertation. In this chapter an introduction is provided on photogrammetry and the applications of close range photogrammetry. An overview of optical pattern projection and its applications in non-contact measurement are also discussed. Then, brief summaries of currently available non-contact 6 DOF measurement techniques are given and their limitations are outlined. The expression of uncertainty was briefly reviewed at the end of this chapter.

2.1 Photogrammetry

Photogrammetry determines the geometric properties of an object of interest by interpreting photographic images of the object. The American Society of Photogrammetry and Remote Sensing (ASPRS) has defined photogrammetry as “the art, science, and technology of obtaining reliable information about physical objects and the environment through processes of recording, measuring and interpreting photographic images and patterns of recorded radiant electromagnetic energy and other phenomena” [24]. Triangulation is the fundamental principle used by photogrammetry. Given images of an object taken from different locations, the 3D *xyz* coordinates of the points of interest can be determined by calculating the mathematical intersection of different lines of sight developed from each camera to points on the object. Photogrammetry can provide measurement accuracy up to parts in 10^6 of the largest dimension of the object being measured [25]. And it can be applied to object ranging from a few millimeters to many meters in size. Photogrammetry can also record multiple points at one instant in time with high measurement frequency, up to thousands hertz [26-28, 34-38].

2.1.1 General Process of Photogrammetry

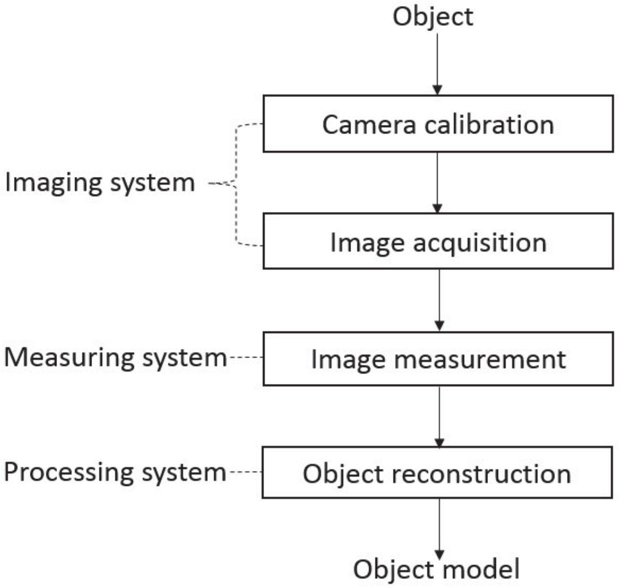

Figure 2.1: The photogrammetric process: from object to model.

Figure 2.1 shows the simplified process of the photogrammetric measurement. Four main steps of the photogrammetric measurement are: (1) camera calibration, (2) image acquisition, (3) image measurement, and (4) object reconstruction. Generally speaking, in order to achieve accurate measurement results, camera calibration is a necessary step of the photogrammetric measurement. Camera calibration is the process of determining the internal characteristics of a camera, which include the focal length of the lens (the principal distance), the digitizing scale (the format size of imaging area), the position of the principal point and the distortion characteristics of the lens. The process of camera calibration is discussed in detail in section 3.2.2. After the cameras are calibrated, they can be used to capture images of the object of interest. An image only records 2D information of an object, so multiple images (at least 2 images) are required in order to reconstruct the 3D object. In the image measurement step, the images of the object of interest are loaded into photogrammetry software. Common features and common points on the object in the different images are marked and referenced in this step. Here referencing is the process of identifying those marks on two or more different photographs representing the same physical object in space, which is discussed in detail in section 3.3.2. After all the common points are referenced, the 3D model of the object is solved through the bundle adjustment algorithm in the last step. The actual size and the coordinate information of the object are obtained after defining a coordinate system and a reference length in the same set of photographs. The reference length and the coordinate system are critical to the photogrammetric measurement if the actual size information is required.

2.1.2 Close Range Photogrammetry

There are many ways to classify photogrammetry. Based on camera position during photography, it can be split into Aerial Photogrammetry and Close-range Photogrammetry. In Aerial Photogrammetry the camera is mounted in an aircraft and is usually pointed vertically towards the ground. The geometry of a portion of the earth can be effectively recreated by using large-format imagery and ground coordinates information in a virtual environment [19, 29]. In Close-range photogrammetry (CRP) the camera is close to the subject and is typically hand held or on a tripod with an object-to-camera distance of less than 300 meters [19]. With the rapid advance of technology of electro-optics and computers, the availability of high resolution video and digital cameras extends the applications of close-range photogrammetry to manufacturing [30, 31], the analysis of architecture and structure [32, 33], robot calibration [15, 17, 18], and plastic surgery applications [19].

2.1.3 Mathematical Basics of Photogrammetry

There are mainly three coordinate systems involved in photogrammetry, image coordinate system, camera coordinate system and object coordinate system. The goal of photogrammetry is to determine the 3D *xyz* coordinates of the points of interest in the defined coordinate system (usually the object coordinate system) by interpreting the relationship between these coordinate systems with the help of photogrammetric observations and survey observations. In this section an introduction to coordinate transformation is given first, through which the relationship between different coordinate systems can be described. Then the three coordinate systems are discussed in detail. The collinearity equations are derived at the end of this section, which demonstrate that each object point is projected into a unique image point. The collinearity equations provide a mathematical model for a photogrammetric bundle adjustment.

2.1.3.1 Coordinate Transformation

A coordinate transformation transforms the coordinates of a point in one coordinate system into the coordinates of the same point in a second coordinate system. The affine transformation is the most general transformation model which preserves straight lines and ratios of distances between points lying on straight lines while changes in position, size and shape of a network are allowed. Usually a total of 12 parameters are used to define relationship between a three dimensional Cartesian initial coordinate system xyz and a corresponding target system x'y'z'. Each transformed coordinate is dependent on all 3 coordinates in the initial system.

$$\begin{aligned} x' &= x_0 + a_1 x + a_2 y + a_3 z \\ y' &= y_0 + a_4 x + a_5 y + a_6 z \\ z' &= z_0 + a_7 x + a_8 y + a_9 z \end{aligned} \tag{2.1}$$

Here x_0, y_0, z_0 stand for the translation and a_1 to a_9 stand for nine additional affine parameters. Nine affine parameters a_1 to a_9 need to be used to describe only six geometric parameters: 3 rotations and 3 scaling factors (one per axis), therefore, the values of the affine parameters do not have geometric meaning directly.

A transformation in which the scale factor is the same in all directions is called similarity transformation. A similarity transformation preserves angles and changes all distance in the same ratio, so shape will not change, but the lengths of lines and the position of points may change. Mathematically speaking, similarity transformations are just a special case of affine transformations. Seven parameters (3 translations to the origin of the xyz system, 3 rotations α, β, γ and 1 scaling factor m) are used to describe similarity transformations in 3D, see equation (2.2). These parameters can be calculated by use of a least-square adjustment if sufficient identical points are given to solve the corresponding equation system (3 points in 3D). Also it needs to make sure that those points are not close to the same plane in 3D.

$$\begin{bmatrix} x' \\ y' \\ z' \end{bmatrix} = \begin{bmatrix} x_0 \\ y_0 \\ z_0 \end{bmatrix} + m \bullet R(\alpha, \beta, \gamma) \bullet \begin{bmatrix} x \\ y \\ z \end{bmatrix} \tag{2.2}$$

The spatial similarity transformation is functionally equivalent to central projection in 3D space. Central projection is used to drive the collinearity equations, which are the fundamental equations of analytical photogrammetry [19, 24]. Also, the spatial similarity transformation is used for the transformation of local 3D coordinates into world coordinate system. Transformation formulas are highly non-linear and therefore need to be linearized when parameters are estimated. The spatial similarity transformation is often used if rotation angles are small [39]. For big rotation angles in 3D, adjustment may fail if initial approximation values are not good enough. Thus, an estimation of the most probably result should be known in advance. To overcome such limitation, if at least 4 identical points are given, an affine transformation can be used instead of a similarity transformation.

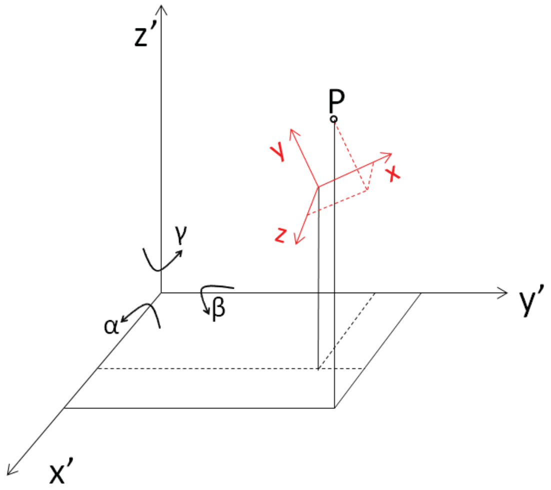

Figure 2.2: Spatial similarity transformation.

2.1.3.2 Coordinate Systems

Image coordinate system, camera coordinate system and object coordinate system are the three main coordinate systems used in photogrammetry. The image coordinate system is a two-dimensional rectangular Cartesian coordinates reference system, $x'y'$, defined on the image plane of a camera, as shown in Figure 2.3. In a digital imaging system, the image coordinate system is defined by the imaging sensor matrix and the origin of the coordinate system usually locates at the image center.

A camera can be modeled as a spatial system that consists of an image plane and the lens with its perspective center. The origin of the camera coordinate system is at the perspective center. Mathematically, the perspective center of a camera is the point of central perspective that is the point through which all straight lines from all image rays pass. The spatial position of the perspective center in the image coordinate system is given by the parameters of interior orientation. The interior orientation parameters (IOPs) of a camera define the spatial position of the perspective center, the principal distance and the location of the principal point. Radial and tangential distortion, image affinity and orthogonally are also described by these parameters. The schematic of interior orientation of a camera is shown in Figure 2.3. The parameters of interior orientation are

- center of the image M'
- perspective center O'

  The point inside a camera which all straight lines from all image rays pass.
- principal point H' :

  Nadir of the perspective center with image coordinates (x_0, y_0). It approximately equal to the center of the image: $H' \approx M'$
- principal distance c:

  Normal distance to the perspective center from the image plane in the negative z direction. It approximately equals to the focal length of the lens when focused at infinity: $c \approx f$
- parameters of functions describing imaging errors:

  Parameters that describe deviations from the central perspective model are dominated by the effect of radial-symmetric distortion

For the parameters shown in Figure 2.3:

- (x', y') are the measured coordinates of image point P'
- (x_0, y_0) are the coordinates of the principal point H'
- $(\Delta x, \Delta y)$ are the distortion in image space.

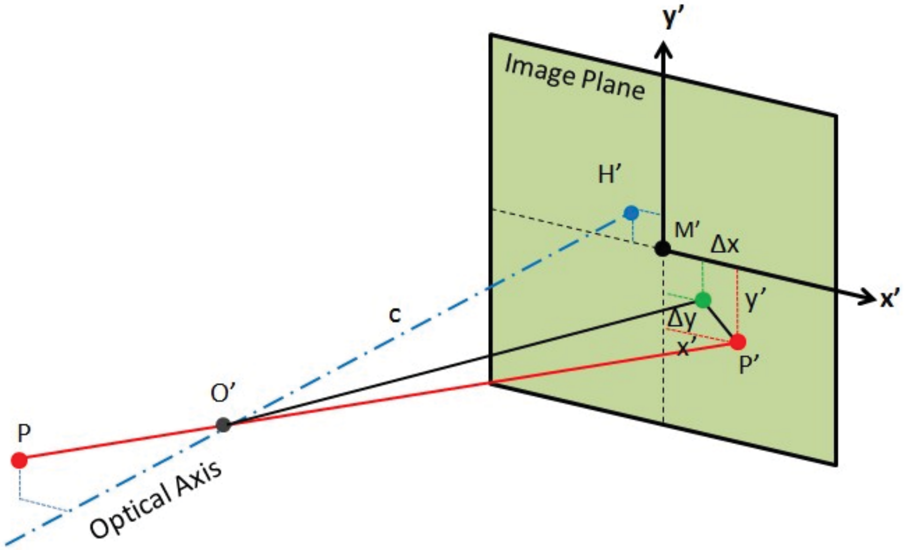

Figure 2.3: Interior orientation of a camera

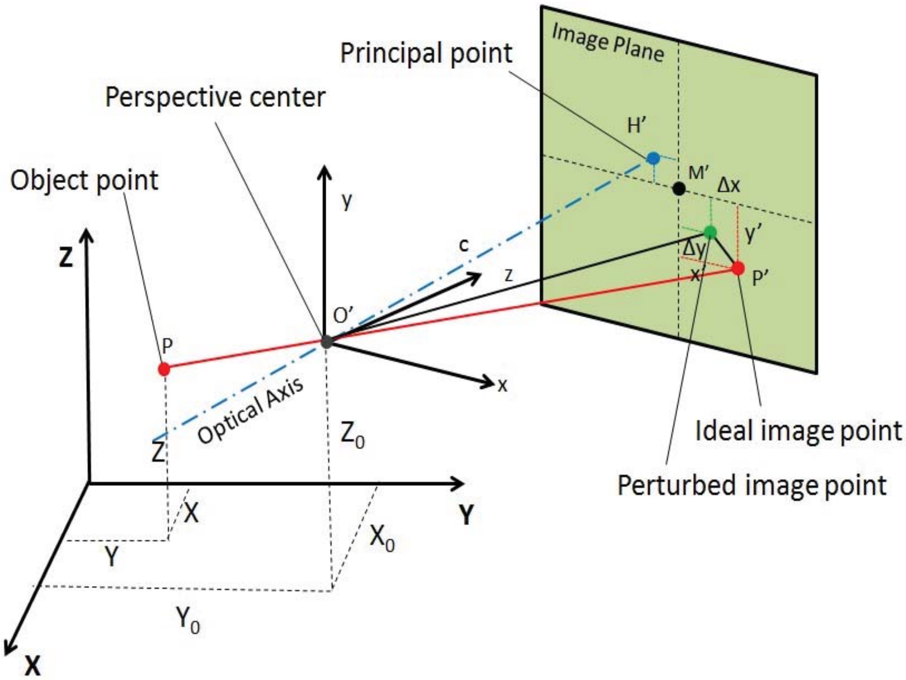

Figure 2.4: Perspective projections from the 3D object space to the image plane.

The object coordinate system is also known as world/global coordinate system, which is a spatial Cartesian coordinates system *XYZ* that is defined by reference points on an object. The exterior orientation parameters (EOPs) describe the spatial position and orientation of the camera coordinate system with respect to the object coordinate system. Figure 2.4 illustrates the perspective projection relationship between the 3D coordinates (*X, Y, Z*) in the object space and the corresponding 2D *xy* coordinates in the image plane. The projection of an image point into a corresponding object is given by equation (2.3).

$$\begin{bmatrix} X \\ Y \\ Z \end{bmatrix} = \begin{bmatrix} X_0 \\ Y_0 \\ Z_0 \end{bmatrix} + mR \begin{bmatrix} x \\ y \\ z \end{bmatrix} \tag{2.3}$$

where

- (*X,Y,Z*) are the coordinates of object point in the object coordinate system
- (X_0, Y_0, Z_0) are the coordinates of the perspective center
- *m* is the scaling factor of transformation
- (*x, y, z*) are the coordinates of object point in the image plane
- *R* is the rotation matrix defined as

$$R = R_\omega R_\varphi R_\kappa = \begin{bmatrix} r_{11} & r_{12} & r_{13} \\ r_{21} & r_{22} & r_{23} \\ r_{31} & r_{32} & r_{33} \end{bmatrix}$$

$$= \begin{bmatrix} \cos\varphi\cos\kappa & -\cos\varphi\sin\kappa & \sin\varphi \\ \cos\omega\sin\kappa + \sin\omega\sin\varphi\cos\kappa & \cos\omega\cos\kappa - \sin\omega\sin\varphi\sin\kappa & -\sin\omega\cos\varphi \\ \sin\omega\sin\kappa - \cos\omega\sin\varphi\cos\kappa & \sin\omega\cos\kappa + \cos\omega\sin\varphi\sin\kappa & \cos\omega\cos\varphi \end{bmatrix} \tag{2.4}$$

The first rotation R_ω is around the object-space coordinate X axis, the second rotation R_φ is around a new object-space coordinate Y axis (after the first rotation) and the third rotation R_κ is around a new Z axis (after the first and second rotations).

2.1.3.3 Collinearity Equations

By inverting equation (2.3), adding the principal point H' (x_0, y_0) and introducing correction terms ($\Delta x, \Delta y$) (image distortion parameters), the image coordinates are given by:

$$\begin{bmatrix} x - x_0 - \Delta x \\ y - y_0 - \Delta y \\ z \end{bmatrix} = \frac{1}{m} \begin{bmatrix} r_{11} & r_{12} & r_{13} \\ r_{21} & r_{22} & r_{23} \\ r_{31} & r_{32} & r_{33} \end{bmatrix} \begin{bmatrix} X - X_0 \\ Y - Y_0 \\ Z - Z_0 \end{bmatrix} \tag{2.5}$$

The unknown scaling factor m can be eliminated by dividing the first and second equation by the third equation in equation (2.5), which leads to the collinearity equations

$$\begin{aligned} x &= x_0 + z\frac{r_{11}(X - X_0) + r_{12}(Y - Y_0) + r_{31}(Z - Z_0)}{r_{13}(X - X_0) + r_{23}(Y - Y_0) + r_{33}(Z - Z_0)} + \Delta x \\ y &= y_0 + z\frac{r_{12}(X - X_0) + r_{22}(Y - Y_0) + r_{32}(Z - Z_0)}{r_{13}(X - X_0) + r_{23}(Y - Y_0) + r_{33}(Z - Z_0)} + \Delta y \end{aligned} \tag{2.6}$$

The collinearity equations describe the transformation of object coordinates (*X,Y,Z*) into corresponding image coordinates (*x, y*) as functions of the interior orientation parameters (x_0, $y_0, c, \Delta x$, Δy) and exterior orientation parameters ($X_0, Y_0, Z_0, \omega, \varphi, \kappa$) of one image. It is demonstrated by collinearity equations that each object point is projected into a unique image point. These collinearity equations provide a mathematical model for a photogrammetric bundle adjustment [12, 30].

Bundle adjustment is a method for simultaneous numerical fit to refine the 3D coordinates of a scene geometry as well as the parameters of the cameras employed to acquire the images by using photogrammetric observations, survey observations and an object coordinate system [19]. With a minimum number of reference points (tie points), each image is merged into a global 3D model, which is the reconstruction of the object. It is of the most importance that “all corresponding image rays should intersect in their corresponding object point with minimum inconsistency” [19].

2.2 Applications of Close Range Photogrammetry

The conditions under which photogrammetric methods of measurement are helpful were first summarized by E.H. Thompson in 1962. Considering the advance of technologies recent years, T. Luhmann listed additional conditions. These conditions are:

1. when the object to be measured is inaccessible or difficult of access
2. when the object is not rigid and its instantaneous dimensions are required
3. when it is not certain which measurements will be required
4. when the object is very small
5. when the use of direct measurement would influence the measured object or would disturb a procedure going on around the object
6. when real-time results are required
7. when the simultaneous recording and the measurement of a very large number of points is required.

The above distinct conditions where CRP can be applied indicate the wide and diverse applications of CRP and discussion will be given on its applications in aerospace industry, architecture and heritage conservation, automotive and machine industries and engineering in the following with examples.

2.2.1 Photogrammetry in Aerospace Industry

Photogrammetric techniques have been found to be very useful in aerospace industry for measurement of parabolic antennae, tunnel testing, control of assembly, aircraft flight testing, flight testing of large space structures and space simulations [40-41, 71-79]. Barrows et al. [40] from National Aeronautics and Space Administration (NASA) utilize multi-camera photogrammetric system to measure the blade deformation of the four-bladed rotor. A commercial photogrammetric measurement system V-STARS and eight cameras were used. Figure 2.5 illustrates the schematic of the setup and a sample image of rotor blades. Another example shown in Figure 2.6 shows the application of videogrammetric method for measurement of static and dynamical aeroelastic deformation of aircraft wings during flight testing [41]. A standard resolution flight-hardened video camera used for surveillance was used to record the image sequences of the left wing. Coordinates of installed targets could be determined so that the deformation of aircraft wing can be computed.

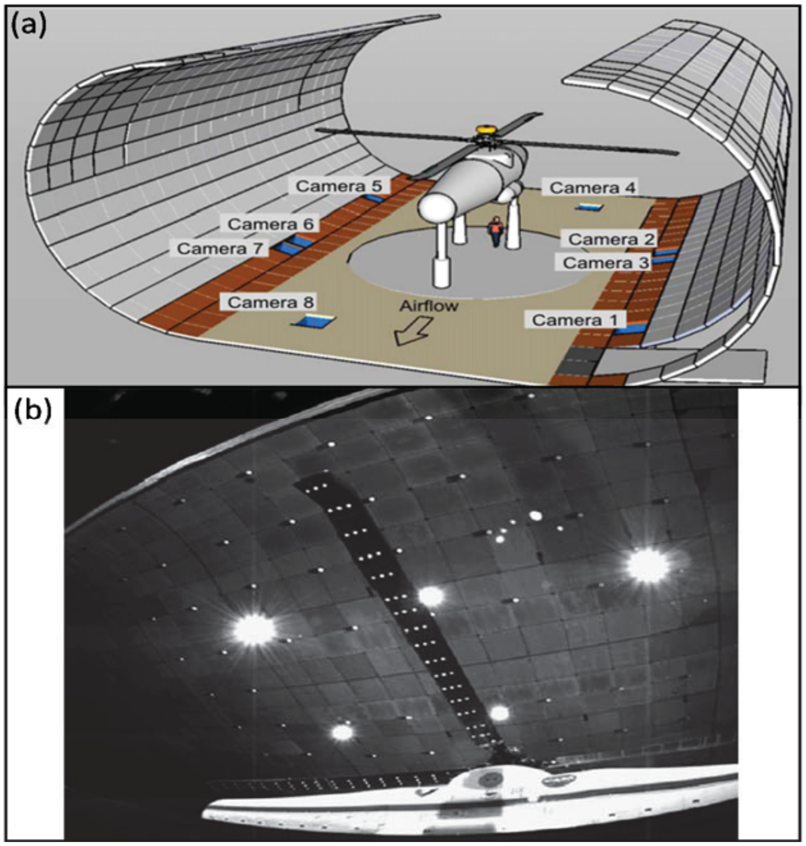

Figure 2.5: Multi-camera photogrammetric system used to measure the blade deformation of four-bladed rotor [40]: (a) schematic showing the floor cavity location in which digital cameras and strobes are installed, (b) rotor blades with retro-reflective targets installed onto the test-section ceiling for camera orientation.

F/A – 18 Active Aeroelastic Wing research aircraft.

Camera pod and left wing.

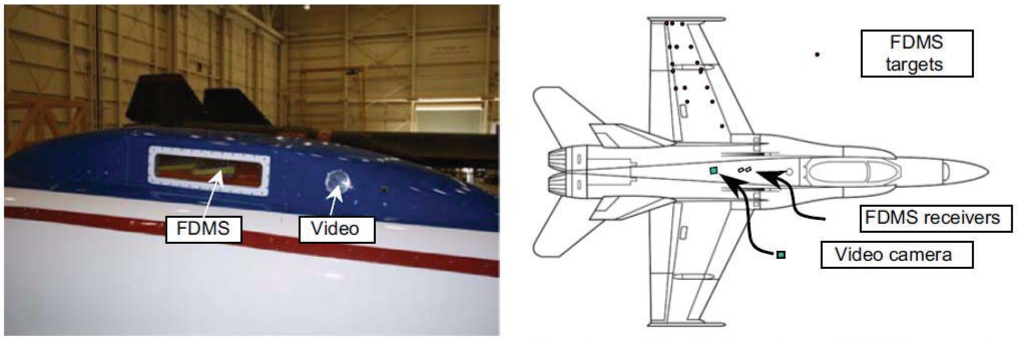

Camera pod viewports.

Planview with video camera, FDMS receivers and targets (circles) indicated

Figure 2.6: Videogrammetric method for the measurement of static and dynamical aeroelastic deformation of aircraft at NASA's Dryden Flight Research Center (DFRC) [41].

2.2.2 Photogrammetry in Architecture and Heritage Conservation

Photogrammetry can supply documentation in measuring inaccessible/dangerous areas and historic buildings, and it has been proved to be of great importance in architecture, heritage conservation and archaeology areas for facade measurement, historic building documentation, reconstruction of damaged buildings, mapping of excavation sites and 3D city models [42-43, 46-47]. An example of reconstruction of damaged buildings using photogrammetry method is shown in Figure 2.7. The building located on Konya (Figure 2.7(a)), Turkey, was built in the 18th century and was accidently damaged by fire. Photogrammetry was used to determine the original status and measurements of building so that the building could be restored. Figure 2.7 (b) shows an image of the building and the 3D model of such building was solved through photogrammetry and was illustrated in Figure 2.7 (c). The building was reconstructed with the help of the 3D model of building and the reconstructed situation of the building was shown in Figure 2.7 (d).

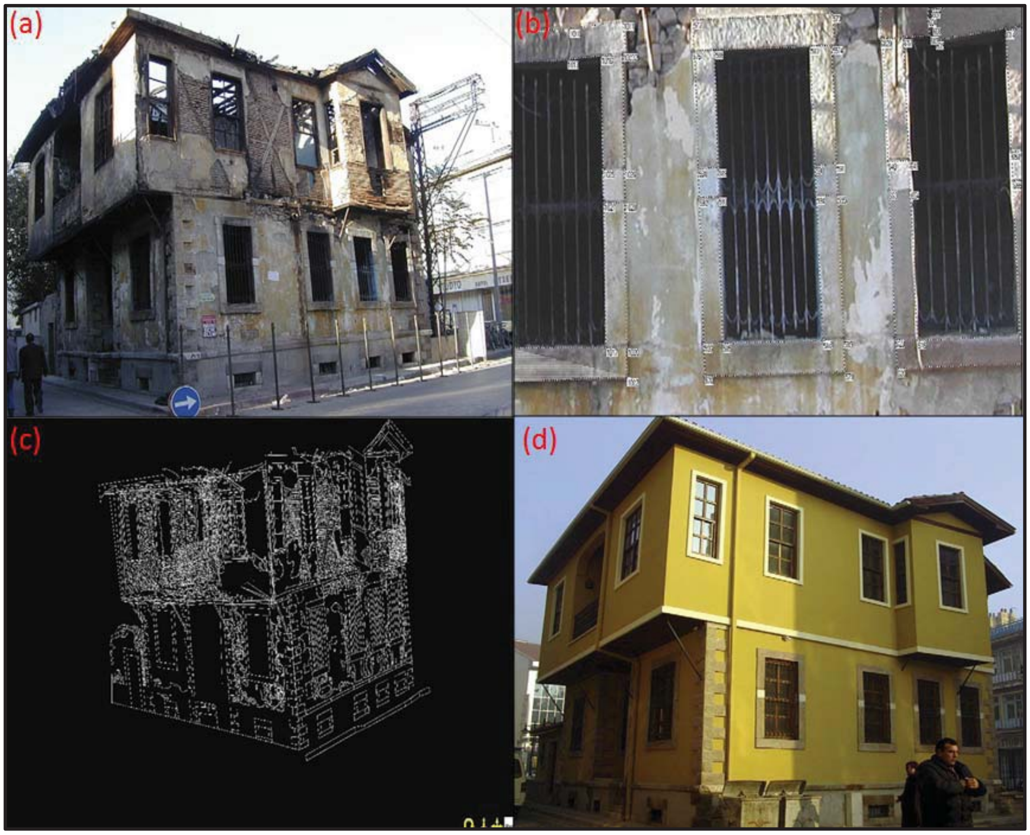

Figure 2.7: Reconstruction of damaged buildings using photogrammetry method [42]: (a) the situation of the building after fire, (b) control points on photograph, (c) 3D model of building solved with photogrammetry, (d) the reconstructed situation of the building.

2.2.3 Photogrammetry in Automotive, Machine and Shipbuilding Industries

Digital photogrammetric system has been used in automotive manufacturing to measure car body deformation, adjust tooling and rigs and control supplier parts [14-18, 45, 84-85]. In shipbuilding industry photogrammetry based system also is considered as a flexible and effective method to measure ship hull shapes. Figure 2.8 shows an example of utilizing photogrammetry to measure the damage (a large hole due to a collision in this case) in the fore ship of an inland waterway vessel so that it can be re-engineered and repaired [45]. On-line and off-line photogrammetry systems are also used in the industry of robot calibration. By measuring and tracking the position and orientation of the target applied to the end of the robot arm, the accuracy of the robotic measurement can be improved. Figure 2.9 (a) illustrates off-line measurement system. The end effector installed to the end of robot arm has a grid of dot targets attached and it moved along with the movement of robot arm. Additional dot pattern was projected to the stationary background surface. Two cameras were positioned to cover the measurement area so that the end effector is tracked with respect to the stationary camera stations. An on-line photogrammetry system is shown in Figure 2.9 (b) and a camera is attached to the end effector of the robot [17]. During the calibration process the camera moved together with the robot while the targets are fixed to a concrete factory floor.

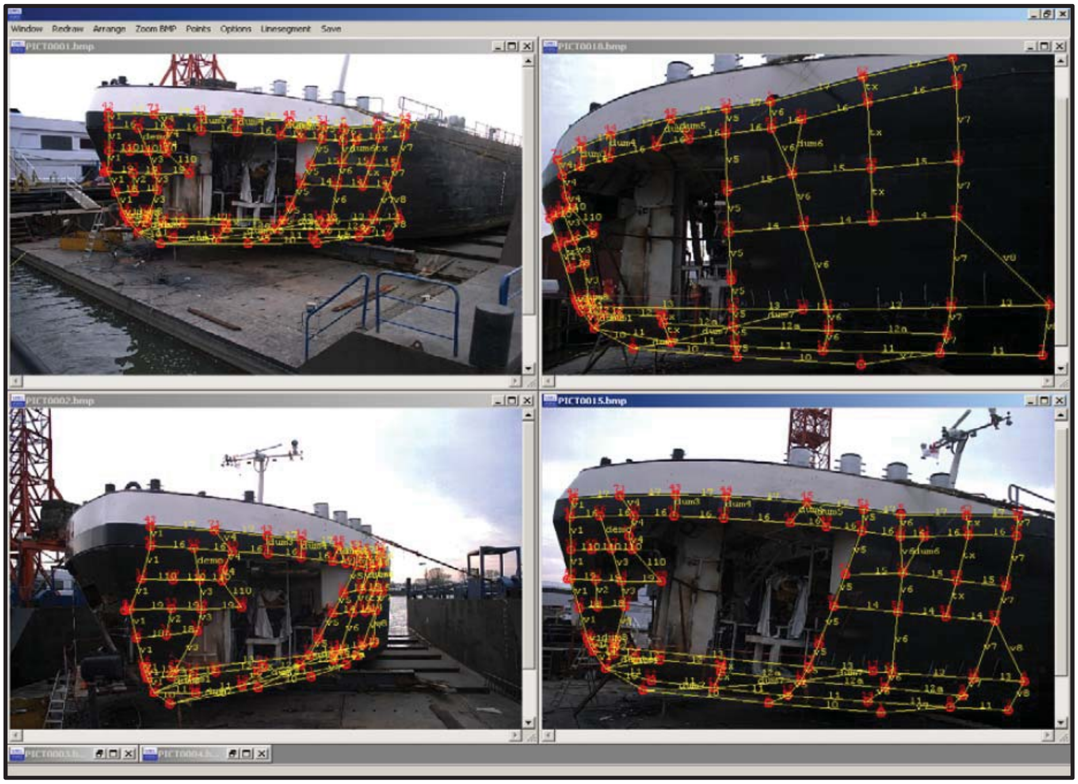

Figure 2.8: Reconstruction of damaged buildings using photogrammetry method [45]: (a) the situation of the building after fire, (b) control points on photograph, (c) 3D model of building solved with photogrammetry, (d) the reconstructed situation of the building.

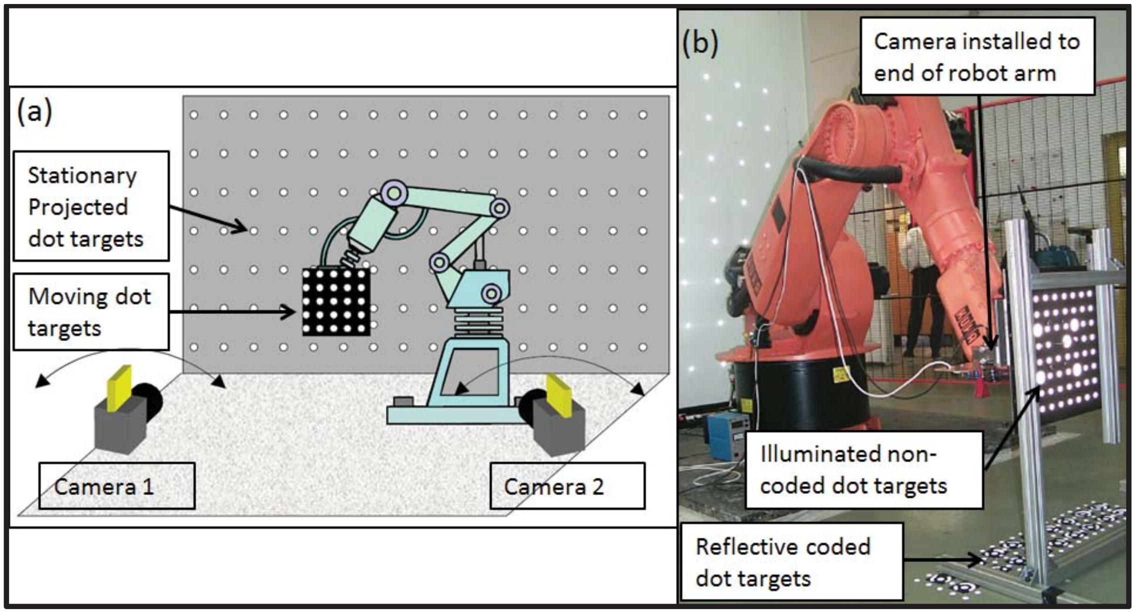

Figure 2.9: Robot calibrations using off-line and online photogrammetric systems developed in University of Stuttgart by Hefele (a) off-line measurement system, (b) on-line measurement system [17].

2.2.4 Photogrammetry in Engineering

In engineering, photogrammetry has been used for measurement of large civil engineering sites, pipework and tunnel measurement, mining, as-built measurement of process plants and structure deformation measurement [80-83]. Photogrammetry has been used in bridge measurement for long term deformation in bridges since 1985 [19]. An example shown below is studies on deformation measurement of a laboratory beam and a field bridge using a single camera setup [19]. Figure 2.10 (a) illustrates the laboratory study, where the deflection of a 2 m concrete beam was measured. The field study was performed to measure the vertical deflection of an unreinforced concrete arch bridge located in Erfurt, Germany (see Figure 2.10 (b)). The photogrammetric measurement showed a maximum vertical deflection of the bridge of 2 mm was measured.

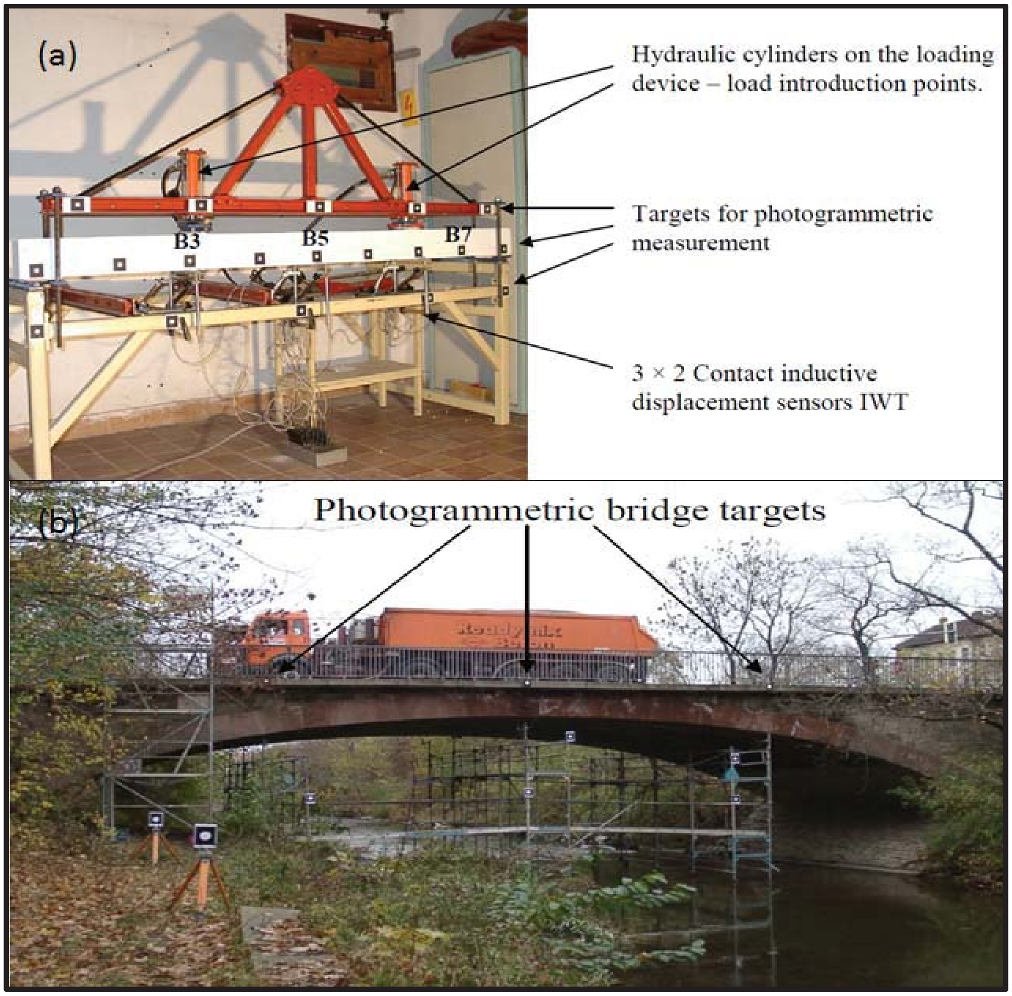

Figure 2.10: Photogrammetry deflection measurement of bridge, (a) beam, (b) the field bridge.

2.3 Optical Pattern Projection and Applications in Non-contact Measurement

Optical pattern projection (or structured light projection) is the process to project a known optical pattern on to a scene so that the information of the object of interest in the scene can be determined by vision systems, which assess the level of pattern distortion. The optical pattern can be generated by sinusoidal fringe projection techniques or coded light projection techniques. The known property/codification of the optical pattern is either used to perform triangulation between the pattern projector and at least one camera or provides photogrammetric feature for multi-camera configuration.

Optical pattern projection has been widely used to measure three dimensional profiles of object with diverse applications in engineering field like online inspection of product quality, body surface evaluation for orthotics and navigation in biomedical engineering [63-70]. A schematic diagram of pattern projection system was shown in Figure 2.11. An optical pattern generated by a projector is projected onto the object being measured. A camera located in the direction different from the projector capture the optical pattern on the object surface. The profile of the object can be calculated based on the deformed image of the optical pattern corresponding to the object height from the reference plane.

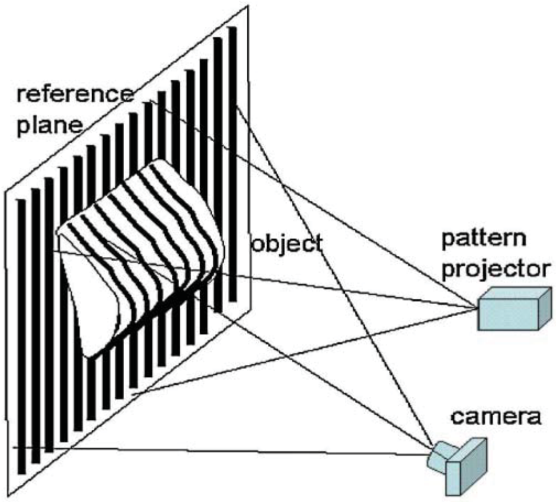

Figure 2.11: Schematic diagram of pattern projection system.

Figure 2.12 illustrates the on-machine measurement system developed by National Institute of Standards and Technology (NIST) [48] for improvements in machine positioning and optical fabrication. This system can be used for a meso-scale milling machine where the machines performance will be improved significantly. A commercial surface measurement system of 3D parts using fringe projection technique developed by Carl Zeiss Ltd. is illustrated in Figure 2.13. Based on phase-measuring deflectometry method [49-51], images captured by camera will provide information on difference in brightness, recognition of matt and glossy area and recognition of geometric flaws for the entire surface. Such system can provide inline automatic surface inspection on various matte to glossy surface including metallic, painted, galvanized surfaces as well as plastics [52].

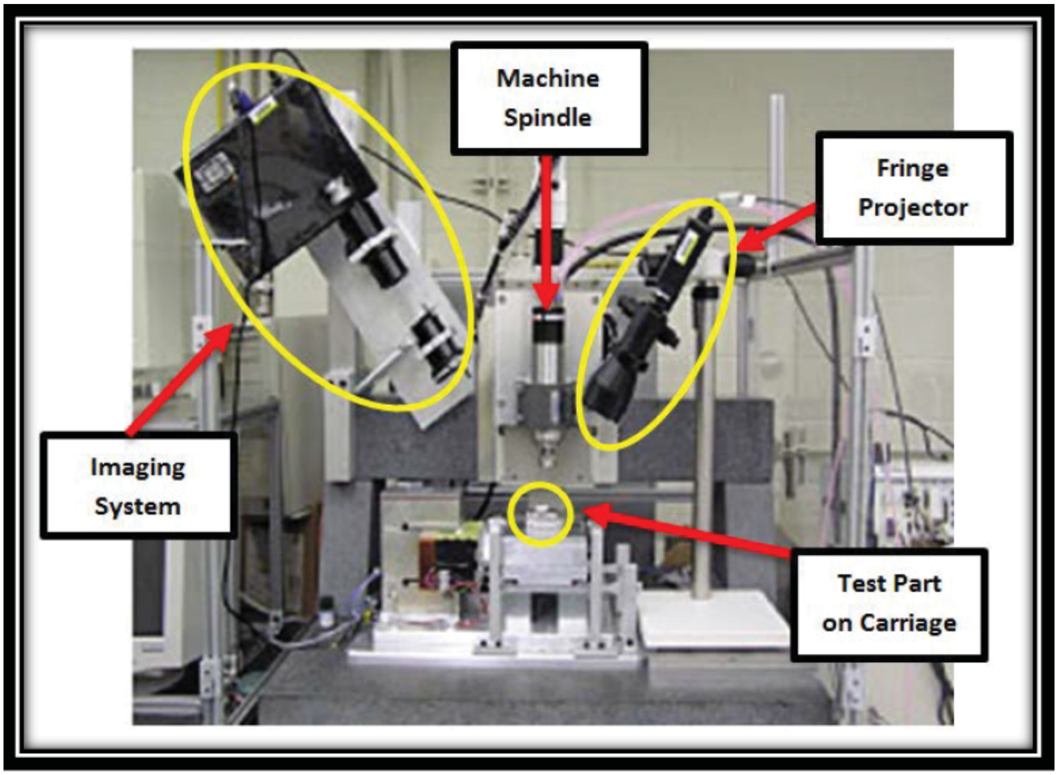

Figure 2.12 NIST in-situ fringe projection measurement system [48].

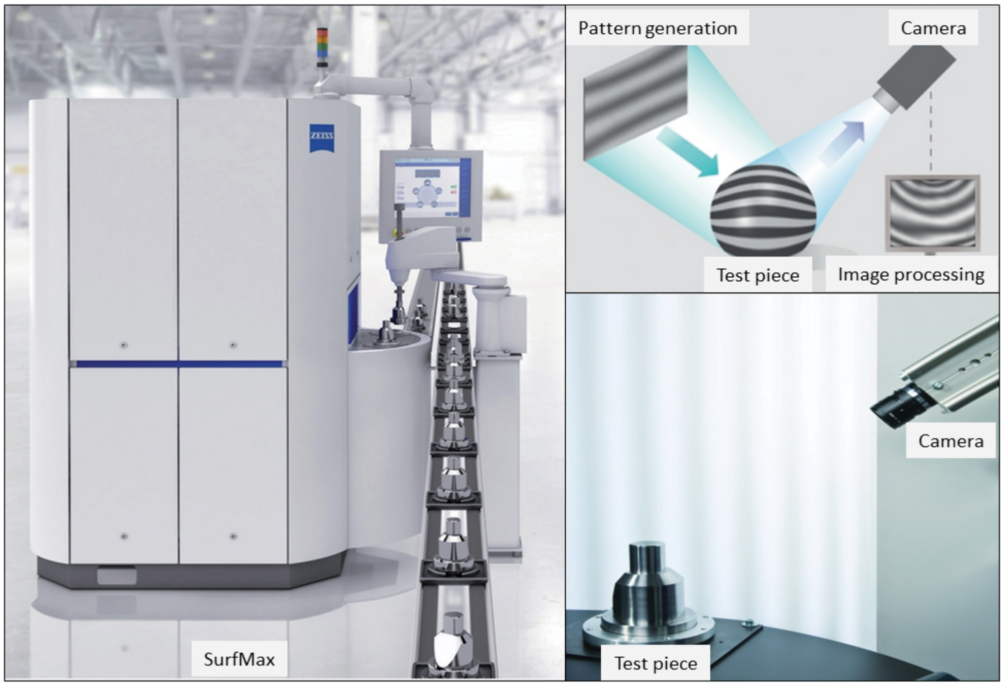

Figure 2.13: SurfMax inline tester for the surface evaluation of 3D parts [52]

Optical pattern projection generated by the combination of laser and diffractive elements has been used for aerospace industry [54-62]. In 1995, Matthies et al. from JPL (Jet Propulsion Laboratory) first proposed the combination of the laser dot diffraction pattern and stereo cameras for hazard detection for planetary rovers [53, 54]. A laser-based optical sensor system was developed based on optical pattern projection to provide hazard detection for planetary rover, as shown in Figure 2.14. The location of the projected laser spots is be determined by images taken by two cameras through triangulation method and this location information is used to declare a hazard.

NASA employs the combination of optical pattern projection and photogrammetry to perform static shape measurement of reflective membrane surfaces and dynamic measurement of diffuse white surface. Figure 2.15 shows the schematic of test setup and an image of fluorescence dot projection on membrane surface [55-57].

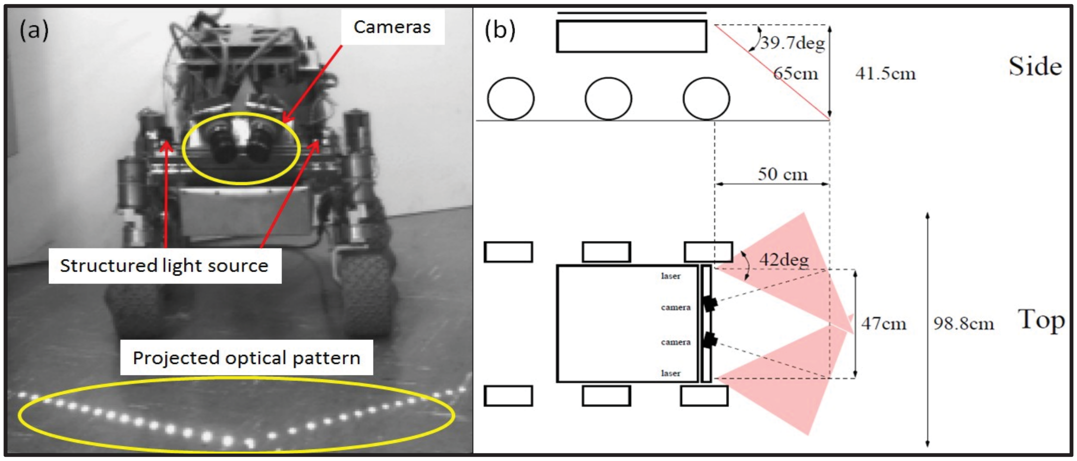

Figure 2.14: Hazard detection for planetary rovers using optical pattern projection proposed by Matthies in JPL [53, 54]. (a) Front view of the robot Rocky III rover. The laser spots are arranged as a "push-broom" ahead of it. (b) Schematic of laser and camera configuration aboard the Lightweight Survivable Rover (LSR-1). The shaded areas represent distributed laser beams.

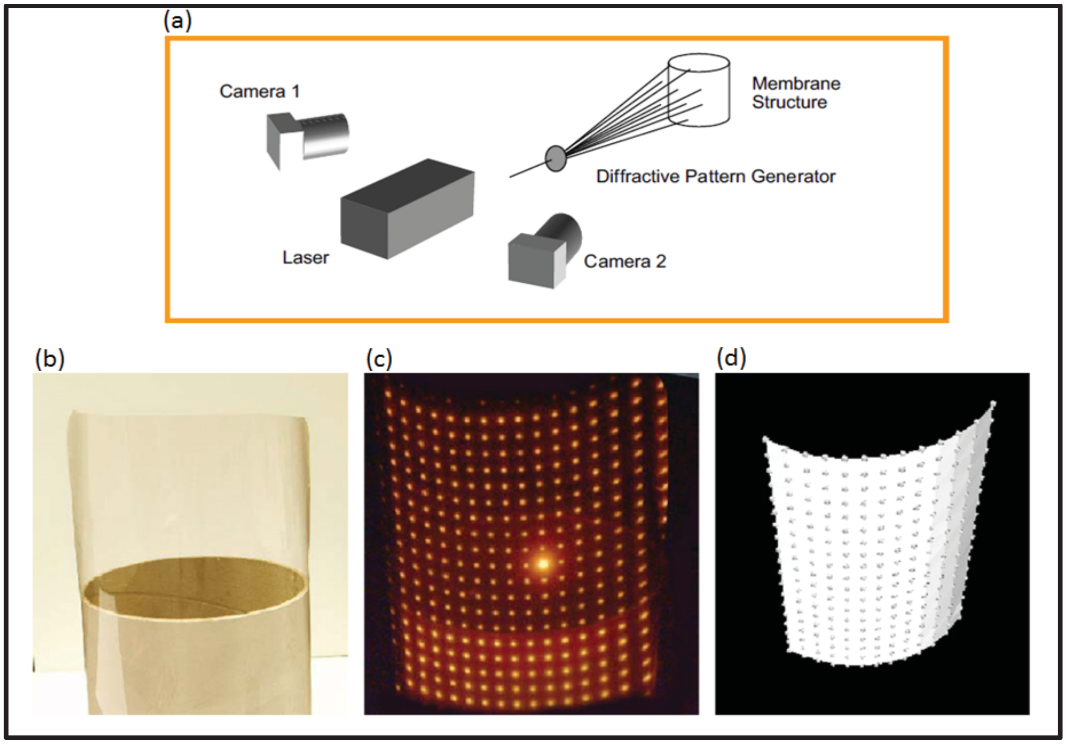

Figure 2.15: NASA implementation of photogrammetry and optical pattern projection to measure space structures [55-57]: (a) test configuration to measure transparent membranes using laser-induced fluorescence for dot-projection photogrammetry, (b) transparent CP-2+dye, (c) fluorescence from laser dot projection, (d) 3D surface by photogrammetry.

2.4 Non-contact Six Degree of Freedom Measurement Techniques

The 3-dimensional position and orientation of a rigid body are usually described by six spatial parameters, (x, y, z) for translation, and pitch, roll, and yaw for rotation. The ability to estimate the pose of an object or to measure the relative position and orientation between objects is of great interest in a diverse range of applications including machine tool metrology, robot calibration, motion control, motion analysis, and reconstructive surgery. Several solutions have been proposed for 6 DOF navigation and tracking tasks that work with different technologies, such as the indoor global positioning system (iGPS), inertial navigation systems (INS), laser based sensor, computer vision technique, pure photogrammetric solution for object tracking and laser tracker.

2.4.1 Indoor GPS

The Global Positioning System (GPS) is "a space-based global navigation satellite system (GNSS) that provides reliable location and time information in all weather and at all times and anywhere on or near the Earth when and where there is an unobstructed line of sight to four or more GPS satellites" [101]. It depends on the signals of 24 satellites that are circling at a height of 19, 300 km around the earth. Based on triangulation of the signals to several satellites, the position of an earth station can be calculated. However, the GPS system is generally not suitable to estimate indoor locations due to the fact that microwaves will be attenuated and scattered by roofs and other objects. In order to make positioning signals obtainable everywhere, integration between GPS and indoor positioning must be made.

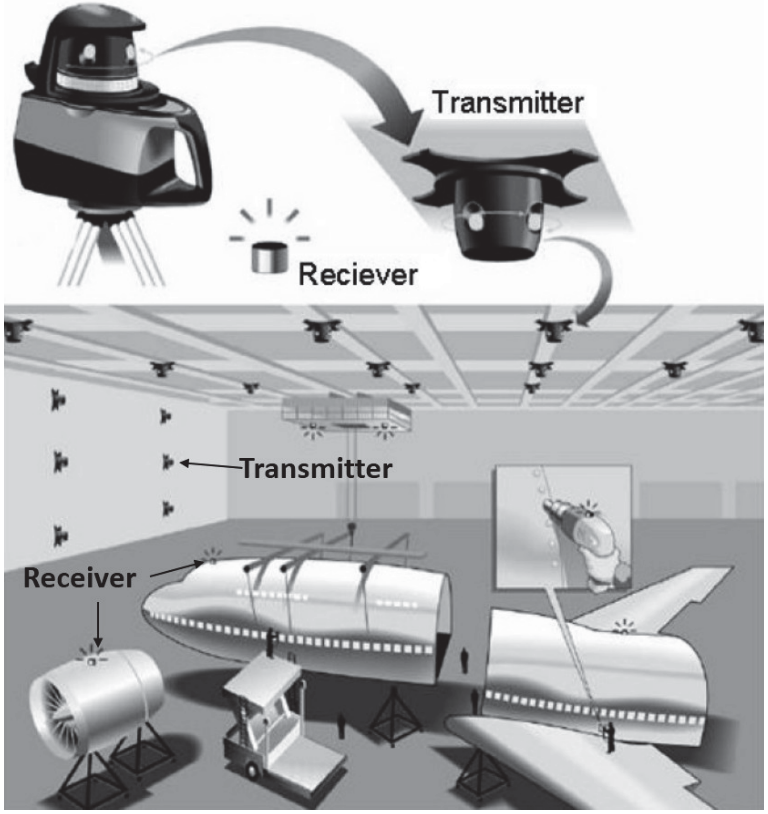

Figure 2.16: Indoor GPS

To make the Indoor GPS (iGPS) available, the satellites have to be replaced by three or more infrared-transmitters on the ceiling or walls. Receivers must be mounted on the measured object to pick up the signals. In this way the object can be measured in a coordinate system created in the building. Figure 2.16 displays a sample of the indoor GPS. The typical accuracy of iGPS is around 200 μm for a typical measurement volume of 40× 40 m [2, 114-116]. A major problem existing in Indoor GPS is called "fading" [1]. Because in the majority of cases the navigation signal does not reach the receiver antenna via a direct line-of-sight, but rather experiences such phenomena as reflections, diffraction, or scattering when entering a building and propagating indoors. These effects typically lead to severe deterioration of position accuracy.

2.4.2 Inertial Sensing Technique

The 6 DOF inertial sensors generally consist of a tri-axial accelerometer along with three gyroscopes. The 6 DOF inertial sensors measure linear and angular accelerations and integrate them with respect to time to estimate 3D position (x, y, z coordinates) and 3D rotation (roll, pitch and yaw). Systems based on inertial navigation units provide very fast tracking and navigation of object without any line of sight restrictions in real-time. Other advantages of such technique include their low cost, small size and source-less nature. They are often used for 6 DOF human body motion tracking and for 6 DOF motions estimation of aircraft, missiles and rockets. However, errors in all six components are accumulated and keep increasing over time. These drawbacks make this technique not suitable for precise measurement. The “Military grade” inertial measurement unit (IMU) is reported to have position performance to 2 cm/s [102].

2.4.3 Laser Based Sensor

Optical system implementing position sensitive detectors (PSDs) and laser has been proposed to simultaneously measure 6 DOF motion of an object. However, the measurement ranges are usually limited. In 1997 Lee et al. proposed a 6 DOF displacement monitoring system by using four PSDs and collimated laser [7]. The diagram of their system is shown in Figure 2.17. Lateral resolution better than 50 nm and angular displacement resolution better than 0.25 μrad were achieved with their system while the measured ranges were limited to 200 μm and 2500 μrad for lateral and angular measurement respectively.

In 1998, Vann from Lawrence Livermore National Laboratory (LLNL) employed the same combination of laser and PSDs to develop a small non-contact optical sensor for the application in the robot industry [8]. The 6 DOF sensor (Figure 2.18) can sense its position relative to a piece being machined, allowing the robot to autonomously follow a pre-described machining or manufacturing path. Park et al. mount a three-facet mirror to the object to be measured, so that three beams reflected from the mirror were detected by three PSDs as shown in Figure 2.19. The 3D position and orientation of the three-facet mirror can be calculated from the output signals of the PSDs, thus the 3D position and orientation of the objects of interest can be determined. Their system shown in Figure 2.19 realize measurement accuracy of 3 μm in translation and 13 μrad in rotation, but the measurement range is limited to 202 μm for translation and 2449 μrad in rotation [5, 6].

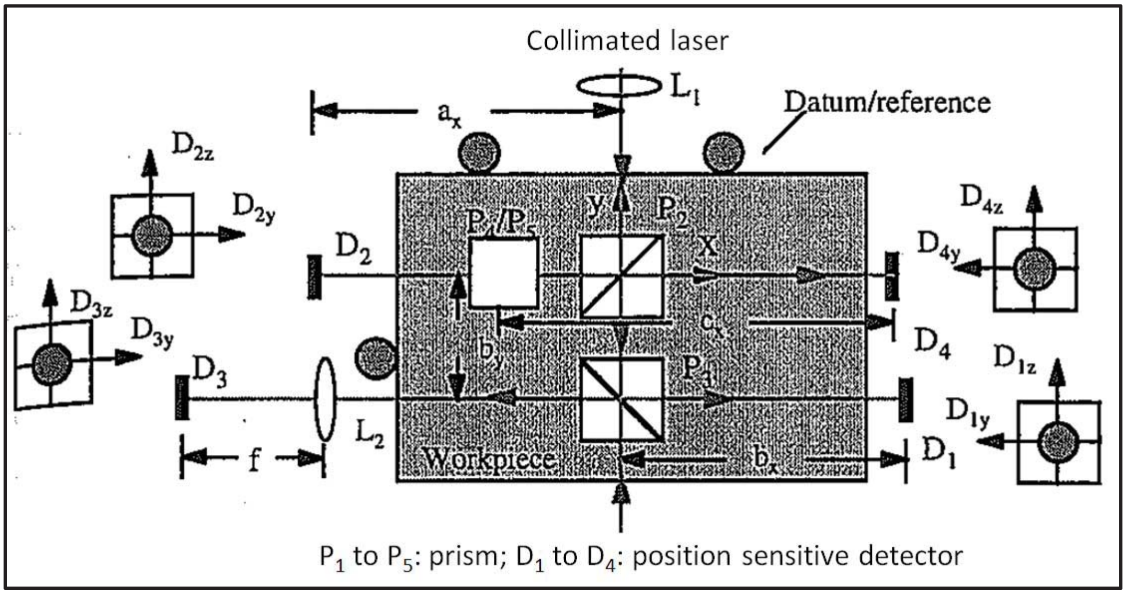

Figure 2.17: 6 DOF displacement monitoring system by using position sensitive detector and laser proposed by Lee et al. in 1997 [7].

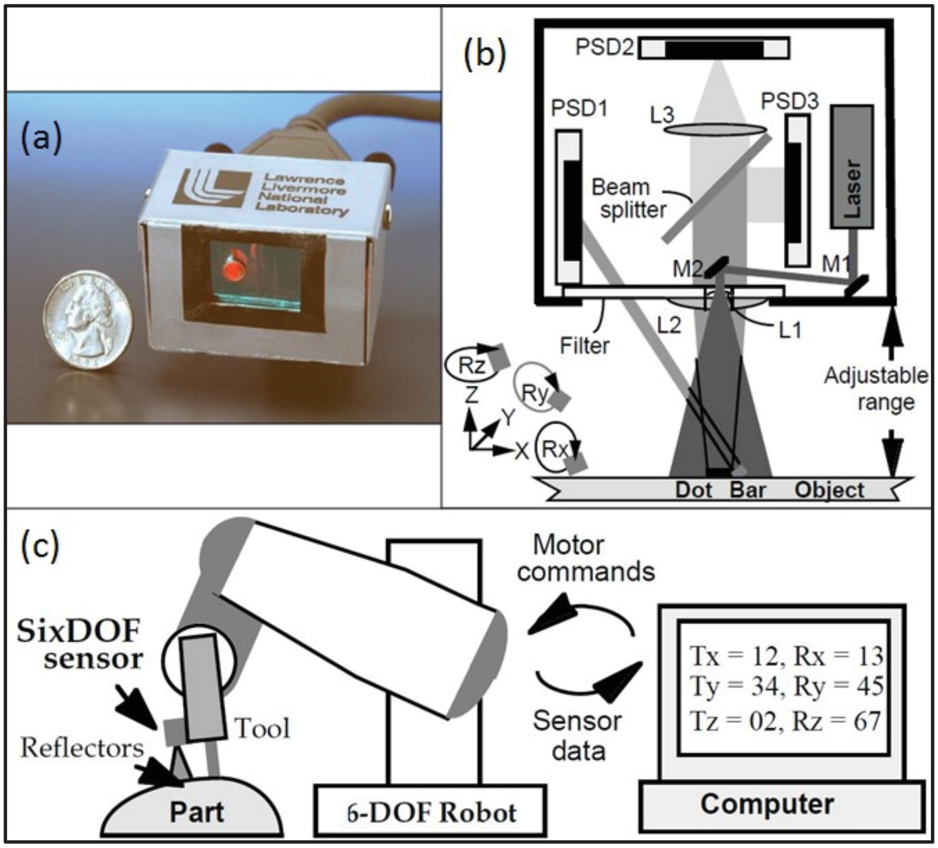

Figure 2.18: 6 DOF position sensor proposed by Vann in LLNL [8]: (a) outlook of position sensor, (b) inside the 6 DOF position sensor, (c) a 6 DOF sensor guiding a robot.

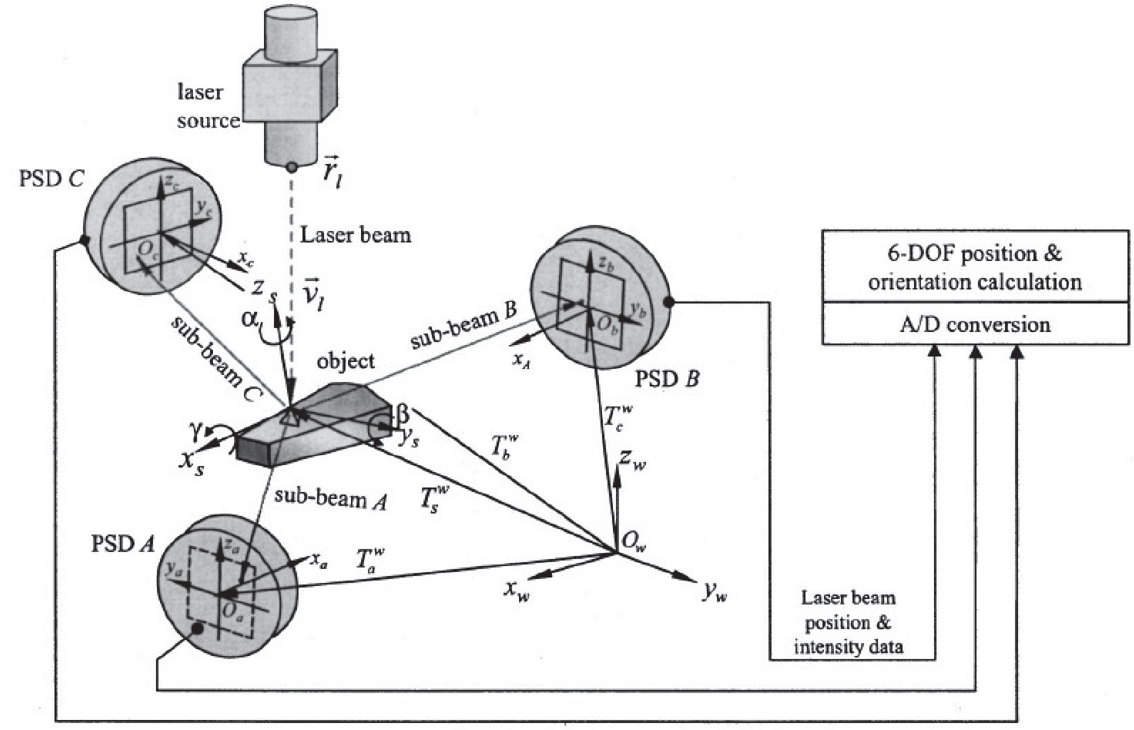

Figure 2.19: 6 DOF displacement measurements of rigid bodies through splitting a laser beam proposed by Park et al. [5, 6].

2.4.4 Laser Tracker

A laser tracker is a device that measures coordinates by tracking a laser beam to a retroreflective target held in contact with the object of interest. The laser tracker was first introduced in the late 1980s [104]. In principle, the laser tracker measures two angles (the azimuth angle and the elevation angle) and a distance [104]. A retroreflective target is held against the object to be measured, and then a laser beam is sent to a retroreflective target by the laser tracker. The laser beam will re-enter the tracker at the same position it left after it is reflected from the target. The spherically mounted retroreflector (SMR) is the most popular retroreflective target. The distance can be measured through the distance meter. The two types of distance meter used in the laser tracker are absolute distance meter (ADM) and interferometer. An interferometer together with a frequency-stabilized helium-neon laser can provide incremental distance measurement. As the laser beam re-enters the tracker, some of it goes to an interferometer so that the distance travelled can be measured. The path from a helium-neon laser to the retroreflector and back into the interferometer is shown in Figure 2.20 (a). The absolute distance can be measured by ADM with the principle of time of flight. For the ADM system inside a tracker (Figure 2.20 (a)), part of the laser re-entering the tracker is converted into an electrical signal so that the time of flight of the laser can be determined. The angular encoders (the azimuth encoder and the elevation encoder shown in Figure 2.20 (a)) measure the angular orientation of the tracker's two mechanical axes: the azimuth axis and the elevation axis. The center of the SMR can be located precisely with the information of the encoders' angle and the measured distance. The general configuration of a laser tracker is shown in Figure 2.20 (b).

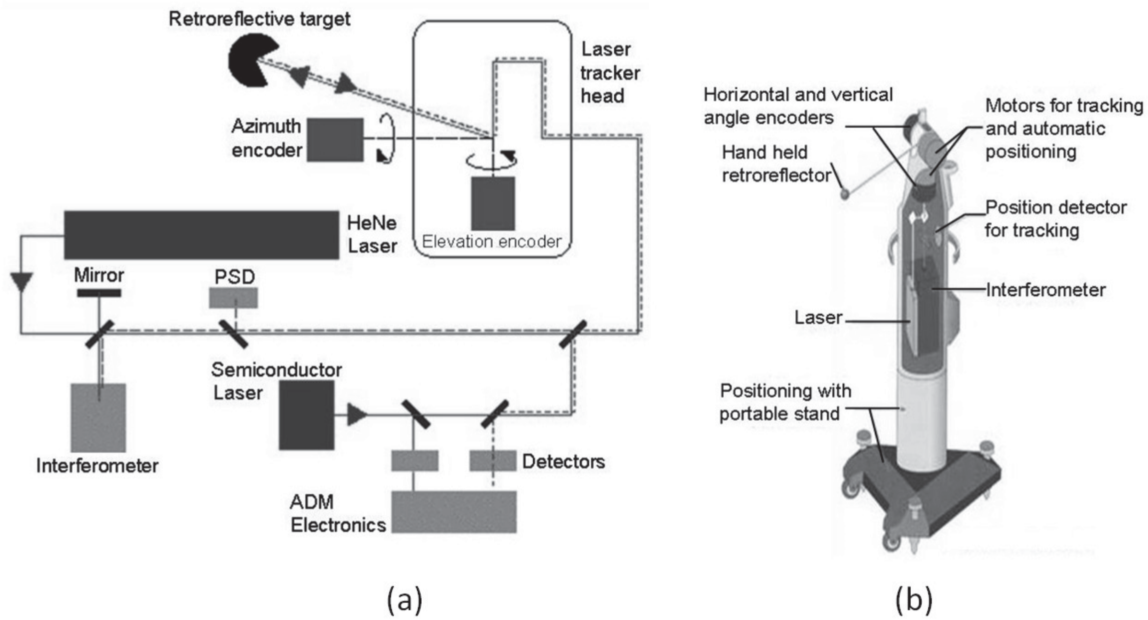

Figure 2.20: The laser tracker system [22]: (a) the path from a HeNe laser to the reflector and back, (b) general configuration inside the laser tracker.

Leica Geosystems presented their laser tracker system Leica AT402, and the accuracy of this laser tracker system is specified to about 10 µm at a 160 m distance [103]. However, the laser tracker system is expensive (hundreds of thousands of dollars) and also requires the object to remain within the sensor's line of sight.

2.4.5 Computer Vision Technique

Computer vision [11, 12] is often used by people who work on virtual environment interaction and in the field of mobile robot navigation. Cameras with known orientation are used to perform space resection to get the so-called 6 DOF or 3D pose estimations of a target. Usually only one camera is employed to monitor one scene. This system has limited measurement accuracy that is on the order of a hundred micrometers [6, 9-12].

In 2005 Vorozcovs et al. [13] proposed the 'Hedgehog' for virtual environment interaction applications. They used the projective surface outside of the view of the user to estimate and track their head pose within the environment. The user worn a helmet with a fixed arrangement of laser diodes attached to, see Figure 2.21.

Cameras behinds screens are used to track the projections of the laser beams and the single-constraint-at-a-time (SCAAT) approach is employed to enable measurement from a locally unobservable system to estimate a globally observable system. They demonstrated the ability to determine the 6 DOF with an angular resolution of 0.01° root mean square (RMS) and position resolution of 0.2 mm RMS. However, the relative error is larger than 10 mm compared with results provided by the IS-900 [117] motion tracking system (using time-of-flight of ultrasonic chirps to determine the pose of the user) employed in the experiment. Cameras were positioned behind each display wall viewing the projection surface, and calibration was required to estimate the plane transformation for each wall surface. In addition, the 'Hedgehog' requires a rather complex hardware installation.

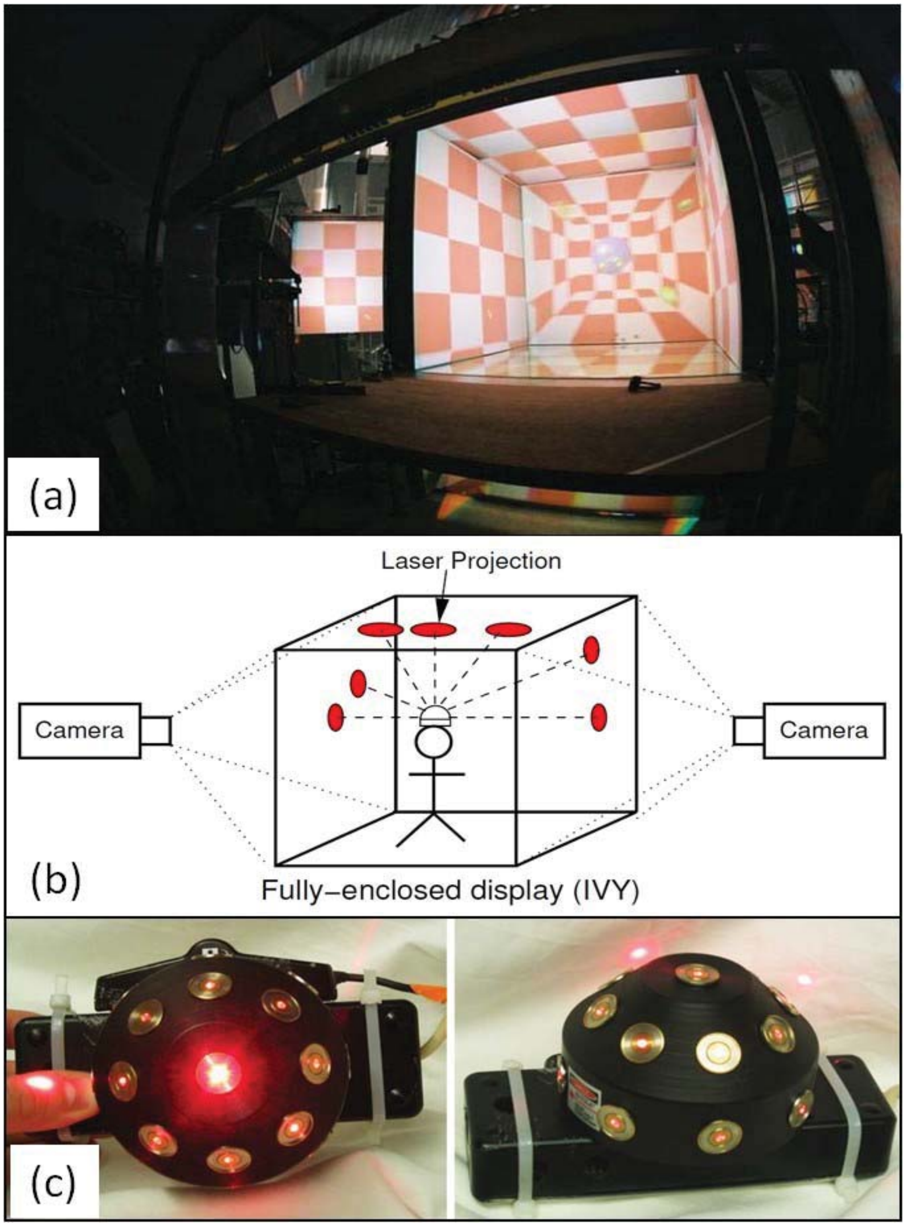

Figure 2.21: The Hedgehog developed in York University [13, 14]: (a) the Immersive Visual environment at York (IVY), (b) the diagram of the optical racking approach, (c) the Hedgehog hardware. A total of 17 laser diodes are arranged in a symmetrical hemispherical arrangement.

2.4.6 Pure Photogrammetric Solution

The multi-camera system has the advantage of supplying absolute object coordinates of target with respect to a fixed coordinate system by using two or more synchronized and oriented cameras. The absolute measurement of all 6 DOF parameters of a moving targeted can be obtained from the multi-camera system. Figure 2.22 displays the online photogrammetry system, AICON TraceCAM system [16], which is used for tracking and positioning. Four CMOS cameras are mounted in a fixed housing as shown in Figure 2.22 (a), and the additional touch probe shown in Figure 2.22 (b) allows combine optical and tactile measurements. For more complex scenes, an arbitrary number of cameras can be used for body tracking in sport sciences or the movies industry. Recent studies on using a photogrammetric method to achieve high precision 6 DOF measurements with a single camera were investigated by Thomas Luhmann [20, 21]. Based on the mathematical model and Monte-Carlo simulations, he showed that a pure photogrammetric approach can reach an accuracy of better than 1:10000 of the maximum dimension of the measurement volume and a precision of the angular orientation of better than 0.05° with a single camera. For commercial available product, an accuracy of 15 μm is reported from the specifications of GOM Tritop [105] when a volume of $1\times0.5\times0.5$ m^3 is measured. However, both multi-camera and single camera photogrammetric systems require line of sight between the object and camera at all times.

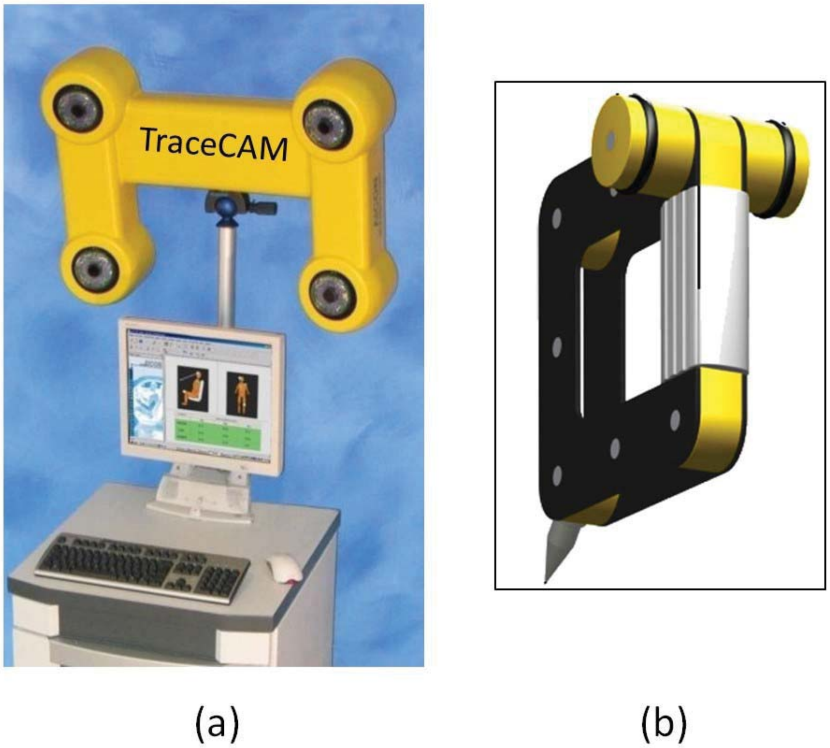

Figure 2.22: The online multi-camera photogrammetry system TraceCAM [16]: (a) TraceCAM online system, (b) a touch probe.

2.4.7 Summary

A summary of the current non-contact 6 DOF measurement techniques is given in Table 2.1. As indicated in Table 2.1, both indoor GPS and inertial sensor techniques have limited accuracy and the indoor GPS can suffer from “fading” fact, which could result in deterioration of position accuracy. Although the laser based sensor technique can provide accuracy to nm level, the measurement range of this technique is limited by mm level. The laser tracker is able to measure an accuracy of 10 µm for measurement range up to 160 m. The laser tracker is expensive (up to hundreds thousand) and requires the SMR to remain within the sensor’s line of sight. It is also demonstrated in Table 2.1 that line of sight restrictions is a shortcoming existing in most current techniques (except the inertial sensor technique). In this dissertation, a technique is proposed to overcome line of sight restrictions. Such technique can reduce system costs, allow large dynamic range and has the potential to provide high measurement accuracy. The proposed metrology system together with other current non-contact 6 DOF measurement techniques are displayed in Figure 2.24.

Table 2.1: Summary of the current non-contact 6 DOF measurement techniques.

Technique	Measurement Range	Measurement Accuracy	Limitation
Indoor GPS(iGPS)	tens of meters*	~200 µm*	"Fading" effect; line of sight restriction
Inertial Sensor	~km**	~2 cm/s** (Military grade)	Limited accuracy
Laser Based Sensor	~mm	~nm	Limited range; line of sight restriction
Photogrammetric Solution	tens of meters***	15 µm***	Line of sight restriction
Laser Tracker	160 m	10 µm	High cost; line of sight restriction

*accuracy of 200µm was reported by ref. [115,116] for measurement volume of 40×40m. It was claimed by Nikon Metrology [115] that uniform accuracy could be obtained across the entire measurement volume.

**accuracy of around 2cm/s was for the military grade inertial unit reported in [102].

***accuracy of 15µm was obtained for a measurement range of 2m. Absolute accuracy to 5µm + 5µm/m of the size of the object was reported by V-STARS system [128]. Photogrammetric solution has very good scalability.

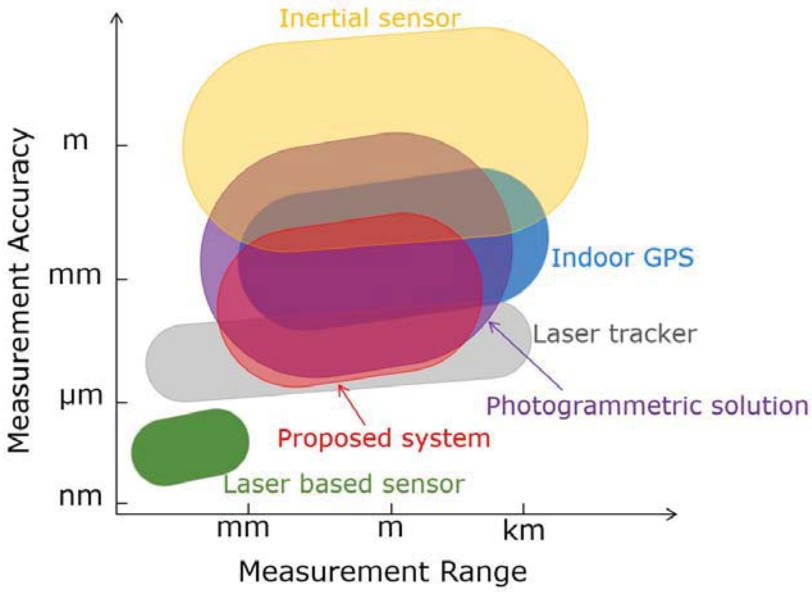

Figure 2.23: The summary of the current non-contact 6 DOF measurement techniques and the proposed metrology system.

2.5 Expression of Measurand and Uncertainty in Measurement

General speaking, the measurand (the output quality in a measurement model) is not completed until it is accompanied by a quantitative statement of its uncertainty. As described in the GUM [122], the uncertainty of measurement is defined as "parameter, associated with the results of a measurement, which characterizes the dispersion of the values that could reasonably be attributed to the measurand". In this section, a classification of components of uncertainty is expressed to classify the terms used in this dissertation. Throughout this dissertation, the word "uncertainty" without adjective refers both to general concept of uncertainty and to any or all quantitative measures of that concept. Appropriate adjectives will be used when a specific measure is intended.

Depending on the method used to estimate the values of uncertainty, uncertainty can be grouped into two categories: Type A evaluation of uncertainty, those which are evaluated by statistical analysis of series of observations; Type B evaluation of uncertainty, those which are evaluated by means other than the statistical analysis of series of observations.

2.5.1 Standard Deviation

The standard deviation is a numerical value used to indicate the variation or dispersion from the mean of a population. In this dissertation, the sample standard deviation of measured data is defined by equation (2.7).

$$s = \sqrt{\frac{1}{N-1}\sum_{i=1}^{N}(x_i - \bar{x})^2} \qquad (2.7)$$

The sample variance (s^2) is an unbiased estimator of the population variance (σ^2).

2.5.2 Standard Uncertainty

Standard uncertainty is defined as "uncertainty of the result of a measurement expressed as a standard deviation" [122], which is equal to the positive square root of the estimated variance. A Type A evaluation of standard uncertainty could be obtained from any valid statistical method for treating series of observations. A Type B evaluation of standard deviation could be obtained from scientific judgment using all the relevant information. The information may include "(1) previous measurement data, (2) experience with, of general knowledge of, the behavior and property of relevant materials and instruments, (3) manufacture's specifications, (4) data provided in calibration and other report, (5) uncertainties assigned to reference data taken from handbook" [122].

2.5.3 Combined Standard Uncertainty

In the GUM [122], the combined standard uncertainty is defined as "standard uncertainty of the results of a measurement when that result is obtained from the values of a number of other quantities, equal to the positive square root of a sum of terms, the terms being the variances or covariances of these other quantities weighted according to how the measurement results varies with changes in these quantities". The combined standard uncertainty, with suggested symbol u_c, is usually obtained by combining the individual standard uncertainties. These individual standard uncertainties could either arise from a Type A evaluation or a Type B evaluation, as described in section 2.5.

2.5.4 Expanded Uncertainty

For some commercial, industrial, and regulatory applications, it is required that a measure of uncertainty that defines an interval about the measurement result y within which the value of the measurand Y is confidently believed to lie. Thus the term expanded uncertainty is introduced, with suggested symbol U, which is defined as "quantity defining an interval about the result of a measurement that may be expected to encompass a large fraction of the distribution of values that could reasonably be attributed to the measurand" [123]. The expanded uncertainty can be obtained by multiplying the combined uncertainty $u_c(y)$ by a coverage factor, k, as shown in equation (2.8).

$$U = ku_c(y) \tag{2.8}$$

Thus it is confidently believed that $y - U \leq Y \leq y + U$, which is commonly written as $Y = y \pm U$.

CHAPTER 3: POSITIONING SENSOR BY COMBINING OPTICAL PROJECTION AND PHOTOGRAMMETRY

3.1 Principal of Proposed Technique

The proposed technique in this dissertation uses optical projection with close range photogrammetry to achieve a 6 DOF optical sensor. This method starts with the projection of an optical pattern (see Figure 3.1). The optical pattern is generated by passing a laser beam through a diffractive element (a transmission diffraction grating) to produce an array of dots on any surface that intersects the projected, diffracted beams. The diffractive element leads to a defined, known angular relationship between the diffracted beams and their origin, and this is defined by the design of the diffractive element and the wavelength of the laser used. Thus if the *xyz* locations of the dots where the beams intersect a surface in the environment are known, it is possible through a minimization algorithm to determine the *xyz* coordinates of the source of the beams, that is the point in space where all diffracted beams originate. In the proposed system, this point is the location of a module (consisting of a laser diode and a diffractive element) and the orientation of the zero-order beam of the projection pattern defines the orientation of the module. The photogrammetric measurement is used to determine the absolute *xyz* coordinates of the dots observed in the environment with respect to the global coordinate system. The module location and orientation are then determined using the developed algorithm.

For each module position, several images of the observable pattern are taken by different cameras. These images are processed by a photogrammetry package to return the *xyz* coordinates of the dots. This data is then passed to a minimization algorithm to determine the location of the module that produced the diffracted beam pattern. Knowing the angular relationship between the diffracted beams is critical, see Figure 3.1 for an example of a 7×7 dot matrix generated by a commercially available projection head [112]. The angles between adjacent optical beams (the vertical and horizontal angles shown in Figure 3.1), θ_{VH}, and the diagonal beams, θ_{Dia}, will be provided by the manufacture or can be obtained through a calibration procedure. The following describes the relationship between the angles and the *xyz* coordinates of the projected dots, and the calculation of the module location.

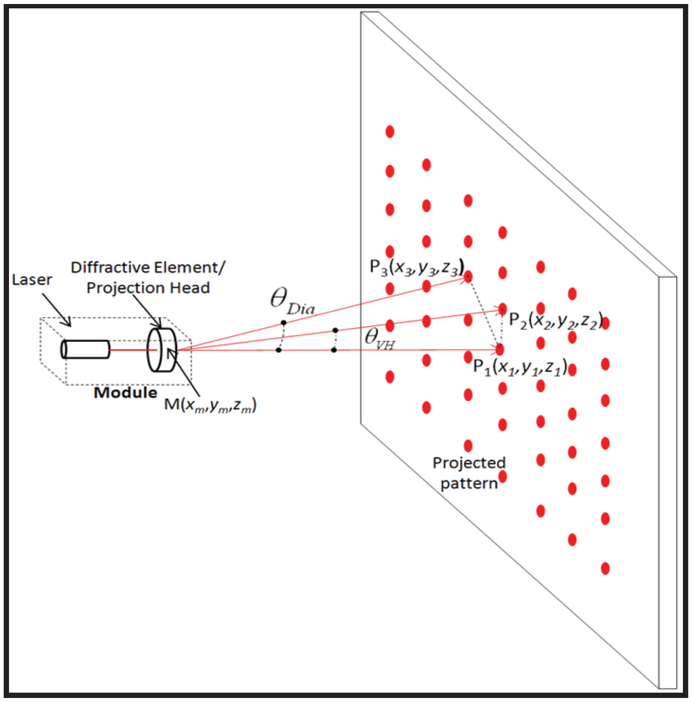

Figure 3.1: Schematic diagram of the module and projected dot matrix.

The location of the module is defined by M (x_m, y_m, z_m). The absolute coordinates, P_i (x_i, y_i, z_i), of each dot in the projected pattern are determined by a photogrammetric bundle adjustment. Three sample vectors, shown in Figure 3.1, are represented by $\overrightarrow{MP_1}$, $\overrightarrow{MP_2}$, $\overrightarrow{MP_3}$. Such vectors can be defined for every dot in the projected pattern. The vectors are mathematically given by equation (3.1), where x_m, y_m, and z_m are the unknown coordinates of the module position. The angle between adjacent beams, θ_{VH}, and between diagonal adjacent beams, θ_{Dia}, can be calculated from the dot product rule between appropriate vectors (equations (3.2) and (3.3)).

$$\overrightarrow{MP_i} = (x_i - x_m, y_i - y_m, z_i - z_m) \tag{3.1}$$

$$\theta_{VH} = \cos^{-1}\left(\frac{\overrightarrow{MP_1} \bullet \overrightarrow{MP_2}}{\left|\overrightarrow{MP_1}\right| \bullet \left|\overrightarrow{MP_2}\right|}\right) \tag{3.2}$$

$$\theta_{Dia} = \cos^{-1}\left(\frac{\overrightarrow{MP_1} \bullet \overrightarrow{MP_3}}{\left|\overrightarrow{MP_1}\right| \bullet \left|\overrightarrow{MP_3}\right|}\right) \tag{3.3}$$

The best-fit values for x_m, y_m, and z_m are arrived through a least-square (LS) minimization algorithm. First, the dot coordinates obtained from the photogrammetric measurement are combined with an initial guess for x_m, y_m, and z_m. This enables an initial calculation of θ^c_{VH} and θ^c_{Dia}. These calculated values are compared to their known values θ^r_{VH} and θ^r_{Dia}, which are called reference angles, and a Nelder-Mead optimization method [91], combined with a LS minimization (see equation (3.4)), is implemented in MATLAB® [111] to iteratively converge to the best fit x_m, y_m, and z_m. That is to find x_m, y_m, z_m values to give the lowest value of the least-square sum defined by

$$\chi^2 = \sum_i^m (\theta^c_{VHi} - \theta^r_{VHi})^2 + \sum_j^n (\theta^c_{Diaj} - \theta^r_{Diaj})^2 \tag{3.4}$$

The Nelder-Mead algorithm can converge to a local minima, so the selection of the initial starting value can determine the outcome of the optimization [106]. In the experiment, the initial starting value is selected based on experimental observation. The process is then repeated for each module location.

3.2 Factors Affecting Uncertainty of Photogrammetric Measurement

The accuracy of the photogrammetric measurement depends on a number of factors. The resolution of the images is one factor affecting the accuracy. The higher the resolution of the images, the more precisely the target can be located in the images. Therefore, higher accuracy can be achieved with higher resolution. Photo redundancy also contributes to the accuracy of the photogrammetric measurement. The more photographs the target appears in, the more accurately the position of the target can be computed. Other than these two factors mentioned above, the geometry of camera station (angles between photos), camera calibration, stability of employed camera and target recognition are also involved in determining the accuracy of the photogrammetric measurement.

3.2.1 Camera Position Geometry

The main applications of photogrammetry focus on the reconstruction of a 3D object by extracting the information contained in a 2D photograph so that the 3D measurement of the object can be performed. However, 3D information of an object cannot be obtained from a single image without the help of extra information. Therefore, usually two or more images of the object of interest should be taken. This can be realized by using a single camera to capture multiple images of the object from different locations and angles in the 3D environment around the object if the object is stationary. If the object under measurement is not stationary or real time measurement is needed, multiple cameras are commonly employed to be placed around the object so that images of the object can be captured simultaneously. The second method has been used for the proposed metrology system discussed in this dissertation.

As mentioned in section 2.1, triangulation is the fundamental principle used by photogrammetry. The rays can be developed from each camera to the target by taking images of the target from at least two different positions. The 3D coordinates of the target can be determined by finding the mathematical intersections of these rays. As the images are taken from different camera locations and different camera angles, these parameters (which are called camera position geometry here) have a substantial effect on the accuracies of the photogrammetric measurement [86]. Figure 3.2 illustrates how the angle between cameras affects the measurement error of a point. The areas in red stand for the residual errors in determining the target location through the intersection of rays from two different camera positions. It shows clearly that the error in the y coordinate (e_y) is larger than the error in the x coordinate (e_x) when the angle between cameras is smaller than 90°. When the angle between cameras is larger than 90°, the error in the x coordinate (e_x) is larger than the error in the y coordinate (e_y). The measurement error e reaches the minimum value when the errors in the x and y coordinates are equal, which is at an optimum angle of 90 ° between two cameras. This relation is shown in equation (3.5). The minimum value of e can be reached only when $e_x = e_y$.

$$e = \left(e_x^2 + e_y^2\right)^{1/2} \geq \sqrt{2e_x e_y} \tag{3.5}$$

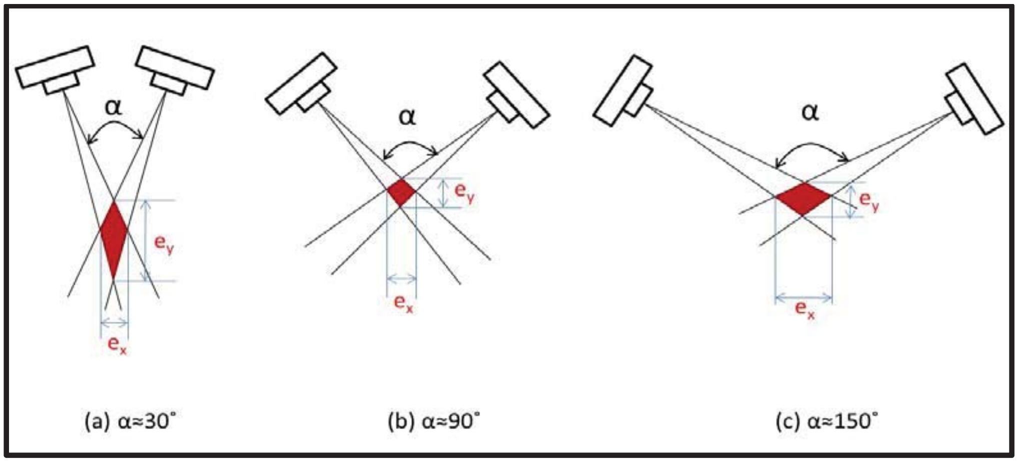

Figure 3.2: Schematic diagram of how camera geometry affects the measurement error. (a)The error in the y coordinate (e_y) is larger than the error in the x coordinate (e_x) when the angle between cameras is smaller than 90˚, (b) the errors in the x and y coordinate are equal at an optimum angle of 90 ˚, (c) the error in the x coordinate (e_x) is larger than the error in the y coordinate (e_y) when the angle between cameras is larger than 90˚.

Besides the angles between cameras, the camera position geometry is also of importance, which should be taken into consideration. Photogrammetry can be completed either by completely overlapping measurements or partially overlapping measurements based on different camera position geometry. In a completely overlapping measurement the entire object can be captured by the cameras at each position so that it has the ability to measure all the targets on an object. In a partially overlapping measurement only fragments of the object being measured are photographed by the cameras. Therefore, sufficient tie points are needed in order to tie the entire measurement together. In the proposed metrology system discussed in this dissertation, completed overlapping measurement is used to obtain the 3D *xyz* coordinates of the projected laser dots.

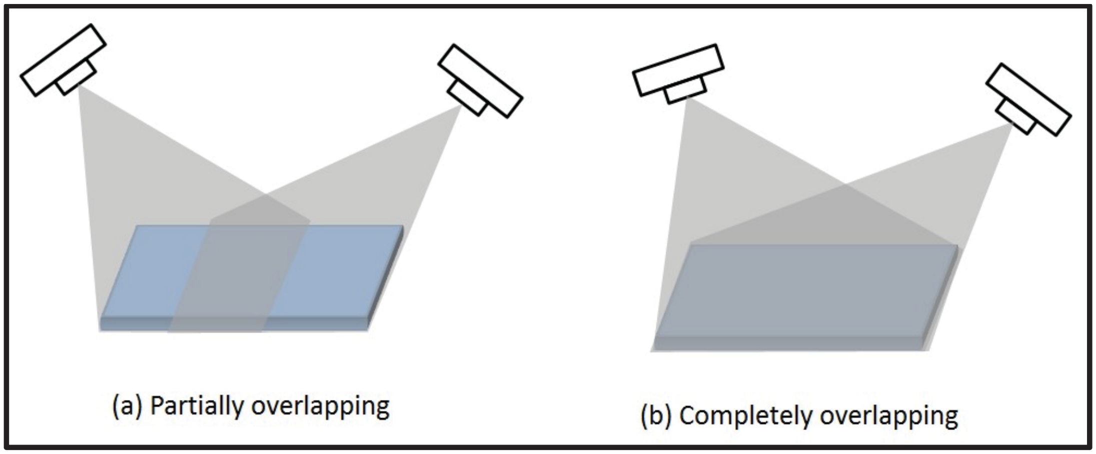

Figure 3.3: Schematic diagram of the camera position geometry: (a) partially overlapping measurement, (b) completely overlapping measurements.

3.2.2 Camera Calibration

Camera calibration is the process of determining the internal characteristics of a camera, which are customarily known as the interior orientation parameters (IOPs). The IOPs of a camera include the focal length of the lens (the principal distance), the distortion characteristics of the lens, the digitizing scale (the format size of imaging area), and the position of the principal point. More details about definitions of IOPs can be found in section 2.1.2. The accurate determination of IOPs of a camera is very important for recovering the three-dimensional information from imaging systems reliably and accurately. Once a camera is calibrated, it can provide accurate measurements.

The common technique to determine the IOPs is through a bundle adjustment with self-calibration. A test field is commonly employed to provide control information for the calibration procedure. This procedure can solve the desired IOPs as well as the exterior orientation parameters (EOPs) of the images involved. The EOPs include the location of the perspective center and the orientation of the camera with respect to the object space coordinate system as show in section 2.1.2. In-door test fields can be either a 2D test field like a single wall in a room, or a 3D test field like a cube as shown in Figure 3.4. A 3D cube or cage with points filled up a 3D volume is an ideal test field for calibrating a camera. In traditional photogrammetry, all the target points within the test field need to be surveyed by specialists with specialized instruments. This makes the calibration procedure expensive. Also, it is difficult and expensive to secure space for such calibration cage. To avoid high cost, a 2D test field is used as suggested by PhotoModeler® [86], which is shown in Figure 3.5.

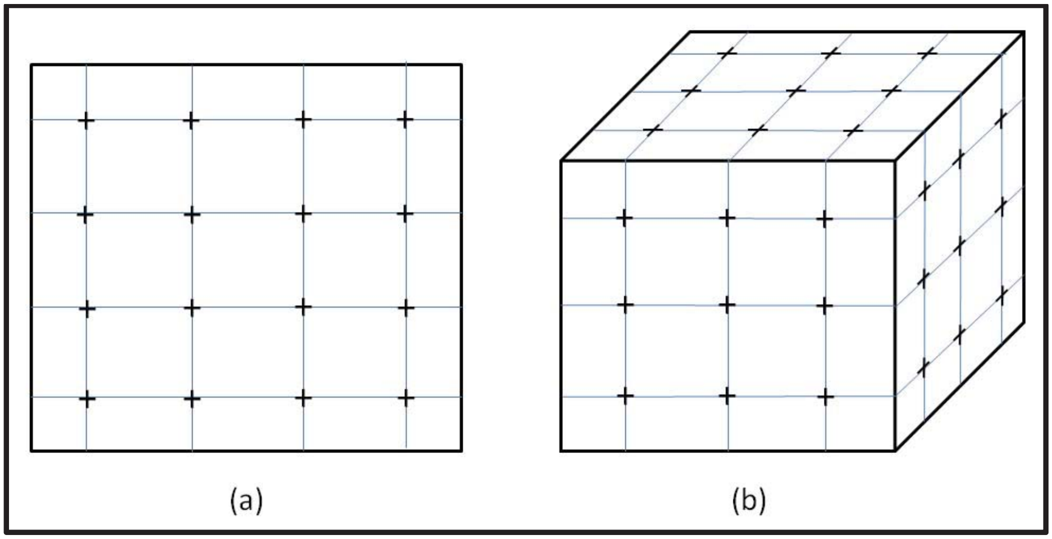

Figure 3.4: Examples of calibration test fields: (a) 2D calibration test field, (b) 3D calibration test field.

The calibration grid shown in Figure 3.5 consists of 144 circular dot targets and 4 control points for the purposes of an automated in-door calibration. The design of high contrast circular target is suitable for automatically detecting the center of the target. It is important to keep the size of the calibration gird nearly the same scale of the object to be measured. The calibration grid is printed to the size of 36 inch by 36 inch, which is nearly the same scale as the measurement field. The printed calibration grid is applied to the floor surface and it is kept static and rigid. In order to calibrate the camera, PhotoModeler® requires 12 images taken by the camera to cover the entire test field from four different sides, as shown in Figure 3.6. At each side of the calibration grid, three images are taken. For each image, the camera station has been rotated 90˚ about the optical axis as shown in Figure 3.6. During calibration process, the image area should be covered as much as possible so that dots appear in all location. This helps improve point “coverage” in the lens and helps ensure the entire lens is calibrated. After 12 images of the test field are processed by PhotoModeler®, IOPs of the camera including focal length, principal point, CCD format size and lens distortion will be determined and a corresponding calibration file containing all these parameters will be saved in the camera library of PhotoModeler® so that it can be used for further measurement.

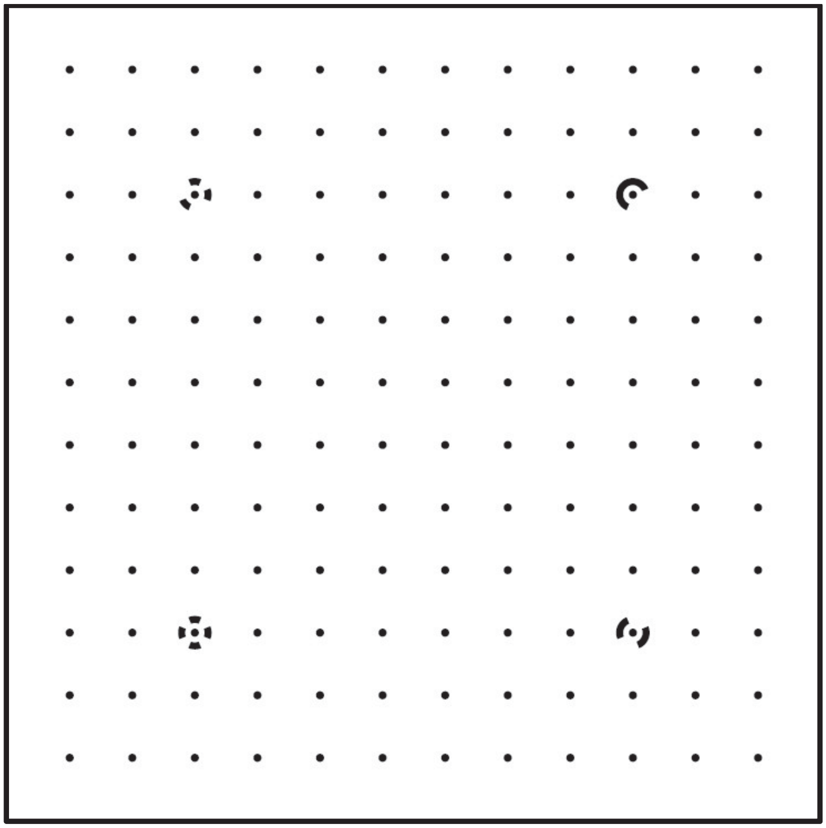

Figure 3.5: 2D calibration test field used in PhotoModeler®.

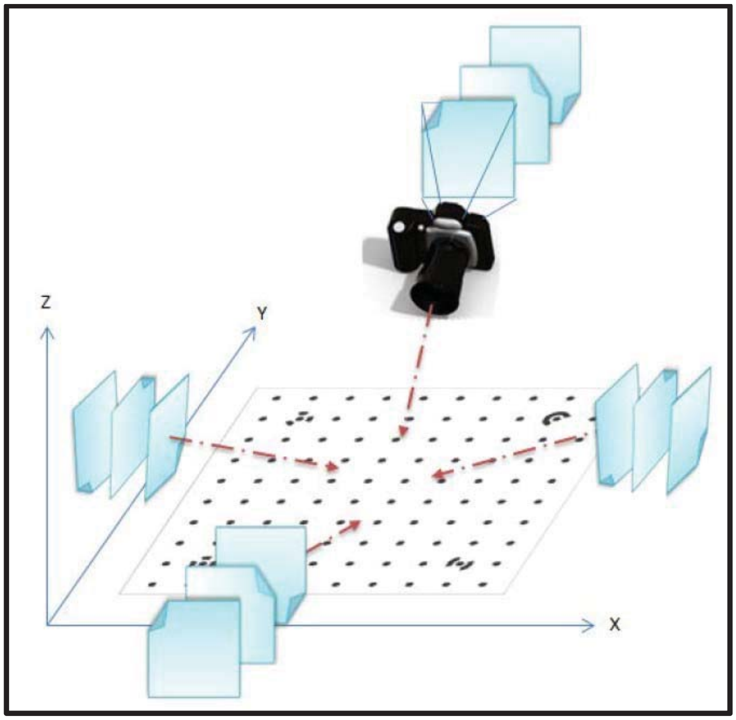

Figure 3.6: Schematic diagram of the camera calibration process. At each side of the calibration grid, three images are taken with camera rotated -90°, 0°, and 90° about the optical axis of the camera [130].

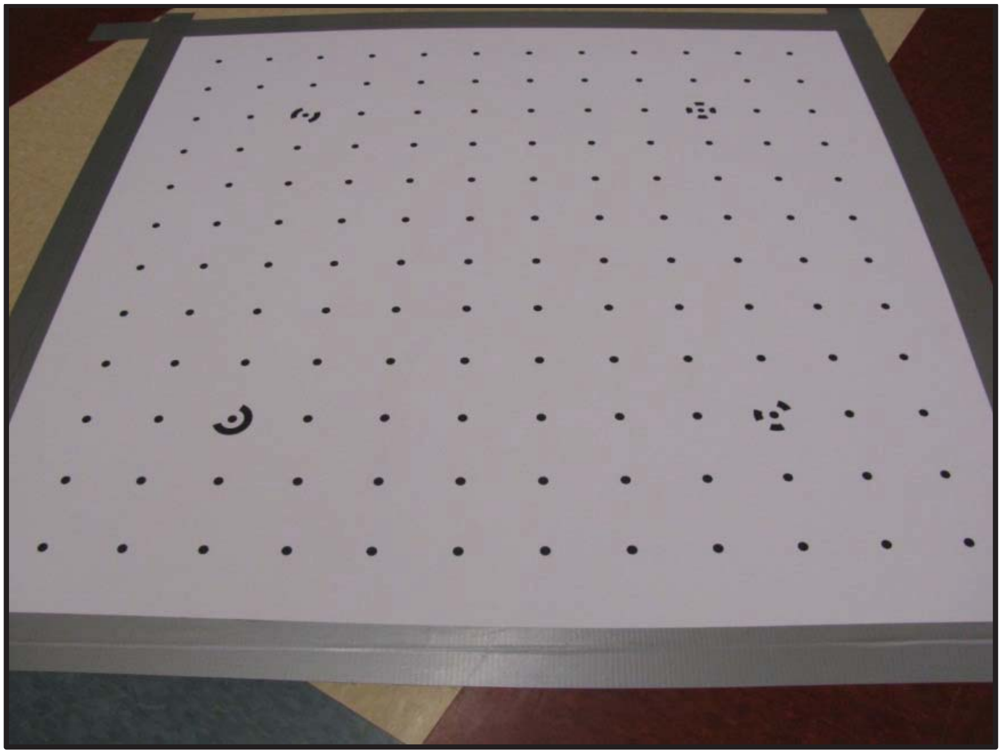

Figure 3.7: An image of the calibration grid taken by Canon Powershot SX110IS.

3.2.3 Camera Stability Analysis

Traditional metric cameras are designed and built with high accuracy and long term stability of internal characteristics, so the IOPs can be treated as constant over an extended time. Most commercial digital cameras on the market are not built for photogrammetric applications, which are referred as amateur camera in the photogrammetry community. However, consumer-grade digital cameras have been widely applied to lots of photogrammetric applications due to the advantages of high resolution and low cost. In order to achieve better accuracy, the temporal and long term stability of IOPs and manufacturing consistency of such cameras need to be investigated before they are used for the photogrammetric measurements. The deviation of these parameters is usually achieved by implementing camera calibration.

In the following research, the stability of digital point-and-shoot camera has been investigated for over 2 hours and for over a period of ten weeks. The digital point-and-shoot camera is Canon PowerShot SX110IS with charged-coupled device (CCD) sensors. The characteristics of the implemented camera are summarized in Table 3.1. The stability of the Canon PowerShot SX110IS camera is first investigated following the calibration procedure discussed above. Since this camera has a 10X zoom lens (6 mm-60 mm), the shortest focal length is used for all the measurements and so this focal length is chosen for calibration. Before calibrating the camera, the Image Optical Image Stabilization function, Auto-rotation function and Auto-focus function were turned off so that more repeatable IOPs can be achieved. Figure 3.7 shows a sample calibration image taken by the Canon PowerShot SX110IS camera during the calibration process.

Table 3.1: Characteristics of implemented cameras used for camera calibration and stability analysis

Camera Name	Price Range ($ US)	Image Resolution (pixels)	Pixel Size (mm/pixel)	Effective Pixels (Mega Pixels)
Canon PowerShot SX110IS	$250	3456×2592	0.0017	8.96

The zoom lens of Canon PowerShot SX110IS camera moves each time the camera is turned on/off. The first ten sets of calibration are done within two hours without turning off the camera. The deviation of the focal length with respect to the minimum focal length value based on ten sets of calibration is shown in Figure 3.8 (a). For these ten sets of calibration, the change range of the focal length is around 5 μm with a standard deviation of 1.6 μm. The positions of the principal point are shown in Figure 3.8 (a). The standard deviations for the x coordinate and y coordinate of the principal point are 1.4 μm and 0.6 μm respectively, which lead to 1.5 μm spatial offset of the principal point defined by equation (3.6) assuming they are uncorrelated.

$$\sigma = (\sigma_x^2 + \sigma_y^2)^{1/2} \tag{3.6}$$

Then another ten sets of calibration are performed for the same camera. This time the camera is turned off after each calibration. Figure 3.9 (a) shows that the deviation of the focal length (deviation compared with the shortest focal length) is around 21 μm with a standard deviation of 5.6 μm for the case that the camera is turned off after each calibration. And the spatial offset of the principal point is 3.4 μm and the position of principal point is shown in Figure 3.9 (b). These results indicate that the Canon PowerShot SX110IS camera has better stability if the zoom lens has not been moved mechanically (for example, the camera is not turned on/off).

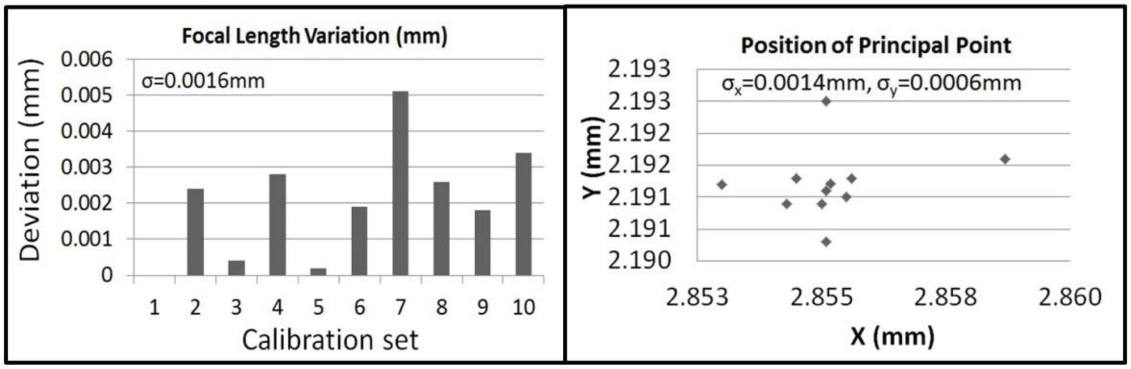

(a) (b)

Figure 3.8: Stability test of the camera with continued power: (a) focal length variation, (b) the position of the principal point.

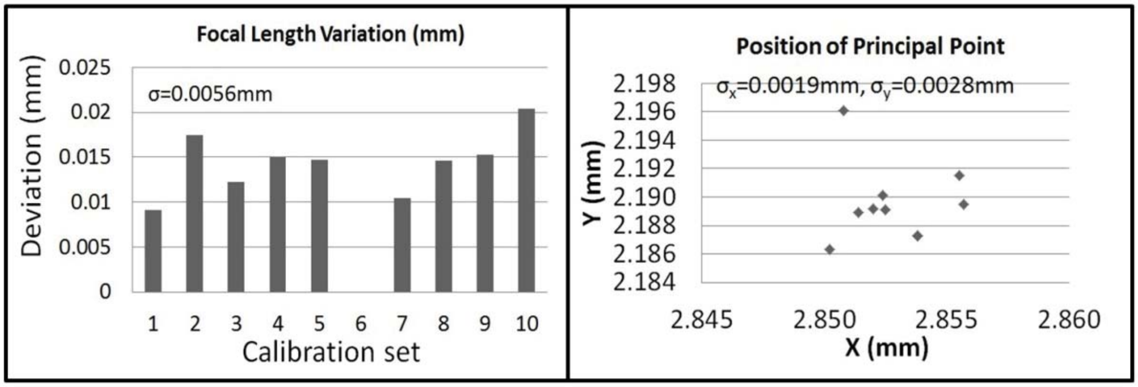

(a) (b)

Figure 3.9: Stability test of the camera with power on/off between every two calibrations: (a) focal length variation, (b) the position of the principal point.

3.2.4 Target Recognition

The quality of the photogrammetric measurement also depends on the type of targets and how well the targets can be identified in the image. In many applications, locations to be measured on an object need to be identified by an artificial target. Circular targets are best suited for the photogrammetric measurement due to their radial-symmetric design. The center of circular target represents the actual 3D point to be measured.

Targets used in proposed system include luminous targets and adhesive coded targets on printed paper. Luminous targets can be realized through different ways. They can be constructed by placing a semi-transparent plastic cover on the top of a light emitting diode (LED), or by placing a diffuser on the top of the large diameter multimode fiber with LED light coupled into the fiber from another end (Figure 3.10), or by laser projection (Figure 3.11). In the proposed system the multiple luminous targets on the wall surface are generated by passing a collimated laser beam through a transmission diffraction grating. This method is chosen because the laser dot targets are highly luminous due to the laser has relative high intensity and multiple easy-identify luminous targets can be easily obtained by passing a laser beam through a diffraction grating. With a well collimated laser passing through the diffraction grating, the laser dot targets on the wall surface are equally circular shape. By carefully choosing the design of diffraction grating, the projection pattern can be a dot matrix as shown in Figure 3.11, where multiple targets can be measured so that the module position can be computed. Coded targets (CT) (targets coded with individual identification number) are used in the proposed metrology system to provide additional information and tie points. These coded targets can be automatically recognized so that they can provide the ability to automatically mark, recognize and reference targets in a scene.

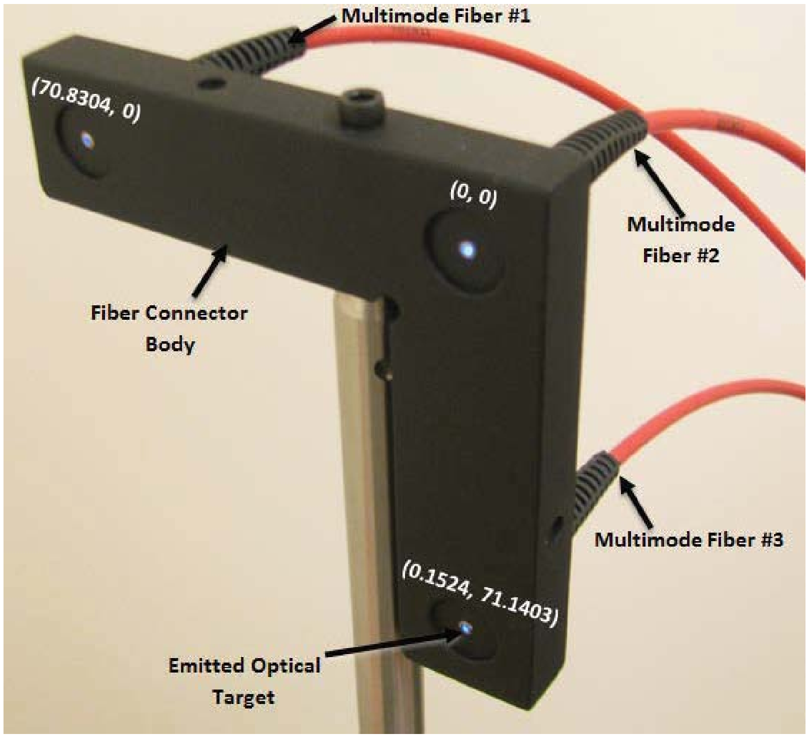

Figure 3.10: Luminous targets utilizing three 1000 µm multimode fibers powered by a blue LED source, developed by Beth Konarski, a summer research undergraduate at UNCC. Holographic diffuser covers not shown.

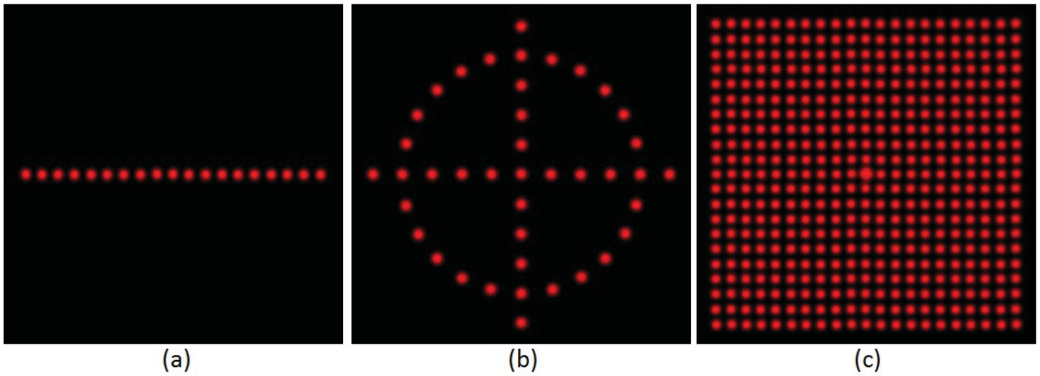

Figure 3.11: Luminous targets generated through laser projection: (a) 1:19 dot line, (b) viewfinder, (c) 21×21 dots array.

The main drawback of the laser dot projection is its irregularity in the dot shape caused by laser speckle and surface texture. The principle of laser speckle pattern and the speckle reduction solution are discussed in Appendix A. This irregularity will induce error in determining the centroid of the target. Investigations are given below on uncertainty of target centroiding, which could affect the uncertainty of the photogrammetric measurement. Factors affecting the uncertainty in target centroid measurement include camera noise, centroid calculation method, target size, and surface texture. The camera noise level can be represented by the centroid variations for spatially fixed targets. Noise level of the cameras used in the proposed system has been tested by using the camera to view a circular coded paper target fixed on the wall surface. A total of 1000 images of the same coded target are taken with 5 second intervals and the centroid of coded target is determined by PhotoModeler® using least square matching (LSM) method. The camera has a resolution of 3456×2592 pixel and the CCD sensor has a format size of 5.8×4.3 mm. Figure 3.12 shows the centroid variations of the coded target in the horizontal (x) and vertical (y) coordinates on the image plane over 80 minutes and the histograms of the centroid variations are shown in Figure 3.13. The standard deviations of the centroid variations in the x and y directions in the images are 0.09 and 0.11 pixel respectively. The uncertainties in the spatial coordinates caused by such random centroid variations are 2.6×10^{-5} (0.09/3456) in x direction and 4.2×10^{-5} (0.11/2592) in y direction assuming the (X, Y) plane in the spatial coordinates is parallel to the image plane. Compared with the coded target printed on the paper, it was shown that the laser dot target on the drywall surface has relative larger centroid variations due to the irregularity of dot shape caused by laser speckle and the wall texture. This will be discussed in section 3.2.4.1.

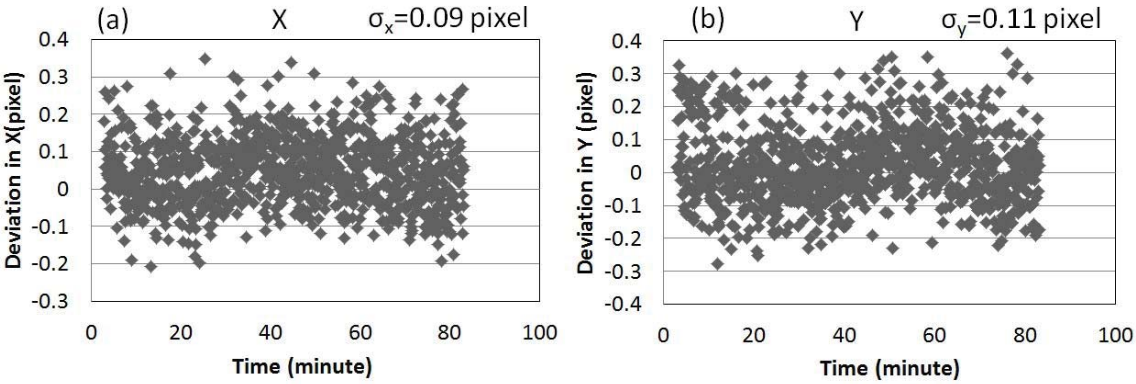

Figure 3.12: Centroid variation of the coded target over time: (a) horizontal direction x, (b) vertical direction y.

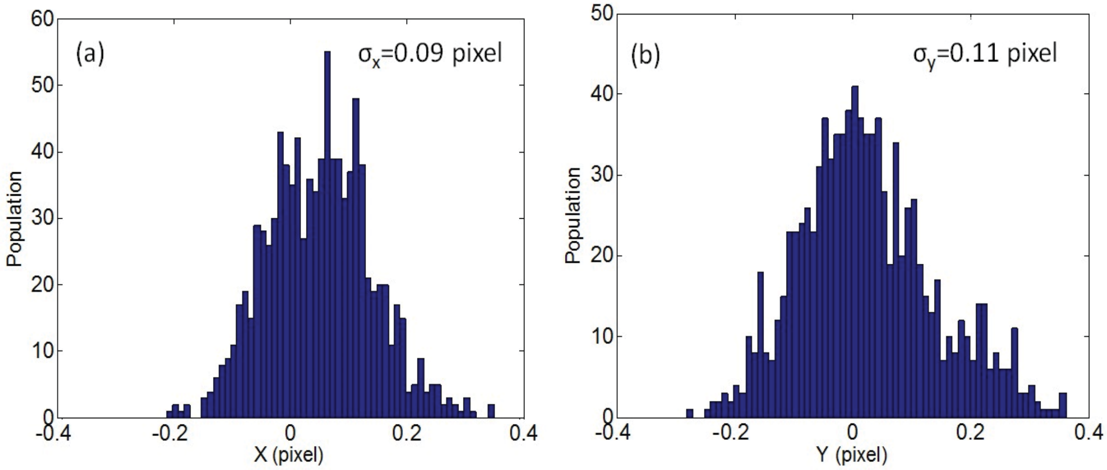

Figure 3.13: Histograms of centroid variation of the coded target: (a) horizontal direction x, (b) vertical direction y.

Due to perspective imaging and lens distortion, the center of the target will not coincide with the geometrical center of the target. This could lead to a bias error in the centroid calculation [127]. The pixels diameter of a target in the image is one factor affecting the accuracy of the centroid calculation. A few investigations are done as in [107,127] and it is suggested that a target pixel diameter of larger than 5 pixels is preferred for high accuracy measurement purpose. The diameter of most targets is between 7 and 25 pixels from the images used in the measurements discussed in section 3.3, section 4.4 and section 4.5.

3.2.4.1 Surface Texture

As mentioned above, the shape of the laser dot target is affected by the surface texture, which causes the uncertainty in determining the centroid of the laser dot target. For the proposed metrology system, the optical projection is projected onto a drywall surface. In this section, the drywall is first inspected with an optical microscope. Then the roughness of a sample drywall surface is measured by using Olympus LEXT OLS4000 3D laser confocal microscope and Taylor Hobson Talysurf-120L separately. An experiment investigating light scattering of a drywall surface is conducted in the next. The uncertainty of the laser dot centroid on the drywall surface is evaluated and discussed at the end of this section.

1. Roughness of Drywall Surface

The sample of drywall was cut to around 100×96×16 mm in size (see Figure 3.14) in order to be suitable for measurement with both the confocal microscope and the Talysurf-120L profilometer. The drywall was first inspected with an optical microscope (National Optical Model DC5-420TH). Figure 3.15 shows the image of the drywall surface obtained from digital microscope and the black circle indicates the possible laser beam size (diameter= 1 ~ 2 mm) on the wall. As shown in Figure 3.15, the surface is rough and bumps of diameter around 100 μm can be easily seen within the area the laser beam could possibly cover.

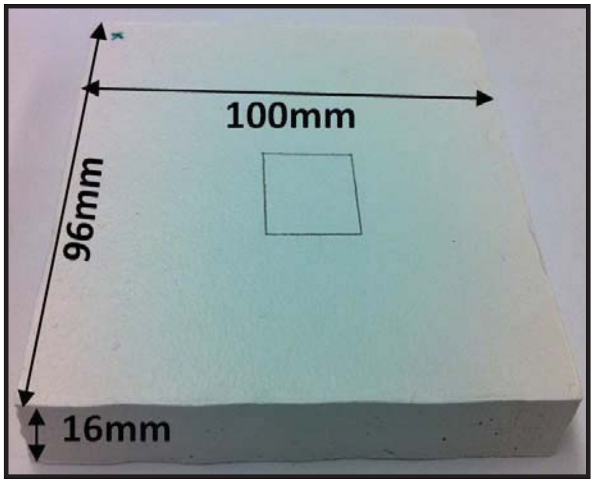

Figure 3.14: The sample of drywall surface.

Then the drywall sample was measured with the Olympus LEXT OLS4000 3D laser confocal microscope. Based on the measurement from the optical microscope, an objective lens with magnification of 5X was chosen to measure an area of 2.57×2.57 mm. Figure 3.16 shows a line height profile measured by confocal microscope with length of 2.57 mm. Four different areas A, B, C and D on the sample surface were measured and the results were shown in Figure 3.17. The peak to valley value of profiles changes in a range of about 100 μm and there is no surface uniformity over the four locations. Two area roughness parameters (ASME B46.1) S_a (average roughness) and S_q (root mean square roughness), were calculated following the equation (3.7) and (3.8):

$$S_a = \frac{1}{nx, ny} \sum_{i=1}^{nx} \sum_{j=1}^{ny} \left| z(j,i) \right| \tag{3.7}$$

$$S_q = \sqrt{\frac{1}{nx, ny} \sum_{i=1}^{nx} \sum_{j=1}^{ny} (z(j,i)^2)} \tag{3.8}$$

where *z(j,i)* is the ordinate of the point at the jth row and ith column, and nx and ny are the number of points along the two directions.

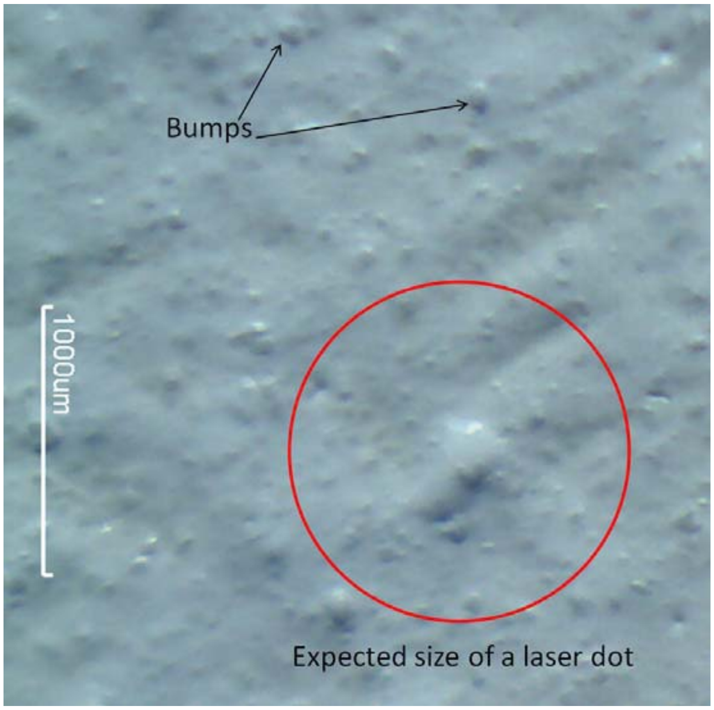

Figure 3.15: An image of the drywall surface taken with an optical microscope.

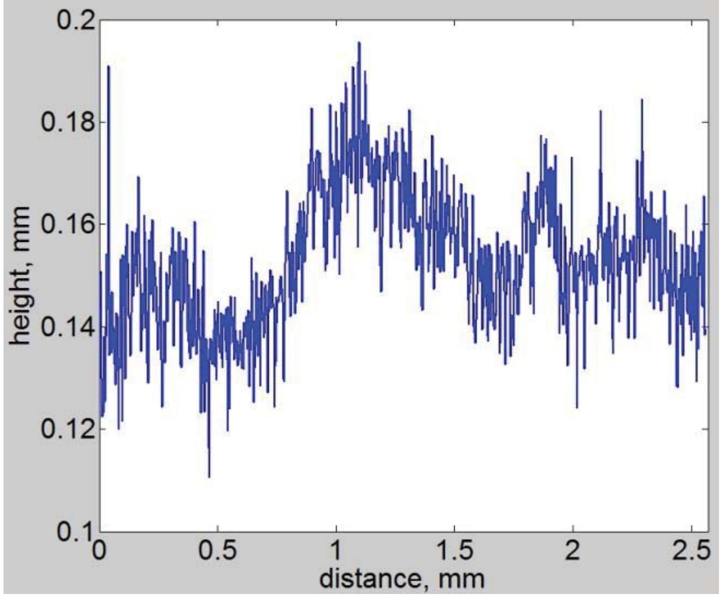

Figure 3.16: Line profile of the drywall surface measured by confocal microscope with 2.57 mm length (raw data).

The value of S_a ranges from 10.6 µm to 13.7 µm while the value of S_q changes from 13.3 µm to 16.7 µm. Power spectral density (PSD) function is an alternative way to evaluate a surface, which performs a decomposition of the surface profile into its spatial wavelengths and allows comparison of roughness measurement over different spatial frequency ranges. The PSD is the square of the Fourier transform of the profile [113]. For a discrete profile z whose discrete Fourier transform is given by zf, the PSD is given by equation (3.9)

$$PSD(f) = \frac{\Delta x}{n}\left|zf(f)\right|^2 \tag{3.9}$$

where f is the spatial frequency (reciprocal of the spatial wavelength) given by *k/l*, *k* is an integer ranging from 1 to n/2 and Δx is the spacing. The PSD function can be used to study the periodicity of the surface.

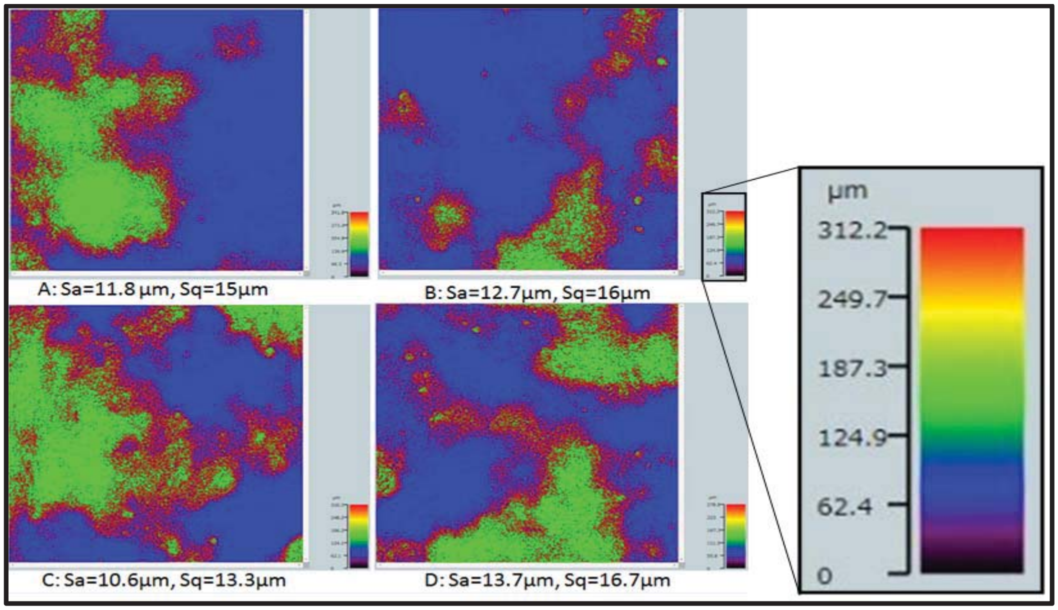
A: Sa=11.8 µm, Sq=15µm

B: Sa=12.7µm, Sq=16µm

C: Sa=10.6µm, Sq=13.3µm

D: Sa=13.7µm, Sq=16.7µm

Figure 3.17: Drywall surface measured by confocal microscope at a, b, c, and d four different areas (2.57 mm×2.57 mm) (Raw data).

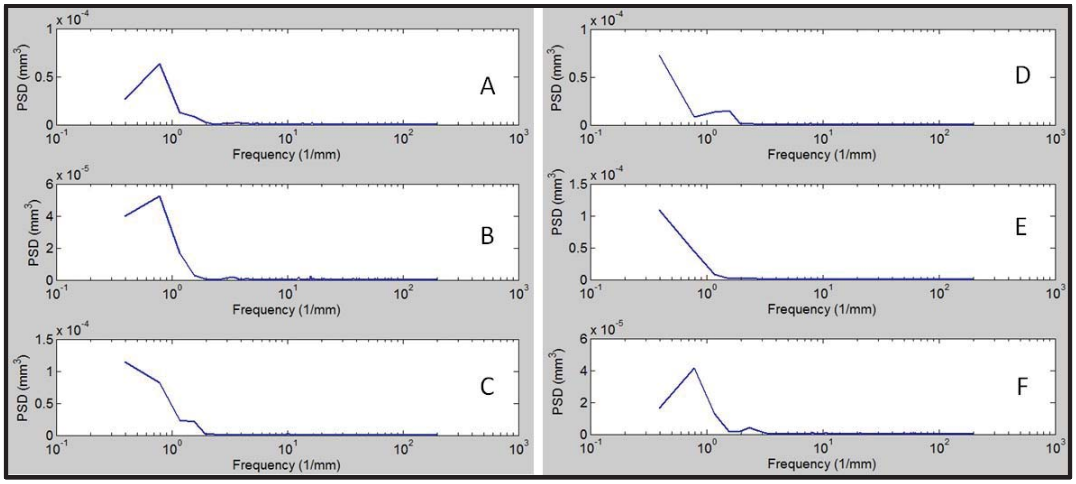

Figure 3.18: PSD (power spectral density) of 6 different line profiles (A-F) from confocal microscope measurements. Scan length: 2.57 mm (Raw data with first three data points removed).

The PSD for six line profiles, each with length of 2.57 mm, measured with confocal microscope are plotted in Figure 3.18 and the spacing is 2.5 μm. The PSD shown in Figure 3.18 indicates the wall surface is a random surface and has no particular high spatial frequency content. In order to explore the low spatial frequency components of the surface, Talysurf measurements were conducted and six line profiles (G-L) with length of 20 mm were obtained. The profile of one Talysurf measurement is shown in Figure 3.19. The profile displayed in Figure 3.19 is separated into waviness and roughness by choosing cutoff wavelength of 1 mm and 4 mm and the results are shown in Figure 3.20 (a) and Figure 3.20 (b) respectively. The PSD curves for each profile are also plotted and shown in Figure 3.21. Low spatial frequencies between 0.2 mm^{-1} and 0.5 mm^{-1} were observed from different PSD curves.

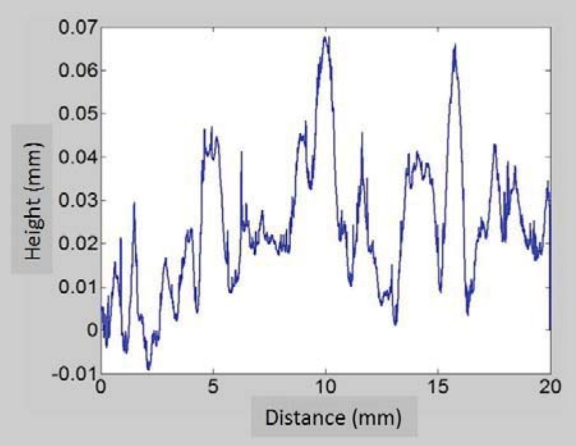

Figure 3.19: Line profile of the drywall surface measured by Talysurf-L120 with 20 mm length.

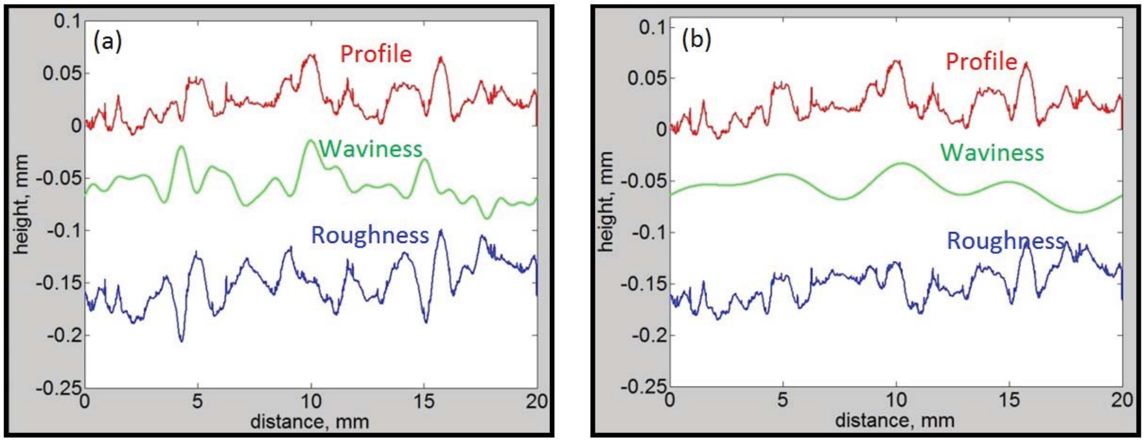

Figure 3.20: Profile, waviness and roughness of the profile shown in Figure 3.19, (a) cutoff wavelength of 1 mm, (b) cutoff wavelength of 4 mm.

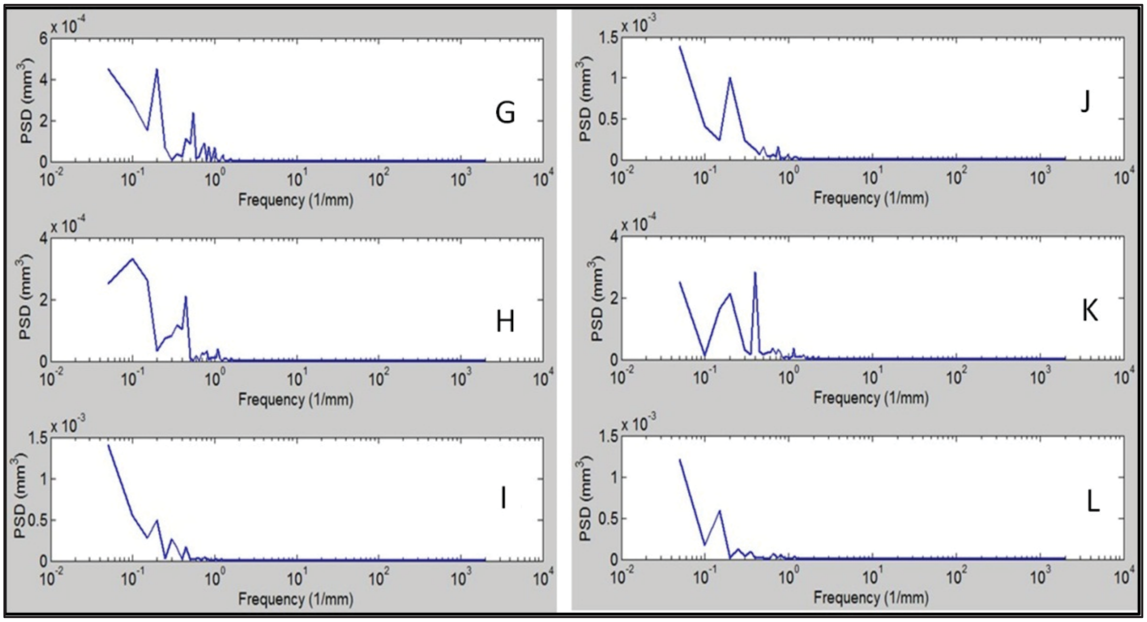

Figure 3.21: PSD (power spectral density) of 6 different line profiles (G-L) from Talysurf-120L measurement with 20 mm profile length (Raw data with first three data points removed).

2. Uncertainty of Laser Dot Centroid On Drywall Surface

An experiment of light scattering property of a drywall surface is also conducted. Figure 3.22 shows the experimental setup. The drywall sample was mounted to a stage connected to two motorized actuators and this motorized actuation position system has resolution of 50 nm in the x axis and 7 nm in y axis, respectively. The laser diode with a wavelength of 658 nm was located about 0.3 m away from the wall and a laser beam size of ~2 mm can be observed on the wall. Three 9 megapixel digital cameras [108] were positioned at various orientations with respect to the wall. An aluminum reference artifact with multi-mode fiber illumination was used in order to provide a global coordinate system. Repeatability was tested while all the components were kept stationary. Fifteen sets of images of the same laser dot on the wall were taken by the three cameras. From each camera view, the standard deviation of the laser dot centroid in pixel coordinate (σ_x, σ_y) can be calculated based on 15 images. The final combined standard deviation σ by combining *x* and *y* direction is given by

$$\sigma = \sqrt{\sigma_x^2 + \sigma_y^2} \tag{3.10}$$

Then the wall was moved in the *x* and *y* directions separately in a range of 15 mm with 1 mm step while the other components were still kept stationary. By doing this the same laser dot on different locations of the wall surface was captured by three cameras at the same time, so that the effect of the wall roughness to centroid of the laser dot can be investigated. The calculation of the standard deviation also follows equation (3.10) and the misalignment error was removed by deducting the linear fit value for both *x* and *y* coordinates. The standard deviations of the laser dot centroid under three conditions were given by Figure 3.23 from three different camera views. It can be seen clearly that by moving the wall in the *x/y* directions (which means the drywall texture has changed), the standard deviation of the laser dot centroid increases significantly, from 0.2 pixels to 0.45 pixels in *x* and from 0.2 pixels to 0.65 pixels in *y*, for example. This indicates that the drywall surface contributes significantly to the uncertainty of the laser dot centroid. Since the global *xyz* coordinates of the laser dot centroid is what being input to the algorithm, the standard uncertainty of the laser dot centroid in the global *xyz* coordinates is investigated. For the laser dot at each location, three images are taken by the three cameras at different locations. By inputting these three images of the same laser dot into the photogrammetry software, PhotoModeler®, the *xyz* coordinates of the laser dot centroid will be solved through the photogrammetric bundle adjustment. The standard deviations of the laser dot centroids in the global coordinate system σ_x, σ_y and σ_z were calculated based on 15 sets of images for the stationary wall, the wall moving both in the *x* and *y* directions separately.

Here σ is used to describe the combined standard deviation combining *xyz* directions, which is calculated by equation (3.11), where σ_x, σ_y and σ_z are the standard deviations in *x*, *y* and *z* directions respectively.

$$\sigma = \sqrt{\sigma_x^2 + \sigma_y^2 + \sigma_z^2} \tag{3.11}$$

The results of combined standard deviation in the global coordinate are shown in Figure 3.24. The results show that the combined standard deviation increases by 31% when the wall was moved in *x* direction and increases by 63% when the wall was moved in *y* direction. Measurements of the drywall surface indicate the roughness of drywall surface is very high, with S_a value varies from 10.6 μm to 13.7 μm for different areas, for example. PSD function of Talysurf measurement shows large structure exists on the wall surface with period around 2 mm to 5 mm. Results shown in Figure 3.23 and Figure 3.24 prove that such drywall surface will increase the standard deviation of the centroid of the laser dot on the wall significantly both in pixel and global coordinate systems. Based on the results obtained so far, the uncertainty of the laser dot centroid caused by the wall surface is one important factor contributing to the uncertainty of the final module location and which should be considered in the future uncertainty analysis of the system.

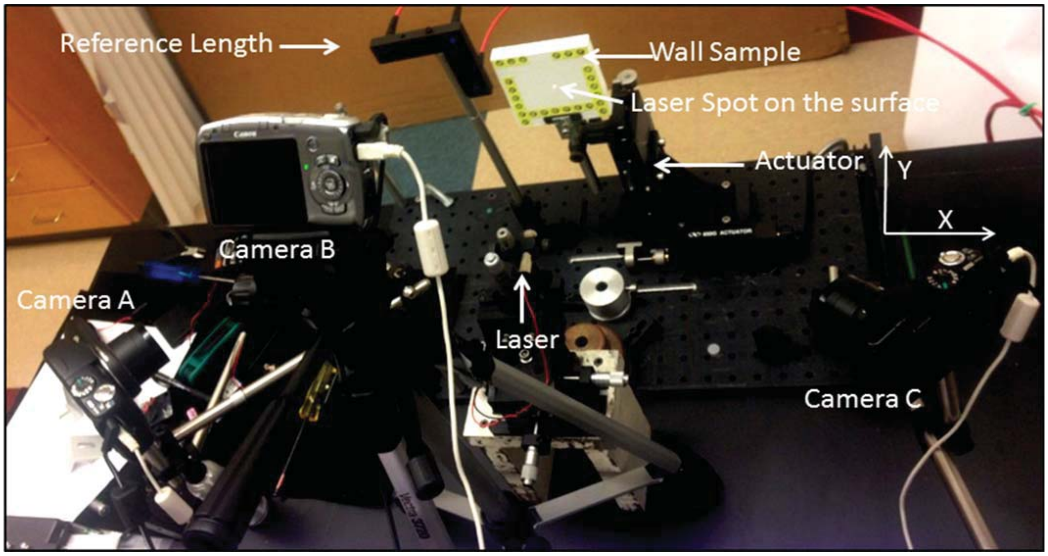

Figure 3.22: Experimental setup to evaluate uncertainty of the laser dot centroid on wall surface.

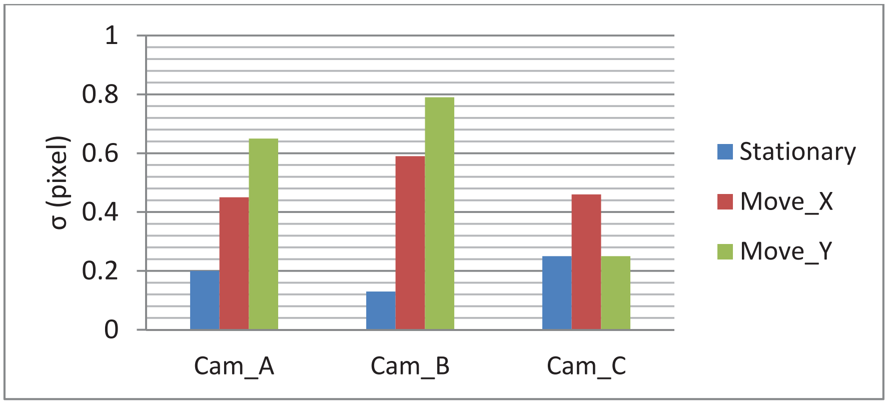

Figure 3.23: Standard deviation (σ) of the laser dot centroid from views of three cameras under three different conditions: (1) the wall is kept stationary, (2) the wall is moved in x direction, (3) the wall is moved in y direction. Cam_A, Cam_B and Cam_C stand for the standard deviations from the perspectives of camera A, B and C shown in Figure 3.22.

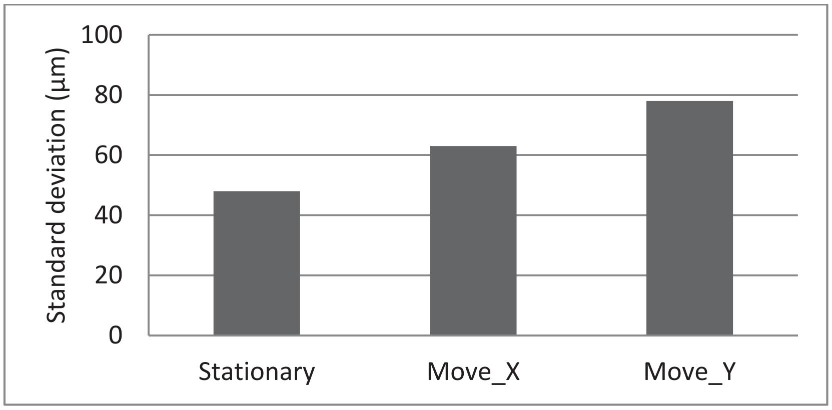

Figure 3.24: Standard deviation of the laser dot centroid in 3D (*x*, *y*, *z*) space coordinate measured by photogrammetry under three different conditions: (1) the wall is kept stationary, (2) the wall is moved in x direction, (3) the wall is moved in y direction.

3.3 Preliminary Translation and Rotation Test

3.3.1Experimental Setup and Procedure

The proposed technique was first demonstrated through experiment. The experimental setup is show in Figure 3.25. The module consists of a red laser and a diffraction grating. The laser has a wavelength of 658 nm and a power of 40 mW. As previously stated, the diffraction grating is designed to generate a 7×7 dot matrix with a full view angle of 11.4°×11.4° (1.9°×1.9° between adjacent beams). The module is mounted on a 360° rotation stage that has scale divisions of 2±0.2°. The rotation stage is mounted on a precision translation rail (Trimos Inc. Switzerland) that has a resolution of 1 µm, and translation range of 1.05 m. Three 9 megapixel digital cameras [108] are positioned at various orientations with respect to the wall. They are connected to the computer through a USB (Universal Serial Bus) hub where a remote control software package (PSRemote Multi-Camera [89]) is used to trigger the cameras to take pictures within 50 ms of each other. The images are processed by a photogrammetry package called PhotoModeler® [86]. A reference length is attached to the wall to provide a known length and a global coordinate system (see inset in Figure 3.25). The designed Y axis of the reference artifact was measured to have a length of 254±0.1 mm. Prior to testing, all three cameras were calibrated. A representative image of the projected dot matrix pattern is shown in Figure 3.26. For the proposed system, the absolute coordinate of the module location and the three orientation parameters can be determined for each module position in the defined coordinate system. An intercomparison with an independent measurement of the absolute coordinates of the module location was not possible, so only the relative distance and angle change are reported for experimental results discussed below.

During the experiment, the technique was investigated experimentally following these steps:

1. The module is placed at a start position and is turned on generating the 7×7 dot matrix array of beams. The beams intersect the wall and generate an observable pattern on the wall. The first measurement position is arbitrarily defined as zero.
2. Three photos of the projected optical pattern are simultaneously taken by the three cameras.
3. The three photos are opened in PhotoModeler®. For the initial experiments the dots observed in the photographs were identified and marked as targets in the photogrammetry software for the bundle adjustment and absolute coordinate determination. Forty-nine points in the projected pattern as well as the reference length points are marked with PhotoModeler®. The bundle adjustment is performed by PhotoModeler® to yield the absolute coordinates of the forty-nine dots.

4. The coordinates of the forty-nine dots are imported into the MATLAB® algorithm to determine the best-fit x_m, y_m, and z_m coordinates of the module.
5. The module is then moved to the next position and the steps are repeated.

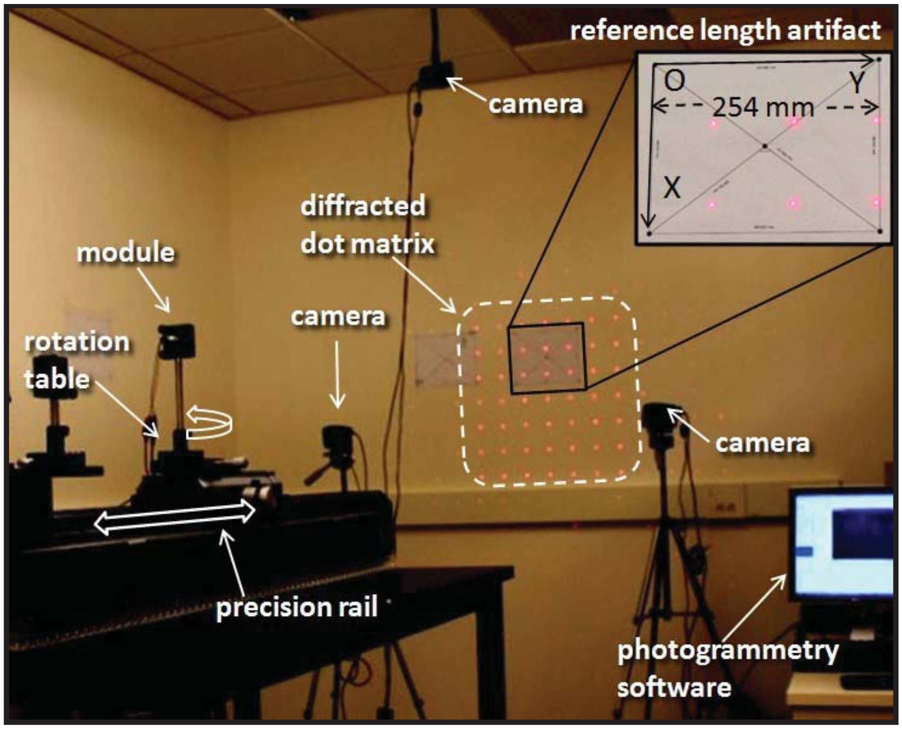

Figure 3.25: Experimental setup. Inset: defined reference length artifact.

3.3.2 Photogrammetric Measurement Process

The photogrammetric measurement starts with importing all the images of the same scene to PhotoModeler® and each image is matched to the camera calibration file corresponding to the camera used to record the image. Next step is to mark point, during which the laser dots and the reference frame dots are marked using sub-pixel target marking function in PhotoModeler®. This function marks the center of target with least-squares matching (LSM) method and can mark the points in an accurate and consistent manner. Generally five to twenty times improvement in the accuracy of the photogrammetric measurement can be expected if circular targets are used and captured with a calibrated camera. Although auto-marking function can make most of the targets automatically, there are still some laser dots targets marked manually during the experiment. Once all the laser dots targets and reference frame targets on all images are marked, they need to be referenced together through referencing function. Referencing is the process to identify that marks on two or more different photographs represent the same physical object in space. This is the key step to make sure the photogrammetry measurement will be processed properly and ensure that objects get computed with 3D positions. The images can be oriented by PhotoModeler® after enough targets are manually referenced. All the rest of the targets can be automatically referenced after the images are oriented. The 3D locations of all the targets are calculated through a bundle adjustment algorithm by processing the photogrammetric measurement. The reference frame dots are used to define the global coordinate system, which includes the scale, the origin, the x and y axis directions. The coordinates of all targets in PhotoModeler® are adjusted to the defined coordinate system.

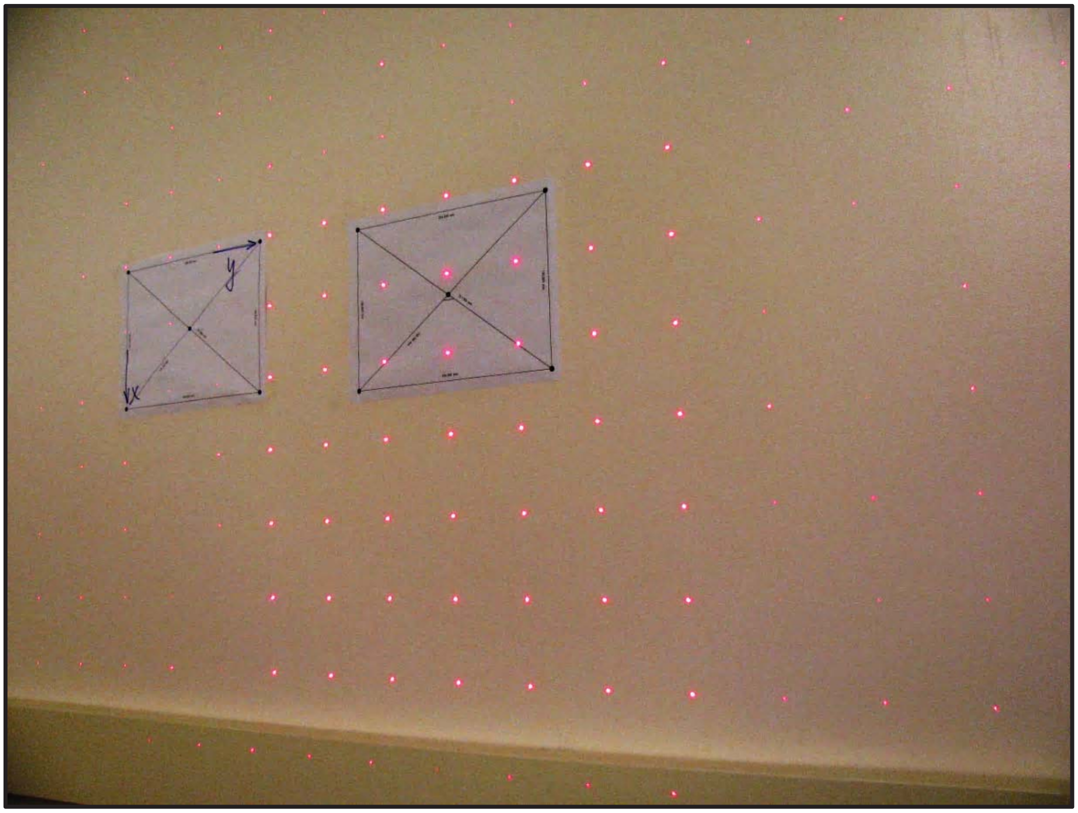

Figure 3.26: An original image of the dot projection pattern taken by the camera in the experiment.

3.3.3 Rail Calibration

The precision rail was calibrated to determine the positional accuracy by using a laser interferometer following the guidelines in ASME (American Society of Mechanical Engineers) B5.54-2005 [90]. The pitch, yaw, roll, linear displacement and straightness were measured using a laser interferometer and electronic levels. The coordinate system and the setup are shown in Figure 3.27. Based on six repeated measurements over the length of the rail, the mean values of the rail straightness d_{yz} with the standard deviation at each position are shown in Figure 3.28 (a). The error bars, representing one standard deviation, are less than 1 μm at most positions. The positive Y direction is defined to point upwards, so results shown in Figure 3.28 (a) indicate that the rail is lower in the center of its travel.

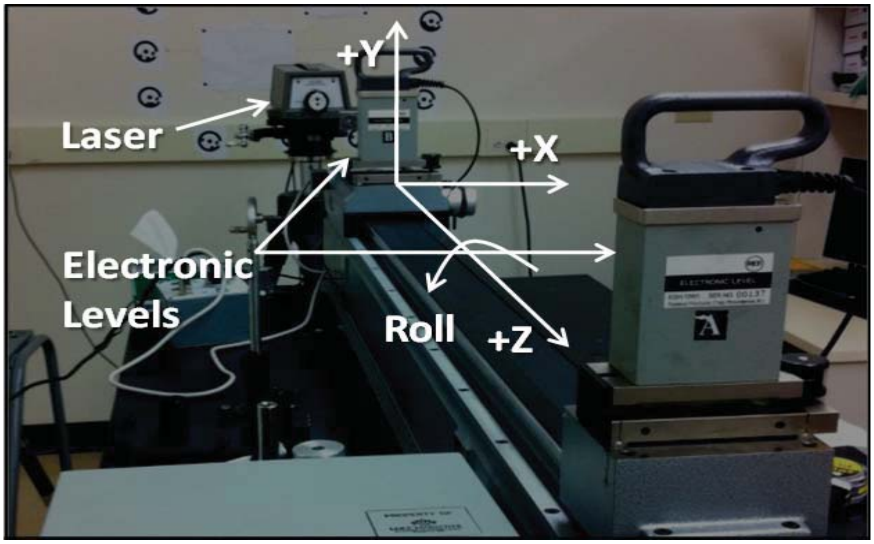

Figure 3.27. Rail calibration setup used in the experiment.

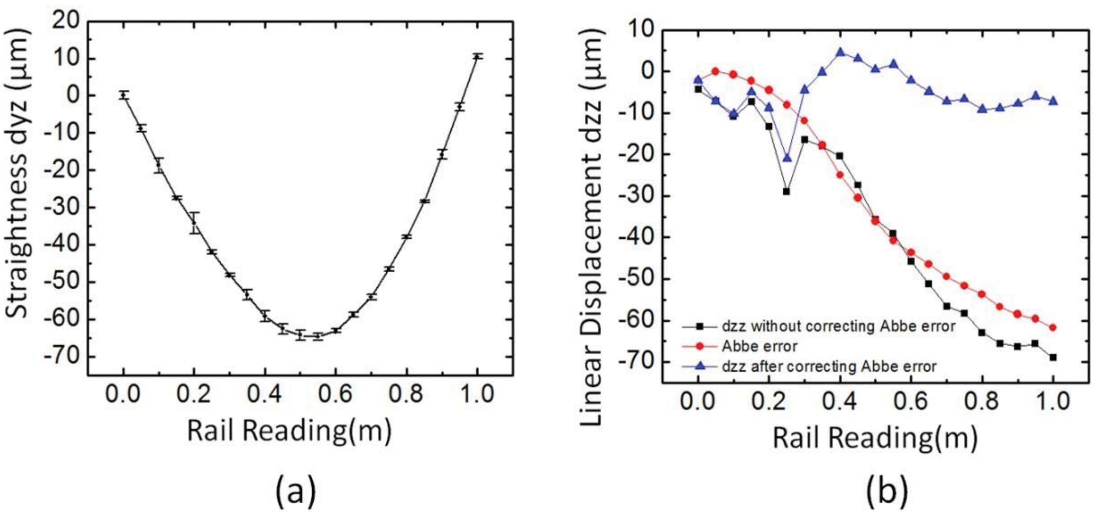

Figure 3.28: Rail calibration results: (a) straightness (d_{yz}) of the rail, (b) linear displacement (d_{zz}) of the rail.

The raw linear displacement (d_{zz}) data from the interferometer measurements of the rail is the black curve (■) shown in Figure 3.28 (b). Since the beam path (the laser and the diffraction grating) in the experiments was approximately 130 mm above the location of the rail encoder, there is an error introduced by this Abbe offset and the rail straightness. This Abbe error is shown as the red curve (●) in the figure. The corrected linear displacement of the rail is shown as the blue curve (▲). It can be seen that the rail encoder reading of the linear displacement of the rail, as measured with the displacement measuring interferometer, is less than 20 µm at most positions. This is significantly less than the variability observed in the measurements, as seen in Figure 3.29.

3.3.4 Translation Test Results

The module was translated 0.9 m along the precision rail in increments of 0.1 m. At each position the module location was measured using the proposed method, as outlined in section 3.3.1. The translated distances are calculated using the coordinates of the module (x_m, y_m, z_m) between adjacent positions as a vector length change (the translation rail is not necessarily exactly aligned to the z axis of the global coordinate system). The translation test was conducted ten times and the average measured distance at each position versus the rail reading is shown in Figure 3.29 (a). The linear fit equation is $Y=1.0008\times X -0.00001$, and this agreement is reasonable in light of the uncertainty analysis in section 6.3.

Figure 3.29 (b) illustrates the mean value of the differences between the measured distance and the rail reading at each position. The results show that the measurement differences at all positions are smaller than 1.2 mm. And the uncertainties of the measurement are within 0.3 mm and are dominated by the repeatability of the photogrammetric measurement. The positional accuracy of the rail was determined with a laser interferometer following the guidelines in ASME B5.54-2005. The standard uncertainty of the rail linear displacement is less than 20 µm after correcting the error motion (dominated by the Abbe error), see section 3.3.3. This is significantly less than the variability observed in the measurements, as shown in Figure 3.29.

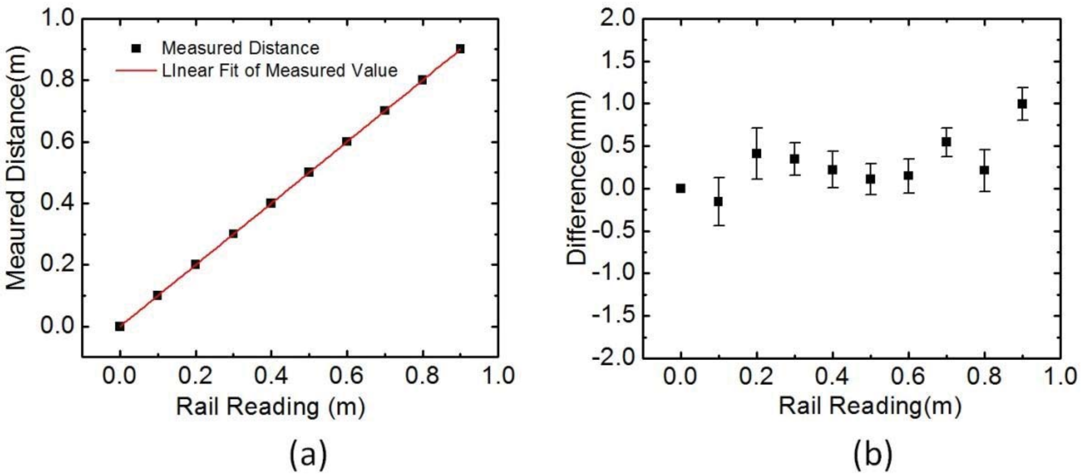

Figure 3.29: Translation test results. (a) Measured distance versus rail reading, (b) measured distance difference versus the rail reading.

3.3.5 Rotation Test Results

The module was rotated through 60°. The rotated angle is calculated based on the angle change of the $\overrightarrow{MP_1}$ vector. The test was repeated three times. The average values of measured angles versus angle reading are shown in Figure 3.30 (a). The resolution uncertainty ($u_{reading}$) of the angle encoder is about ±0.2°, which is a Type B uncertainty estimated based on experimental experience and manufacture specification. The angle differences, i.e. the difference between the measured angles and those read from the stage scale, are shown in Figure 3.30 (b).The absolute values of angle differences are smaller than 0.3° for all measurements. The vertical error bars represent the combined standard uncertainty of the measurement, where this is a combination of the measurement standard deviation, $u_{measured}$ and the resolution uncertainty of the angle encoder $u_{reading}$ by using equation (3.12):

$$u = \sqrt{u_{measured}^2 + u_{reading}^2} \tag{3.12}$$

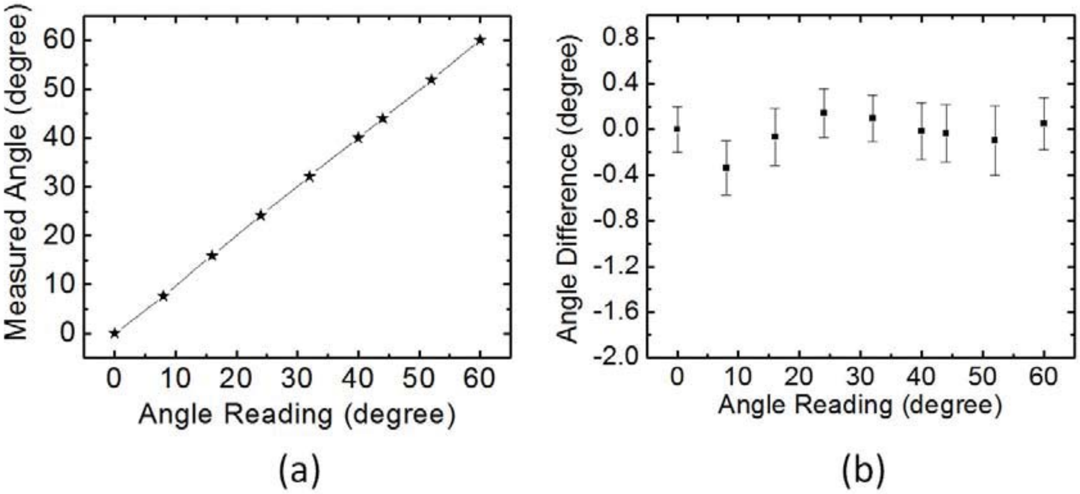

Figure 3.30: Rotation test results. (a) Measured angles versus angle reading, (b) angle differences versus the angle reading.

3.3.6 Preliminary Test on Robot

3.3.6.1 Experimental Setup and Procedure

The proposed metrology system was applied to check the positioning repeatability, distance accuracy and distance repeatability of an industrial robot, ABB IRB140 [109]. The experimental setup of the test on robot is show in Figure 3.34. The laser employed in the module has a wavelength of 658 nm and a power of 40 mW. The module generates an 11×11 dot matrix with a full view angle of 29°×29° (2.9°×2.9° between adjacent beams). The reference angles of the optical pattern have not been calibrated yet for the test discussed in this section. The same three 9 megapixel digital cameras (Canon PowerShot SX110IS) are positioned at various orientations with respect to the projection board. The remote control software package (PSRemote Multi-Camera) is used to trigger the three cameras to take pictures within 50 ms of each other. A reference length of 253.5 mm is attached to the projection form board to provide a known length and a global coordinate system. The software and measurement procedure are the same as that mentioned in section 3.3.1. All three cameras were calibrated beforehand following the procedure described in section 3.2.2. In order to better evaluate the measurement ability of the proposed metrology system, a laser tracker [110] was employed to simultaneously measure the distances moved by the robot.

In order to use the laser tracker system as the reference, the retro-reflector of the laser tracker system needs to be mounted to the robot arm. During the experiment, the robot arm needs to follow the path shown in Figure 3.33 and the retro-reflector requires a free line-of-sight to the sensor so that the laser beam can be reflected back to the sensor. A fixture was designed to satisfy the free line-of-sight requirement of the laser retro-reflector so that the laser tracker system and the proposed metrology system can measure the movement of the robot arm at the same time. The design of the fixture is shown in Figure 3.31. The fixture is designed to have the module mounted on the top, and the magnetic nest for retro-reflector can be mounted to either the front plate or the side plate where a free line-of-sight is possible for the chosen movement path. The mounting plate is on the rear side, which is designed to facilitate attachment to the robot arm. The position that the laser tracker measured is the center of the retro-reflector, which is the center of the sphere shown in Figure 3.32. The position that the proposed metrology system measured is the module position, which is the intersection of the laser and the projection head, as shown in Figure 3.32. In the defined coordinate system shown in Figure 3.32, the sphere center locates at (-66.919, 0.776, -34.319) mm while the module locates at (-3.361, 59.287, -38.882) mm. The proposed metrology system is called as “photogrammetric sensor” in the measurement results discussed in the following.

According to ISO 9283: 1998 (E) [123], a test cube should be chosen to test the performance of the robot and all measurement points should be inside of the test cube and should be as far away from each other as possible. A test cube with side of length of 250 mm was chosen for ABB IRB 140, as shown in Figure 3.33 (a). A linear path in the diagonal of the cube was selected and the length of the path is 80% of the distance between opposite corner of the diagonal plane (for example, D_P_{23}=D_P_{45}=200 mm). The robot was programmed to go through the cycles shown in Figure 3.33 (b). Starting from P_1, the robot successively moved the mechanical interface of the robot arm to the poses P_5, P_4, P_3, P_2, and P_1 using a unidirectional approach as illustrated in Figure 3.33 (b). No measurement was taken at P_1 in the 0^{th} cycle. The robot was programmed to complete 5 cycles. At each point the robot stops for 30 seconds in order to allow the laser tracker and the proposed metrology system to record the position. According to ISO 9283: 1998 (E), the ambient temperature of the testing environment should be 20 °C and the testing temperature shall be maintained at (20±2) °C. During the test the room temperature was 22.2 °C, which is very close to the requirement. The maximum payload is 5 kg for the robot ABB IRB 140. The payload of the robot arm was about 0.5 kg, which can be treated as a test with the mass of rated loaded reduced to 10%, specified in ISO 9283: 1998 (E). The robot was running with 50% rated speed (500 mm/s).

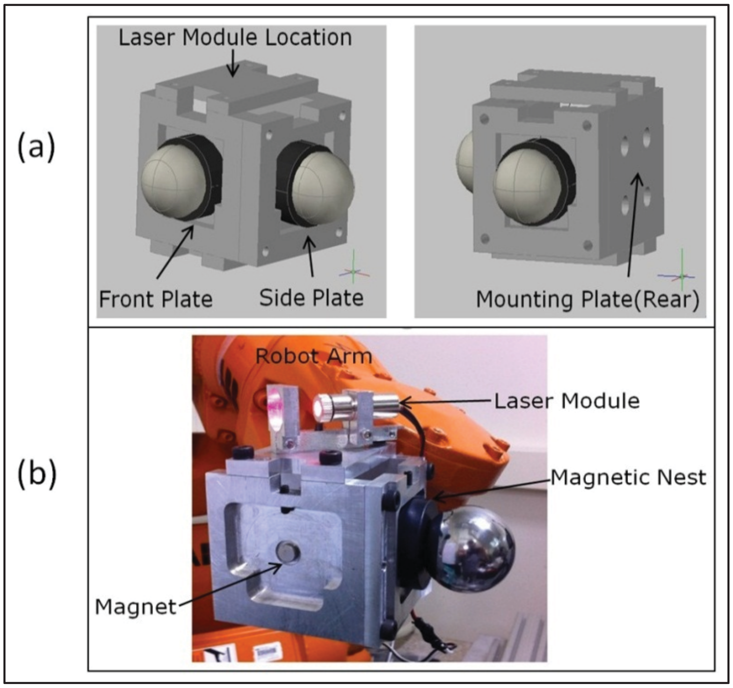

Figure 3.31: Fixture design for test on the robot: (a) CAD model of the fixture, (b) image of the fixture in the experiment.

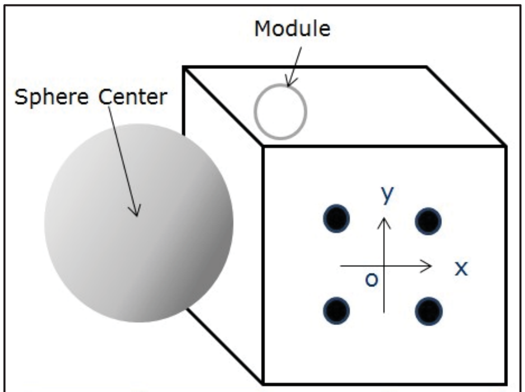

Feature	X(mm)	Y(mm)	Z(mm)
Sphere center	-66.919	0.776	-34.319
Module	-3.361	59.287	-38.882

Figure 3.32: Relative positions of the module and the sphere center measured by a coordinate measurement machine.

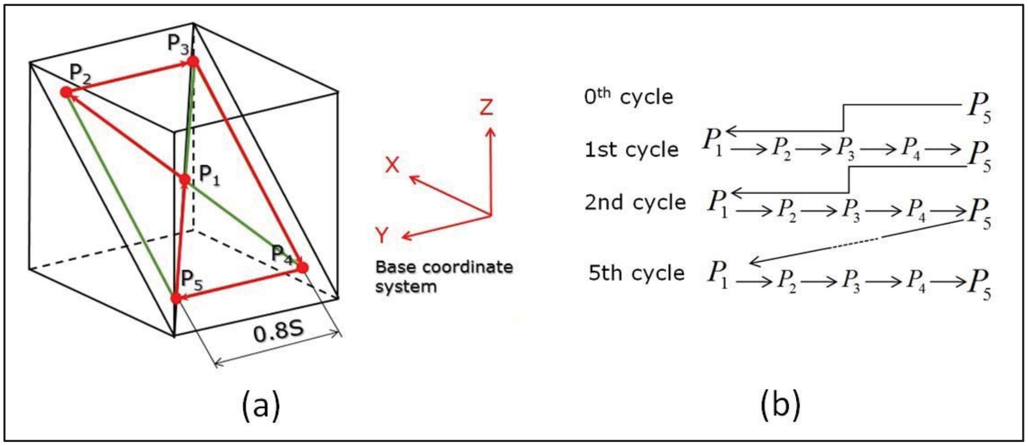

Figure 3.33: (a) Test paths for the robot test (ISO 9283: 1998E), (b) test cycles for the robot test.

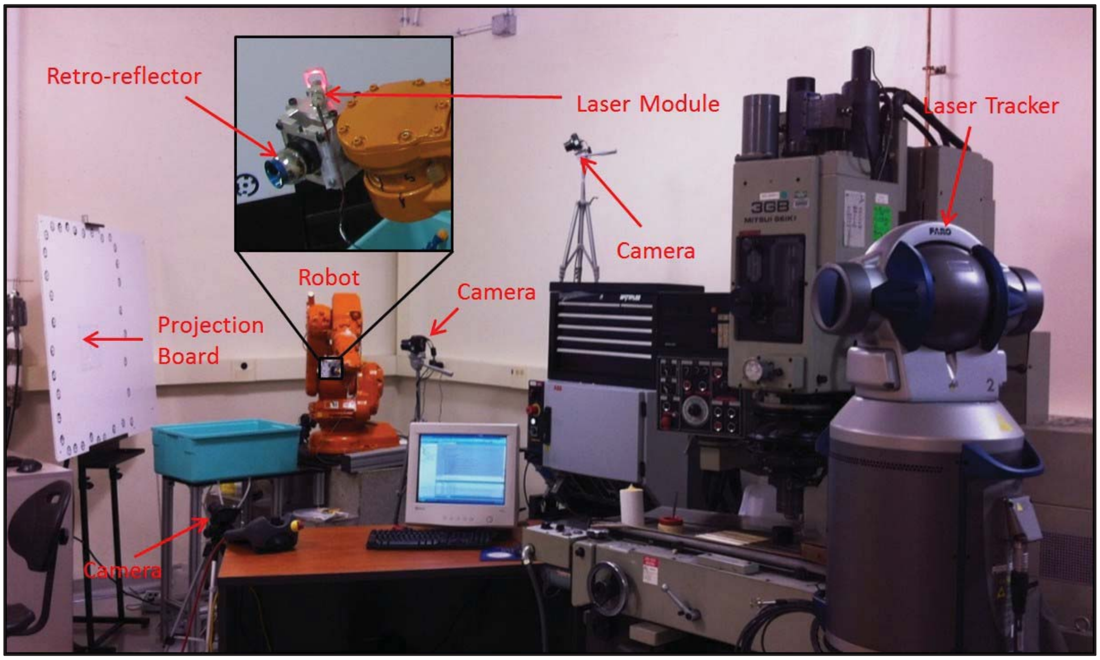

Figure 3.34: Experimental setup for the robot test.

3.3.6.2 Measurement Results

1. Robot Positioning Repeatability

The positioning repeatability of the robot was investigated first. The positioning repeatability expresses the closeness of agreement between the attained positions after *n* repeat visits to the same command position in the same direction. The positioning repeatability is defined in equation (3.13).

$$RP_l = \bar{l} + 3S_l \tag{3.13}$$

with

$$\bar{l} = \frac{1}{n}\sum_{i=1}^{n} l_i \ , \tag{3.14}$$

$$l_i = \sqrt{(x_i - \bar{x})^2 + (y_i - \bar{y})^2 + (z_i - \bar{z})^2} \tag{3.15}$$

with

$$S_l = \sqrt{\frac{\sum_{i=1}^{n}(l_i - \bar{l})^2}{n-1}} \tag{3.16}$$

$\bar{x}$, $\bar{y}$ and $\bar{z}$ are the coordinates of the barycenter of the cluster of points obtained after repeating the same pose *n* times (see Figure 3.35). x_i , y_i and z_i are the coordinates of the $i-th$ attained pose.

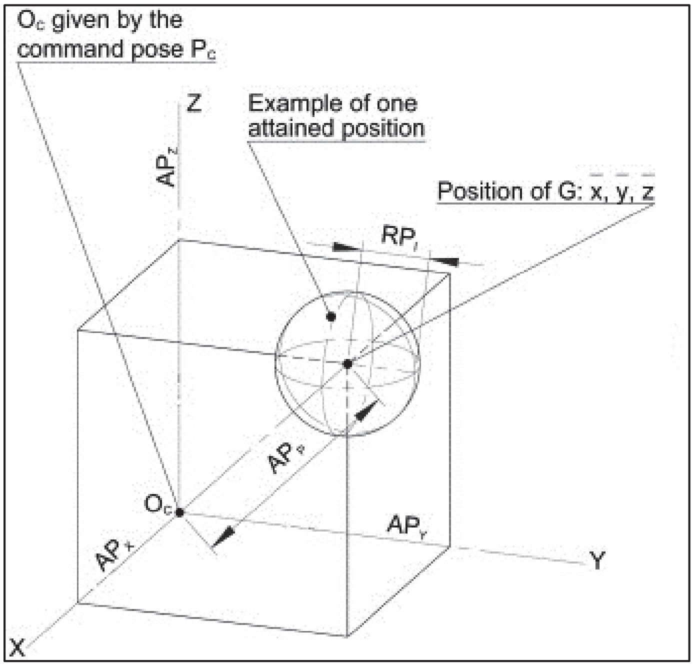

Figure 3.35: Positioning accuracy and repeatability defined in ISO 9283: 1998 (E).

According to the results obtained from the laser tracker, the positioning repeatability of the robot is 0.03 mm, 0.04 mm, 0.02 mm, 0.03 mm and 0.03 mm for points P_1 to P_5 respectively, as shown in Figure 3.36 (b). This indicates that the robot has positioning repeatability better than 0.04 mm. This result matches specifications of the robot. However, the photogrammetric sensor reports that the robot has positioning repeatability larger than 1.2 mm. One important factor contributing to this is that the photogrammetric sensor method itself has a measurement repeatability of 0.5 mm.

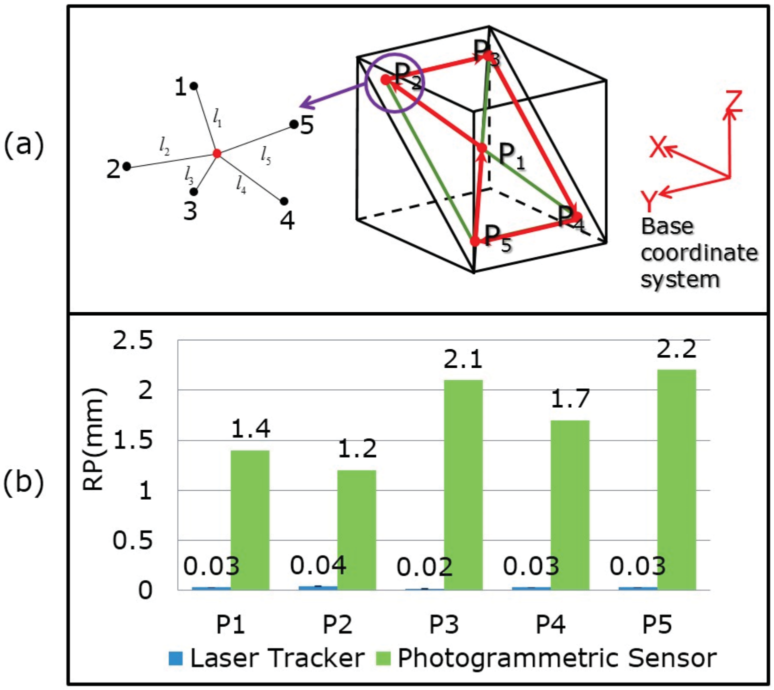

Figure 3.36: (a) Diagram of the positioning repeatability of the robot, (b) positioning repeatability measured by two methods, red bar stands for the measurement repeatability of photogrammetric sensor.

2. Robot Distance Accuracy and Repeatability

The mean value of each distance the robot travelled is shown in Figure 3.37. The mean value reported by the laser tracker is used as reference. For the distances between point P_1 and P_2, P5 and P_1, the robot command value is 173.2 mm. The laser tracker result shows that the real distance the robot travelled is larger than the robot command (the red dashed line). The true distance travelled by the robot between points P_1 and P_2 is 0.9 mm larger than the commanded value and the traveled distance between P_5 and P_1 is 0.5 mm larger than the commanded value. The result reported by the photogrammetric sensor is about 1 mm less than the result reported by the laser tracker. For the distance between points P_2 and P_3, the robot actually travelled 0.6 mm less than the command value. For the same command value, the distance the robot travelled is 0.2 mm larger than command value for the distance between points P_4 and P_5 (Figure 3.37 (b)). The results for these two distances reported by photogrammetric sensor are about 1.5 mm smaller than the results reported by the laser tracker. The command value for distance between points P_3 and P_4 is 282.8 mm. However, the results reported by the laser tracker show that the robot actually travelled 284.2 mm, which is 1.4 mm larger than the command value. These results indicate that the robot has position repeatability to 0.04 mm level, which agrees with the specification of the robot. The commanded distance has distance different up to 1.6 mm compared with the results obtained from the laser tracker. Results shown in Figure 3.37 indicate that the robot actually travels different distances even with the same commanded value. Different axes of the robot were involved to complete different travel paths, which leads to different distances travelled by the robot even with the same command value shown in Figure 3.37.

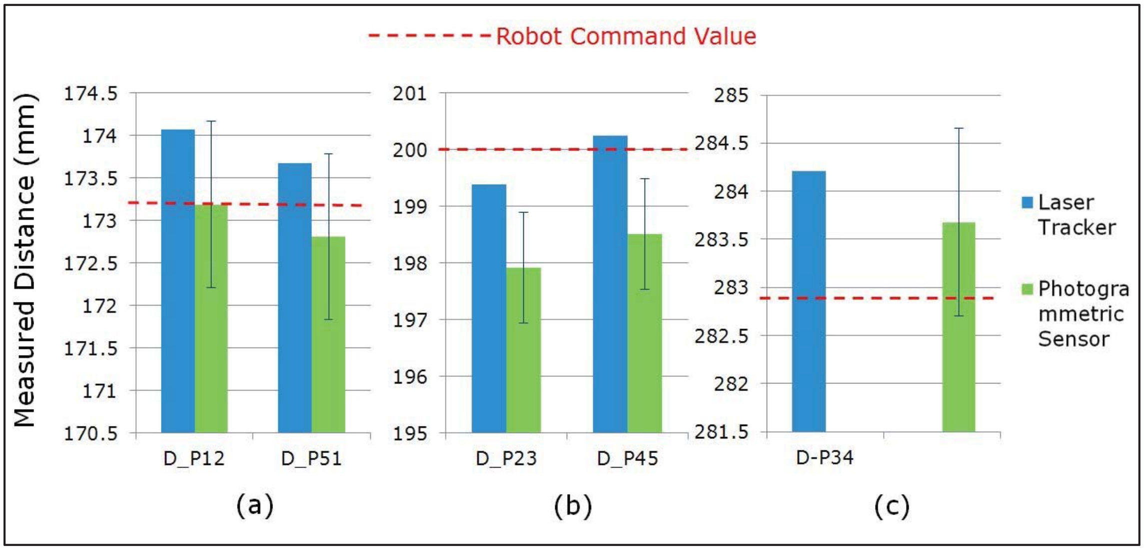

Figure 3.37: Measured distance of the robot movement: (a) measured distance between P_1 and P_2, P_5 and P_1, (b) measured distance between P_2 and P_3, P_4 and P_5, (c) measured distance between P_3 and P_4 and P_5. Red dash line stands for the robot command value and error bar stands for 1σ of 5 measurements.

The position distance accuracy (AD) and distance repeatability (RD) is defined by equation (3.17) and (3.18) (ISO 9283:1998 (E)).

$$\mathrm{AD}_p = \overline{D} - D_c \tag{3.17}$$

$$RD = 3\sqrt{\frac{\sum_{i=1}^{n}(D_i - \overline{D})^2}{n-1}} \tag{3.18}$$

with

$$\overline{\mathrm{D}} = \frac{1}{n}\sum_{i=1}^{n} D_i \, , \tag{3.19}$$

$$D_i = \left|P_{1i} - P_{2i}\right| = \sqrt{(x_{1i} - x_{2i})^2 + (y_{1i} - y_{2i})^2 + (z_{1i} - z_{2i})^2} \tag{3.20}$$

$$D_{\mathrm{c}} = \left|P_{c1} - P_{c2}\right| = \sqrt{(x_{c1} - x_{c2})^2 + (y_{c1} - y_{c2})^2 + (z_{c1} - z_{c2})^2} \tag{3.21}$$

with

P_{c1} and P_{c2}: the command positions

P_{1i} and P_{2i} : the attained positions

x_{1i}, y_{1i} and z_{1i}: the coordinates of P_{1i}

x_{2i}, y_{2i} and z_{2i}: the coordinates of P_{2i}

x_{c1}, y_{c1} and z_{c1}: the coordinates of P_{c1}

x_{c2}, y_{c2} and z_{c2}: the coordinates of P_{c2}

The positioning distance accuracy of the robot performance is shown in Figure 3.38 (a). According to the laser tracker measurement, the robot has a distance accuracy of 1.37 mm for distance between P_3 and P_4. This indicates that the distance the robot arm actually travelled has a 1.37 mm offset with the commanded distance. The distance repeatability is shown in Figure 3.38 (b). The laser tracker measurement indicates that the robot has distance repeatability better than 0.04 mm. The measurement from the photogrammetric sensor shows that the robot has distance repeatability larger than 1.5 mm for all the distances measured in the experiment. The repeatability of the photogrammetric sensor is around 0.6 mm, which is a major factor contributing to the distance repeatability reported by the photogrammetric sensor.

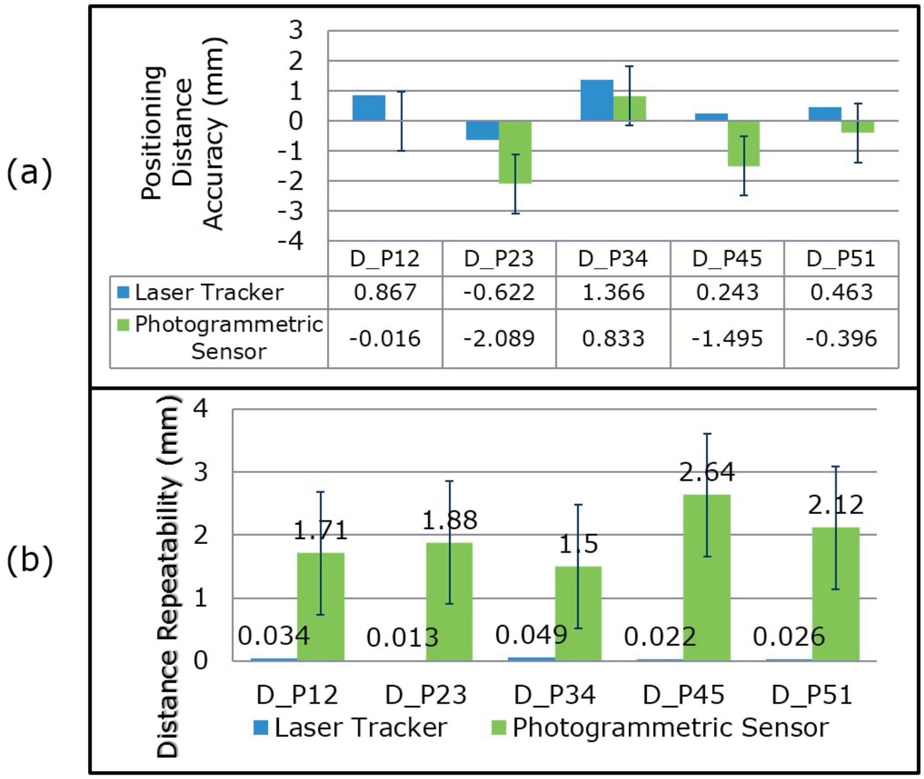

	D_P12	D_P23	D_P34	D_P45	D_P51
Laser Tracker	0.867	-0.622	1.366	0.243	0.463
Photogrammetric Sensor	-0.016	-2.089	0.833	-1.495	-0.396

Figure 3.38: (a) The measured positioning distance accuracy of the robot. (b) Measured distance repeatability of the robot.

3.3.6.3 Robot Test Results Discussion

The results discussed in section 3.3.6.2 indicate that the robot has positioning repeatability smaller than 0.04 mm as reported by the laser tracker measurement, which agrees with the robot specifications. The distance repeatability of the robot is smaller than 0.05 mm. Compared with the distance repeatability, the robot has a relative large distance accuracy (<1.37 mm). Through the tests on the robot, it has been proved that the proposed photogrammetric sensor can be used to measure the 6 DOFs of a target. As shown in Figure 3.37, the mean values of different distances obtained from the photogrammetric sensor are always smaller (around 1 mm smaller) than those reported by the laser tracker. This indicates that systematic error exists in the proposed metrology system. The systematic error may be caused by the uncertainty of the reference length and the un-calibrated inter-beam angles in the optical pattern. The measurement uncertainty of the photogrammetric sensor can be reduced and a detailed discussion will be given in Chapter 4. In addition, the proposed metrology has the capability of large range measurement (up to tens of meters). However, limited by the robot capability, the measured distances in the test are smaller than 300 mm.

3.3.7 Preliminary Experimental Results Discussion

Based on the results presented in section 3.3.4 and section 3.3.5, a standard uncertainty was observed at the level of 1 part in 10^3 for the one dimension translation test, and 5 parts in 10^3 for the rotation test. Though only two degrees of freedom were tested in the experiments, these results demonstrate that the technique can be used to trace the motion of the target in all 6 DOFs. This is possible because the coordinates of the module, as well as the vectors from the module to each dot, can be solved for at each module position, thus establishing the complete angular orientation in the global coordinate system. The test results on robot presented in section 3.3.6 confirmed that the proposed metrology system has the ability to measure 6 DOFs movement of the robot arm in 3D space. Limited by the repeatability of photogrammetric measurement and the repeatability of the current setup of the proposed system, the current system could only be used for robot calibration for certain categories of robots, which have positional repeatability larger than 0.6 mm. All these experimental results in conjunction with the simulation detailed in section 4.1 indicate that further improvements in the measurement can be obtained by either one of two approaches: improved photogrammetric measurements of the projected dots and/or improved projection head design. The accuracy of the photogrammetric measurements can be improved by using high resolution and high quality cameras with fixed focal length, performing field calibration, and taking more images to improve photo redundancy. The improvements possible from optimum optical design of the projection head will be addressed in section 4.1. In addition, an improved calibrated length standard and improved angular characterization of the projected pattern will also improve the measurement. The angle calibration for the projected optical pattern will be addressed in section 4.2.

CHAPTER 4: SYSTEM MODELING AND IMPROVEMENTS

In this chapter, the proposed metrology system is first modeled through numerical simulations. The factors affecting the system sensitivity, such as the noise on the dot centroid, the number of dots, the full view angle of the optical pattern and the errors associated with reference angles of the module are investigated. Based on the simulation results, some system improvements are made, including the calibration to the reference angles associated with the module and a virtual camera approach to determine the module position. Then the improvements have been validated through experimental tests on the precision rail. Implementation of multiple coordinate systems is discussed at the end of this chapter and a rotation test on a precision rotation stage is conducted by using the multiple coordinate systems to increase the measurement range of proposed system.

4.1 System Modeling

The numerical simulations were performed to investigate the consequence of the uncertainty of the photogrammetric measurement and the design of the optical pattern on the uncertainty of the measured module location. In the simulation, the photogrammetry step is replaced by numerically generating the *xyz* coordinates of the dots where the diffracted beams intersect a plane from a known module location. Then these coordinates are input into the least-square minimization algorithm to determine the measured module location. In this way the noise can be added to the dot coordinates (the noise stands for the uncertainty of the photogrammetric measurement on each dot), thus the system sensitivity to the optical pattern parameters can be tested. These parameters include the number of dots in the pattern, N, on any one side of a square projected pattern, the full view angle, β, of the pattern, and the geometry of projection surface.

The module is modeled to be at a known position M (x_m, y_m, z_m) with respect to a defined global coordinate system. The projected pattern is generated by finding the intersection of the beams with a plane that is perpendicular to the optical axis of the module and offsets $d=2\ m$ (from the module to the central dot). See Figure 4.1 for a schematic of the simulation setup. The noise from the photogrammetric measurement is represented by adding random normal distribution noise at a level of $\delta_x=\delta_y=\delta_z$ to the *xyz* coordinates of each dot. The noise sampled forms a normal distribution for each axis and the noise values in *xyz* directions are not the same for each iteration. These coordinates ($x+\delta_x, y+\delta_y, z+\delta_z$) are put into the least-square minimization algorithm to determine the module position, i.e. step 4 as outlined in section 2.3.

It needs to mention that contributions to the standard deviations $\sigma_x, \sigma_y,$ and σ_z in the module position made by the noise added to *xyz* coordinates of the dot position was investigated first. Simulation results indicate that contributions to the standard deviations $\sigma_x, \sigma_y,$ and σ_z in the module position made by the noise added to *xyz* coordinates of the dot position are corrected. When noise is only added to z coordinate of the dot position, it has about the same contributions to the standard deviations σ_x and σ_y. It is also found that σ_z is 10 times smaller than σ_x and σ_y, and a detailed discussion will be given in section 4.1.3 and section 4.1.5. When noise is only added to x coordinate of the dot position, the value of σ_x is about twice as the value of σ_y. On the other hand, the value of σ_y is about twice as the value of σ_x when noise is only added to y coordinate of the dot position.

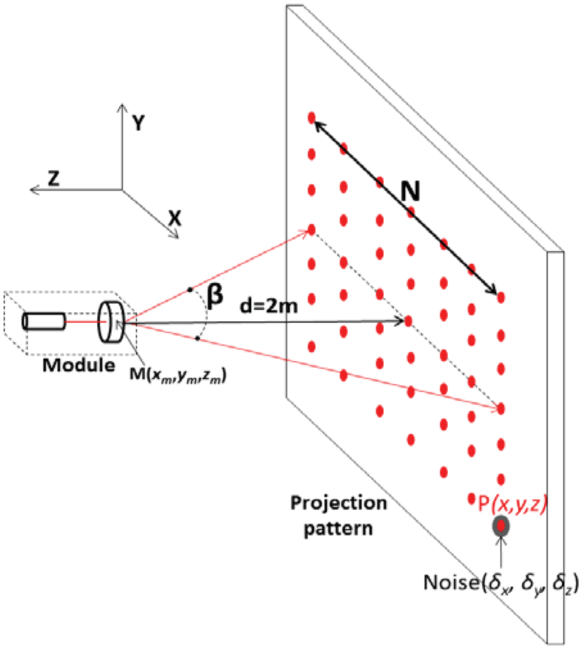

Figure 4.1: Schematic of the simulation configuration.

4.1.1 Position Sensitivity to Random Noise on Dot Centroid

The effect of random noise added to the dot centroid on the calculated module position was investigated first. Following the procedure presented above, a random normal distribution noise at different levels ($\delta_x=\delta_y=\delta_z$ increases from 1 μm to 1000 μm) was added to the *xyz* coordinates of each dot. The module position is determined by inputting ($x+\delta_x$, $y+\delta_y$, $z+\delta_z$) into the least-square minimization algorithm. This procedure is repeated 1,000 times and the standard deviations σ_x, σ_y, and σ_z in the module position are reported for different values of δ. For the simulation results shown below, the full view angle was set to 35° while N was set to 21. The combined standard deviation of the module position in *xyz* directions is given by equation (4.1).

$$\sigma = \sqrt{\sigma_x^2 + \sigma_y^2 + \sigma_z^2} \tag{4.1}$$

The results shown in Figure 4.2 (a) indicate that the standard deviation of the module position increases linearly with the increase of the noise. Thus, the standard deviation of the module position measurement can be reduced by reducing the uncertainty of the photogrammetric measurement.

The standard deviations σ_x, σ_y, and σ_z in the module position are shown in Figure 4.2 (b). With the increase of the noise level, all three components σ_x, σ_y, and σ_z increase linearly. The standard deviations in x direction (σ_x) and y direction (σ_y) are about 30 times that of the noise, while the standard deviation of the module position in z direction (σ_z) is around twice the noise level. The standard deviation in z direction, σ_z is 10 times smaller than σ_x and σ_y. This is due to the fact that the least-square value expressed in equation (3.4) is more sensitive to the module position in z direction than those in x and y directions. A detail discussion on this will be given in section 4.1.3 and section 4.1.5.

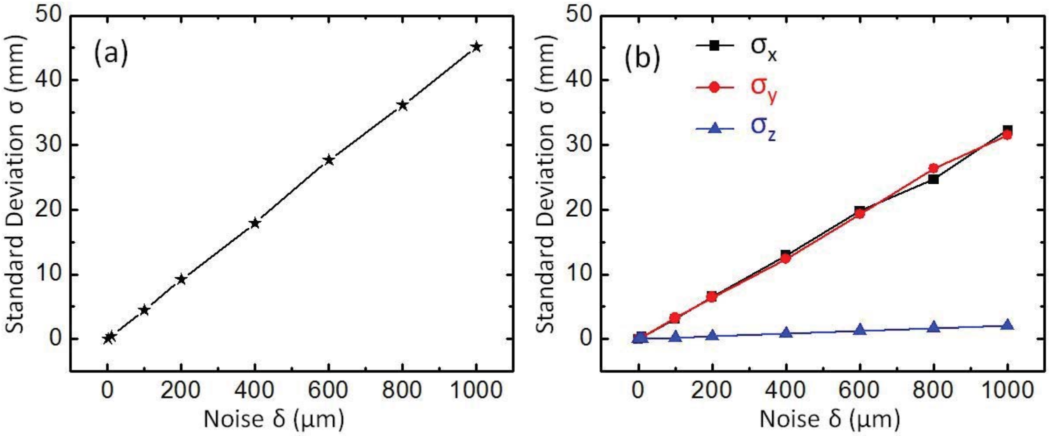

Figure 4.2: The relationship between the noise and the standard deviation of the module position with *N=21* and *β=35°*: (a)standard deviation of the module position (σ) as a function of the noise (δ), (b) standard deviation of the module position in *xyz* directions (σ_x, σ_y, σ_z) as a function of the noise (δ).

4.1.2 Position Sensitivity to Dot Number

The total number of dots in the optical pattern affects the uncertainty of the measured module position. A range of values of *N*, the number of dot on any one side of a square projected pattern, were investigated to explore the relationship between *N* and the uncertainty of the measured module position. The simulation configuration is the same with Figure 4.1, in which the optical axis of the module is perpendicular with the projection plane. The module has a 2 m offset with the central dot on the plane and the full view angle (FVA) was set to 35°. The values of N increase from 7 to 81. Random normal distribution noise at the level of 100 µm was added to each axis to represent the uncertainties of the dot coordinate observed in the experiment. The noise values in *xyz* directions are not the same for each iteration. By inputting $(x+\delta_{xi}, y+\delta_{yi}, z+\delta_{zi})$ into the least-square minimization algorithm, the module position is calculated. After repeating this procedure 1,000 times the standard deviations σ_x, σ_y, and σ_z in module position are reported for different values of N. Figure 4.3 (a) shows the standard deviation of the module position (σ, as defined in equation 4.1) as a function of N. The value of σ decreases from 0.53 mm to 0.18 mm when the value of N increases from 7 to 41. Such decrement slows down when the value of N increases from 41 to 81. The value of σ decreases from 0.18 mm to 0.12 mm. Figure 4.3 (b) shows that the standard deviations of the module position, σ_x, σ_y, and σ_z, decrease as the number of dots in the projected pattern increases. The values of σ_x and σ_y (they are in the directions that parallels with the plane) are very close and they share similar behavior. On the other hand, the value of σ_z (σ_z is in the direction that is perpendicular with the plane) is much lower than those of σ_x and σ_y. The reason caused such behavior in *xyz* directions is discussed in section 4.1.3. From the results shown in Figure 4.3, it can be concluded that increasing the value of N decreases the standard deviation of the measured module position. Therefore, a large number of dots ($N > 40$) are preferred for the design of the diffraction grating.

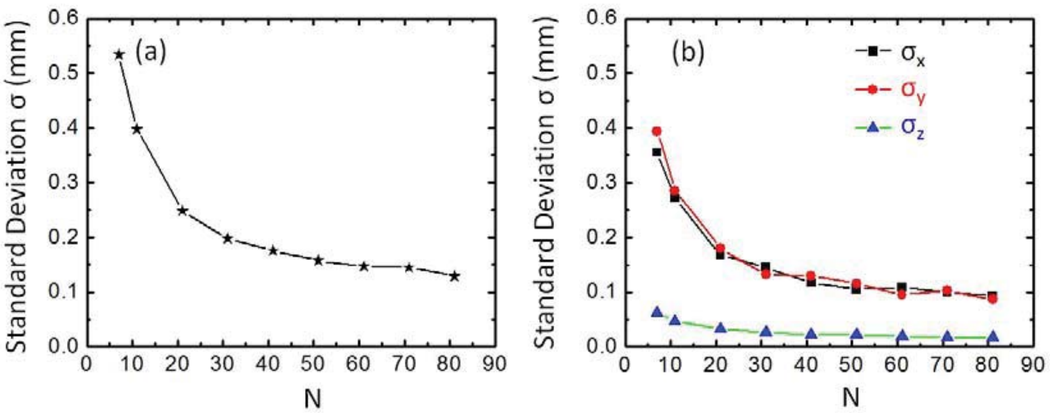

Figure 4.3: The relationship between the number of dots and the standard deviation of the module position with $\beta=35°$: (a) standard deviation of the module position (σ) as a function of N, (b) standard deviation of the module position in *xyz* directions (σ_x, σ_y, σ_z) as a function of N.

4.1.3 Position Sensitivity to Full View Angle

The effect of changing the full view angle, β, on the module location is illustrated in Figure 4.4. For all the data points shown in Figure 4.4, the module is 2 m away from the wall. And noise in random normal distribution at the level of $\delta_x=\delta_y=\delta_z=100\ \mu m$ was added to the dot coordinates in *xyz* directions, while N was set to 21. The noise values in *xyz* directions are not the same for each iteration. Only a range of β values larger than 10° are considered here, a range over which the z module coordinate is well defined and the algorithm converges well. (For a very small full view angle, the module position becomes very uncertain and the algorithm does not converge well). For these geometry conditions, the standard deviations of the module position are larger than 3 mm when the full view angle is approximately 10° (see Figure 4.4 (a)). They drop to smaller than 0.19 mm when the full view angle increases to 40°. The decrement becomes slow when the full angle increases from 40° to 80°. From the results shown in Figure 4.4 (a) it can be concluded that increasing the full view angle decreases the standard deviation of the module position. Hence, a full view angle larger than 40° is desired for the design of the diffraction grating.

The standard deviations of the module position in *xyz* directions (σ_x, σ_y, σ_z) as a function of β are given in Figure 4.4 (b). As shown in Figure 4.4 (b), σ_x and σ_y share the same behavior for each value of β. For a small full view angle $\beta=10°$, the values of σ_x and σ_y are around 2.4 mm while the value of σ_z is about 0.13 mm. With the increase of β, σ_x and σ_y decrease very fast and the difference between σ_x, σ_y and σ_z becomes smaller. The values of σ_x and σ_y are around 0.13 mm while the value of σ_z is about 0.03 mm for $\beta=40°$. The difference between them can be further reduced with the increase of β. Therefore, it can be concluded that σ_z is much lower than σ_x and σ_y when the full view angle is small (for example, $\beta<30°$). The increase of the full view angle brings σ_x, σ_y and σ_z to the same level (for example, $\beta=80°$). In practical application, an optical pattern with a larger full view angle requires larger projection area.

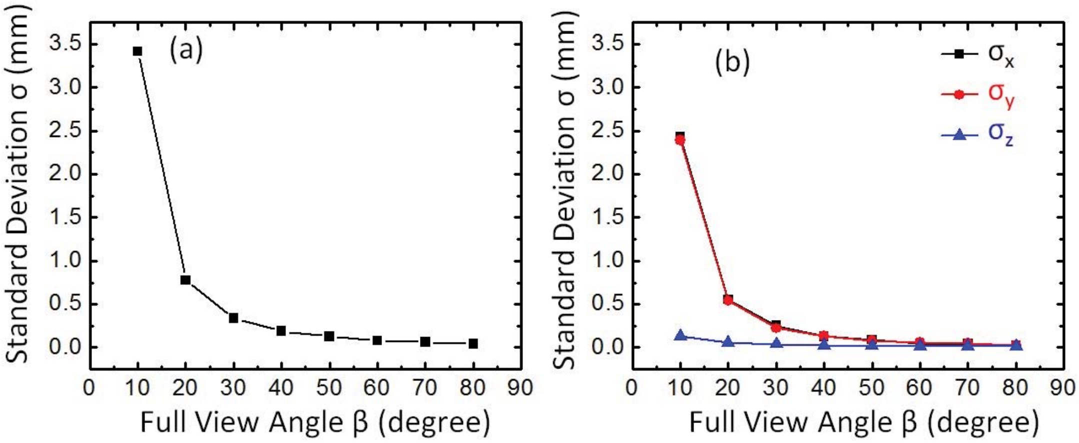

Figure 4.4: The relationship between full view angle and standard deviation of module position with $N=21$. (a)Standard deviation of module position (σ) as a function of β, (b) standard deviation of module position (σ_x, σ_y, σ_z) as a function of β.

Another simulation is performed to investigate the relationship between the behavior of σ_x, σ_y and σ_z and the full view angle of the optical pattern, β. In this simulation, the least-square sensitivity to the offset of the module position in *xyz* directions is investigated for different values of β with $N=21$ and $\delta_x=\delta_y=\delta_z=100\ \mu m$. By using the same simulation configuration presented in Figure 4.1, the value of χ^2 (the expression of χ^2 is given in equation (3.4) in section 3.1) as a function of the offset of the module position is reported for different values of β. The values of χ^2 as a function of the offset of the module position in X, Y, and Z directions for $\beta=10°$, $\beta=40°$ and $\beta=80°$ are shown in Figure 4.5 (a), Figure 4.5 (b) and Figure 4.5 (c), respectively.

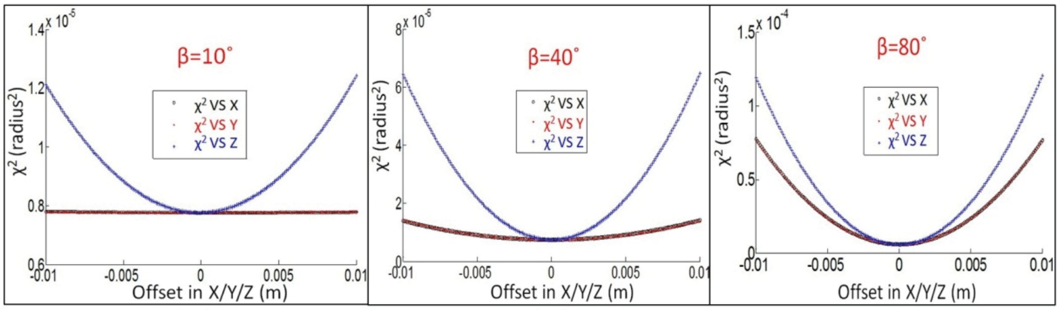

(a) (b) (C)

Figure 4.5: The value of χ^2 as a function of the offset of the module position in X/Y/Z directions when $N=21$, $\delta_x=\delta_y=\delta_z=100\ \mu m$: (a) $\beta=10°$, (a) $\beta=40°$, (a) $\beta=80°$.

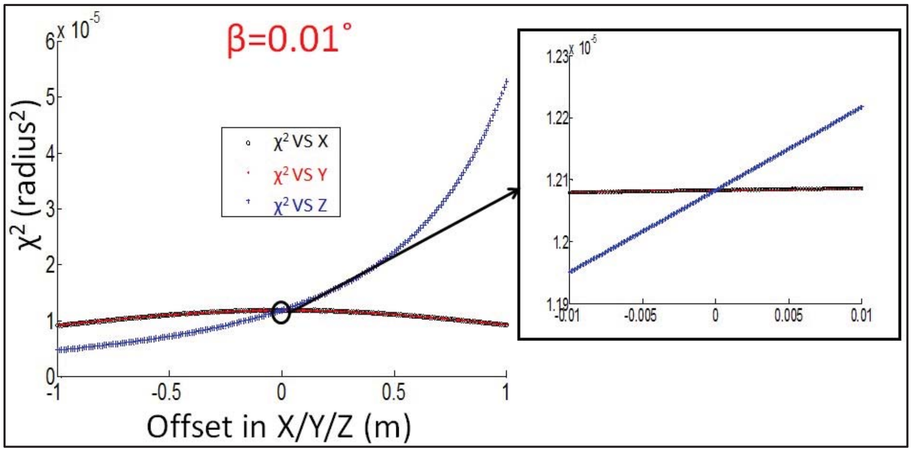

Figure 4.6: The value of χ^2 as a function of the offset of the module position in X/Y/Z directions when $N=21$, $\delta_x=\delta_y=\delta_z=100\ \mu m$ and $\beta=0.01°$.

As illustrated in Figure 4.5 (a), where $\beta=10°$, the values of χ^2 is sensitive to the change of the module position in Z direction. However, the changes of the module position in X and Y directions don't affect the value of χ^2 greatly. This explains the value of σ_z is much lower than those of σ_x and σ_y when the value of β is small (for example, $\beta=10^{\circ}$). The sensitivity of χ^2 to the changes of the module position in X and Y directions increases with the increase of β (see Figure 4.5 (b) and Figure 4.5 (c)). This makes the difference between σ_x, σ_y and σ_z smaller. The sensitivities of χ^2 in X and Y directions are close to that in Z direction when $\beta=80^{\circ}$, which explains the values of σ_x, σ_y and σ_z are at the same level in Figure 4.4. Figure 4.6 shows a special case, the value of χ^2 as a function of the offset of the module position in X, Y and Z directions when $\beta=0.01^{\circ}$. It is indicated that the algorithm does not converge very well for such small value of β and the module position becomes very uncertain. Thus, a small full view angle should be avoided for the design of the diffraction grating.

Based on discussions given above, it can be concluded that the standard deviation of the module position depends on the sensitivity of χ^2. The higher the sensitivity is, the lower the standard deviation is. The sensitivity of χ^2 to the changes of the module position in X, Y and Z directions depends on the full view angle of the optical pattern. The sensitivity of χ^2 increases with the increase of β. Therefore, a large value of β is preferred for the design of the diffraction grating.

4.1.4 Position Sensitivity to Reference Angles

The position sensitivity to the random noise on laser dot coordinates has been discussed in section 4.1.1. As shown in section 3.1, the dot coordinates are used to calculate the inter-beam angles and then they are compared with the reference angles. The reference angles are the values of the inter-beam angles in the optical pattern, which are obtained through angle calibration process. Hence, the effect of the random noise (uncorrelated) on reference angles is similar with the effect of the random noise on dot coordinates. In this section, the effect of correlated errors on reference angles is investigated. These correlated errors can be caused by misalignment between the laser and the diffraction grating, or caused by the change of the wavelength of the laser diode. The correlated error caused by change of wavelength is presented in section 4.2.

The simulation configuration is the same as shown in Figure 4.1. The module is modeled to be at a known position M (x_m, y_m, z_m) with respect to a defined global coordinate system. The *xyz* coordinates of each dot in the optical projection pattern are determined by finding the intersection of the beams with the plane, which is perpendicular to the optical axis of the module and offset $d=2\ m$ (from the module to the central dot). The module position was determined through the algorithm by finding the minimum $\chi 2$ value, as shown in Equation 3.4. The correlated errors were added to all reference angles to investigate the effect to the module position. The simulation was performed following these steps:

1. The module is set at a known position M (x_m, y_m, z_m) with its optical axis perpendicular to the projection plane and it has an offset of $d=2\ m$. The *xyz* coordinates of each dot in the projection pattern are determined by finding the intersection of the beams with the plane by defining $N=11$ and $\beta=30°$.
2. With the known module position and known *xyz* coordinates of all dots in the optical projection pattern obtained from step 1, the correct reference angles can be calculated.
3. The *xyz* coordinates of all dots and the correct reference angles with a certain offset added (the values of added offset are from -0.024° to 0.024° with an interval of

0.006°) are input into the algorithm and the module position is determined by using the reference angles with offset added.

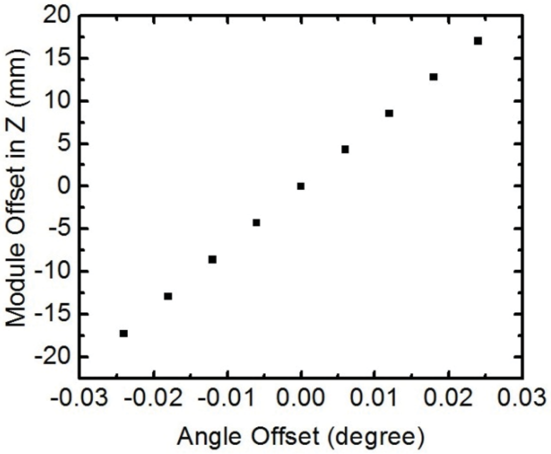

Figure 4.7: The offset of the module position in Z direction as the function of the offset of all the inter-beam angles.

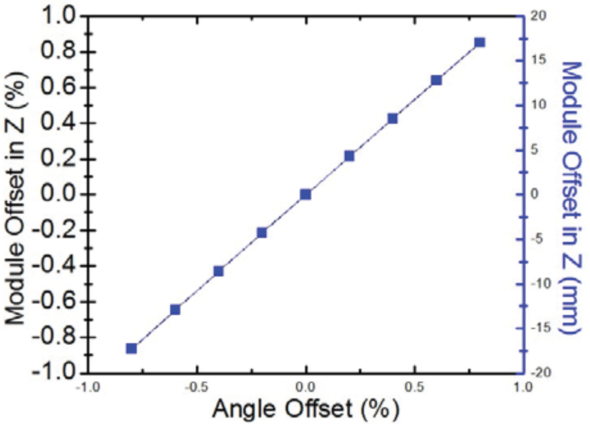

Figure 4.8: The offset of the module position in Z direction as the function of the offset of all inter-beam angles (in percentage).

The result of the offset of the module position in Z direction as the function of the offset of all the inter-beam angles is shown in Figure 4.7. The effect of the offset of reference angles on the module position in X and Y directions cancel out with each other due to the symmetric property of the optical projection pattern. Thus, the module position only has an offset in Z direction. As shown in Figure 4.7, the offset in Z direction increases linearly with the increase of the offset of reference angles. The module position has around

17 mm offset in Z direction when there is 0.024° offset added to the reference angles. When the pre-defined inter-beam angle is 3° and the pre-defined distance between the module and the plane is 2 m, the offset of the module position in Z direction as the function of the offset of the reference angles in percentage is shown in Figure 4.8. The angle offset of 0.024° is corresponding to 0.8%, which leads to around 0.86% offset of the module position in Z direction (~17 mm). These results indicate that 1% correlated error in reference angles can lead to around 1.08% error in the module position. Hence, the correlated error in reference angles needs to be corrected in order to achieve high accuracy measurement in the module position.

4.1.5 Position Sensitivity to Geometry of Projection Surface

Simulations were also conducted to investigate the effect of the geometry of the projection surface on the position sensitivity of the module. The simulation configuration is shown in Figure 4.9, which is similar with the configuration shown in Figure 4.1. Instead of being perpendicular with the optical axis of the module, the plane is tilted an arbitrary 45° to the optical axis and offsets $d = 2\ m$. The sensitivity of the module position to N is investigated and compared with the situation shown in Figure 4.1. In this simulation, a random noise (normal distribution) at a level of $\delta_x = \delta_y = \delta_z = 100$ μm was added to the *xyz* coordinates of each dot and β was fixed at 35°. A noise level of 100 μm is representative of the coordinate repeatability experimentally observed with the photogrammetric measurements under current laboratory conditions. The noise values in *xyz* directions are not the same for each iteration. The procedure is the same with section 4.1.2.

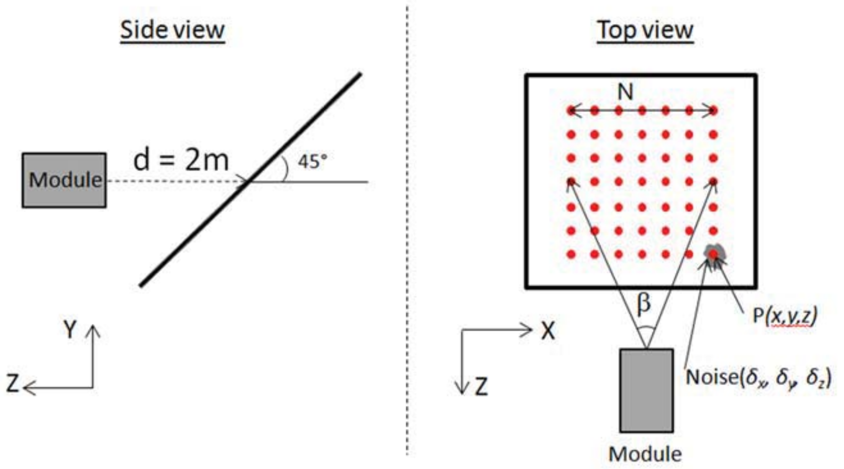

Figure 4.9: Schematic of the simulation configuration to investigate the effect of geometry of projection surface.

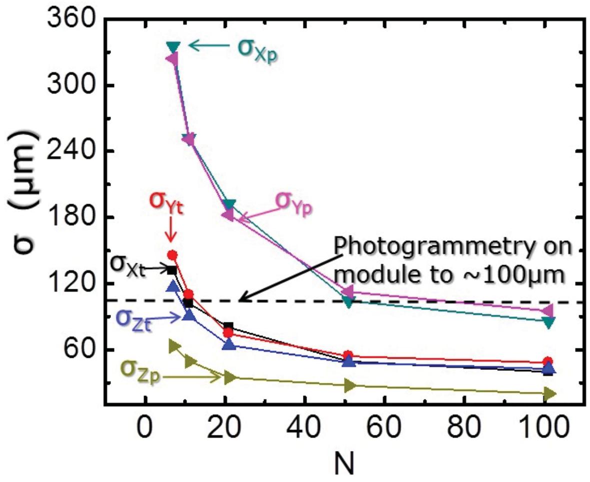

Figure 4.10: The standard deviation of the module position, σ_p for perpendicular plane and σ_t for 45˚ tilt plane, versus dimension of dot matrix pattern, *N*.

The standard deviations of the module position versus *N* under two different conditions are illustrated in Figure 4.10. In this figure, σ_p is the standard deviation of the module position when the plane is perpendicular with the optical axis of the module and σ_t is the standard deviation of the module position when the plane is tilted 45° with respect to the optical axis of the module. As illustrated in Figure 4.10, both σ_p and σ_t decrease with the increase of *N*. This confirms that a large value of *N* leads to lower uncertainty of the measured module position. As shown in Figure 4.10, σ_{Zp} is much lower than σ_{Xp} and σ_{Yp} for the perpendicular plane, in which case all the dots are well spread in X and Y directions but they share the same Z coordinate. With the plane tilted by 45°, all the dots are well distributed in X, Y and Z directions and the difference between σ_{Xt}, σ_{Yt} and σ_{Zt} get smaller for this case. The values of σ_{Xt}, σ_{Yt} and σ_{Zt} are getting lower than 100 µm when N is larger than 11. When N increases to 50, the standard deviation in the module location drops to approximately 50 µm. This indicates that averaging a large number of dots can lead to a better measurement result than using the photogrammetric measurement on tie points alone. The 100 µm photogrammetric repeatability of a single dot level is indicated in the graph by the dashed line. Further simulations have confirmed that the standard deviation of the module shares the same behavior with the tilt plane condition when the dots are well distributed in 3D space. The projection plane is tilted with respect to the module, which can represent the general situation whereby the module will be at an arbitrary angle to the wall, as is likely to be the case in practice.

4.2 System Improvement: Angle Calibration

As described in section 3.1, the module consists of a laser and a projection head, which is actually a diffraction grating. A diffraction grating is a diffractive optical element with periodic structure, which splits the incident light beam into several beams travelling in different directions through the use of interference and phase control. A diffraction grating can be either a reflection grating, which consists of a grating superimposed on a reflective surface, or a transmission grating, which consists of a grating superimposed on a transparent surface. The diffraction grating used in the proposed system is a transmission diffraction grating.

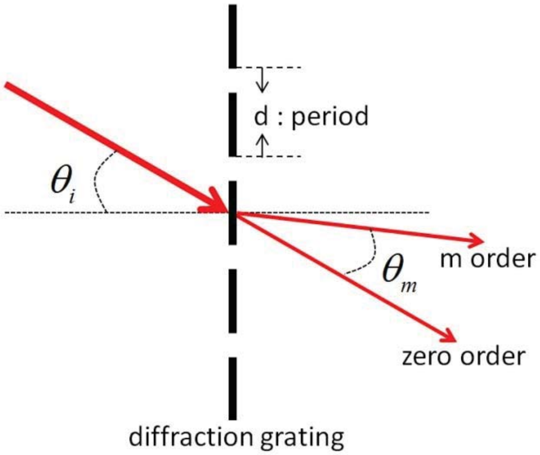

Figure 4.11: Schematic of a transmission diffraction grating.

The diffraction grating equation used to describe the relationship between the period of grating and the angles of incident and diffracted beams is given in equation (4.2) , where m is an integer standing for the propagation-mode of interest, d is the period of the diffraction (which is the distance from the center of one slit to the center of the adjacent slit), θ_i is the incident beam angle, θ_m is the angle that the m^{th} order maxima occurs, λ is the wavelength of the incident light. Figure 4.11 shows a schematic of a transmission grating.

$$d(\sin\theta_i + \sin\theta_m) = m\lambda \tag{4.2}$$

As mentioned in section 3.1, all the calculated angles (θ^c_{VHi} and θ^c_{Diaj} in equation 3.4) will be compared with the reference angles (θ^r_{VHi} and θ^r_{Diaj} in equation 3.4 in section 3.1.), so that the best fit module location can be calculated. It should be pointed out that how well the reference angles are calibrated will affect the measurement accuracy directly. The angle information of the module is calibrated by using a high precision rotation stage and a CCD camera. The schematic of the calibration setup is shown in Figure 4.12, where C is the center of the rotation stage, M is the position of the module (where the laser beam interests the diffraction grating). The calibration is conducted following these steps:

1. The module is placed onto the center of the rotation stage. The center of the module should be aligned to the center of the rotation stage.
2. The module is turned on, generating an array of beams that intersect the projection plane.
3. A CCD camera is positioned in front of the projection plane to capture the coordinates of the first laser dot of interest (the zero order beam, for example) on the projection plane, point D in Figure 4.12.
4. The precision stage is carefully rotated to ensure that the coordinates of the second laser dot of interest (the first order beam, for example, point F in Figure 4.12.) captured by the camera are the same with those of the first laser dot. The inter-beam angle between the zero order beam and first order beam can be read directly from encoder of the rotation stage.

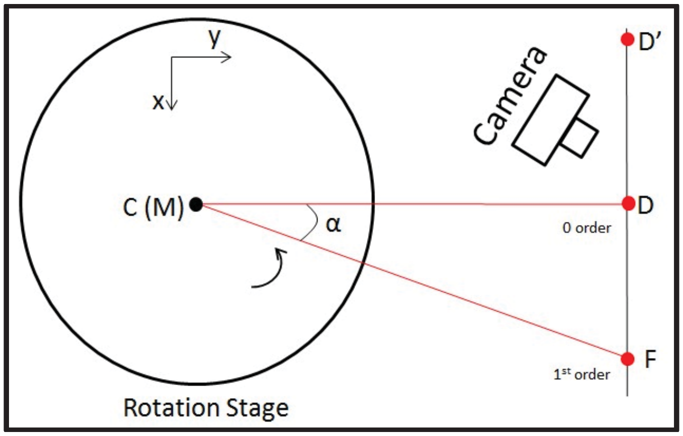

Figure 4.12: The experimental setup of the angle calibration using a rotation stage.

4.2.1 Factors Affecting the Uncertainty of Calibrated Angle

Before the experiment is conducted, the factors contributing to uncertainty of calibrated angle are investigated. These factors include the uncertainty of the rotation stage reading, the misalignment between the module and the center of the rotation stage, the position error of laser dot detected by the CCD camera and the wavelength stability of the laser diode.

4.2.1.1 Uncertainty of the Rotation Stage Reading

As described in the calibration procedure mentioned in section 4.2, the inter-beam angle will be read directly from the encoder of the rotation stage. Therefore, the resolution and uncertainty of the rotation stages' encoder reading has a direct effect on the uncertainty of the angle measurement. The rotation stage used in the experiment was made by Zeiss, part # LRT-625 SPECIAL. It has a resolution of 1", which is 0.000278°. According to the specifications, this rotation stage is guaranteed to make angle settings within ±0.0005°.

4.2.1.2 The Misalignment

When the module is mounted to the rotation stage, the center of the diffraction grating should be co-linear with the rotational axis of the rotation table. However, there will be some misalignment between the two. The misalignment can be separated into two parts: the misalignment in X direction, as shown in Figure 4.13 (b), and the misalignment in Y direction, as shown in Figure 4.13 (a). The effect of misalignment in X direction is first investigated and the schematic of such misalignment is shown in Figure 4.13 (b). In Figure 4.13 (b), *CM* is the misalignment in X direction. At the start position, the location of the zero order beam is projected onto the projection plane at point D and the location of the first order beam is at point F. In this case angle α is the inter-beam angle to be measured.

Assuming the rotation stage is rotated by angle β, so that the first order beam moves to point F', which is the original location of D. Here β is the angle read from encoder of the rotation stage while α is the angle to be measured. The difference between α and β is the angle error (e_a) caused by the misalignment in X direction. Based on the relationship expressed in the equations (4.3) and (4.4), the angle error e_a can be calculated through equation (4.5), where MD is the distance between the rotation stage and the projection plane.

$$\alpha + \measuredangle MFD + \measuredangle MDF = 180^\circ \tag{4.3}$$

$$\beta + \measuredangle MFD + \measuredangle MDF + \measuredangle M'DF = 180^\circ \tag{4.4}$$

$$e_a = \alpha - \beta = \tan^{-1}\left(\frac{a}{MD - b}\right) \tag{4.5}$$

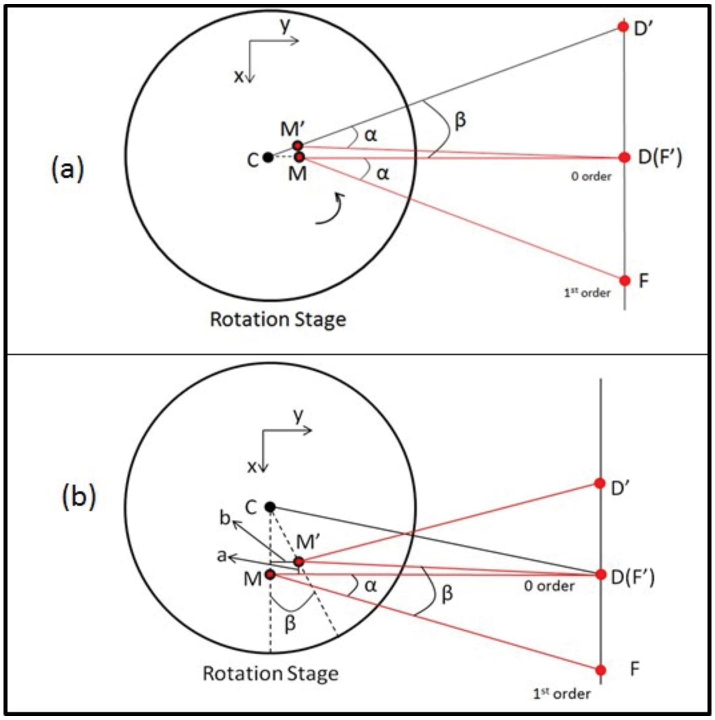

Figure 4.13: (a) Schematic of misalignment error in Y direction on rotation stage (top view), (b) schematic of misalignment in X direction on rotation stage (top view).

As shown in equation (4.3), the angle error e_a caused by the misalignment in X direction depends on *MD*, the distance between the rotation stage and the projection plane. Figure 4.14 (a) shows the angle error versus the distance *MD* when the misalignment errors are 1 mm and 3 mm along the x axis. If the distance *MD* is 4 m, 3 mm misalignment in X direction only leads to 0.0001° angle error. If the misalignment is 1 mm, the angle error smaller than 0.0001° can be achieved by choosing the distance *MD* larger than 1 m. Compared with the uncertainty of the rotation stage reading (±0.0005°), the angle error caused by the misalignment in X direction can be neglected.

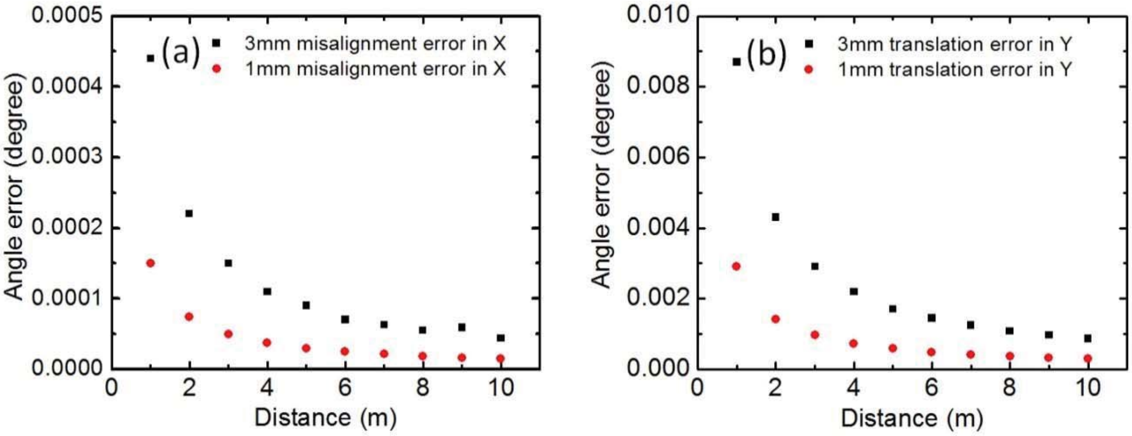

Figure 4.14: Angle error versus distance (*MD*): (a) in X direction, (b) in Y direction.

The angle error caused by the misalignment in Y direction is also investigated. The schematic of misalignment in Y direction on the rotation stage is shown in Figure 4.13 (b). In Figure 4.13 (b), the center of the diffraction grating is at point M, which has an offset in Y direction with C, the center of the rotation stage. Based on the geometrical relationship in Figure 4.13 (b), the angle to be measured (α) and the measured angle (β) can be calculated from equations (4.6) and (4.7).

$$\tan(\alpha) = \frac{DF}{MD} \tag{4.6}$$

$$\tan(\beta) = \frac{D'F'}{CD} \tag{4.7}$$

With $DF \cong D'F'$, the inter-beam angle α will be given by equation (4.8).

$$\alpha = \tan^{-1}(\frac{CD}{MD} * \tan(\beta)) \tag{4.8}$$

Thus, the angle error can be determined by equation (4.9), where *CD* is the distance between the rotation stage and the projection plane, and *CM* is the misalignment in Y direction.

$$e_a = \tan^{-1}(\frac{CD}{MD}\tan(\beta)) - \beta \tag{4.9}$$

When there is 3 mm misalgnment in Y direction, the black square in Figure 4.14 (b) shows how the change of the distance between the rotation stage and the projection plane affects the angle error. With the increase of distance, the angle error decreases. When the distance is larger than 5 m, angle error smaller than 0.002° can be achieved. Red dots in Figures 4.14 (b) show the effect of the distance between the rotation stage and the projection plane on angle error when there is 1 mm misalignment in Y direction. It is demonstrated that angle error smaller than 0.001° can be achieved with the distance larger than 3 m if there is 1mm misalignment in Y direction.

4.2.1.3 Laser Dot Position Error on Projection Plane

As described in the procedure of the angle calibration, the first order laser beam on the projection plane should have the same coordinates with the previous zero order beam through rotating the stage by the inter-beam angle. However, there will be position error between the coordinates of these two positions in the experiment. The position error can be separated into position error in X direction (see Figure 4.15 (a)) and position error in Z direction (see Figure 4.15 (b)) on the projection plane.

In Figure 4.15 (a), DF' is the position error in X direction on the projection plane. The angle error caused by this error can be calculated through equation (4.10).

$$e_a = \tan^{-1}\left(\frac{DF'}{CD}\right) \tag{4.10}$$

It was observed in the experiment that the position error in X direction is around 100 μm. With 100 μm position error in X direction, the relationship between the angle error and the distance *CD* is shown in Figure 4.16 (a). Thus, angle error smaller than 0.002° can be achieved when *CD* is larger than 5 m.

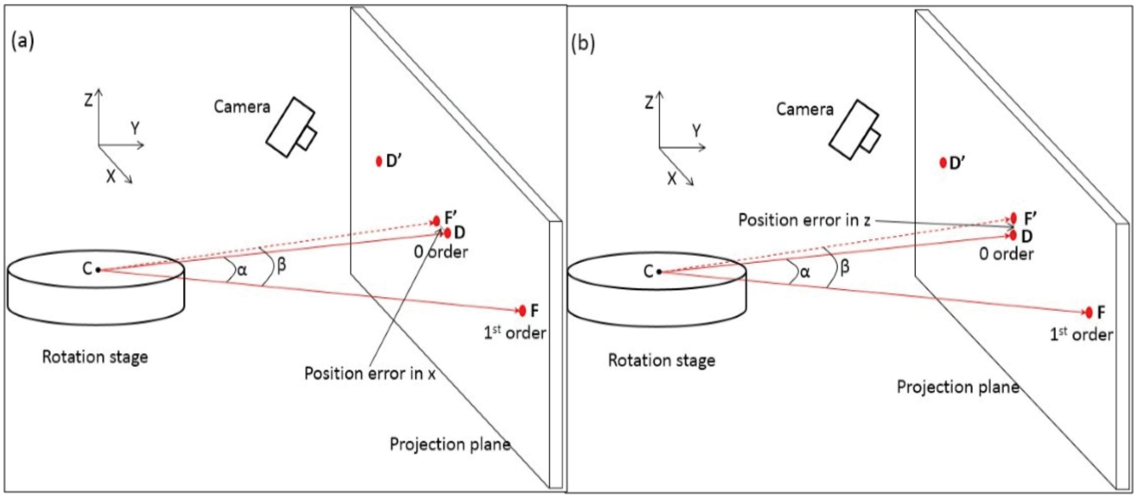

Figure 4.15: Schematic of the position error on the projection plane: (a) the position error in X direction, (b) the position error in Z direction.

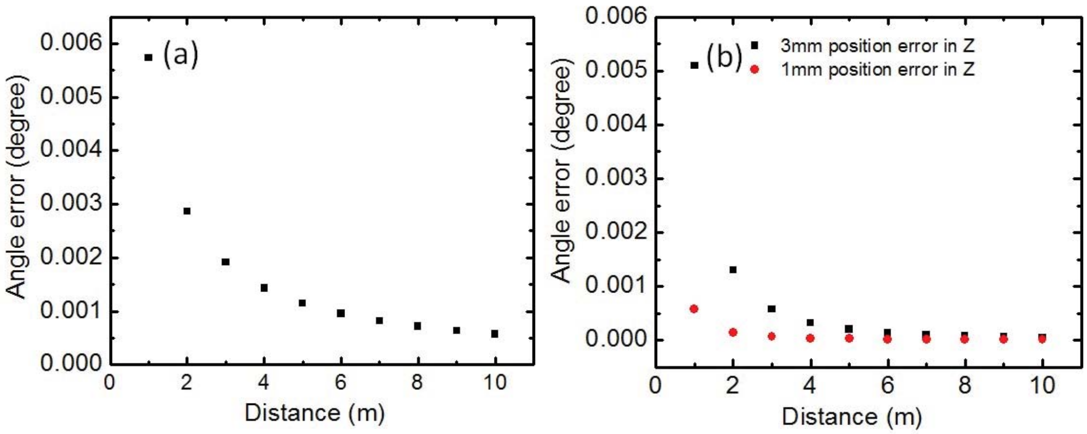

Figure 4.16: Angle error versus distance (*CD*) for given amount of position errors: (a) the angle error caused by 100 μm position error in X direction, (b) the angle error caused by the position error in Z direction.

The position error in Z direction is most caused by the misalignment between the plane DMF and the plane of the rotation stage. In Figure 4.15 (b), *DF'* is the position error in Z direction on the projection plane. Figure 4.16 (b) displays how the angle error changes with the distance *CD* for the given amount of position error in Z direction. It is demonstrated that the angle error is smaller than 0.001° when the distance between the center of the stage and the projection is larger than 1 m for 1 mm position error in Z direction.

4.2.1.4 Wavelength stability of the laser diode (LD)

The output of a laser diode is sensitive to temperature. The wavelength of a typical Fabry-Perot laser diode typically changes 0.3 nm per degree Centigrade. When the light is normally incident on the diffraction grating, the diffraction equation can be written as equation (4.11):

$$d\sin(\theta_m) = m\lambda \qquad (4.11).$$

Therefore, the angle error e_a caused by the wavelength change of the laser diode can be determined through equation (4.12), where d is the period of diffraction grating, λ is the wavelength of the laser diode and $\Delta\lambda$ is the change of the wavelength.

$$e_a{}^m = \sin^{-1}\left(\frac{m*(\lambda+\Delta\lambda)}{d}\right) - \sin^{-1}\left(\frac{m*\lambda}{d}\right) \tag{4.12}$$

The results of the wavelength stability test over six minutes and one hundred minutes period are shown in Figure 4.17 (a) and Figure 4.17 (b) separately. The room temperature under test is 24° during both tests reported by a thermometer. It is shown in both (a) and (b) that the wavelength of the laser diode changes by 0.4 nm with a controlled room temperature. Considering the wavelength of 658 nm and inter-beam angle of 3°, a change of 0.4 nm in the wavelength leads to 0.0018° angle error (0.06%).

Table 4.1 summarizes the factors contributing to the angle error if the rotation stage and CCD camera method is used to calibrate the angle information of the module. When the distance *CD* is 5 m and inter-beam angle is 2.9°, under the current laboratory conditions, the typical value of each error source contributing to angle error has been listed in Table 4.1. Thus, the best ability to measure all the angles, is expressed through the combined standard uncertainty, u_a^c. This combined standard uncertainty is Type B uncertainty defined in the GUM (Guide to the expression of uncertainty in measurement) [122]. The typical values of error source are based on experimental observation and experience. If all the error sources are independent, the combined standard uncertainty is given in equation (4.13), where u_{ai}^c stands for the combined standard uncertainty caused by each error source alone.

$$u_a^{\ c} = \sqrt{\sum_i u_{ai}^{\ 2}} \tag{4.13}$$

Based on equation (4.13) and the typical values of the error sources listed in Table (4.1), the lowest combined standard uncertainty achievable under the current laboratory conditions is 0.0022°. This combined standard uncertainty includes the uncertainty caused by the random errors, 0.0013°, and the uncertainty caused by the systematic errors, 0.0018°. These results show that the wavelength change of the laser diode, dot position error in X direction on the projection plane and the misalignment in Y direction on the rotation stage are the top three factors contributing to the measured angle error.

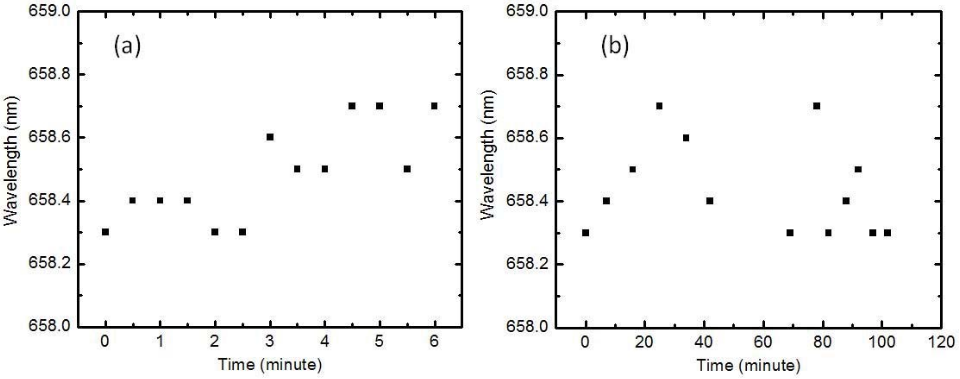

Figure 4.17: Wavelength stability: (a) wavelength stability test over six minutes; (b) wavelength stability test over one hundred minutes.

Table 4.1: Factors contributing to the angle error.

	Typical value of error source	Contribution to angle error (degree)	Contribution to angle error (%)
Uncertainty of rotation stage reading	0.0005°	0.00050	0.01724
Misalignment in X on rotation stage	1 mm	0.00003	0.00103
Misalignment in Y on rotation stage	1 mm	0.00058	0.02000
Position error in X on the projection plane	100 µm	0.00100	0.03450
Position error in Z on the projection plane	1 mm	0.00002	0.00069
Change of wavelength	0.4 nm	0.00180	0.06000

4.2.2 Experimental Setup for Angle Calibration and Calibration Results

4.2.2.1 Experimental Setup

The experimental setup for the angle calibration is shown in Figure 4.18. A fixture is designed to hold the module rigidly and helps to align the center of the diffraction grating to the center of the rotation table (see Figure 4.18 (b)). From the study in section 4.2.1, it is shown that the angle error can be reduced by increasing the distance between the rotation stage and the projection plane. Therefore, two mirrors (Mirror#1 and Mirror #2 in Figure 4.18 (a)) are used to reflect the laser beam of interest to the projection plane so that a distance of 5 m between the rotation stage and the projection is achieved. A CCD camera is mounted in front of the projection plane to capture the position of the laser dot on the projection plane. The camera is connected to a computer and controlled by a remote software, PSRemote.

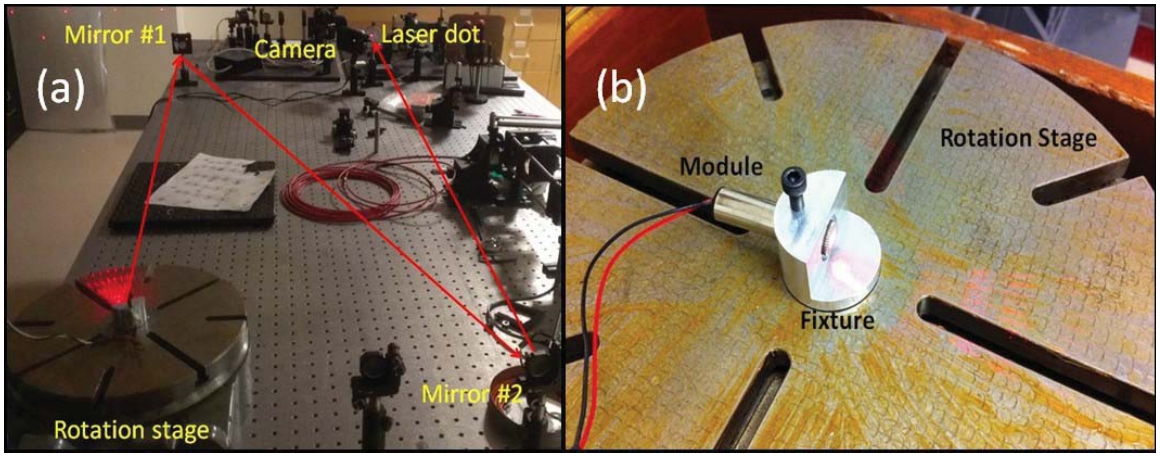

Figure 4.18: Angle calibration: (a) the experimental setup, (b) the designed fixture used to align the module to the center of the rotation stage.

4.2.2.2 Calibration Results

A total of ten vertical and ten horizontal angles are measured, as shown in Figure 4.19. Each angle is measured five times. The measurement results of ten vertical angles are shown in Figure 4.20 (a). Vertical angles #1 to # 10 are corresponding to ten vertical angles marked in Figure 4.19, from the top to the bottom. Results shown in Figure 4.20 (a) indicate that the module has larger inter-beam angles in the middle and smaller inter-beam angles on the edge. The one standard deviation of five angle measurements is around 0.002°, which is close to the combined standard uncertainty expected from the analysis. The measured angle information can be converted into inter-beam distance if the distance between the projection plane and the rotation stage is known. Assuming the distance is 1 m, the corresponding inter-beam distances for ten inter-beam angles are shown in Figure 4.20 (b). Based on the specifications given by the manufacture, the angle information and the inter-beam distance information obtained, the diffraction grating is initially designed to have equal distance for adjacent beams. However, the radial distortion exists in the diffraction pattern as seen from the optical pattern. Having twenty measured angles, the mathematic model of the diffraction grating can be derived and all the other angles can be calculated after applying the radial distortion.

The radial distortion can be described by equation (4.14) [92-94], where r is the original coordinate of the point of interest, r_d is the distorted coordinate and k is the vector of distortion coefficient. By taking the first order of equation (4.14) to model the distortion, it turns into equation (4.15).

$$r_d = r + \delta_r = rf(r,k) = r(1 + k_1 r^2 + k_2 r^4 + k_3 r^6 + \cdots) \tag{4.14}$$

$$r_d = r(1 + k_1 r^2) = r + k_1 r^3 \tag{4.15}$$

In Cartesian coordinate, equation (4.15) is equivalent to equation (4.16)

$$x_d = x + k_1 x(x^2 + y^2), y_d = y + k_1 y(x^2 + y^2) \qquad (4.16).$$

Considering the projection pattern in Figure 4.21, equation (4.17) can be written as

$$x_d = md + k_1(md)\left[(md)^2 + (nd)^2\right], y_d = nd + k_1(nd)\left[(md)^2 + (nd)^2\right] \qquad (4.17).$$

The period of the diffraction grating, d, and the distortion coefficient k can be solved by using equation (4.17) to perform least-square fitting to the measured angles. Given the distance between the projection plane and the module is 1 m, the period of the diffraction grating is 52.22 mm and the distortion coefficient k is 3.5×10^{-8} for the distorted optical pattern. Thus, all the inter-beam angles can be calculated based on the diffraction equation and the distortion model. All the calculated angles can be found in Appendix B, and these angles are used as reference angles for the measurement.

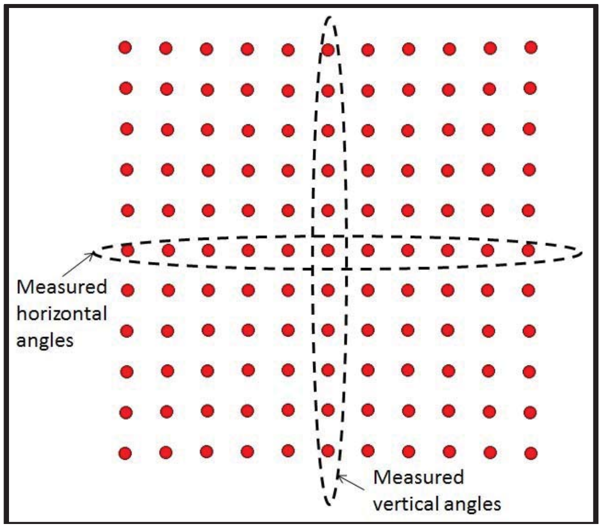

Figure 4.19: Diagram of ten vertical angles and ten horizontal angles measured in the experiment.

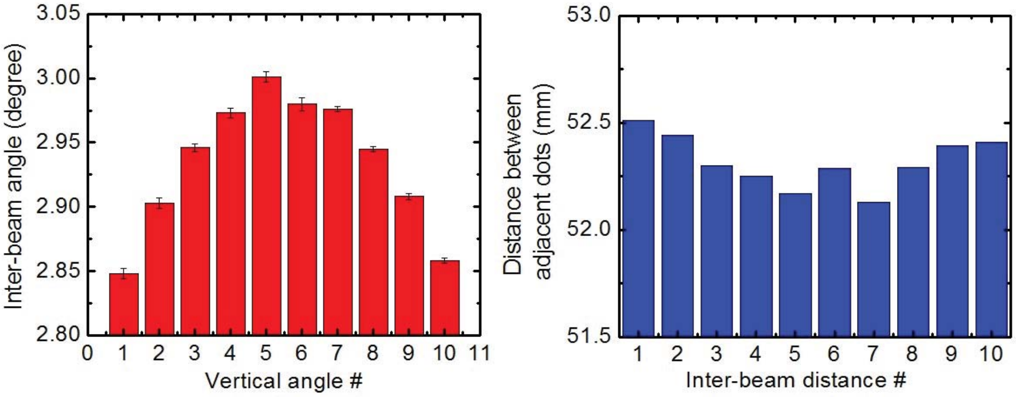

Figure 4.20: (a) Measurement results of ten vertical angles. Error bars stand for one standard deviation (1σ) of five measurement results. (b) Inter-beam distance for ten vertical angles given the projection plane is 1 m away from the rotation stage.

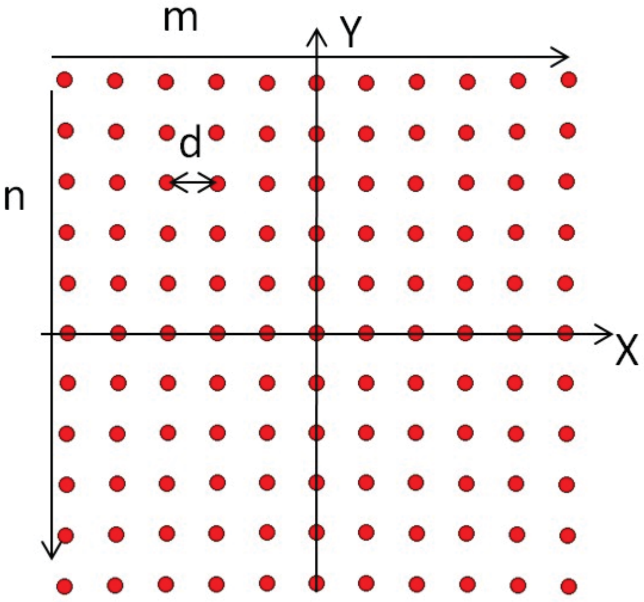

Figure 4.21: The schematic of building the distortion model for the projection pattern.

4.3 Measurement with Calibrated Angles

Based on the simulation results presented in section 4.1.4, it was shown that 1% offset in all the reference angles can lead to about 1% offset in the module position. Thus, it is very important to calibrate the angles of the optical projection pattern in order to achieve a better measurement accuracy of the module position. The method to calibrate the angles and the calibration procedure are discussed in section 4.2.2. A total of 20 angles in the 11×11 dot matrix optical pattern were measured with the calibration setup mentioned in section 4.2.2 and all the inter-beam angles were calculated with the fitted distortion model for the diffraction grating. This 11×11 dot matrix optical pattern with calibrated angles was employed in the experiment and the translation test present in section 3.3.5 was redone. The experimental setup and procedure are the same as discussed in section 3.3.5.

Figure 4.22 shows the comparison between translation test results calculated using algorithm with calibrated angles and using algorithm with un-calibrated angles. The red dot stands for the measurement differences reported by algorithm with calibrated angle. As discussed above, the measurement differences at all positions are smaller than 0.42 mm (the difference is 0.42 mm at 900 mm position). The black triangle in Figure 4.22 is the measurement difference at each position and the result indicates that the un-calibrated angles for the optical projection pattern leads to correlated error to the measurement difference. The measurement difference is 1.7 mm at 900 mm position if un-calibrated angles are used in the algorithm. This result confirms the effect of the reference angles on the module position presented in section 4.1.4. Thus, in order to achieve better accuracy of the module position, the angles of the projection head should be calibrated first.

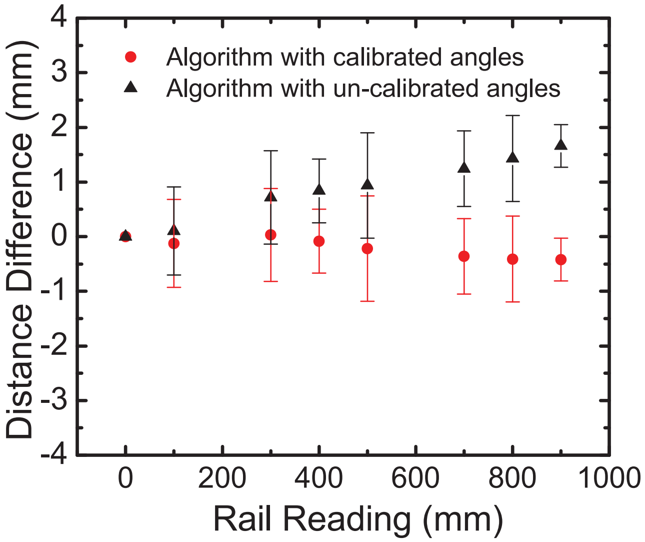

Figure 4.22: Measured distance versus rail reading for the translation test on the rail obtained from calibrated angles and un-calibrated angles.

4.4 Processing Time Consideration

The processing time is one limitation of the current system. For the tests performed with 11×11 dot matrix optical pattern it takes around eight minutes to get the location of the module. Figure 4.23 shows the pie chart of the processing time of the proposed system.

Around 39% was consumed by the manual marking process (identify the dot manually) and this is because that not all the laser dots could be marked by photogrammetric software automatically. Thus manual marking needs to be involved to mark those which couldn't be marked automatically. The process of manual referencing consumed almost 52% of the processing time due to large number of dot in each image. Using costumed designed optical pattern with coded targets embedded could reference all the targets automatically to reduce the referencing time. The manual marking time can be reduced by using virtual camera approach, which will be discussed in chapter 5.

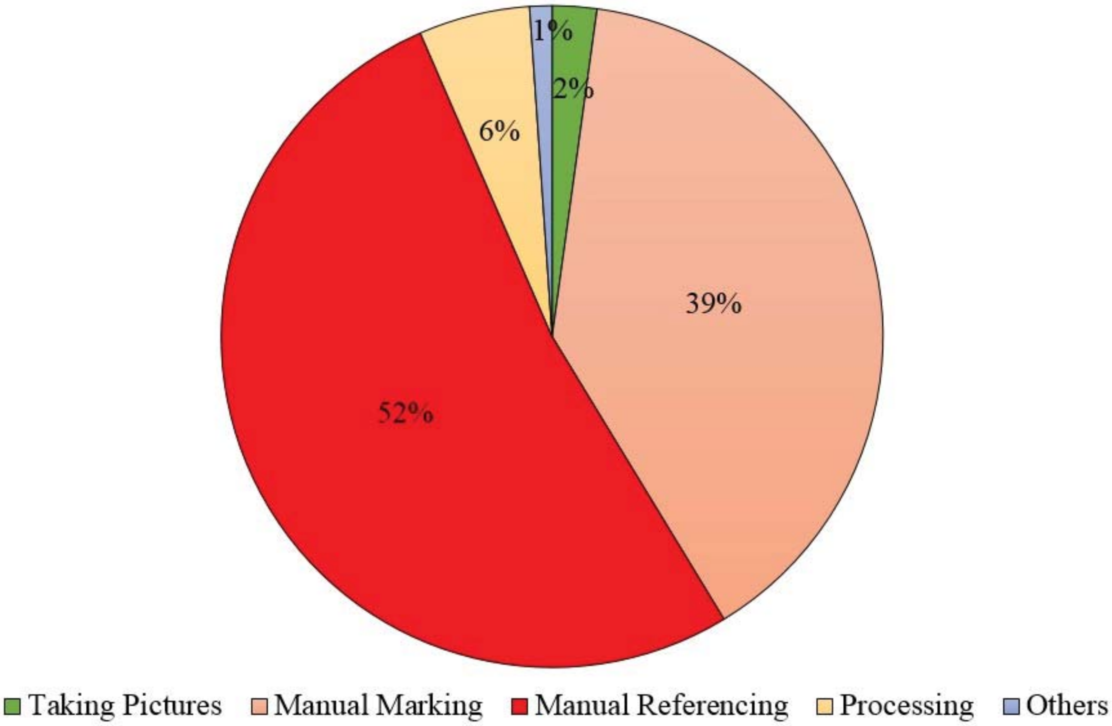

Figure 4.23: Pie chart of the processing time of the proposed system.

4.5 Multiple Coordinate Systems for Rotation Test

As presented in section 2.1.3, a reference artifact and a coordinate system are necessary for each photogrammetric measurement. In order to obtain the location information of the module in the proposed metrology system, the reference artifact and the optical pattern should be observable from at least a subset of the cameras. In the case that the optical pattern and the reference artifact are on two different scenes, field of view (FOV) limitations make it challenging for them to be captured by the cameras at the same time. Thus, the measurement cannot be performed. This limits the measurement range of the proposed metrology system. Such limitation can be overcome by employing multiple reference artifacts to define multiple coordinate systems, so that large range rotation can be measured. In this method, one of the coordinate systems is chosen as the global coordinate system, and then all the other coordinate systems are transformed into the global coordinate system through coordinate transformation. Affine transformation and similarity transformation are discussed in details in section 2.1.2. Due to the large angles limitation in similarity transformation (see detail in section 2.1.2), affine transformation is chosen to translate the coordinates in local coordinate systems to the global coordinate system in this dissertation.

4.5.1 Coordinate Transformations in Rotation Test

Coordinate transformations will be conducted before the measurements to tie all the local coordinate systems to the global coordinate system. Figure 4.24 shows the three coordinate systems used in the rotation test. For instance, the coordinate transformation between the local coordinate system C_{x2y2} and the global coordinate system C_{xy} follows these steps.

1. Multiple images are taken so that both the local coordinate system C_{x2y2} and the global coordinate system C_{xy} are captured on the same images.

2. Images obtained in step 1 are loaded to PhotoModeler®. After all the points in the images are marked in PhotoModeler®, the bundle adjustment is performed by PhotoModeler® to yield the 3D model of the two coordinate systems.
3. Define the local coordinate system C_{x2y2} to be the reference coordinate system in the solved 3D model in PhotoModeler® and the coordinates of all the points in the local coordinate system C_{x2y2} are obtained.
4. Define the global coordinate system C_{xy} to be the reference coordinates system in the solved 3D model in PhotoModeler®. The coordinates of all the points in global coordinate system C_{xy} are obtained.
5. An affine transformation is performed to calculate the twelve affine transformation parameters based on the coordinates of the identical points (>4) obtained in step 3 and step 4.
6. Coordinate transformation is performed to translate the coordinates in C_{x2y2} to C_{xy} with the twelve affine transformation parameters calculated in step 5.

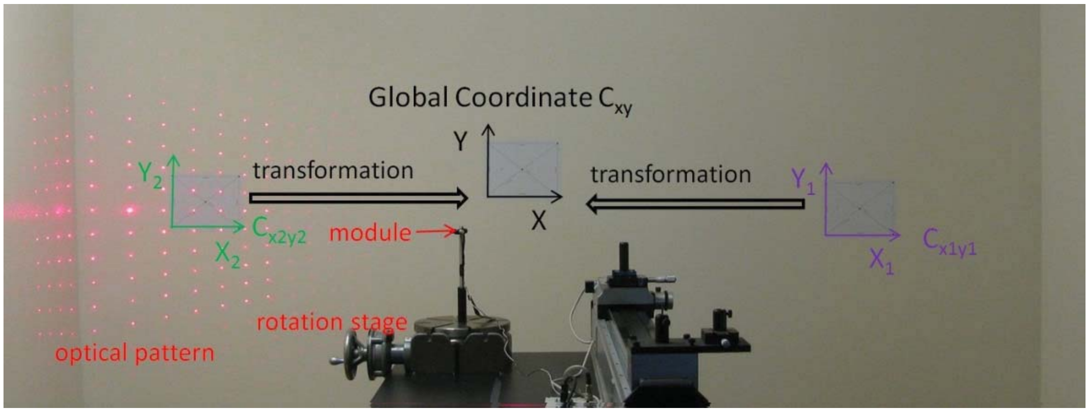

Figure 4.24: Coordinate transformation in the experiment.

4.5.2 Rotation Test Using Multiple Coordinate Systems

The rotation test is conducted with the same 11×11 module as used in section 4.4.1 and the measurement configuration is shown in Figure 4.24. The module is mounted 200 mm above the center of the precision rotation stage and rotated through 120°. The same three 9 megapixel digital cameras [108] are positioned at various orientations with respect to the wall (not shown in Figure 4.23). Three coordinate systems are used in the experiment. The coordinate system C_{x1y1} is used as the reference coordinate system when the module is rotated from 0 to 30° (Figure 4.25(a)), and C_{xy} is used as the reference coordinate system when the module is rotated from 30 to 90° (Figure 4.25(b)). When the module is rotated from 90 to 120° (Figure 4.25(c)), C_{x2y2} is used as the reference coordinate system. The rotated angle is calculated based on the angle change of the vector from the module to the central dot in the optical pattern, the same method as used in section 3.3.5. The experiment is conducted for one run with 10° interval and the preliminary experimental results are shown in Figure 4.26. As presented in the Figure 4.26, the absolute values of the angle differences between the measured angle and the encoder reading are smaller than 0.23° for all measurements by employing three coordinate systems in the measurement. These results indicate that this proposed metrology system has the ability to measure larger angle range (up to 360°) by using multiple coordinate systems.

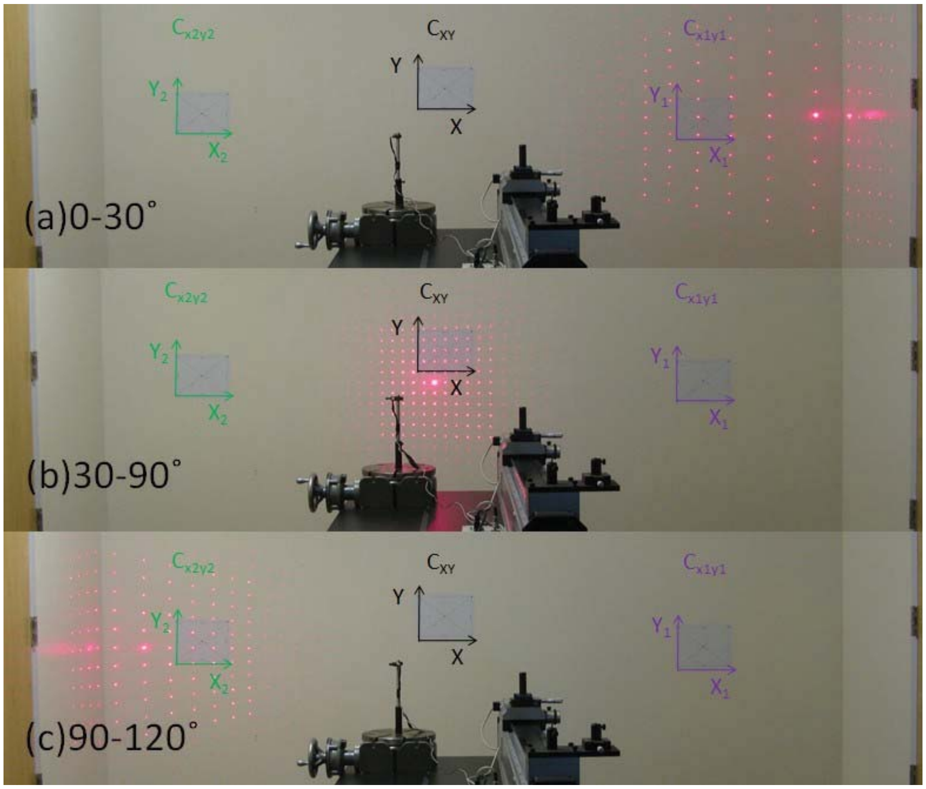

Figure 4.25: Rotation test using multiple coordinates systems: (a) C_{x1y1} is used as the coordinate system in the measurement when the rotation angle is between 0° and 30°, (b) C_{xy} is used as the coordinate system in the measurement when the rotation angle is between 30° and 90°, (c) C_{x2y2} is used as the coordinate system in the measurement when the rotation angle is between 90° and 120°.

During the rotation test, the module was located about 0.9 m away from the global coordinate system (C_{xy}). An error of 0.5 mm in the module position leads to 0.06° angle error on the rotated angle. The coordinate transformation also brings an error to the rotated angle. In order to analyze the uncertainty of the measured angles, a repeated rotation test is preferred. However, limited by the repeatability of the rotation stage used in the experiment, the rotated test cannot be repeated very well. Thus, a detailed analysis on the uncertainty of the measured angles was not given in this dissertation. The rotation test results in this section demonstrate the proof of principal to achieve large range rotation measurement by employing multiple coordinate systems.

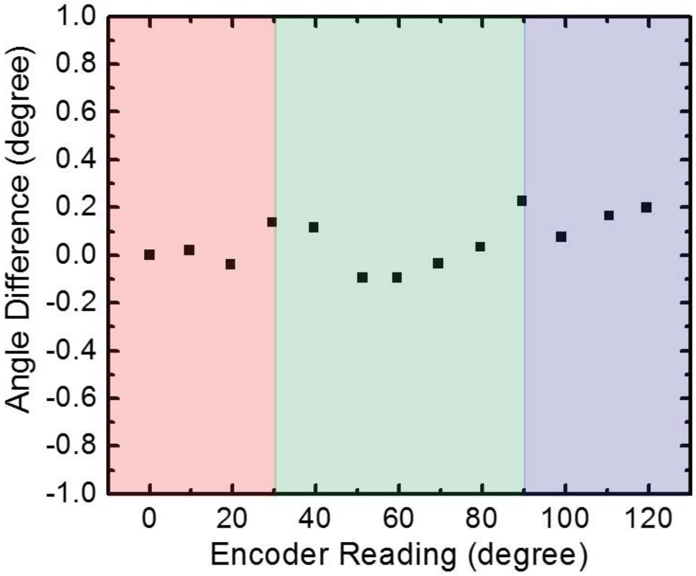

Figure 4.26: Angle difference for the rotation test using three coordinates systems. C_{x1y1} is used as the coordinate system in the measurement when the rotation angle is between 0° and 30° (red area), C_{xy} is used as the coordinate system in the measurement when the rotation angle is between 30° and 90° (green area), and C_{x2y2} is used as the coordinate system in the measurement when the rotation angle is between 90° and 120° (purple area).

CHAPTER 5: THE VIRTUAL CAMERA MODEL

For the measurement results obtained in Chapter 3 and Chapter 4, the locations of the module were calculated by inputting the dot coordinates into a least square (LS) minimization algorithm. However, coordinate estimates of all dots in the optical pattern are required in order to determine the module’s location, and consequently the application of their system is limited to environments with smooth wall geometries where all spots are clearly seen.

These limitations could be circumvented by advanced image processing, point recognition and additional processing algorithms, however instead a variation of this technique is introduced in this chapter that is inherently simpler, more robust and more elegant. A virtual camera variation is proposed where the module projecting the optical pattern is itself treated as a virtual pinhole camera. This is possible because of the basic operating principle of the diffractive element used for the pattern generation. An array of diffracted beams that is generated by the diffractive element is analogous to the array of chief rays from targets that are traced back to a camera and used in the constraint of active triangulation. Thus a picture is not actually taken at the module location, but the principle of the diffractive element allows us to predict what such a picture would look like and then use it as part of the active triangulation constraint. A virtual image of the optical pattern is generated for this virtual camera by knowing the angular characteristics of the optical pattern generated by the module. The virtual image is generated by projecting the diffracted beams back into the virtual pinhole camera to an analysis plane. From the perspective of the module, this is the correct image of the array of dots observed on any surface in front of the module that intersects the projected beams. As described in the previous chapters, real images of the optical pattern on the walls are also captured by cameras at different positions. These images and the virtual image are then loaded into photogrammetry software, and processed through the bundle adjustment. This results in a position and orientation estimate of all cameras, including the virtual camera, and thus results in the 6 DOF estimate for the module. The additional minimization analysis is no longer needed with this method, and it is no longer necessary to identify all dots in the pattern. Thus the virtual camera model is more sophisticated and yet easier to implement than the LS algorithm. This makes the measurement more practical in realistic and usually complicated environments. This chapter describes the virtual camera model in detail and a simulation with ray-trace software that validates the approach. In the simulation, the new method is compared to the previous method that uses the LS algorithm.

The virtual camera method has been used for geometric camera calibration [118] and 3-D motion analysis using camera-mirror system [119-121]. In this chapter, the optical sensing module is treated as a virtual camera, as shown in Figure 5.1. For the virtual pinhole camera with a defined focal length *f*, a virtual image can be captured on the image plane of the virtual camera. This virtual image carries the same information of the optical projection pattern as the real image. In addition, the same virtual image can be used for any scene, which is independent of the location and orientation of the module.

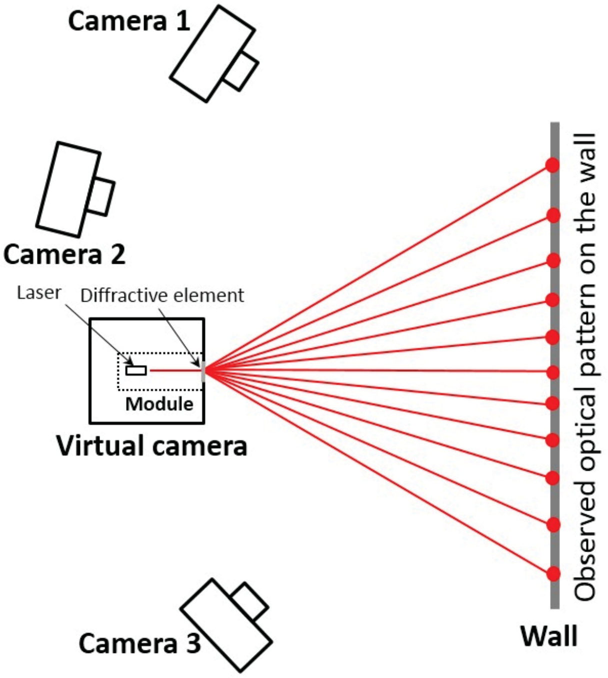

Figure 5.1: The principal of the proposed technique using the virtual camera model.

5.1 Procedure of the Virtual Camera Approach

During the measurement, the proposed technique using the virtual camera model works following these steps:

1. With the information of calibrated angles for the optical pattern generator being used, a virtual image on the film plane of the pinhole camera is generated with MATLAB®. The virtual camera information such as the exposure time, the focal length and the format size is added to the virtual image. This information is used for the bundle adjustment, so that the virtual camera position can be calculated correctly.
2. At each position, three images of the projection pattern are simultaneously taken by the three real cameras. The three real images together with the virtual image are opened in PhotoModeler®. After points in the projected pattern as well as the

reference length points are marked with PhotoModeler®, the bundle adjustment is performed by PhotoModeler® to yield the absolute position and orientation of all cameras, including the virtual camera.

In step 1, the position of each dot on the image plane of the virtual pinhole camera is calculated based on the position of the pinhole, the focal length of the virtual camera (*f*), the film size of the camera and the inter-beam angles of the optical projection pattern (see Figure 4.23). In this section, the virtual pinhole camera has a focal length of is 25 mm and a film size of 15×15 mm. A virtual image of the projection pattern on the film is generated through MATLAB® with the known information above. The same virtual image can be used for any scene, which is independent of the location and orientation of the module. A real digital image processed by PhotoModeler® should contain the information for the corresponding camera and the camera setting during the moment the image was taken, such as the focal length, the film size, the exposure time and the numerical aperture. Such information (known as the exchangeable image file (EXIF)) is embedded into the virtual image by using a free software, Exif Pilot [87].

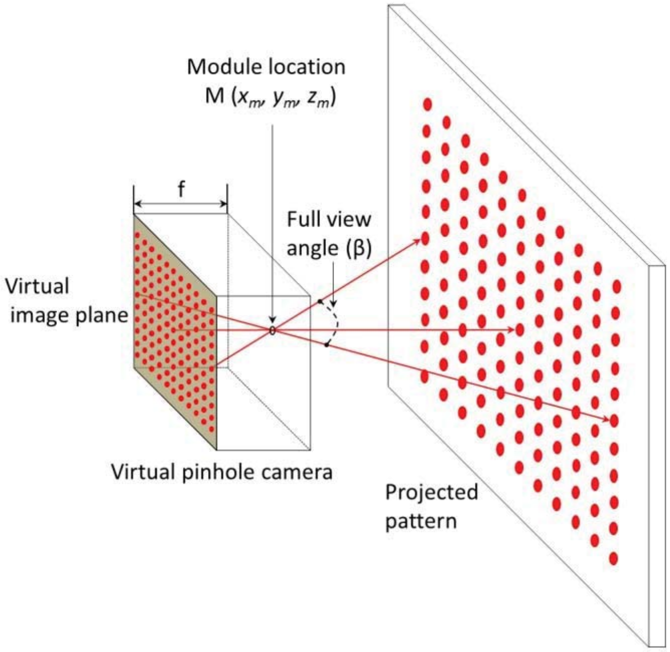

Figure 5.2: The diagram of treating the module as a virtual pinhole camera.

5.2 Validation of Virtual Camera Approach through Simulation

FRED® [88] simulations were performed to evaluate the measurement of the module position obtained from two different approaches: the least-square algorithm and the virtual camera approach. FRED® can simulate the propagation of both coherent and incoherent beams through optical systems and their interaction with a diverse range of surfaces. With FRED® and its 3D computer-aided-design (CAD) environment, the virtual optical projection pattern and the virtual photographs of this projection pattern on the analysis planes of three virtual cameras can be simulated in FRED® by tracing rays through a lens assembly representative of an actual camera.

The simulation follows these steps:

1. The module position is defined in FRED® and the known angle characteristics of the beams generated by the module are used to define the optical pattern on a virtual wall.

2. The optical pattern on the wall is simulated by defining a pattern in the scattering properties of the wall surface. The wall is illuminated by a plane source and the scattered light leaving the wall matches the required optical pattern on the wall.
3. The scattered light from the pattern on the wall is then ray-traced through three simulated cameras. The resulting irradiance pattern in the image plane of each simulated camera is then loaded into MATLAB® to generate a JPEG image.
4. The exchangeable image file (EXIF)) is embedded into the JPEG image by using the free software, Exif Pilot. A total of three simulated images are obtained.
5. The three images are loaded into PhotoModeler®. Once all the points in the projected pattern as well as the reference length points are marked in PhotoModeler®, the bundle adjustment is performed by PhotoModeler® to yield the absolute coordinates of all the dots in the optical pattern on the wall.
6. The coordinates of all the dots are imported into the LS algorithm to determine the absolute coordinates of the module.
7. The virtual camera method is carried out by first generating the virtual pinhole camera image with MATLAB® using the appropriate inter beam angles. Then EXIF information is embedded into this virtual image.
8. The three images from step 5 and the virtual image from step 7 are input into PhotoModeler® and the absolute position and orientation of the virtual camera (the module) are then obtained.
9. The module positions obtained from the LS algorithm (step 6) and from the virtual camera approach are compared with the predefined module position in FRED ® (step 1).

As shown in Figure 5.3, three real cameras were simulated in FRED® and each camera consists of a Cooke Triplet lens system [95], an aperture stop and an image plane. The effective focal length of the triplet is 49 mm and an aperture stop with inner diameter of 2.54 mm is placed between the left and the middle lenses to mitigate aberration effect and improve image quality. On the image plane, the film size is 10.16 cm × 10.16 cm and the film is defined to be 1000×1000 pixels. Therefore, three images taken by 1 megapixel digital camera can be simulated in FRED®. The optical pattern simulated in FRED® is a 2D 11×11 dot matrix and it has a full view angle of 29°×29° (2.9°×2.9° between adjacent beams), as shown in Figure 5.2. In FRED® the axes of the coordinate system are defined as shown in Figure 5.3, where the centre dot of the optical pattern is the origin. With module location defined at (0, 0, 1200) mm in FRED®, the optical pattern on the wall surface is achieved by defining two close layers in FRED®. A white layer represents the wall surface, which scatters incident rays. The other layer is comprised of a collection of coplanar black circles, representing the dots in the projection pattern. There is a spatial separation of 0.25 mm between these two layers. Four coded targets (see Figure 5.3) are added to the optical pattern so that PhotoModeler® can automatically locate and reference the dots among photographs taken from different positions and orientations. As shown in Figure 5.3, the 2D optical pattern is illuminated by a monochromatic collimated planar source (800×800 array) that is placed to the left of the pattern. A wavelength of 550 nm is chosen for the source. The source is chosen to be incoherent, which is a better representative of realistic illumination properties. The wall surface is defined to be a Lambertian scatter model, thus the orientations of the rays reflecting from the wall are random. Each scattered ray that enters the entrance pupil of each camera is ray-traced through the camera and recorded at the analysis plane. The intensity matrix obtained from the image plane in FRED® is loaded into MATLAB® to generate a JPEG image. The EXIF information is embedded into the JPEG file using the same method mentioned in section 5.2. A sample image of the optical pattern taken by the Cooke Triplet camera in FRED® is shown in Figure 5.4. Following this process three images of the optical pattern were generated in FRED®. In order to achieve better measurement results, the camera used in the photogrammetric measurement needs to be calibrated beforehand. The Cooke Triplet camera defined in FRED® was calibrated by taking a total of 12 images of a calibration grid simulated in FRED® following the procedure suggested by PhotoModeler®.

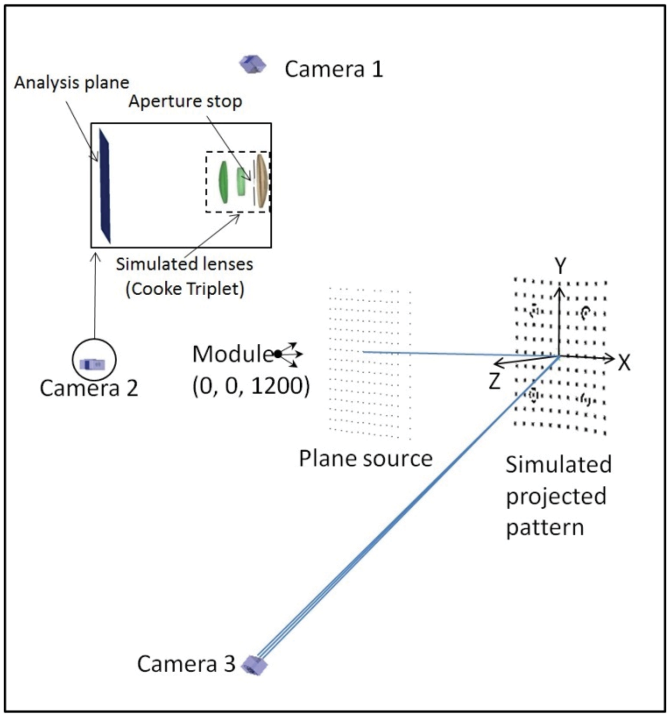

Figure 5.3: The configuration of FRED® simulation.

The evaluation contains two parts. In the first part (step 2 to step 6), the three virtual images are opened in PhotoModeler®. All the points in the optical pattern were identified and marked as targets in the photogrammetry software. After the reference length and reference coordinate system are defined, the absolute coordinates of the dots are yield through the bundle adjustment performed by PhotoModeler®. The coordinates of the dots are then imported into the least-square algorithm to determine the best-fit x_m, y_m, and z_m coordinates of the module. In the second part (step 7 and step 8), the three images from FRED® together with the virtual image generated from MATLAB® are loaded into PhotoModeler®. Following the same photogrammetric measurement procedure presented above, the 3D model of the optical pattern is solved and the camera stations for those four images are determined after the reference length and reference coordinate system are defined. The coordinates of the camera station for the virtual image generated by MATLAB® are actually the coordinates of the module position. Since the module position has been predefined in FRED®, the measurement results from the least-square algorithm and the virtual camera approach are compared with the defined values of the module position in step 9.

The overall accuracy of the photogrammetric measurement depends on several inter-related factors, such as camera resolution, camera calibration method, angles between photos, photo orientation quality, photo redundancy, type of targets and mechanical stability of the camera. With the three images taken by three cameras simulated in FRED®, it was found that the dot coordinates measured with PhotoModeler® have errors up to 100 μm compared with the true values. Investigation indicates that 100 μm noise in dot coordinates leads to uncertainty of ±0.52 mm in the module location.

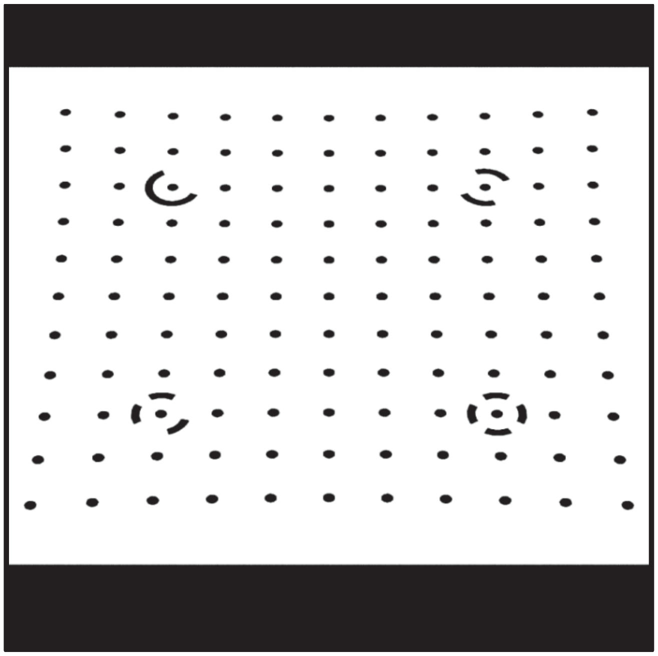

Figure 5.4: A sample of the image taken by the camera simulated in FRED®.

Table 5.1 shows the measured module position error obtained from two different approaches. In Table 5.1, e_X, e_Y , and e_Z represent the position error in X, Y, and Z directions respectively. The module position error, e, is given by equation (5.1).

$$e = \sqrt{e_X^2 + e_Y^2 + e_Z^2} \tag{5.1}$$

Compared with the true value of the module position defined in FRED®, the least-square algorithm has errors of 0.19 mm, 0.33 mm and -0.17 mm in X, Y, and Z directions respectively. This leads to a position error of 0.42 mm based on equation (5.1). The position error obtained from the least-square algorithm is smaller than 0.52 mm, which is within the expectation as presented above. Errors of 0.22 mm, 0.08 mm and 0.20 mm in X, Y, and Z directions are reported from the virtual camera approach and the module position error is 0.30 mm. Compared with the expected uncertainty of 0.5 mm mentioned in section 4.3, the results obtained from the least-square algorithm and the virtual camera approach are comparable with each other and both of them are within the expected range. The experiment measurement results presented in section 5.3 also confirm this conclusion.

Table 5.1: Module position measured with the least-square algorithm and virtual camera approach.

11×11 optical pattern	**e_X (mm)**	**e_Y (mm)**	**e_Z (mm)**	**e (mm)**	**Within Expectation(<±0.52 mm)**
Least-square algorithm	0.19	0.33	-0.17	0.42	Yes
Virtual camera approach	0.21	0.08	0.20	0.30	Yes

5.3 Validation of Virtual Camera Approach through Experimental Test

The virtual camera approach is also validated through experimental tests. The experimental setup is shown in Figure 5.5. The module with 11×11 dot matrix optical pattern was tested on the precision rail with calibrated angles. The module consists of a red laser and a diffraction grating. The laser has a wavelength of 658 nm and a power of 40 mW. The module generates a 11×11 dot matrix with a full view angle around 29° (~2.9° between adjacent beams). The module is mounted on a precision translation rail (Trimos Inc. Switzerland) that has a resolution of 1 μm, and translation range of 1.05 m. Three 9 megapixel digital cameras [108] are positioned at various orientations with respect to the wall. A remote control software package, PSRemote Multi-Camera [89], is used to trigger the three cameras to take pictures within 50 ms of each other. PhotoModeler®, a photogrammetry software package, is used to process the images. A reference length is attached to the wall to provide a known length and a global coordinate system (see inset in Figure 5.5). The designed X axis of the reference artefact was measured to have a length of 253.5± 0.1 mm. All three cameras were calibrated beforehand. For the proposed system, the absolute coordinate of the module can be determined for each module position in our defined coordinate system. An intercomparison with an independent measurement of the absolute coordinates of the module was not possible, so the relative distance change for experimental results is reported.

As mentioned in section 3.3.3, the position accuracy of the rail was determined with a laser interferometer following the guidelines in ASME B5.54-2005 [90]. The uncertainty of the rail linear displacement is less than 20 μm after correcting the error motions (dominated by the Abbe error). This is significantly less than the variability observed in the measurements (see Figure 5.7). The angular characteristic of the module was calibrated by using a precision rotation stage, a projection plane and a camera before the experimental tests. Before the experiment a virtual image was generated following the procedure presented in section 4.3 and such image is used to determine the camera station of the virtual pinhole camera through the bundle adjustment.

The validation through experimental tests is following these steps:

1. An 11×11 dot matrix array of beams is generated by the module at a start position after the module is turned on. The beams intersect the wall and generate an observable pattern. The first measurement position is arbitrarily defined as zero.
2. Three images of the dot matrix pattern on the wall are simultaneously taken by the three cameras controlled by the PSRemote Multi-Camera software package. The three images are loaded into PhotoModeler® and the absolute coordinates of the dots are determined through the bundle adjustment after the reference length and the coordinate system are defined.
3. The coordinates of the dots are imported into MATLAB® and the least-square algorithm is used to determine the best-fit x_m, y_m, and z_m coordinates of the module.

4. Three images obtained from step 2 and the virtual image carrying the angular characteristic of the module are processed in PhotoModeler®, resulting in the camera station of the virtual pinhole camera. The camera station contains a position and orientation estimate of the module.
5. The module is then moved to the next position and the steps are repeated.

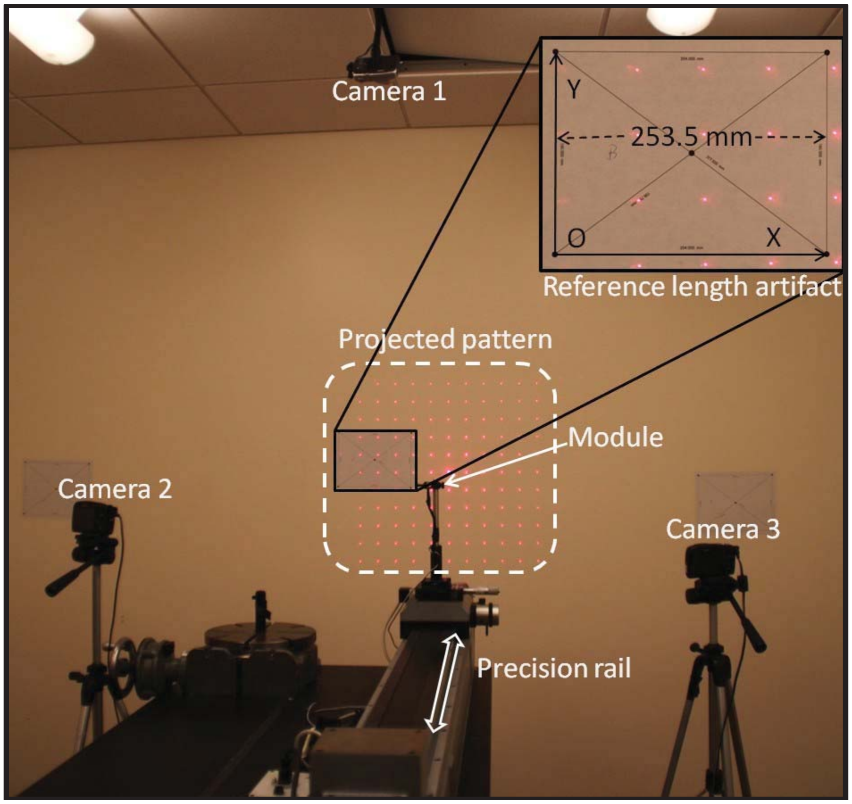

Figure 5.5: Experimental setup. Inset: defined reference length artefact.

At each position the module position was measured using the algorithm with least-square minimization mentioned in section 3.1, as well as using the virtual camera approach mentioned in section 5.2. The translation test was conducted six times and the average measured distances at each position versus the rail reading obtained by two methods are shown in Figure 5.6. The linear fit equations are $Y=-1.00018\times X-0.08687$, with an adjusted R^2 of 1 for the virtual camera approach result and $Y=0.9995\times X+0.03263$, with an adjusted

R^2 of 1 for the least-square algorithm result. For an ideal condition, the measured value should equal the rail reading, which is $Y = X$. The value of the adjusted R^2 and the linear fit equation indicate that the measured distances from both methods have reasonable agreement with the rail readings in light of the uncertainty analysis in section 6.3. The mean values of the differences between the measured distance and the rail reading at each position are illustrated in Figure 5.7 The error bar represents the standard uncertainty of the measurement, u, at each position. It is determined by the standard deviation of six measurements.

The results show that measurement differences at all positions are smaller than 0.42 mm from the least-square algorithm (the red dot in Figure 5.7) and smaller than 0.23 mm from the virtual camera approach (the black square in Figure 5.7). These results indicate that experimental agreement at the level of 3 parts in 10^4 was observed from the virtual camera approach by using the 11×11 dot matrix optical pattern with calibrated angles. The standard uncertainties of the measurement are within 0.34 mm for both methods and are dominated by the uncertainty of the photogrammetric measurement caused by noise on the dot centroid location. These results prove that the results obtained from the virtual camera approach are comparable with those obtained from the least-square algorithm.

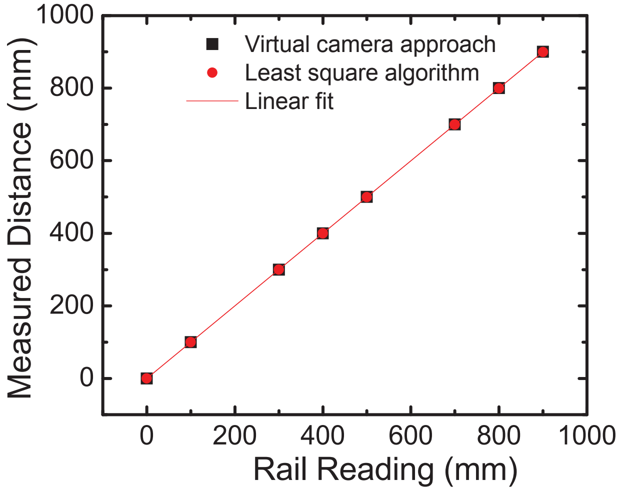

Figure 5.6: Measured distance versus rail reading for the translation test on the rail.

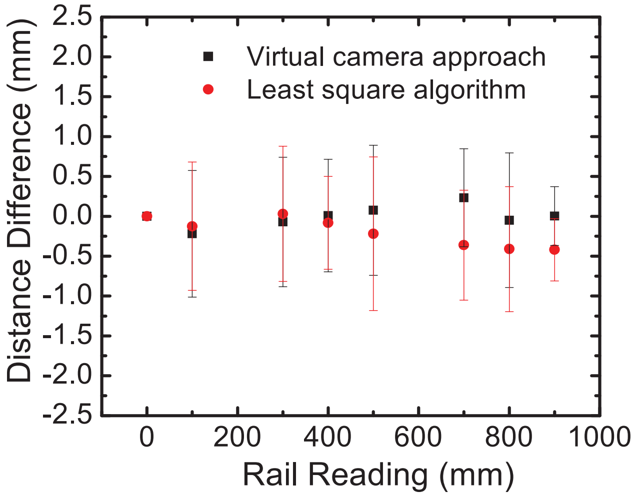

Figure 5.7: Distance difference for translation test on the rail obtained with two approaches. The error bar represents the standard uncertainty.

5.4 Processing Time Consideration

As mentioned in section 4.4, the processing time is one limitation of the current system. For the measurements processed with the virtual camera approach, it takes around seven minutes to get the location of the module. Figure 5.8 shows the pie chart of the processing time of the current measurement using the virtual camera approach.

With the virtual camera approach, not all the dots need to be marked on each image. Thus the manual making time can be saved at least 30 seconds compared with those processed by the algorithm. However, the time consumed by the manual marking process is still the largest portion, which is around 59%. This time can be reduced significantly if costumed algorithm is developed for the specific application. Around 37% of the processing time was consumed by the process of manual referencing because of large number of dots in each image. The referencing time could be reduced by using costumed designed optical pattern with coded targets embedded. Compared with the measurements processed by the algorithm, the processing time of the measurements processed by the virtual camera approach was 20 seconds less. This is due to the module's location was determined through the photogrammetric bundle adjustment. There is no need to calculate the dot coordinates first and additional algorithm is not necessary.

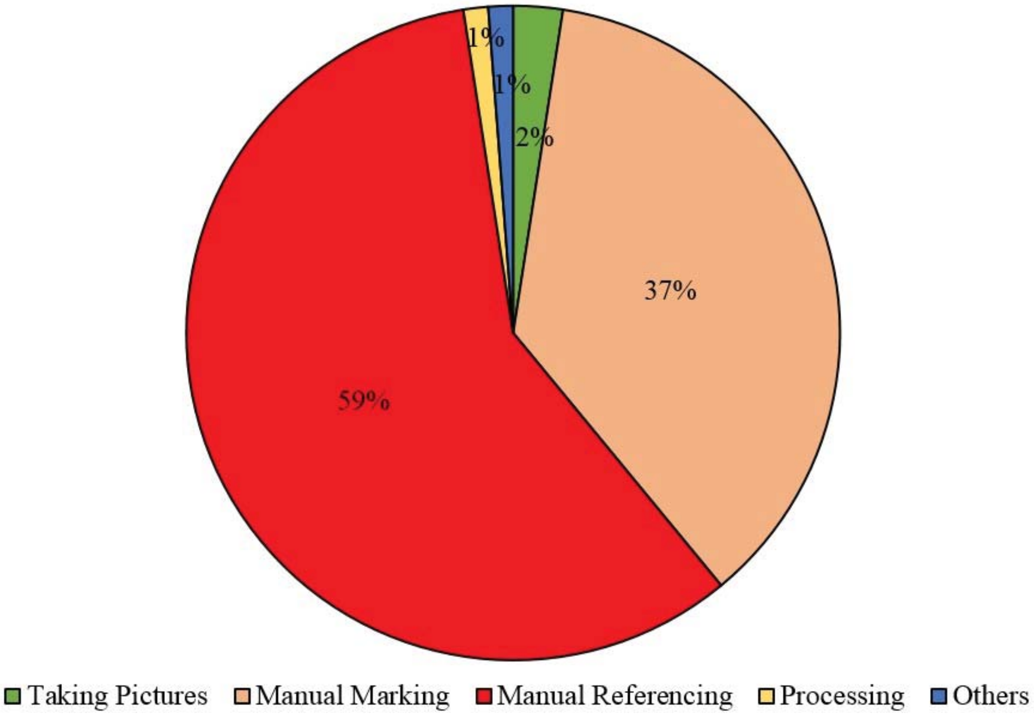

Figure 5.8: Pie chart of the processing time of the proposed system.

5.5 Results Discussion

As demonstrated through simulation in section 5.2, the position error obtained from the proposed virtual camera approach is 0.30 mm, which is smaller than 0.42 mm, the position error reported by the least-square algorithm. The position errors from both methods are within the expectation (< 0.5 mm). The proposed virtual camera approach was also tested experimentally by translating the module in one dimension over 0.9 m in section 5.3. The proposed virtual camera approach reported distance difference smaller than 0.23 mm for each position, which is smaller than 0.42 mm, the distance difference reported by the least-square algorithm. Thus, it is safe to conclude that the proposed virtual camera approach can determine the position of the module with lower uncertainty. With the virtual camera approach, experimental agreement at the level of 3 parts in 10^4 was observed for the one dimension translation test by using the 11×11 dot matrix optical pattern with calibrated angles.

The virtual camera approach also offers several advantages over the least-square algorithm. One advantage is that the virtual camera approach is faster than the least-square algorithm. Unlike the least-square algorithm which needs the coordinates of all the dots in the optical pattern to calculate the module location, the virtual camera approach can determine the module position through the bundle adjustment without knowing all the dot coordinates. There is no need to load the dot coordinates into the algorithm to calculate the module position. Currently the time required to take the images and determine the module position using the virtual camera approach is around 7 minutes (this is dominated by the time consumed on manually marking and referencing), which is 12.5% less than using the least-square algorithm. Additionally, the virtual camera approach is more flexible than the least-square algorithm method. In order to use the least-square algorithm, all the dots or certain dots need to be marked and solved for the module location calculation. The module position cannot be calculated by the least-square algorithm if some key points are missing. The virtual camera approach doesn't have this limitation. As long as enough dots have been marked so that the bundle adjustment can be performed, the module location can be determined. Given these advantages, the virtual camera approach is preferable to provide real time measurements in simple-to-complex environments.

Based on the results presented in section 5.3, a standard uncertainty was observed at the level of 3 part in 10^4 for the one dimension translation test by using 11×11 dot matrix optical pattern with calibrated angles. Compared with measurement results with un-calibrated angles, the distance difference of the module was reduced from 1.7 mm to 0.4 mm by using calibrated angles. Recall that the distance difference from the translation test done with 7×7 dot matrix optical pattern was 1.2 mm (1 part in 10^3). Therefore, these results show that the distance difference of the module was reduced to 0.23 mm by using the new 11×11 projection pattern with calibrated angles. These studies confirm the simulation results discussed in section 4.1, which indicated that the improvements in the measurement can be obtained by improving the design of diffraction element and improving angle characterization of the module.

CHAPTER 6: UNCERTAINTY ANALYSIS

In this chapter, the measurement uncertainty of the proposed module location is explored by performing an uncertainty analysis that traces system uncertainty, component by component, from system input to system output. A brief literature review was given in section 2.5 on the expression of the uncertainty of the result of a measurement. In the analysis performed in this chapter, the sources of uncertainty are treated as either a Type A evaluation [125], "the evaluation of uncertainty by the statistical analysis of series of observations", or a Type B evaluation [125], "the evaluation of uncertainty by means other than the statistical analysis of series of observations", such as evaluation based on scientific judgment using manufacture's specifications, general knowledge, and so on.

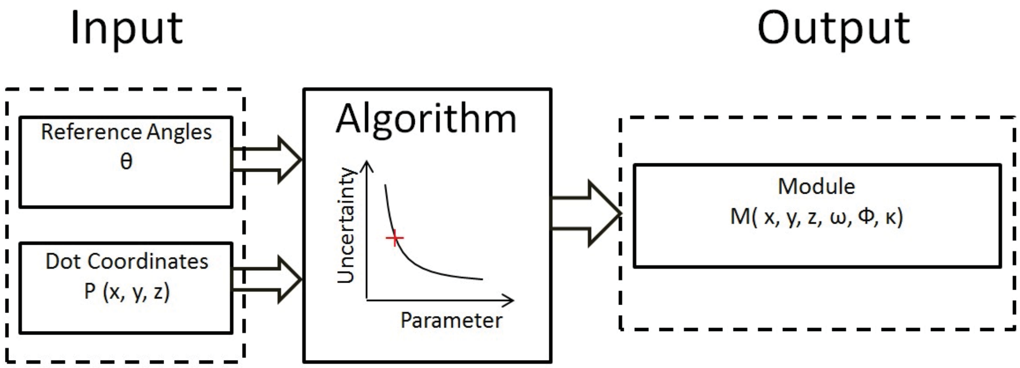

Figure 6.1: Block diagram for the proposed metrology system.

The output of the metrology system is the module location and orientation, which is determined by the algorithm/the bundle adjustment of the photogrammetric measurement. It was demonstrated in section 4.1 that the uncertainty of the measured module position depends on the characteristics of the optical pattern: full view angle and number of dots, both of which are a fixed number for given designed module. The module discussed can generate an 11×11 optical pattern with a full view angle about 29°. A block diagram of the proposed metrology system is shown in Figure 6.1. The uncertainty of the measured module position depends on two system inputs: reference angles of the optical pattern and the dot coordinates in the optical pattern. In order to explore the uncertainty of the measured module position, the uncertainties of these two system inputs are analyzed first.

6.1 Uncertainty Analysis of Reference Angles

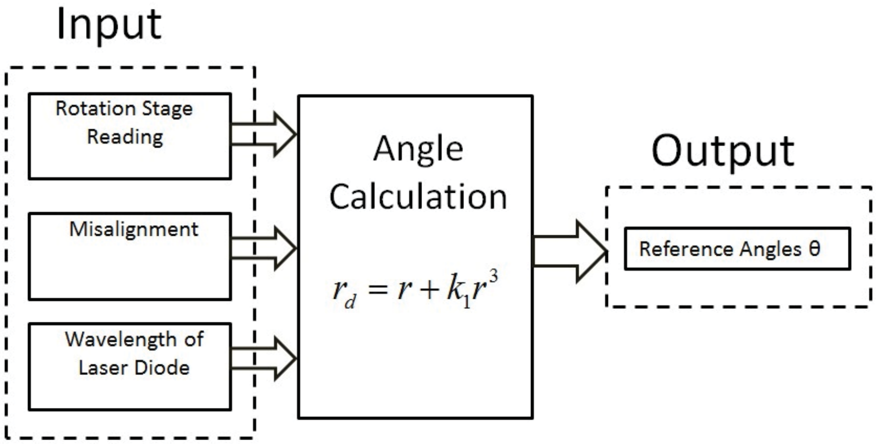

Figure 6.2: Block diagram for calculation of reference angles.

As described in section 4.2.2, the reference angles of the optical pattern were calibrated using a precision rotation stage and a CCD camera. The error sources contributing to the uncertainty of the reference angles can be divided into two categories: uncorrelated error and correlated error. The change of the wavelength of the laser diode leads to correlated error in reference angles. The block diagram of the determination of reference angles is shown Figure 6.2. A detailed discussion on factors contributing to the uncertainty of the reference angles was given in section 4.2.1. The typical values of all main factors contributing to the uncertainty of the reference angles were displayed in Table

4.1. It can be found that the typical value of the correlated error is about 0.0018° because that the wavelength of the laser diode varies by 0.4 nm, according to the analysis in section 4.2. The uncorrelated error sources include the uncertainty of the rotation stage, the misalignment between the module and the center of the rotation stage and the position error of the laser dot detected by the CCD camera. These error sources are assumed to be independent in the following analysis. Based on the calibration method described in section 4.2, the combined standard uncertainty of reference angles from uncorrelated error is calculated through equation (6.1).

$$u_a^{\ c} = \sqrt{u_{a1}^{\ 2} + u_{a2}^{\ 2} + u_{a3}^{\ 2} + u_{a4}^{\ 2} + u_{a5}^{\ 2}} \tag{6.1}$$

Where

u_a^c is the combined standard uncertainty of reference angles,

u_{a1} is the angle uncertainty caused by the uncertainty of rotation stage reading,

u_{a2} is the angle uncertainty caused by misalignment in x direction on rotation stage,

u_{a3} is the angle uncertainty caused by misalignment in y direction on rotation stage,

u_{a4} is the angle uncertainty caused by the reading error in x direction on detection plane,

u_{a5} is the angle uncertainty caused by the reading error in z direction on detection plane,

and u_{a1} to u_{a5} are all treated as Type B uncertainties.

A detailed discussion on these factors were provided in section 4.2.1 and the typical value of each error source listed in Table 4.1, the standard uncertainty of the reference angles is about 0.0013° based on the values listed in Table 4.1 and equation (6.1).

6.2 Uncertainty Analysis of Dot Coordinates

The dot coordinates are determined through the photogrammetric measurement. The accuracy of the photogrammetric measurement depends on factors like the accuracy of reference length, the number of images, the quality of camera calibration and the variance of laser dot centroid. Among these factors, the variance of dot centroid depends on camera parameters (such as the resolution of the image, the camera noise), quality of laser dot, surface texture, reference length used in the experiment and the algorithm used to calculate the centroid. Figure 6.3 shows the diagram of factors contributing to the uncertainty of the dot coordinates. The reference length is the scale factor of the whole system, which affects the coordinates of each dot as well as the measurement result. Thus, the effect of the uncertainty of reference length will be discussed in section 6.3. In 2D pixel coordinates, the uncertainty of dot centroid caused by camera noise has been evaluated in section 3.2.4. The centroid variations are 0.09 pixels and 0.11 pixels in x and y directions respectively.

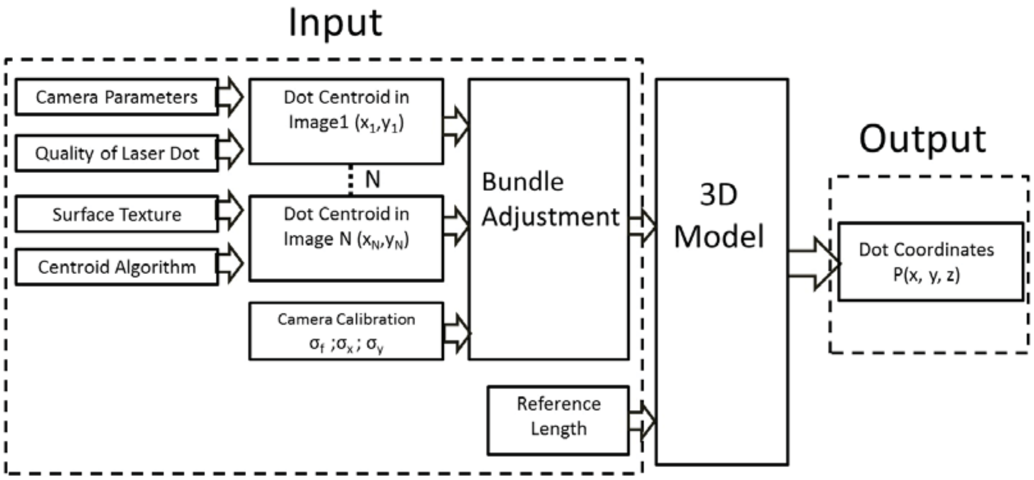

Figure 6.3: Block diagram for dot coordinates determination.

The typical variations in camera parameters such as the focal length and the position of principal point were investigated by repeating the camera calibration 10 times for a single camera. For the camera employed in the experiment, the focal length, the principal point in x direction and the principal point in y direction vary by 5.1 μm, 5.7 μm and 2.2 μm respectively. Analysis based on the repeatability test of the photogrammetric measurement indicates that the changes of these cameras parameters can lead to an uncertainty of 16 μm in dot coordinates (details on the repeatability test is not given in this dissertation).

The factors affecting the uncertainty of the laser dot coordinates are correlated and their relationships are complicated. It is difficult to analyze how much contribution is made to the uncertainty of dot coordinates by each factor. However, all these factors are included in the bundle adjustment process of the photogrammetric measurement. Thus, the uncertainty of the laser dot coordinates can be estimated by combining the uncertainty of the dot coordinates reported by the photogrammetric measurement and the uncertainty of the dot coordinates caused by the change of the wall surface (section 3.2.4.1). The measurement result shows that the combined standard uncertainties (they are defined by the root-sum-of-square (RSS) of the uncertainty of the dot coordinates reported by the photogrammetric measurement and the uncertainty of the dot coordinates caused by the change of the wall surface) of dot coordinates are between 80 μm and 125 μm for different dots in the optical pattern, with a majority value around 100 μm based on experimental observations and engineering judgment.

6.3 Uncertainty Analysis through Monte Carlo Simulations

In order to analyze the uncertainty of a measurement system, the measurement process needs to be defined first. The measurement process of the proposed metrology system is defined by the block diagram shown in Figure 6.1. The two system inputs are the reference angles of the optical pattern and the coordinates of dots in the optical pattern. There is no direct mathematic equation to describe the relationship between the system output (the module location and orientation) and the system inputs (the reference angles and the coordinates of dots), and the correlations between two system inputs are unclear. As suggested by JCGM 101:2008 [129], the propagation of probability distributions can be analyzed through a mathematical model of measurement to evaluate the uncertainty of the measurement, which can be implemented by a Monte Carlo method (MCM). This method can be applied to a model having a single output quantity, and any number of input quantities. Thus, Monte Carlo method is chosen to investigate the uncertainty of the measured module position.

Monte Carlo simulation is a reiterative process of analysis, which uses repeated samples from probability distributions as the inputs for models. The uncertainties in the models can be investigated by generating a distribution of outputs through simulation. For the proposed metrology system, the mean value of the module location and the associated standard deviation (combined standard uncertainty) can be estimated through Monte Carlo simulation.

The Monte Carlo simulation proceeded by randomly adding noise to each input variable (a total of 220 reference angles and the x, y, and z coordinates of 121 dots) from the specified distribution, calculating the module location, and repeating these steps over many iterations (1×10^4). The mean value of the adjacent inter-beam angle is 2.9°, and the mean values of all the other reference angles are calculated based on the geometry of the optical pattern. The mean values for all reference angles can be found from Appendix E. The uncorrelated noise (normal distribution) with a standard deviation of 0.0013° was added to 220 reference angles and these reference angles were associated with different values of noise for each iteration. The values of the added uncorrelated noise to the reference angles were different for different iterations. The correlated noise on reference angles was added by randomly selecting noise in uniform distribution within a range of -0.0009°~ +0.0009°. For each iteration the values of the correlated noise added to the reference angles were the same and they changed randomly for different iterations. Thus, for one iteration of the MC simulation, each angle had a value of (2.9°+uncorrelated noise +correlated noise), where the correlated error was the same for all angles, and the uncorrelated noises were different for all angles. The mean values of the dot coordinates were calculated based on the configuration shown in Figure 6.4. The module was set to be the origin of the coordinate system (0, 0, 0). Uncorrelated noise in normal distribution with a standard deviation of 100 μm was added to all the dot coordinates. The heart of the Monte Carlo simulation is repeated sampling and the evaluation of the model in each case. The effectiveness of MCM depends on the use of an adequately large value of iteration times [129], and each MCM was repeated 10,000 times for the simulation mentioned below.

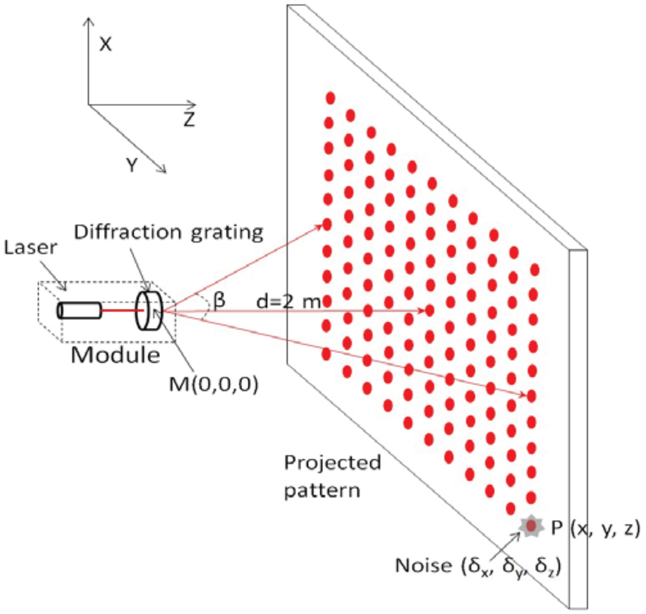

Figure 6.4: The diagram for dot coordinates calculation.

6.3.1 Relationship between Two System Inputs

In order to explore the relationship between the uncertainties of the two system inputs, a few simulations were conducted as detailed in cases 1 to 3. In these three cases the simulation configuration was shown in Figure 6.4 and the projection plane is 2 m away from the module and perpendicular with the optical axis of the module. In case 1 the Monte Carlo simulation was repeated 10,000 times with only uncorrelated noise added to the reference angles. No noise was added to the coordinates of all the dots. In case 2, the Monte Carlo simulation was repeated 10,000 times with only uncorrelated noise added to the coordinates of 121 dots. This time no noise was added to the reference angles. In case 3, uncorrelated noise was added to the reference angles and random noise was added to the coordinates of all the dots. The standard uncertainties of the module location were reported for the three analysis approaches and they are displayed in Table 6.1. The standard uncertainties of the module location in three cases are represented by u_1, u_2 and u_3 as shown in Table 6.1. For the three simulations mentioned above, the true value of the module location is set to be (0, 0, 0) mm. The combined standard uncertainty of the measured module location is given by equation (6.2), where u_x, u_y and u_z are the standard uncertainties of the module position in x, y and z directions respectively.

$$u_c = \sqrt{u_x^2 + u_y^2 + u_z^2} \tag{6.2}$$

Table 6.1: The standard uncertainties of the module location obtained from Monte Carlo simulations.

	Uncorrelated noise on reference angles (degree)	Uncorrelated noise on dot coordinates (mm)	u_x (mm)	u_y (mm)	u_z (mm)	u_c (mm)
u_{c1}	0.0013	0	0.16	0.17	0.04	0.23
u_{c2}	0	0.1	0.37	0.36	0.06	0.52
u_{c3}	0.0013	0.1	0.40	0.40	0.07	0.57

Based on the results shown in Table 6.1, the relationship between u_{c1}, u_{c2} and u_{c3} can be described as $u_{c3}^2 \approx u_{c1}^2 + u_{c2}^2$. Thus, it can be assumed that the two sources are independently based on this result. This relationship was further confirmed by repeating case 1 to case 3 using uncorrelated noise with values of 0.002°, 0.004°, 0.006°, 0.008°, 0.01° and 0.02° . This relationship implies that the uncertainty of the measured module position caused by the reference angles can be treated as independent with the uncertainty of the measured module position caused by the dot coordinates for the noise level discussed above.

6.3.2 Uncertainty Analysis of the Module Position and the Travelled Distance

In order to estimate the uncertainty of the module position in the proposed system mentioned in section 4.4, the uncertainty of the dot centroid, the uncorrelated noise in the reference angles and the correlated noise in the reference angles were included in the Monte

Carlo simulation. The uncorrelated noise with a normal distribution (standard deviation of 0.0013°) was added to 220 reference angles. The correlated noise on reference angles was added by randomly selecting noise in uniform distribution within a range of -0.0009°~ +0.0009°, which could be caused by the drift of the wavelength of the laser diode. And uncorrelated noise in normal distribution with a standard deviation of 100 µm was added to all the dot coordinates. Monte Carlo simulation was repeated 10,000 times for each module position as measured in the experiment. The standard uncertainties of the measured module location are shown in Table 6.2 when the module was at the starting position, which has a distance of 0.9 m between the module and the projection plane. The parameters used in Monte Carlo simulation are chosen as close as possible to the parameters used in the experimental test.

Table 6.2: The standard uncertainty of the module position at the start position obtained from Monte Carlo simulation with all noise added.

Systematic noise on reference angles (degree)	Uncorrelated noise on reference angles (degree)	Noise on dot coordinates (mm)	u_x (mm)	u_y (mm)	u_z (mm)	u (mm)
±0.0009	0.0013	0.1	0.38	0.38	0.15	0.55

Table 6.3: The combined standard uncertainty of the module position at each position on the rail obtained from Monte Carlo simulation with all noise added.

Position on the rail (mm)	0	100	300	400	500	700	800	900
u_x (mm)	0.38	0.38	0.38	0.38	0.39	0.39	0.39	0.40
u_y (mm)	0.38	0.38	0.38	0.39	0.39	0.39	0.39	0.40
u_z (mm)	0.15	0.17	0.18	0.21	0.23	0.26	0.27	0.29

u_c (mm)	0.55	0.56	0.57	0.58	0.60	0.61	0.62	0.63

In the experiment, the distance the module travelled was calculated with respect to the starting position. Thus, the combined standard uncertainty of the distance measurement is calculated based on the standard uncertainties of the start module position and the end module position from Monte Carlo simulation results shown in Table 6.3. As shown in Table 6.3, the values of u_x, u_y and u_z increase with the increase of the distance the module travelled. This is caused by the correlated noise in the reference angles, a detailed discussion of this can be found in section 4.1.4. For the measurement results displayed in Figure 4.28 in section 4.4.1, the uncertainty of the scale should also be considered. The uncertainty of the reference length (Type B) is estimated to be 0.04%, and the uncertainty of the measured distance is proportional to the uncertainty of the scale. The combined standard uncertainty of distance measurement obtained by Monte Carlo simulation, u_M, the uncertainty of the measured distance caused by the uncertainty of the scale, u_s, and the combined standard uncertainty of the distance measurement, u_c, are displayed in Table 6.4. The value of u_c is given by equation (6.3) and the value of the expanded uncertainty of the measured distance (U) can be calculated by equation (6.4), where *k* is the coverage factor. The value of U is also listed in Table 6.4 with a coverage factor of 2, which is suggested by NIST [125].

$$u_c = \sqrt{u_M^2 + u_s^2} \tag{5.3}$$

$$U = k \bullet u_c \tag{6.4}$$

Table 6.4: The combined standard uncertainty of measured distance obtained from Monte Carlo simulation, the uncertainty caused by the scale error, and the expanded uncertainty of the measured distance with *k*=2.

Travel distance (mm)	0	100	300	400	500	700	800	900
u_M (mm)	0.55	0.79	0.80	0.80	0.82	0.83	0.83	0.84
u_s (mm)	0.00	0.04	0.12	0.16	0.20	0.28	0.32	0.36
u_c (mm)	0.55	0.79	0.81	0.82	0.84	0.87	0.89	0.92
U (mm)	1.10	1.48	1.62	1.64	1.68	1.74	1.78	1.88

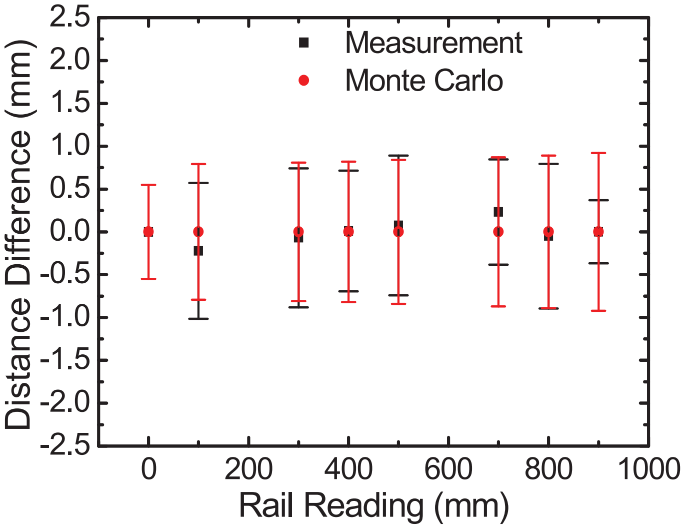

Figure 6.5: The experimental result for the translation test on the rail with combined uncertainty. The black square represents the mean value of 6 measurements and the red dot stands for the mean value of Monte Carlo simulation results. Black error bar represents the uncertainty of the measured distance and red error bar represents the combined standard uncertainty of the measured distance from the analysis.

The measured distances from the translation test in section 4.4.1 together with the combined standard uncertainties obtained above are show in Figure 6.5. The mean value of 6 measurements from the experiment is represented by the black square while the red dot stands for the mean value of the Monte Carlo simulation result. The black error bar in Figure 6.5 represents the standard deviation of six measurements during experiment and the red error bar represents the combined standard uncertainty of the measured distance from the analysis. As shown in Figure 6.5, the measurement result reported by the proposed metrology system is consistent with the analyzed uncertainty based on Monte Carlo simulation.

CHAPTER 7: CONCLUSIONS AND RECOMMENDATIONS FOR FUTURE WORK

7.1 Summary and Conclusions

This dissertation has presented a novel, low cost metrology system to measure the 6 DOF motion of a small, lightweight optical module by combining photogrammetry and optical pattern projection. The approximate cost of the current system (hardware and software) is \$2000. On the open market, the price of a completed system will be higher than \$2000 considering the intellectual merit and development cost, and this is outside the scope of this dissertation. The feasibility of the proposed system was demonstrated by translating the module 0.9 m along a precision rail and rotating it through 60 º on a graduated rotational holder. These tests yielded experimental agreement of 1 part in 10^3 and 5 parts in 10^3 for the translation and rotational tests respectively (chapter 3). The ability of the module to evaluate the performance of a 6 DOF articulated arm was evaluated and compared to the results obtained from a laser tracker system. The experimental results demonstrate the ability of the module to measure the movement of the arm in 3D space and distance errors around 1 mm were observed.

Numerical simulations were carried out to isolate elements within the metrology system that could be optimized to further reduce the measurement uncertainty. The modeling confirmed that the system will perform better than direct photogrammetric measurement with traditional tie points alone, and that the uncertainty can be further reduced by using projection patterns with the following features: (1) larger value of full view angle β, (2) larger value of dot number N, (3) calibrated reference angles (chapter 4). With these changes made to the module the translation test was redone and the measured distance agreed to 5 parts in 10^4, a 65% improvement.

Modeling and experimental work confirmed that the algorithm used to determine the *xyz* coordinates of the module location from the dot locations can be replaced by modeling the module as a virtual camera (chapter 5). Experimental results using the virtual camera approach gave distance agreement to 3 parts in 10^4 for the translation test. Additional advantages of this system include a 12.5% reduction in processing time.

The large dynamic range of the system was demonstrated by mapping multiple local coordinate systems to a central co-ordinate system. The dynamic range was increased from approximately 60° to over 120°. Experimental testing using multiple co-ordinate systems yield an angle difference of 0.23° between the angle encoder reading and the result obtain from the proposed system (chapter 4).

Monte Carlo analysis was undertaken to evaluate the sensitivity of the system to the main sources of uncertainty. The analysis revealed that the four main factors limiting the measurement uncertainty of the current system are the variation of inter-beam angles caused by the change of the wavelength of the laser, the uncertainty of the measured dot centroid, the uncertainty of the reference angles of the module and the uncertainty of the reference length (chapter 6).

A relatively low cost measurement system with large dynamic range is presented within this dissertation. The proposed system also has the potential to provide high measurement accuracy and overcome the line of sight restrictions associated with other comparable measurement systems. In addition, this proposed system has the potential to allow real time measurement during manufacturing process if further improvements can be made to reduce the processing time.

7.2 Recommendations for Future work

The system modeling in chapter 4 and Monte Carlo simulations in chapter 6 indicate that the measurement capabilities of the proposed metrology system can be further enhanced with a few improvements. The improvements to reduce the uncertainty of the measured module position include using optical pattern with large full view angle and large dot number (this depends on the design of the diffractive element), reducing the uncertainty of the reference angles of the module, improving the accuracy of the reference artifact and improving the measurement accuracy of the dot centroid. The improvements to reduce the processing time of the proposed system include improving the visibility of the laser dot and using custom designed optical pattern with embedded coded targets.

7.2.1 Improvement on the Design of Diffraction Grating

A commercially available diffractive element was used in the experimental tests detailed in this dissertation, however simulation results presented in section 4.1 indicate that there is scope to further improve the system's performance through the use of a customized grating. Key elements of an optimal diffraction grating design include a. full view angle greater than 60°, and more than 40 dots per side. Implementation of these elements could result in a further 69% reduction in the associated measurement uncertainty. Also, a custom design of the optical pattern with embedded coded targets can further benefit the automation of the proposed metrology system, which could reduce the processing time by 70% if the automation is achieved.

7.2.2 Reduction on Uncertainty of the Reference Angles

The uncertainty of the reference angles of the module is a critical part in determining the system uncertainty. The wavelength of the current laser diode used in the experimental tests changes by 0.4 nm with controlled room temperature. This variation is the main factor contributing towards the uncertainty of the measured reference angles. Such uncertainty can be reduced significantly by using a laser with high wavelength stability. The uncertainty of the measured module location caused by the change of the wavelength can be neglected if the frequency stability of the laser is better than ±0.2 ppm (part per million). This is possible because the frequency stabilization of commercial laser around ±0.05 ppm over 1 year is available [124]. In addition, improvements to the hardware system used to calibrate the reference angles as mentioned in section 4.2 will also reduce the measurement uncertainty of the reference angles. These improvements include using a high precision 2D rotation stage, adopting high precision PSDs and so on. The uncertainty of the measured reference angles can be reduced to 0.0006° or better if the above improvements are implemented.

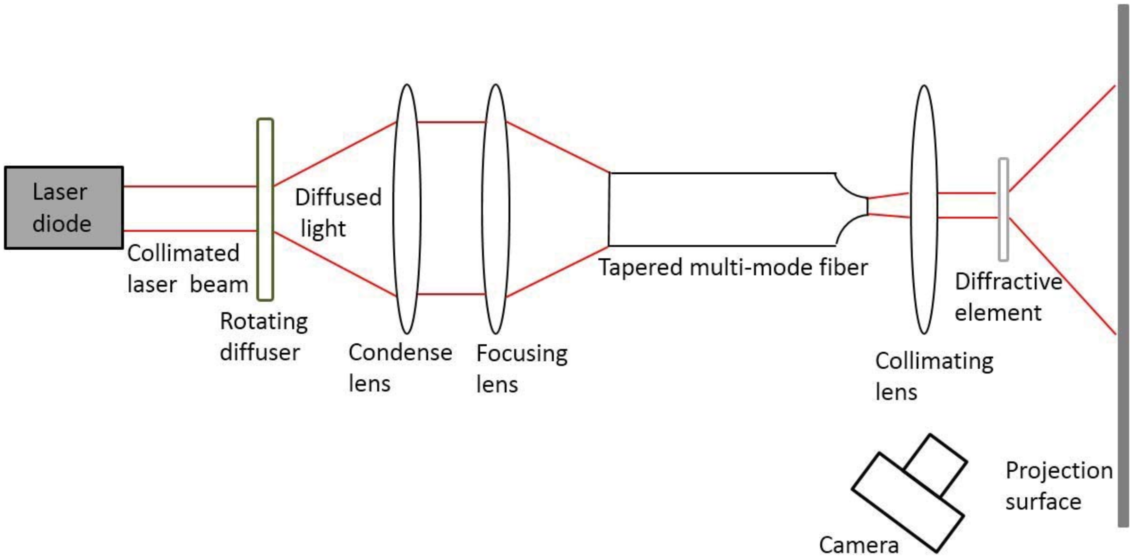

Figure 7.1: Laser speckle reduction setup.

7.2.3 Reduction on Uncertainty of the Dot Centroid

The uncertainty of the dot centroid location is another critical factor affecting the uncertainty of the metrology system proposed in this dissertation. Improving the uniformity of the laser dot and improving the quality of the photogrammetric images of the dots are two ways to reduce this associated uncertainty. Improving the uniformity of the laser dot can be achieved by reducing the speckle in the laser dot. Utilizing a laser speckle reducer in the laser source is one effective way to reduce the speckle. An experimental setup to reduce laser speckle was proposed as shown in Figure 7.1. It was proved that the laser speckle can be reduced significantly with such setup. A detailed discussion on laser speckle and speckle reduction can be found in Appendix A. However, this setup was not included in the module design discussed in this dissertation due to the difficulty in finding a supplier for the tapered multi-mode fiber. On the other hand, improving the quality of the photogrammetric images of the dots may improve the system’s ability to detect the dot centroid location, so that the uncertainty of the dot centroid can be reduced. This improvement can be accomplished by upgrading the hardware system of the proposed technique, such as using high stability cameras with higher resolution, adopting more cameras to take more images of the optical pattern and performing field calibration for all the cameras. The uncertainty of dot centroid around 50 μm for each axis can be achieved if the above improvements are made.

Given the improvements discussed from section 7.2.1 to 7.2.3 are accomplished, results from Monte Carlo simulation indicate that the combined standard uncertainty of the measured module position (u as expressed in equation 6.2 in section 6.3) around 42 μm could be achieved.

7.2.4 Reduction on the Processing Time

Another key aspect of the method that must be addressed concerns the time required for processing. Currently the time required to take the images and determine the module position using the virtual camera approach is around 7 minutes. The bottle neck in the processing sequence is to mark and reference the targets manually, where approximately 71% of the time is consumed. Ways that could reduce this time include improving the visibility of the laser dot (this can be done by increasing the intensity of the laser dot and reduce the speckle on the dot) and using a custom designed optical pattern with embedded coded targets to facilitate automatic identification and referencing of the dots.

REFERENCES

[1] Hein, G., Paonni, M., Kropp, V. and Teuber, A., GNSS Indoors: Fighting the Fading, Part 1. InsideGNSS, work paper, March/April (2008). Also available at: http://www.insidegnss.com/node/458

[2] Hedges, T.M., White paper: Error budget and specifications. Arc Second (2004).

[3] Yang, Z., Shen, Y. and Liu Z., Measurement of six degree-of-freedom ground motion by using eight accelerometers, Earthquake Engineering and Engineering Vibration, 4(2), pp. 229-232 (2005).

[4] Roetenberg, D., Luinge, H. and Slycke, P., 6 DOF Motion Analysis Using Inertial Sensors, In Proc. Of Measuring Behavior, Masstricht, The Netherlands (2008).

[5] Park, W.S, Cho, H.S., Byun, Y.K., Park, N.Y. and Jung D.K., Measurement of 3-D position and orientation of rigid bodies using a 3-facet mirror, In Proc. SPIE Conf. on Three-Dimensional Imaging, Optical Metrology, and Inspection , Vol. 3835, pp. 1–13 (1999).

[6] Park W.S., Cho, H.S., Measurement of fine 6-degrees-of-freedom displacement of rigid bodies through splitting a laser beam: experimental investigation, Opt. Eng., 41(4), pp. 860–871 (2002).

[7] Lee, N., Cai, Y. and Joneja, A., High-resolution multidimensional displacement monitoring system, Opt. Eng. 36(8), pp.2287–2293 (1997).

[8] Vann, C.S., A new six degrees of freedom position sensor greatly improves flexible manufacturing - but will manufacturers adapt?, Sensor Review, 18(2), pp.73 – 74 (1998).

[9] Hofmann M. and Gavrila, D.M., Multi-view 3D human pose estimation in complex environment, International Journal of Computer Vision, Vol.96, pp.103-124 (2012).

[10] Hutson M. and Reiners, D., JanusVF: accurate navigation using SCAAT and virtual fiducials, IEEE Transaction on Visualization and Computer Graphics, 17(1), pp.3-13 (2011).

[11] Murphy-Chutorian E. and Trivedi, M.M., Head pose estimation in Computer Vision: a survey. IEEE Transactions on Pattern Analysis and Machine Intelligence, 31 (4), pp.607-626 (2009).

[12] Ren J., Vlachos, T. and Argyriou, V., Immersive and perceptual human-computer interaction using computer vision techniques, Proc. IEEE Computer Society on Computer Vision and Pattern Recognition Workshop, pp.66-72 (2010).

[13] Vorozcovs, A., Hogue, A. and Stuerzlinger, W., The hedgehog: a novel optical tracking method for spatially immersive displays, Proc. IEEE Conf. on Virtual Reality, pp.83–89 (2005).

[14] Hogue, A., Jenkin, M.R. and Allison, R.S., An optical-Inertial tracking system for fully-enclosed VR displays, Proc. Of The First Canadian Conference on Computer and Robot Vision (2004).

[15] El-Hakim, S.F., A photogrammetric vision system for robots, Photogramm. Eng. Remote Sens., 51(5), pp.545-552 (1985).

[16] Bosemann, W., Advances in photogrammetric measurement solutions. In: Machine Vision. Computers in Industry, 56 (8-9), pp.886-893 (2005).

[17] Hefele, J. and Brenner, C., Robot pose correction using photogrammetric tracking, Machine Vision and Three-Dimensional Imaging Systems for Inspection and Metrology, Photonics East, Boston (2000).

[18] Boochs, F., Schutze, R. and Raab, C., A flexible multi-camera system for precise tracking of moving effectors, Proceeding of Robotics and Applications, 664 (2009).

[19] Luhmann, T., Robson, S., Kyle, S., and Harley, L., Close Range Photogrammetry: Principles, Methods and Applications, Whittles Publishing, pp.528 (2006).

[20] Luhmann, T., On the determination of objects rotation and translation in 3-D space (6DOF) by a single camera. In: Gruen, A., Kahmen, H. (Eds.), Optical 3-D Measurement Techniques VII, Technical University of Vienna, pp.157-166 (2005).

[21] Luhmann, T., Precision potential of photogrammetric 6DOF pose estimation with a single camera, ISPRS J. Photogramm. Remote Sens., 64(3), pp.275-284 (2009).

[22] Bridges, B. and White, D.A, Laser trackers: a new breed of CMM, Quality Digest,18 (2), pp.41-44 (1998).

[23] Hennes, M. and Richter, E., A-TOM –eine neuartige instrumentelle Lösung für die hochpräzise und echtzeitnahe 6DOF-Bestimmung, Allgemeine Vermes-sungsnachrichten, 8(9), pp.301-310 (2008).

[24] McGlone, J.C., Mikhail, E.M, Bethel, J.S. and Mullen, R., Manual of Photogrammetry, fifth edition, American Society of Photogrammetry and Remote Sensing (ASPRS) (2004).

[25] Fraser, C.S., Photogrammetric measurement to one part in a million, Photogramm. Eng. Remote Sens., 58(3), pp.305-310 (1992).

[26] Wallace, I., Lawson, N.J., Harvey, A.R., Jones, J.D.C. and Moore, A.J., High-speed close-range photogrammetry for dynamic shape measurement, Proc. Of SPIE on High-Speed Photography and Photonics, 5580:358-366 (2005).

[27] Wallace, I.D., Lawson N.J., Harvey, A.R., Jones, J.D.C. and Moore, A.J., High-speed photogrammetry system for measuring the kinematics of insect wings, Applied Optics, 45(17), pp.4165-4173 (2006).

[28] Pappa, R.S., Black, J.T., Blandino, J.R., Jones, T.W., Danehy, P.M. and Dorrington, A.A., Dot-projection photogrammetry and videogrammetry of gossamer space structures, Journal of Spacecraft and Rockets, 40(6), pp.858-867 (2003).

[29] Matthews, N.A., Aerial and Close-Range Photogrammetric Technology: Providing Resource Documentation, Interpretation, and Preservation, Technical Note 428. U.S. Department of the Interior, Bureau of Land Management, National Operations Center, Denver, Colorado (2008).

[30] Atkinson, K.B., Close Range Photogrammetry and Machine Vision, Scotland: Whittles Publishing, p371 (1996).

[31] Fraser, C.S., Periodic inspection of industrial tooling by photogrammetry, Photogramm. Eng. Remote Sens., 54(2), pp.211-216 (1988).

[32] Maas, H.G., and Hampel, U., Photogrammetric techniques in civil engineering material testing and structure monitoring, Photogramm. Eng. Remote Sens., 72(1), pp.39-45 (2006).

[33] Martinez, J., Ordonez, C., Arias, P., and Armesto, J., Non-contact 3D measurement of buildings through close range photogrammetry and a laser distance meter, Photogramm. Eng. Remote Sens., 77(8), pp.805-811 (2011).

[34] Lee C.K., Radiometric characteristics of video images for real-time photogrammetric system, KSCE Journal of Civil Engineering, 1(1), pp.67-78 (1997).

[35] Wiora, G., Babrou, P. and Manner, R., Real time high speed measurement of photogrammetric targets, Pattern Recognition Lecture Notes in Computer Science 3175:562-569 (2004).

[36] Villiers, J.D., Real-time photogrammetric stitching of high resolution video on COTS hardware, Optomechatronic Technologies, ISOT 2009 International Symposium, pp.46-51 (2009).

[37] Clarke, T.A., Gooch, R.M., Ariyawansa, D.D.A.P. and Wang, X., 3D-NET-the development of a new real-time photogrammetric system, Proc. Of SPIE on Videometrics V, 3174:222-233.

[38] Wester-Ebbinghaus W. and Zamzow, H., Real-time-photogrammetry by means of high-speed-video, Proc. Of ISPRS, part 5, pp.212-218 (1989).

[39] Wasmeier, P., How to use the "Geodetic Transformations Toolbox"?, (2011).

[40] Barrows, D.A., Burner, A.W., Abrego, A.I. and Olson, L.E., Blade displacement measurements of the full-scale UH-60A airloads rotor, AIAA paper2011-3655, Honolulu, Hawaii (2011).

[41] Burner, A.W., Lokos, W.A. and Barrows, D.A., In-flight aeroelastic measurement technique development, optical diagnostics for fluids, solids and combustion, Proc. Of SPIE, Vol.5191 (2003).

[42] Yilmaz, H.M., Yahar, M., Gulec, S.A. and Dulgerler, O.N., Importance of digital close-range photogrammetry in documentation of cultural heritage, Journal of Cultural Heritage, 8:428-433 (2007).

[43] El-Omari, S. and Moselhi, O., Integrating 3D laser scanning and photogrammetry for progress measurement of construction work, Journal of Automation in Construction, 18(1), pp.1-9 (2008).

[44] ADIS16362: Six Degrees of Freedom Inertial Sensor. Available at: http://www.analog.com/en/mems-sensors/mems-inertial-sensors/adis16362/products/product.html (2013).

[45] Koelman, H.J., Application of a photogrammetry-based system to measure and re-engineer ship hulls and ship parts: An industrial practices-based report, Computer-Aided Design, 42:731-743 (2010).

[46] Arias, P., Herraez, J., Lorenzo, H. and Ordoez C., Control of structural problems in cultural heritage monuments using close-range photogrammetry and computer methods, Computers and Structures, 83:1754-1766 (2005).

[47] Pedersini, A., Sarti, A. and Tubaro, S., Automatic monitoring and 3D reconstruction applied to cultural heritage, Journal of Cultural Heritage, pp.301-313 (2000).

[48] NIST, In-Situ 3D Optical and Mechanical Metrology of Fabricated Parts. Available at: http://www.nist.gov/el/isd/sbm/insitu3d.cfm (2011).

[49] Horneber, C., Knauer, M. and Hausler, G., Phase measuring deflectometry-a new method to measure reflecting surfaces, annual report, Lehrstuhl fur Optik, University of Erlangen-Nuremberg (2000). Available at: http://www.optik.uni-erlangen.de/osmin

[50] Hausler, G., Horneber, C. and Knauer, M., Physical limits of phase measuring deflectometry, annual report, Lehrstuhl fur Optik, University of Erlangen-Nuremberg (2001). Available at: http://www.optik.uni-erlangen.de/osmin

[51] Knauer, M.C., Kaminski J. and Hausler, G., Phase measuring deflectometry: a new approach to measure specular free-form surfaces, Proc. Of SPIE on Optical Manufacturing and Testing VI, pp.58691D1-58691D12 (2005).

[52] SurfMax, CarlZeiss, available at: http://www.zeiss.de/oim/en (last date accessed 04 September 2012).

[53] Matthies, L., Gat, E., Harrison, R., Wilcos, B., Volpe, R. and Litwin, T., Mars microrover navigation: Performance evaluation and enhancement, Autonomous Robots, 2(4), pp.291-312 (1995).

[54] Matthies, L., Balch, T.R. and Wilcox, B.H, Fast optical hazard detection for planetary rovers using multiple spot laser triangulation, Proc. Of IEEE on Robotics and Automation, 1:859-866 (1997).

[55] Ganci, G. and Brown, J., Developments in Non-Contact Measurement Using Videogrammetry, Proc. of the Boeing Large Scale Metrology Conference, (2000).

[56] Jones, T. W. and Pappa, R. S., “Dot Projection Photogrammetric Technique for Shape Measurements of Aerospace Test Articles,” AIAA Paper 2002-0532, Proc. of the 40th AIAA Aerospace Sciences Conference (2002).

[57] Pappa, R.S., Jones, T.W., Black, J.T., Walford, A., Robson, S., and Shortis, M.R., Photogrammetry methodology development for gossamer spacecraft struc- tures, AIAA Paper 2002-1375 (2002).

[58] Pappa, R.S., Jones, T.W., Black, J.T., Walford, A., Robson, S. and Shortis, M.R., Photogrammetry methodology for gossamer spacecraft structures. Sound and Vibration, 36(8), pp.12–21 (2002).

[59] Black, J. T. and Pappa, R. S., Videogrammetry Using Projected Circular Targets: Proof-of-Concept Test, Proc. of the 21st International Modal Analysis Conference, (2003).

[60] Pappa, R.S., Black, J.T., Blandino, J.R., Jones, T.W., Danehy, P.M. and Dorrington, A.A. Dot- projection photogrammetry and videogrammetry of gossamer space structures. Journal of Spacecraft and Rockets, 40(6), pp.858–867 (2003).

[61] Jones, T.W., Dorrington, A.A., Shortis, M.R. and Hendricks, A.R., Validation of laser-induced fluorescent photogrammetric targets on membrane structures, in 45th AIAA/ASME/ASCE/AHS/ASC Structures, Structural Dynamics & Materials Conference, AIAA2004-1663 (2004).

[62] Curtis, D.H., Laser dot projection photogrammetry and force balance measurement techniques for flapping wing micro air vehicles, Thesis, Air Force Institute of Technology, Air University (2009).

[63] Pfeiffer, J. and Schwotzer, A., 3-d camera for recording surface structures, in particular for dental purposes, US Patent 6,885,484 B1, pp.1–7 (1999).

[64] Zhang, S., High-resolution, real-time three-dimensional shape measurement, Opt. Eng. 45:2644–2649 (2006).

[65] Zhang, L., Curless, B. and Seitz, S.M., Rapid shape acquisition using color structured light and multi-pass dynamic programming, in "The 1st IEEE Int'l Symposium on 3D Data Processing, Visualization, and Transmission," pp.24–36, (2002),

[66] Forster, F., A high-resolution and high accuracy real-time 3d sensor based on structured light, Int'l Symposium on 3D Data Processing, Visualization and Transmission pp. 208–215 (2006).

[67] Wissmann, P., Forster, F. and Schmitt, R., Fast and accurate 3d scanning using coded phase shifting and high speed pattern projection, 3D Imaging, Modeling, Processing, Visualization and Transmission, International Conference on pp. 108–115 (2011).

[68] Wissmann, P., Forster, F. and Schmitt, R., Fast and low-cost structured light pattern sequence projection, OPTICS EXPRESS, 19(24), pp.24657-24671 (2011).

[69] Iwata, K., Sando, Y., Satoh, K. and Moriwaki, K., Application of generalized grating imaging to pattern projection in three-dimensional profilometry, Applied Optics, 50(26), pp.5115-5121 (2011).

[70] Kocak, D.M., Jagielo, T.H., Wallace, F. and Kloske, J., Remote sensing using laser projection photogrammetry for underwater surveys, Proceedings of Geoscience and Remote Sensing Symposium, 2:1452-1454 (2004).

[71] Liu, T., Radeztsky, R., Garg, S. and Cattafesta, L., A videogrammetric model deforma- tion system and its integration with pressure paint, AIAA 99-0568(1999).

[72] Barrows, D.A., Videogrammetric model deformation measurement techniques for wind tunnel applications, AIAA Paper 2007-1163 (2007).

[73] Burner, A.W., Liu, T. and DeLoach, R., Uncertainty of videogrammetric techniques used for aerodynamic testing, AIAA 2002-2794(2002).

[74] Spain, C.V., Heeg, J., Ivanco, T.G., Barrows, D., Florance, J.R. and Burner, A.W., Assessing videogrammetry for static aeroelastic testing of a wind-tunnel model, AIAA Paper 2004-1677(2004).

[75] Tian, X., Iriarte-Diaz, J., Middleton, K., Galvao, R., Israeli, E., and Roemer, A., Direct measurements of the kinematics and dynamics of bat flight, Bioinspiration & Biomimetics 1:S10–8 (2006).

[76] Trisiripisal, P., Parks, MR., Abbott, A.L., Liu, T. and Fleming, G.A., Stereo analysis for vision-based guidance and control of aircraft landing, AIAA Paper 2006- 1438 (2006).

[77] Curtis, D.H., Reeder, M.F., Svanberg, C.E. and Cobb, R.G., Flapping wing micro air vehicle bench test set-up, AIAA Paper 2009-1272(2009).

[78] Liu, T. and Fleming, G., Videogrammetric determination of aircraft position and attitude for vision-based autonomous landing, AIAA Paper 2006-1437(2006).

[79] Littell, J.D., Large field photogrammetry techniques in aircraft and spacecraft impact testing, society of experimental mechanics, SEM Annual Conference (2010).

[80] Albert, J., Maas, H., Schade, A., and Schwarz, W., Proc. of the 2nd IAG Commission IV Symposium on Geodesy for Geotechnical and Structural Engineering, 21–24 (2002).

[81] Jauregui, G.V., White, K.R., Woodward, C.B. and Leitch, K.R,
Static Measurement of Beam Deformations via Close-Range Photogrammetry, Journal of the Transportation Research Board, 1814:3-8 (2002).

[82] Jauregui, D.V., White, K.R., Woodward, C.B. and Leitch, K.R., Noncontact photogrammetric measurement of vertical bridge deflection, Journal of Bridge Engineering, 8(4), pp.212-222 (2003).

[83] Maas, H. and Hampel, U., Photogrammetric techniques in civil engineering material testing and structure monitoring, Photogramm. Eng. Remote Sens., 72(1), pp.39-45 (2006).

[84] Bethmann, F., Herd, B., Luhmann, T., and Ohm, J., Free-Form surface measurement with image sequences under consideration of disturbing objects, In: Optical 3D Measurement Techniques. Technical University Vienna, pp.51-61 (2009).

[85] Bethmann, F., Herd, B., Luhmann, T., and Ohm, J., Experiences with 3D reference bodies for quality assessment of free-form surface measurements, International Archives of Photogrammetry, Remote Sensing and Spatial Information Sciences (Part 5), pp.86-91 (2010).

[86] Eos Systems, 2010. Available at: http://www.Photomodeler.com (last date accessed 04 September 2010).

[87] Exif Pilot, 2011. Available at: http://www.exifpilot.com/ (last date accessed 12 December 2012).

[88] Photon Engineering, 2013. Available at: http://www.photonengr.com/software/ (last date accessed: 23 November 2012).

[89] Breeze Systems, 2009. Available at:
http://breezesys.com/MultiCamera/psr_index.htm (last date accessed 08 November 2010).

[90] ASME B5.54, 2005. Methods for Performance Evaluation of Computer Numerically Controlled Machining Centers.

[91] Nelder, J. A. and Mead, R., A simplex method for function minimization, Computer Journal, 7:308–313 (1965).

[92] Weng, J., Cohen, P. and Herniou, M., Camera calibration with distortion models and accuracy evaluation, IEEE TRANSACTIONS ON PATTERN ANALYSIS AND MACHINE INTELLIGENCE, 14(10), pp.965-980(1992).

[93] Ricolfe-Viala, C. and Sanchez-Salmeron, A., APPLIED OPTICS, 49:5914-5928 (2010).

[94] Ayinde, F.O., Sunar, M.S., Adebanjo, A. and Olukayode, O., An approach to minimising estimated pincushion camera distortions, TELKOMNIKA, 9(3), pp.555-564 (2011).

[95] Vasiljevic, D.M., Optimization of the Cooke triplet with various evolution strategies and damped least squares, Proceeding of SPIE 3780, Optical Design and Analysis Software, 207(1999).

[96] Wang, L., Tschudi, T., Boeddinghaus, M., Elbert, A., Halldorsson, T. and Petursson, P., Speckle reduction in laser projections with ultrasonic waves, Opt. Eng. (Bellingham) 39, pp.1659–1664 (2000).

[97] Lowenthal, S. and Joyeux, D., Speckle removal by a slowly moving diffuser associated with a moving diffuser associated with a motionless diffuser, J. Opt. Soc. Am. 61, pp.847–851 (1971).

[98] George, N. and Jain, A., Speckle reduction using multiple tones of illumination, Appl. Opt. 12, pp.1202–1212 (1973).

[99] Trisnadi, J.I., Speckle contrast reduction in laser projection displays, Proc. SPIE 4657, pp.131–137 (2002);

[100] Trisnadi, J.I., Hadamard speckle contrast reduction, Opt. Lett. 29, pp.11–13 (2004).

[101] Riechert, F., Speckle reduction in projection systems, Ph.D. thesis, Karlsruhe Institute of Technology (KIT), (2009).

[101] Global Positioning System, Wikipedia, 2013. Available at: http://en.wikipedia.org/wiki/Global_Positioning_System (last date accessed 12 May 2013).

[102] Gade K., Introduction to Inertial Navigation and Kalman Filtering, Tutorial for IAIN World Congress, Stockholm (2009).

[103] Leica Geosystems, 2013. Available at: http://www.leica-geosystems.us/en/Why-Leica-AT402_81630.htm (last date accessed 22 May 2013).

[104] Bridges, B. and White, D., Laser Trackers: A New Breed of CMM. Available at: http://www.qualitydigest.com/feb98/html/lasertrk.html (last date accessed 22 May 2013).

[105] Voet, A., Cuypers, W., Mingneau, J. and Arras, P., Mobile Measurement Techniques for the Dimensional Analyses and Control of Large Objects by Measuring Individual Points, Nova trendy v knostruovani a v tvorbe technickej dokumentacie, Nitra, 25. Maja (2006).

[106] Lagarias, J.C., Reeds, J.A., Wright, M.H. and Wright, P.E., Convergence Properties of The Nelder-Mead Simplex Method In Low Dimensions, SIAM J. OPTIM, Vol.9, No.1, pp.112-147.

[107] Liu, T., Burner, A.W., Jones, T.W. and Barrows, D.A., Photogrammetric Techniques for Aerospace Applications, Progress in Aerospace Sciences, pp.1-58 (2012).

[108] Canon U.S.A, available at: http://www.usa.canon.com/cusa/support/consumer/ digital_cameras/ other_powershot/powershot_sx110_is_black (last date accessed 22 May 2013).

[109] IRB 140, ABB Product Guide, available at: http://www.abb.us/product/seitp327/7c4717912301eb02c1256efc00278a26.aspx (last date accessed 22 May 2013).

[110] FARO Laser Tracker, available at: http://www.faro.com/en-us/products/metrology/faro-laser-tracker/overview (last date accessed 27 May 2013).

[111] MATLAB, MathWorks, available at: http://www.mathworks.com/products/matlab/ (last date accessed 27 May 2013).

[112] Projection Head Dot Matrix: 7 × 7, Edmund Optics Inc., available at: http://www.edmundoptics.com/lasers/laser-accessories/laser-diode-he-ne-laser-projection-heads/1991 (last date accessed 27 May 2013).

[113] Muralikrishnan, B. and Raja, J., Computational Surface and Roundness Metrology, Springer publishing, pp.193, (2009).

[114] Maisano, D.A, Jamshidi, J., Franceschini, F., Maropoulos, P.G., Mileham, A.T. and Owen, G.W., Indoor GPS: system functionality and initial performance evaluation, Int. J. Manufacturing Research, Vol. 3, No. 3, pp.335-349, (2008).

[115] Nikon Metrology, Product Literature, Available at: http://www.nikonmetrology.com/Products/Large-Volume-Applications/iGPS/ (last date accessed 19 June 2013).

[116] The Metris Inc., Product Literature, Available at: http://www.metris.com/downloads/393.metrology_guide_eng_0409.pdf (last date accessed 19 June 2013).

[117] IS-900 Tracking System, InterSense. Available at : www.intersnese.com/pages/20/14 (last date accessed 19 June 2013).

[118] Cumani, A. and Guiducci, A., Geometric camery calibration: the virtual camera approach, Machine Vision and Applications, 8:375-384(1995).

[119] Putze, T., Geometric modelling and calibration of a virtual four-headed high speed camera-mirror system for 30D motion analysis applications, Grun/Kahmen, Optical 3-D Measurement Techniques VII. II, pp.167-174 (2005).

[120] Hastedt, H., Luhmann, T., Raguse, K., Three dimensional acquisition of high-dynamic processes with a single-camera system and a stereo-beam splitting, Grun/Kahmen, Optical 3-D Measurement Techniques VII, Vol. II, pp. 175-184 (2005).

[121] Mass, H.G., Concepts of single highspeed-camera photogrammetric 3D measurement systems, Proc. Of SPIE Videometrics IX (IS&SPIE 19. Annual Symposium Electronic Imaging), Vol. 6491 (2007).

[122] JCGM 100:2008, Evaluation of measurement data-Guide to the expression of uncertainty in measurement (GUM) (2008).

[123] ISO 9283: 1998(E), Manipulating industrial robots-Performance criteria and related test methods (1998).

[124] Renishaw Inc., Product Literature, XL-80 laser system brochure. Available at: http://www.renishaw.com/en/laser-calibration-and-telescoping-ballbar--6330 (last date accessed 02 July 2013).

[125] NIST Technical Note 1297 1994 Edition, Guidelines for Evaluating and Expressing the Uncertainty of NIST Measurement Results (1994).

[126]Tilch, S., 2012, CLIPS-Development of a Novel Camera and Laser-Based Positioning System (Doctoral dissertation), ETH Zurich.

[127] Lenz R. and Fritsch D., Accuracy of videogrammetry with CCD sensors. ISPRS Journal of Photogrammetry and Remote Sensing (45):90–110 (1990).

[128] Geodetic Systems. Available at:
http://www.geodetic.com/v-stars.aspx (last date accessed 06 Sept. 2013).

[129] JCGM 101:2008, Evaluation of measurement data-Supplement 1 to the "Guide to the expression of uncertainty in measurement"—Propagation of distributions using a Monte Carlo method (2008).

[130] Bowes, K., 2012, Surface form measurements combing beam propagation, optical scattering, and photogrammetry (Thesis), University of North Carolina at Charlotte.

APPENDIX A: LASER SPECKLE AND SPECKLE REDUCTION

A.1 Laser Speckle

Laser light is highly coherent and this property of laser light enables its efficient interference process with applications in many scientific systems. However, this leads to a significant drawback for applications that use a light detector. When a laser beam is scattered from a rough surface, each point on the illuminated rough surface acts as a source of secondary spherical waves. Many of these scattered waves with the same frequency but different phases and amplitudes interference with each other, and therefore a random intensity pattern occurs, which is known as speckle pattern. Figure A.1 (a) show an image of a speckle pattern and Figure A.1 (b) shows its corresponding intensity profile.

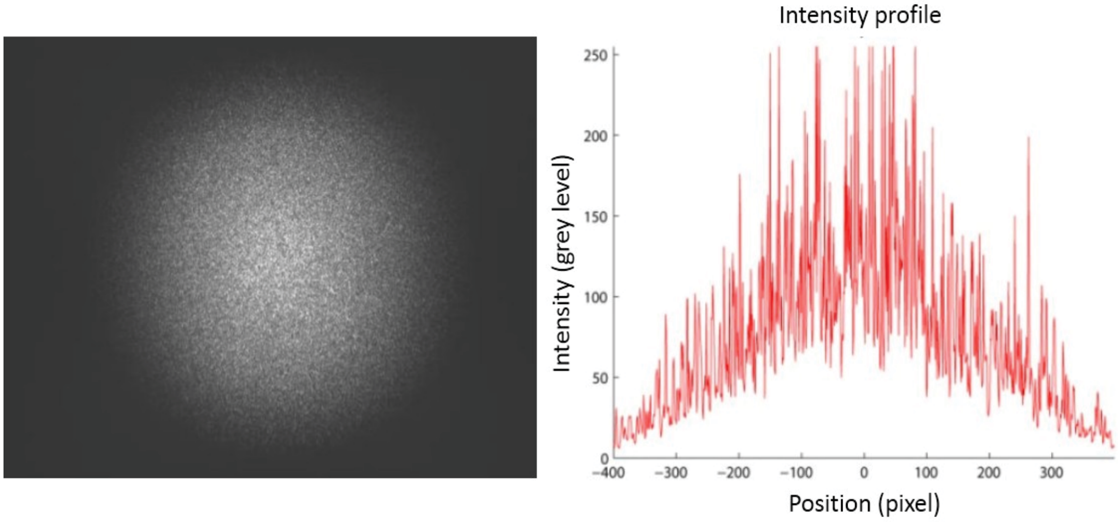

(a) (b)

Figure A.1: (a) Image of a speckle pattern on a CCD camera, (b) measured intensity profile on a horizontal axis through the spots center.

A.2 Speckle Reduction

Necessity for laser speckle reduction was well recognized and different methods have been developed to reduce speckle. These methods includes modulating a laser beam with ultrasonic waves [96], using a moving diffuser associated with a motionless diffuser [97], using several lasers with different wavelengths and incident angles for illumination [98], using changing Hadamard phase patterns inside each detector resolution cell at the intermediate image plane [99,100] Most of these methods are based on the principle of producing an incoherent superposition of several images with statistically independent speckle patterns. In reference [101], these methods are divided into four categories depending on how the superimposed speckle patterns are mutually decorrelated. These four categories are wavelength decorrelation, spatial decorrelation, angular decorrelation and scrambling techniques. Among all the methods for speckle reduction, the moving diffuser method [97] based on spatial decorrelation is recognized as the most effective method. In the proposed system, a moving diffuser was employed to produce a superposition of different speckle patterns over a short period of camera exposure time so that the cameras capture the averaged patterns and hence the speckle can be effectively reduced.

Speckle can be quantified by its speckle contrast value, C, which is defined as the standard deviation of the intensity I_i within a certain area normalized by its mean value I_{mean} as given by equation (A.1),

$$C = \frac{\sqrt{\frac{1}{N}\sum_{i=1}^{N}(I_i - \mathrm{I}_{mean})^2}}{\mathrm{I}_{mean}} \tag{A.1}$$

with

$$\mathrm{I}_{\mathrm{m}ean} = \frac{1}{N}\sum_{i=1}^{N} I_i \tag{A.2}$$

The value of speckle contrast varies between 0 and 1. For images with a small influence of speckle, this value is close to 0.

At a microscopic level, the wavelength of the laser light and the polarization state of the laser light affect the speckle contrast. These two factors together with the properties of the illuminated surface contribute to the speckle process. For a laser with fixed wavelength and state of polarization, the lower the roughness of the illumination surface, the smaller is the speckle contrast. On the other hand, for a fixed surface, the larger the wavelength, the lower is the speckle contrast. At a macroscopic level, the speckle contrast depends on the diffusion angle of the diffuser and the numerical aperture of the detection system. For this later case the reduction factor can be given by (A.3), where $\theta$is the diffusion angle and Ω is the numerical aperture of the detection system.

$$f = \sqrt{\frac{\theta}{\Omega}} \tag{A.3}$$

The purpose of speckle reduction is to reduce the centroid variance of laser dot target in image plane so that direct photogrammetric measurement accuracy on laser dot centroid can be improved. The changes of these two parameters are investigated after speckle reduction.

The efficiency of speckle reduction depends on a number of parameters including motion speed of the diffuser, diffuser structure, exposure time of the camera, and the optical system layout (beam diameter, position of diffuser and additional optics). The higher the motion speed of the diffuser, the more patterns can be overlapped during the exposure time of the camera. The speckle reduction efficiency is proportional to the number of structures passing under the laser dot during exposure time. The addition of N uncorrelated speckle patterns yield a reduction of speckle contrast by 1/SQRT (N). Therefore, the speckle reduction efficiency is also proportional to the size of the laser beam. The goal is thus to create as many uncorrected speckle pattern as possible. Apart from moving the diffuser as much and as fast as possible (high motion speed), this can be influenced by optimizing the structure of the diffuser. The reduction efficiency is better with smaller structures. But that means higher angles, which again leads to a trade-off with beam divergence.

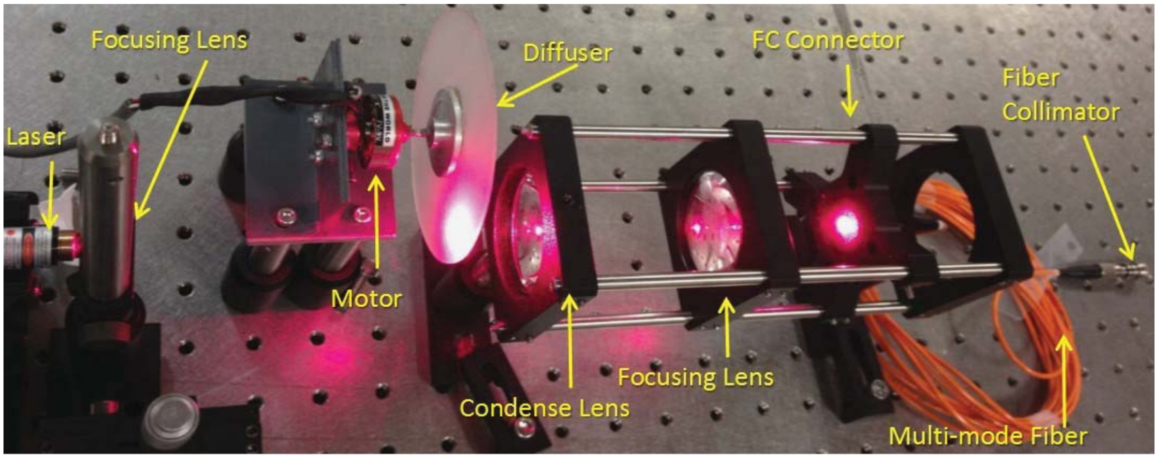

Figure A.2: The experimental setup of laser speckle reduction.

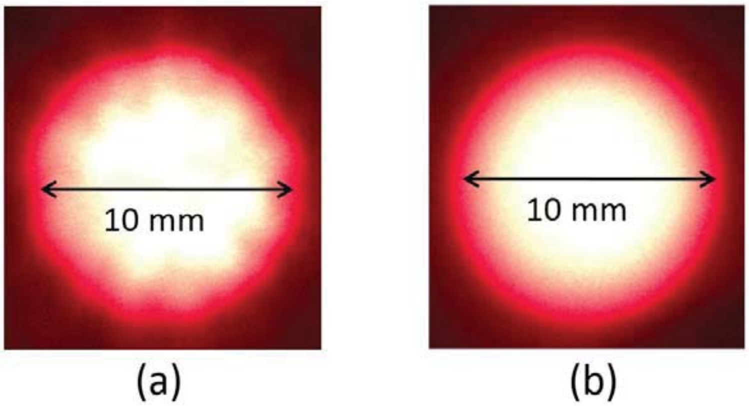

Figure A.3: The images of the laser dot on the drywall (a) The laser dot without using rotating diffuser, (b) the laser dot with rotating diffuser.

Table A.1: Specification of the motor FC 28-05.

Weight (g)	26
Shaft (mm)	3
Motor Length (mm)	37
Diameter (mm)	28
Stator Size	22 × 5
Voltage (v)	7.4
Kv (RPM/V)	2840

An experimental setup was proposed to reduce the laser speckle in the proposed metrology system by employing a rotating diffuser, as shown in Figure A.2. The laser beam was first focused on the diffuser, which is mounted to a motor. In the preliminary test, a 50 mm diameter 120 grit ground grass diffuser (NT83-420) was used and the motor is FC 28-05 brushless outrunner with specification shown in Table A.1. The diffused light passing the diffuser was collected by a condense lens with a diameter of 50 mm and an effective focal length of 44 mm (NT43-593). A bi-convex lens with diameter of 48 mm (f=?) was placed after the condense lens to focus the laser beam into a multimode fiber with a diameter of 50 μm. The multimode fiber was mounted to the cage system through a FC connector. On the output end an adjustable focus FC collimator (CFC-11X-C) was mounted to the fiber with a focal length around 11 mm. The investigation was focused on the effect of the rotating diffuser on the uncertainty of the laser dot centroid on the drywall. In order to optimize the reduction of laser speckle, the laser is collimated first before it passes through the diffuse and the diffuser is positioned perpendicular to the optical axis. Figure A.3 shows the images of the laser dot on the drywall 1 m away from the fiber before and after applying the rotating diffuser. As shown in Figure A.3, the shape of the laser dot after applying the rotating diffuser is much more uniform than the one without using the rotating diffuser.

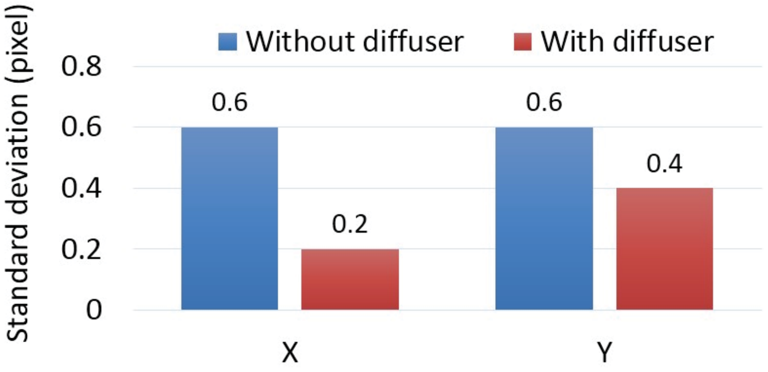

Figure A.4: The standard deviation of the dot centroid w & wt the diffuser in 2D image coordinate system.

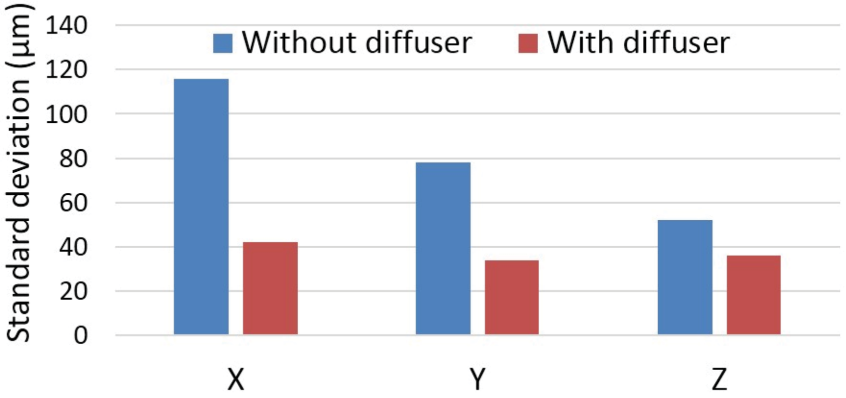

Figure A.5: The standard deviation of the dot centroid w & wt the diffuser in 3D global coordinate system.

The effect of the rotating diffuser was first investigated by using a CCD camera to view the laser dot on the drywall surface 1 m away from the fiber collimator. A total of 20 images of the laser dot were taken with 10 second intervals and the centroid of coded target is determined by PhotoModeler® using LSM (least-square-matching) method. The standard deviations of the centroid variations in the x and y directions in the images before and after applying the rotating diffuser are shown in Figure A.3. As illustrated in Figure A.4, the standard deviations of the dot centroid were reduced from 0.6 pixel to 0.2 pixel in x direction and from 0.6 pixel to 0.4 pixel in y direction by using the rotating diffuser. By using three cameras to capture three images of the laser dot from different locations and orientations, the 3D coordinate of the dot centroid can be determined through photogrammetric measurement. The standard deviations of the dot centroid in 3D spatial space before and after applying the rotating diffuser were shown in Figure A.4. It is shown in Figure A.4 that the standard deviations of the dot centroid were reduced from 118 µm, 79 µm and 54 µm to 42 µm, 36 µm and 38 µm in x, y and z directions respectively. The overall uncertainty with the rotating diffuser is about 56% less than that without the rotating diffuser. These results proved that the uncertainty of the dot centroid can be reduced by using rotating diffuser to reduce the laser speckle.

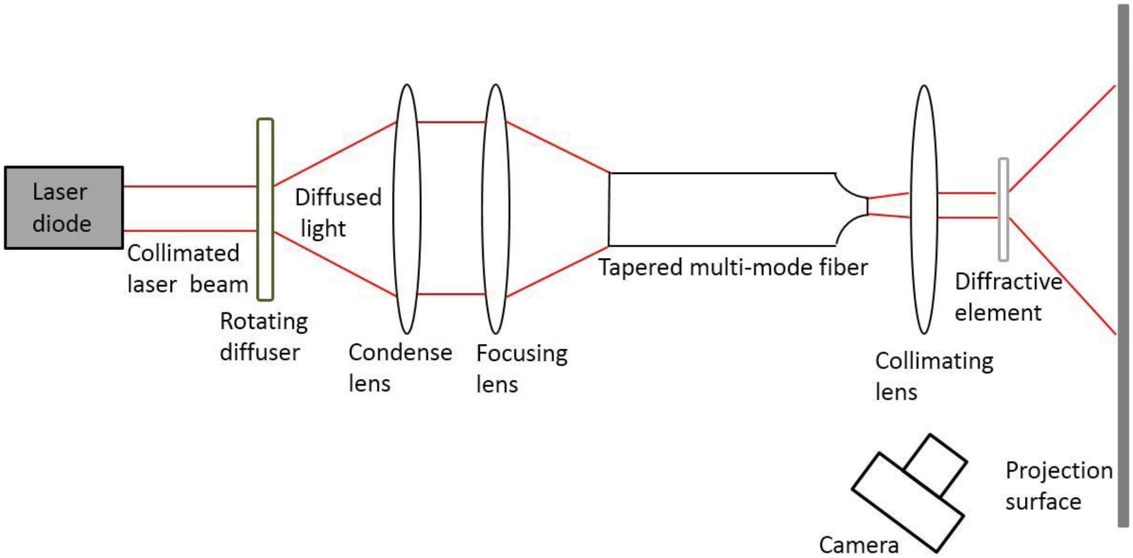

Figure A.6: Laser speckle reduction setup.

The experimental test on laser speckle reduction indicates that the measurement uncertainty of the proposed metrology system discussed in this dissertation can be further reduced by including the laser speckle reduction setup in the module design (see Figure A.5). Due to the fact that an imaging system collecting light from a diffuse source into a fiber cannot collect more than could be collected by butt coupling, a multimode fiber with large diameter and large value of NA (numerical aperture) is preferred considering the coupling efficiency. However, on the output end a multimode fiber with small diameter and small value of NA is preferred in order to get a well collimated laser beam. This limitation can be overcome by using a tapered multimode fiber with large diameter end as the input and the tapered end as the output. Due to the lack of tapered large diameter fiber, the laser speckle reduction setup was not included in the module discussed in this dissertation.

APPENDIX B: VALUES OF CALIBRATED REFERENCE ANGLES

B.1 Values of 110 Calibrated Horizontal Reference Angles

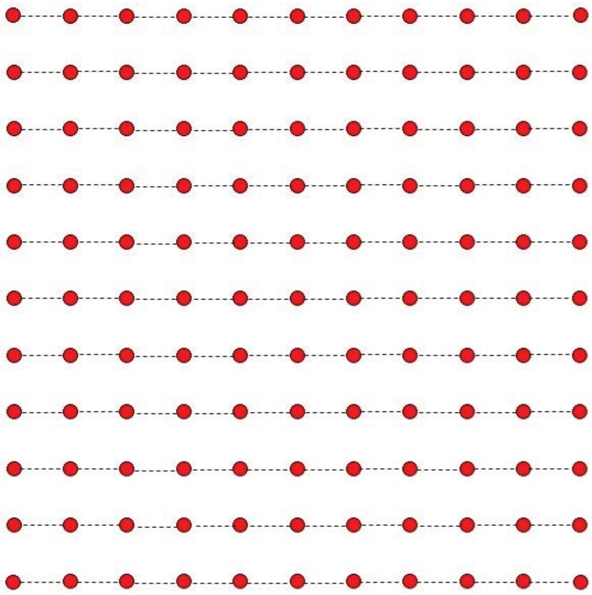

Figure B.1: Diagram of 11 × 11 optical pattern with 110 horizontal reference angles shown.

Table B.1 Values of 110 Calibrated horizontal reference angles shown in Figure B.1. Unit: degree

2.772	2.822	2.860	2.886	2.899	2.899	2.886	2.860	2.822	2.772
2.800	2.851	2.890	2.917	2.931	2.931	2.917	2.890	2.851	2.800
2.822	2.874	2.914	2.942	2.956	2.956	2.942	2.914	2.874	2.822
2.838	2.891	2.932	2.960	2.975	2.975	2.960	2.932	2.891	2.838
2.848	2.901	2.943	2.971	2.986	2.986	2.971	2.943	2.901	2.848
2.851	2.905	2.946	2.975	2.990	2.990	2.975	2.946	2.905	2.851
2.848	2.901	2.943	2.971	2.986	2.986	2.971	2.943	2.901	2.848
2.838	2.891	2.932	2.960	2.975	2.975	2.960	2.932	2.891	2.838
2.822	2.874	2.914	2.942	2.956	2.956	2.942	2.914	2.874	2.822
2.800	2.851	2.890	2.917	2.931	2.931	2.917	2.890	2.851	2.800
2.772	2.822	2.860	2.886	2.899	2.899	2.886	2.860	2.822	2.772

B.2 Values of 110 Calibrated Vertical Reference Angles

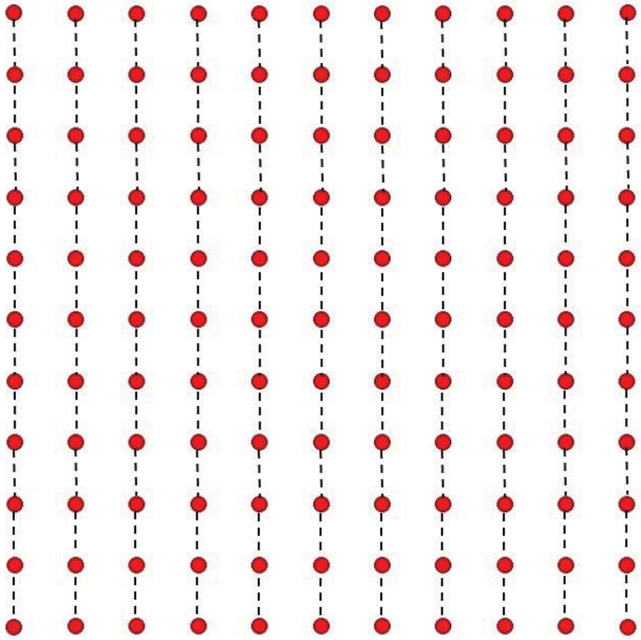

Figure B.2: Diagram of 11 × 11 optical pattern with 110 horizontal reference angles shown.

Table B.2 Values of 110 Calibrated vertical reference angles shown in Figure B.2. Unit: degree

2.772	2.800	2.822	2.838	2.848	2.851	2.848	2.838	2.822	2.800	2.772
2.822	2.851	2.874	2.891	2.901	2.905	2.901	2.891	2.874	2.851	2.822
2.860	2.890	2.914	2.932	2.943	2.946	2.943	2.932	2.914	2.890	2.860
2.886	2.917	2.942	2.960	2.971	2.975	2.971	2.960	2.942	2.917	2.886
2.899	2.931	2.956	2.975	2.986	2.990	2.986	2.975	2.956	2.931	2.899
2.899	2.931	2.956	2.975	2.986	2.990	2.986	2.975	2.956	2.931	2.899
2.886	2.917	2.942	2.960	2.971	2.975	2.971	2.960	2.942	2.917	2.886
2.860	2.890	2.914	2.932	2.943	2.946	2.943	2.932	2.914	2.890	2.860
2.822	2.851	2.874	2.891	2.901	2.905	2.901	2.891	2.874	2.851	2.822
2.772	2.800	2.822	2.838	2.848	2.851	2.848	2.838	2.822	2.800	2.772

B.3 Values of 200 Calibrated Diagonal Reference Angles

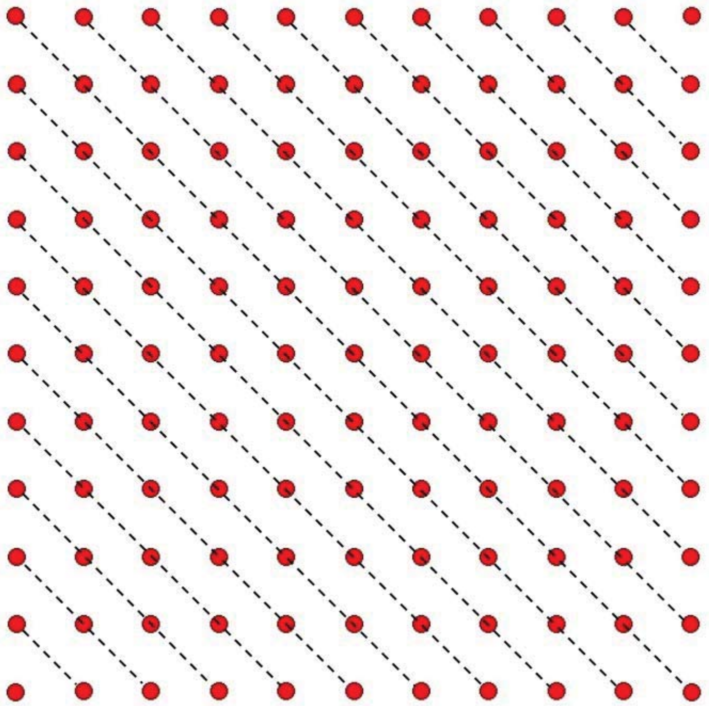

Figure B.3: Diagram of 11 × 11 optical pattern with 100 diagonal reference angles shown.

Table B.3 Values of 100 calibrated diagonal reference angles shown in Figure B.3. Unit: degree

3.851	3.922	3.983	4.031	4.066	4.087	4.093	4.085	4.063	4.028
3.922	3.992	4.050	4.095	4.126	4.143	4.145	4.131	4.104	4.063
3.983	4.050	4.105	4.146	4.173	4.186	4.182	4.164	4.131	4.085
4.031	4.095	4.146	4.184	4.206	4.214	4.206	4.182	4.145	4.093
4.066	4.126	4.173	4.206	4.224	4.227	4.214	4.186	4.143	4.087
4.087	4.143	4.186	4.214	4.227	4.224	4.206	4.173	4.126	4.066
4.093	4.145	4.182	4.206	4.214	4.206	4.184	4.146	4.095	4.031
4.085	4.131	4.164	4.182	4.186	4.173	4.146	4.105	4.050	3.983
4.063	4.104	4.131	4.145	4.143	4.126	4.095	4.050	3.992	3.922
4.028	4.063	4.085	4.093	4.087	4.066	4.031	3.983	3.922	3.851

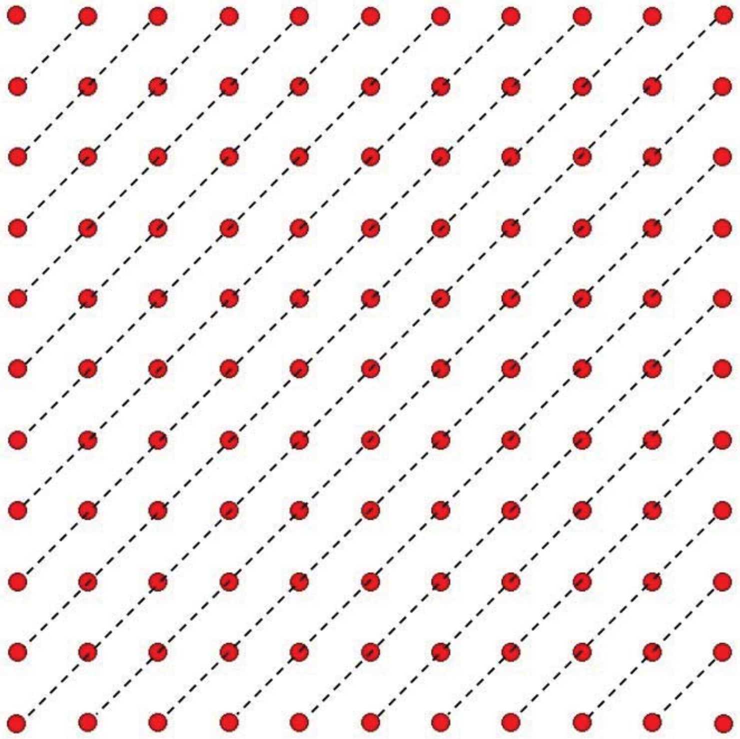

Figure B.4: Diagram of 11 × 11 optical pattern with 100 diagonal reference angles shown.

Table B.4 Values of 100 calibrated diagonal reference angles shown in Figure B.4. Unit: degree

4.028	4.063	4.085	4.093	4.087	4.066	4.031	3.983	3.922	3.851
4.063	4.104	4.131	4.145	4.143	4.126	4.095	4.050	3.992	3.922
4.085	4.131	4.164	4.182	4.186	4.173	4.146	4.105	4.050	3.983
4.093	4.145	4.182	4.206	4.214	4.206	4.184	4.146	4.095	4.031
4.087	4.143	4.186	4.214	4.227	4.224	4.206	4.173	4.126	4.066
4.066	4.126	4.173	4.206	4.224	4.227	4.214	4.186	4.143	4.087
4.031	4.095	4.146	4.184	4.206	4.214	4.206	4.182	4.145	4.093
3.983	4.050	4.105	4.146	4.173	4.186	4.182	4.164	4.131	4.085
3.922	3.992	4.050	4.095	4.126	4.143	4.145	4.131	4.104	4.063
3.851	3.922	3.983	4.031	4.066	4.087	4.093	4.085	4.063	4.028

APPENDIX C: OPTICAL PATTERN GENERATION CODE

```
function [a,m,angle1,angle2,angle3,angle4] = myscatter( n,d,theta0,ori2)

%   Myscatter function creates a n × n dot matrix on the plane d meters away from the
defined module position ori2. The inter-beam angle of the dot matrix is defined by theta0.
%   The xyz dot coordinates are saved in matrix a.

global x;
global y;
global ori;
global theta;
format long
ori=ori2;
theta=theta0/180*pi;
a=cell(n);
a{(n+1)/2,(n+1)/2}=ori+[0,0,d];

for i=1:(n-1)/2
    a{(n+1)/2-i,(n+1)/2}(1,2)=d*tan(theta*i)+a{(n+1)/2,(n+1)/2}(1,2);
    a{(n+1)/2-i,(n+1)/2}(1,1)=a{(n+1)/2,(n+1)/2}(1,1);
    a{(n+1)/2-i,(n+1)/2}(1,3)=a{(n+1)/2,(n+1)/2}(1,3);
    a{(n+1)/2,(n+1)/2+i}(1,1)=d*tan(theta*i)+a{(n+1)/2,(n+1)/2}(1,1);
    a{(n+1)/2,(n+1)/2+i}(1,2)=a{(n+1)/2,(n+1)/2}(1,2);
    a{(n+1)/2,(n+1)/2+i}(1,3)=a{(n+1)/2,(n+1)/2}(1,3);
end

for j=1:(n-1)/2
    for i=j:(n-1)/2
         for t=1:10
        x=a{(n+1)/2-j,(n+1)/2+i-1};
        y=a{(n+1)/2-j+1,(n+1)/2+i};
        options=optimset('Display','off','TolFun',1e-20);
        a{(n+1)/2-j,(n+1)/2+i}=fsolve(@zuobiao,[(a{(n+1)/2-j,(n+1)/2+i-
1}(1,1)+a{(n+1)/2-j+1,(n+1)/2+i}(1,1))/2+t+d,(a{(n+1)/2-j,(n+1)/2+i-1}(1,2)+a{(n+1)/2-
j+1,(n+1)/2+i}(1,2))/2+t+d,d],options);
        if a{(n+1)/2-j,(n+1)/2+i}(1,1)-(a{(n+1)/2-j,(n+1)/2+i-1}(1,1)+a{(n+1)/2-
j+1,(n+1)/2+i}(1,1))/2>0 && a{(n+1)/2-j,(n+1)/2+i}(1,2)-(a{(n+1)/2-j,(n+1)/2+i-
1}(1,2)+a{(n+1)/2-j+1,(n+1)/2+i}(1,2))/2>0
           a{(n+1)/2-j,(n+1)/2+i}=a{(n+1)/2-j,(n+1)/2+i};break;
        end
        end
    end

    for i=j:(n-1)/2
```

```
        for t=1:10
        x=a{(n+1)/2-i+1,(n+1)/2+j};
        y=a{(n+1)/2-i,(n+1)/2+j-1};
        options=optimset('Display','off','TolFun',1e-20);
        a{(n+1)/2-i,(n+1)/2+j}=fsolve(@zuobiao,[(a{(n+1)/2-
i+1,(n+1)/2+j}(1,1)+a{(n+1)/2-i,(n+1)/2+j-1}(1,1))/2+t+d,(a{(n+1)/2-
i+1,(n+1)/2+j}(1,2)+a{(n+1)/2-i,(n+1)/2+j-1}(1,2))/2+t+d,d],options);
       if a{(n+1)/2-i,(n+1)/2+j}(1,1)-(a{(n+1)/2-i+1,(n+1)/2+j}(1,1)+a{(n+1)/2-i,(n+1)/2+j-
1}(1,1))/2>0 &&a{(n+1)/2-i,(n+1)/2+j}(1,2)-(a{(n+1)/2-i+1,(n+1)/2+j}(1,1)+a{(n+1)/2-
i,(n+1)/2+j-1}(1,1))/2>0
           a{(n+1)/2-i,(n+1)/2+j}=a{(n+1)/2-i,(n+1)/2+j};break;
        end
        end
     end
end
for i=1:(n-1)/2
    for j=0:(n-1)/2
        a{(n+1)/2+i,(n+1)/2+j}(1,1)=a{(n+1)/2-i,(n+1)/2+j}(1,1);
         a{(n+1)/2+i,(n+1)/2+j}(1,2)=2*a{(n+1)/2,(n+1)/2}(1,2)-1*a{(n+1)/2-
i,(n+1)/2+j}(1,2);
         a{(n+1)/2+i,(n+1)/2+j}(1,3)=a{(n+1)/2-i,(n+1)/2+j}(1,3);
    end
end

for i=1:(n+1)/2
    for j=1:(n-1)/2
        a{i,(n-1)/2-j+1}(1,1)=2*a{(n+1)/2,(n+1)/2}(1,1)-1*a{i,(n+1)/2+j}(1,1);
         a{i,(n-1)/2-j+1}(1,2)=a{i,(n+1)/2+j}(1,2);
         a{i,(n-1)/2-j+1}(1,3)=a{i,(n+1)/2+j}(1,3);
    end
end
for i=(n+1)/2+1:n
    for j=1:(n-1)/2
        a{i,(n-1)/2-j+1}(1,1)=2*a{(n+1)/2,(n+1)/2}(1,1)-1*a{i,(n+1)/2+j}(1,1);
         a{i,(n-1)/2-j+1}(1,2)=a{i,(n+1)/2+j}(1,2);
         a{i,(n-1)/2-j+1}(1,3)=a{i,(n+1)/2+j}(1,3);
    end
end

m=zeros(n*n,3);
angle1=zeros(n-1,3);
angle2=zeros(n-1,3);
angle3=zeros(n-1,3);
angle4=zeros(n-1,3);
tt=cell2mat(a);
```

```
for i=1:n
   for j=1:n
      m(n*(i-1)+j,1:3)=tt(i,3*j-2:3*j);
   end
end

% plot the optical pattern
xaxis=m(:,1);
yaxis=m(:,2);
zaxis=m(:,3);
scatter3(xaxis,yaxis,zaxis)

% save coordinates in cdt.txt
dlmwrite('cdt.txt',m, 'delimiter','\t','precision',20)

 % ange1 calculates the diagonal inter-beam angles          *
%                                                              *
% angle2 calculates the diagonal inter-beam angles            *
%                                                         *
% angle3 calculates the vertical inter-beam angles          *
%                                                          *
% angle4 calculates the horizontal inter-beam angles          *    *
for i=1:n-1
   for j=1:n-1
  angle1(i,j)=acos(dot(a{i,j}-ori,a{i+1,j+1}-ori)/(norm(a{i+1,j+1}-ori)*norm(a{i,j}-
ori)))*180/pi;
  angle2(i,j)=acos(dot(a{i,j+1}-ori,a{i+1,j}-ori)/(norm(a{i,j+1}-ori)*norm(a{i+1,j}-
ori)))*180/pi;
   end
end
for i=1:n-1
   for j=1:n-1
  angle3(i,j)=acos(dot(a{i,j}-ori,a{i+1,j}-ori)/(norm(a{i+1,j}-ori)*norm(a{i,j}-
ori)))*180/pi;
  angle4(i,j)=acos(dot(a{i,j}-ori,a{i,j+1}-ori)/(norm(a{i,j}-ori)*norm(a{i,j+1}-
ori)))*180/pi;
   end
end
end
```

```
function F = zuobiao(z)

%  zuobiao calculates the intersections between the diffraction beams and the projection plane.


global x;
global y;
global ori;
global theta;
p1=x-ori;
p2=y-ori;
p3=z-ori;
F(1)=1000000*(cos(theta)-dot(p3,p2)/(norm(p3)*norm(p2)));
F(2)=1000000*(cos(theta)-dot(p3,p1)/(norm(p3)*norm(p1)));
F(3)=p3(1,3)-p2(1,3);
end
```

APPENDIX D: MODULE LOCATION DETERMINATION CODE

```
% Filename:  main_ver3.m

%          cleaned up some of the comments
%          added test on fid for filename     (18-May-2010)
% ==============================================================
% This is the main program that first reads a data file with all of the (x, y, z) data in columns.
% The location is found that minimizes the least-squared value
% ==============================================================
% first clear all data from memory and the command window.

clear; clc;
format long

% read xyz dot coordinates from assigned file
fn=input('filename? ', 's');
fid = fopen(fn, 'r');
if fid < 0
   disp('Bad file name, exiting');
   break
end

pt_data = zeros(3,5);
ptnum = 0;
while 1
  tline = fgetl(fid);
  if ~ischar(tline),   break,   end
%
% The first line below (A) extracts coordinates from the standard
% PhotoModeler output, while the second line (B) will work for a
% generic file of x, y, z values.
%
  [A, count, errmsg, nextindex]=sscanf(tline,'%*s %*s %*s %f %*s %f %*s %f');
  [B, countB, errmsgB, nextindexB]=sscanf(tline,'%f %f %f');
  if count == 3
     disp(A)
     ptnum = ptnum+1;
     pt_data(1:3, ptnum) = A;
  elseif countB == 3
     disp(B)
     ptnum = ptnum+1;
     pt_data(1:3, ptnum) = B;
  end
```

```
end

fclose(fid);
n=ptnum.^0.5
pt_data1=reshape(pt_data,n*3,n);
%pt_data1=reshape(pt_data,21,7);
pt_data2=pt_data1';
r=ones(1,n);
rr=3*ones(1,n);
data11=mat2cell(pt_data2,r,rr);
a=data11;

%  Changed guess to give a better starting point (values in meters)
guess=[1; 1; 1];
options = optimset('Display','iter');

%  We use the built-in optimization 'fminsearch' to minimize the
%  least-squared value defined in one of the following functions:

%  Each of these functions is based on the point data we have read in
%  and the nominal value of 2.9 degrees between the points from the
%  projection head.
%
%  Application note:  We have to implicitly call chisq_value with the
%  known parameters already inside.
%
%  For now, we'll display the progress of the optimization, hence the
%  options chosen above.
OPTIONS = optimset('Display','iter','TolFun',1e-24,'TolX',1e-24);
[x1,fval1] = fminsearch(@(x) chisq_value11exp(11,11,data11,x), guess, OPTIONS)


function [value] = chisq_value11exp(m, n, a, start)
format long
value = 0;
%  This function calculates the least-square value.
%  Note the current example is for an m x n grid of points
%  where we find the angles between each pair of adjacent points.

% diaexp_1.mat, diaexp_2.mat, diaexp_3.mat and diaexp_4.mat saved the
% calibrated inter-beam angles measured in the experiment.
%_1  %              _2      %              _3  %        _4 %  %  %
    %                 %                    %
      %             %                      %
load ('diaexp_1.mat');
```

```
load ('diaexp_2.mat');
load ('diaexp_3.mat');
load ('diaexp_4.mat');

for i=1:n-1
    for j=1:n-1
  angle1(i,j)=acos(dot(a{i,j}-start,a{i+1,j+1}-start)./(norm(a{i+1,j+1}-
start).*norm(a{i,j}-start)))*180/pi;
  value=value+(angle1(i,j)-diaexp_1(i,j))^2;
  angle2(i,j)=acos(dot(a{i,j+1}-start,a{i+1,j}-start)./(norm(a{i,j+1}-
start).*norm(a{i+1,j}-start)))*180/pi;
  value=value+(angle2(i,j)-diaexp_2(i,j))^2;
       end
end
for i=1:n-1
    for j=1:n-1
  angle3(i,j)=acos(dot(a{i,j}-start,a{i+1,j}-start)./(norm(a{i+1,j}-start).*norm(a{i,j}-
start)))*180/pi;
  value=value+(angle3(i,j)-diaexp_3(i,j))^2;
  angle4(i,j)=acos(dot(a{i,j}-start,a{i,j+1}-start)./(norm(a{i,j}-start).*norm(a{i,j+1}-
start)))*180/pi;
  value=value+(angle4(i,j)-diaexp_4(i,j))^2;
    end
end
```

APPENDIX E: VALUES OF REFERENCE ANGLES USED IN MONTE CARLO SIMULATION

E.1 Values of 110 Horizontal Reference Angles Used in Monte Carlo Simulation

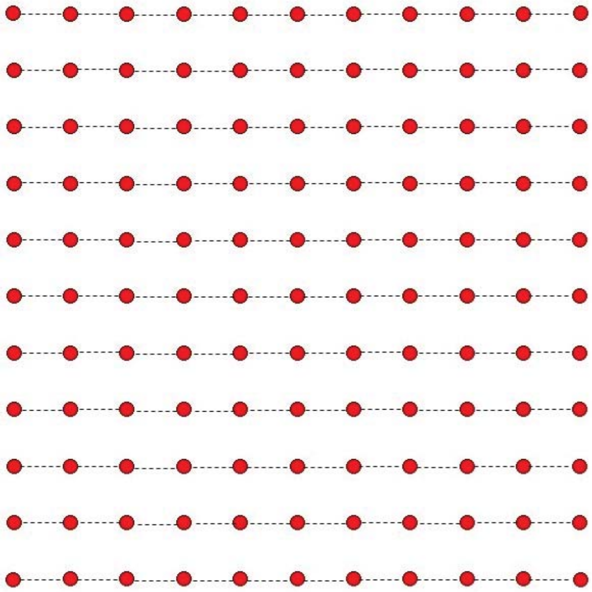

Figure E.1: Diagram of 11 × 11 optical pattern with 110 horizontal reference angles shown.

Table B.1 Values of 110 horizontal reference angles used in Monte Carlo simulation as shown in Figure B.1. Unit: degree

2.900	2.900	2.900	2.900	2.900	2.900	2.900	2.900	2.900	2.900
2.900	2.900	2.900	2.900	2.900	2.900	2.900	2.900	2.900	2.900
2.900	2.900	2.900	2.900	2.900	2.900	2.900	2.900	2.900	2.900
2.900	2.900	2.900	2.900	2.900	2.900	2.900	2.900	2.900	2.900
2.900	2.900	2.900	2.900	2.900	2.900	2.900	2.900	2.900	2.900
2.900	2.900	2.900	2.900	2.900	2.900	2.900	2.900	2.900	2.900
2.900	2.900	2.900	2.900	2.900	2.900	2.900	2.900	2.900	2.900
2.900	2.900	2.900	2.900	2.900	2.900	2.900	2.900	2.900	2.900
2.900	2.900	2.900	2.900	2.900	2.900	2.900	2.900	2.900	2.900
2.900	2.900	2.900	2.900	2.900	2.900	2.900	2.900	2.900	2.900
2.900	2.900	2.900	2.900	2.900	2.900	2.900	2.900	2.900	2.900

E.2 Values of 110 Vertical Reference Angles Used in Monte Carlo Simulation

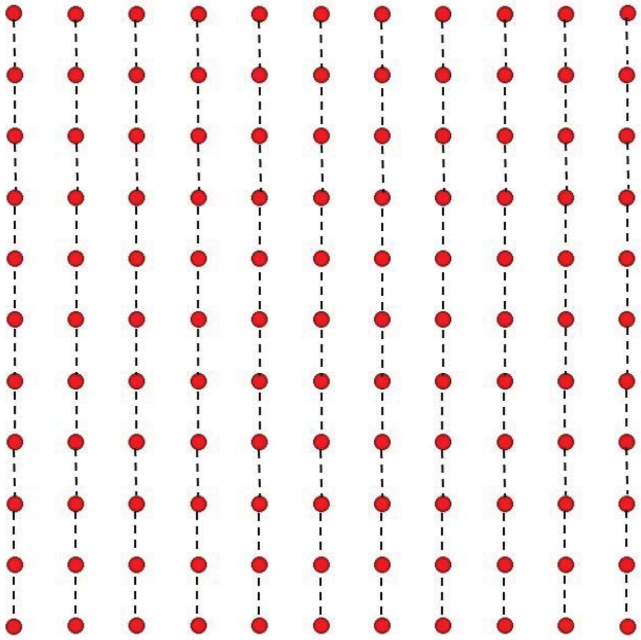

Figure E.2: Diagram of 11 × 11 optical pattern with 110 horizontal reference angles shown.

Table E.2 Values of 110 vertical reference angles used in Monte Carlo simulation as shown in Figure E.2. Unit: degree

2.900	2.900	2.900	2.900	2.900	2.900	2.900	2.900	2.900	2.900	2.900
2.900	2.900	2.900	2.900	2.900	2.900	2.900	2.900	2.900	2.900	2.900
2.900	2.900	2.900	2.900	2.900	2.900	2.900	2.900	2.900	2.900	2.900
2.900	2.900	2.900	2.900	2.900	2.900	2.900	2.900	2.900	2.900	2.900
2.900	2.900	2.900	2.900	2.900	2.900	2.900	2.900	2.900	2.900	2.900
2.900	2.900	2.900	2.900	2.900	2.900	2.900	2.900	2.900	2.900	2.900
2.900	2.900	2.900	2.900	2.900	2.900	2.900	2.900	2.900	2.900	2.900
2.900	2.900	2.900	2.900	2.900	2.900	2.900	2.900	2.900	2.900	2.900
2.900	2.900	2.900	2.900	2.900	2.900	2.900	2.900	2.900	2.900	2.900
2.900	2.900	2.900	2.900	2.900	2.900	2.900	2.900	2.900	2.900	2.900

E.3 Values of 200 Diagonal Reference Angles Used in Monte Carlo Simulation

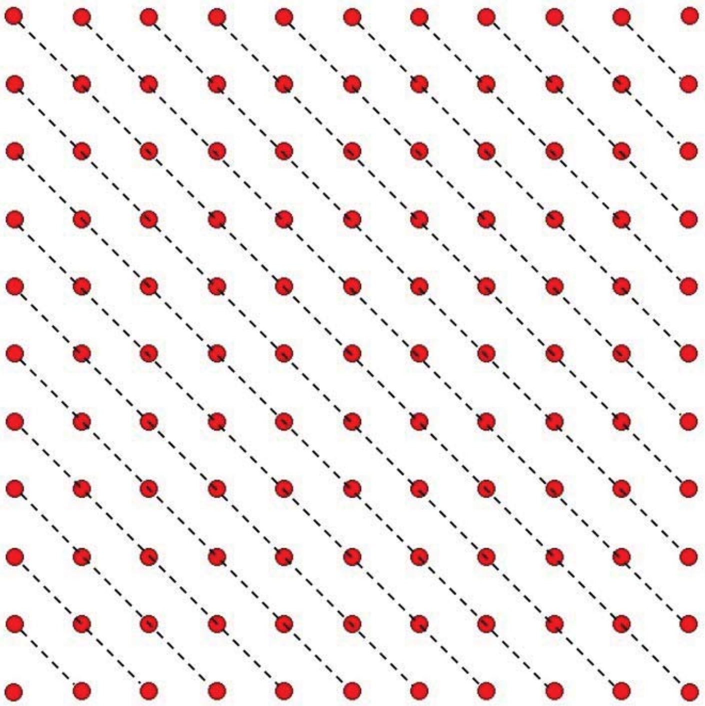

Figure E.3: Diagram of 11 × 11 optical pattern with 100 diagonal reference angles shown.

Table E.3 Values of 100 diagonal reference angles used in Monte Carlo simulation as shown in Figure E.3. Unit: degree

4.207	4.184	4.160	4.137	4.113	4.090	4.066	4.042	4.018	3.994
4.184	4.166	4.147	4.129	4.111	4.092	4.074	4.055	4.037	4.018
4.160	4.147	4.134	4.121	4.108	4.095	4.082	4.069	4.055	4.042
4.137	4.129	4.121	4.113	4.106	4.098	4.090	4.082	4.074	4.066
4.113	4.111	4.108	4.106	4.103	4.100	4.098	4.095	4.092	4.090
4.090	4.092	4.095	4.098	4.100	4.103	4.106	4.108	4.111	4.113
4.066	4.074	4.082	4.090	4.098	4.106	4.113	4.121	4.129	4.137
4.042	4.055	4.069	4.082	4.095	4.108	4.121	4.134	4.147	4.160
4.018	4.037	4.055	4.074	4.092	4.111	4.129	4.147	4.166	4.184
3.994	4.018	4.042	4.066	4.090	4.113	4.137	4.160	4.184	4.207

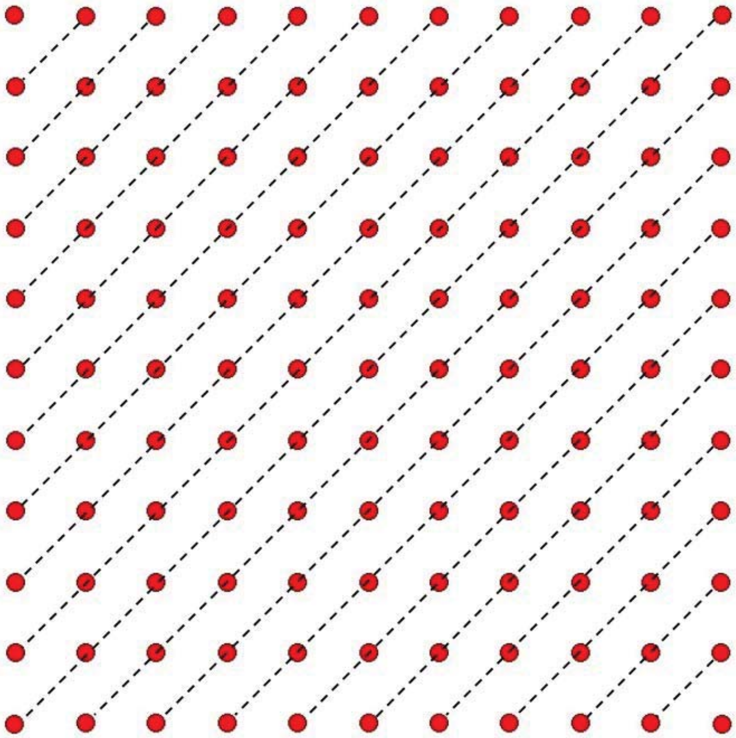

Figure E.4: Diagram of 11 × 11 optical pattern with 100 diagonal reference angles shown.

Table E.4 Values of 100 diagonal reference angles used in Monte Carlo simulation as shown in Figure E.4. Unit: degree

3.994	4.018	4.042	4.066	4.090	4.113	4.137	4.160	4.184	4.207
4.018	4.037	4.055	4.074	4.092	4.111	4.129	4.147	4.166	4.184
4.042	4.055	4.069	4.082	4.095	4.108	4.121	4.134	4.147	4.160
4.066	4.074	4.082	4.090	4.098	4.106	4.113	4.121	4.129	4.137
4.090	4.092	4.095	4.098	4.100	4.103	4.106	4.108	4.111	4.113
4.113	4.111	4.108	4.106	4.103	4.100	4.098	4.095	4.092	4.090
4.137	4.129	4.121	4.113	4.106	4.098	4.090	4.082	4.074	4.066
4.160	4.147	4.134	4.121	4.108	4.095	4.082	4.069	4.055	4.042
4.184	4.166	4.147	4.129	4.111	4.092	4.074	4.055	4.037	4.018
4.207	4.184	4.160	4.137	4.113	4.090	4.066	4.042	4.018	3.994

APPENDIX F: MONTE CARLO SIMULATION CODE

```
% This is the main function for Monte Carlo simulation.
n=input('please input n:')
d=input('please input Initial distance:')
theta0=input('please input Initial interbeam angle:')
ori2=input('please input The origin:')
[a,m] = myscatter( n,d,theta0,ori2)
datacov
% the (x, y, z) of the dot are generated by myscater function and saved in
% the file nt.txt.
b=textread('nt.txt');
b=readaa(b);
s=input('please input the random noise size on dot')
sa=input('please input the random noise size on angle')
sau=input('please input the uniform noise size on angle')
iter=input('please input the iteration times:')
start=input('please input the The initial iteration points:')
tic
devar=myvar_ru(n,s,sa,sau,b,iter,start)
toc
```

```
function datacov
% convert experimental data into the form can be used in the
fid = fopen('cdt.txt', 'r');
if fid < 0
    disp('Bad file name, exiting');
    return
end

pt_data = zeros(3,3);
ptnum = 0;
while 1
   tline = fgetl(fid);
   if ~ischar(tline),   break,   end
%
%  The first line below (A) extracts coordinates from the standard
%  PhotoModeler output, while the second line (B) will work for a
%  generic file of x, y, z values.
%
   [A, count, errmsg, nextindex]=sscanf(tline,'%*s %*s %*s %f %*s %f %*s %f');
   [B, countB, errmsgB, nextindexB]=sscanf(tline,'%f %f %f');
   if count == 3
```

```
    disp(A)
    ptnum = ptnum+1;
    pt_data(1:3, ptnum) = A;
  elseif countB == 3
    disp(B)
    ptnum = ptnum+1;
    pt_data(1:3, ptnum) = B;
  end

end
n=ptnum.^(0.5);
pt_data1=reshape(pt_data,n*3,n);
pt_data2=pt_data1';
r=ones(1,n);
rr=3*ones(1,n);
data=mat2cell(pt_data2,r,rr);
dlmwrite('nt.txt', data, 'delimiter','\t', 'precision',20)



function devar=myvar_ru(n,s,sa,sau,b,iter,start)
% myvar_ru function calculates the locations of the module repeatedly and the standard
deviation of the module is also reported.

load('angles_montecarlo.mat');
 % all the inter-beam angles are saved in angles_montecarlo.mat and the values are
shown in APPENDIX E.

bb=cell(n);
cx=randn(n,n,iter);
cy=randn(n,n,iter);
cz=randn(n,n,iter);
a1=randn(n,n,iter);
a2=randn(n,n,iter);
a3=randn(n-1,n,iter);
a4=randn(n,n-1,iter);
uni=(rand(iter,1)-0.5).*2;


for m=1:iter
% add random noise to dot coordinates in xyz
for i=1:n
   for j=1:n
      bb{i,j}(1,1)=b{i,j}(1,1)+s*cx(i,j,m);
      bb{i,j}(1,2)=b{i,j}(1,2)+s*cy(i,j,m);
      bb{i,j}(1,3)=b{i,j}(1,3)+s*cz(i,j,m);
```

```
    end

end

% add noise to angle1 and angle2
for i=1:n-1
    for j=1:n-1
        angle1n(i,j)=angle1(i,j)+sa*a1(i,j,m)+sau*uni(m);
        angle2n(i,j)=angle2(i,j)+sa*a2(i,j,m)+sau*uni(m);
    end

end
% add noise to angle3
for i=1:n-1
    for j=1:n
   angle3n(i,j)=angle3(i,j)+sa*a3(i,j,m)+sau*uni(m);

    end
end
% add noise to angle4
for i=1:n
    for j=1:n-1
   angle4n(i,j)=angle4(i,j)+sa*a4(i,j,m)+sau*uni(m);

    end
end

OPTIONS = optimset('Display', 'iter','TolFun',1e-24,'TolX',1e-24,'MaxIter',1000);

[x(m,:),fval]= fminsearch(@(x)chisq_MonteCarlo(n,bb,
angle1n,angle2n,angle3n,angle4n,x),start,OPTIONS)
devar=var(x);
dlmwrite('dotcoordinates.txt',x, 'delimiter','\t','precision',20)
end

% calculates the standard deviation, the mean value and the variation of the module
position
std=devar.^(0.5)
meanvalue=mean(x)
range=max(x)-min(x)
dlmwrite('std02.txt',std, 'delimiter','\t','precision',20)
dlmwrite('meanvalue02.txt',meanvalue, 'delimiter','\t','precision',20)
dlmwrite('range02.txt',range, 'delimiter','\t','precision',20)
```

APPENDIX G: VIRTUAL IMAGE GENERATION CODE

```
function [a,m] = virtualimage( n,d,theta0,ori2)
%  This function creates an virtual image with defined module location, the projection
plane, the inter-beam angles.
%   n represents the length of the scattered dot matrix you want to
%   plot, d represents the distance between the scattered dot matrix and
%   light source,theta0 represents the included angle,ori2 stands for the module location,
please enter them in order
%   for example,[a,m]=fourthimage(11,2,2.9,[0 0 0]). a and m are the solution matrix.

global x;
global y;
global ori;
global theta;
ori=ori2;
theta=theta0/180*pi;
a=cell(n);
a{(n+1)/2,(n+1)/2}=ori+[0,0,d];

for i=1:(n-1)/2
   a{(n+1)/2-i,(n+1)/2}(1,2)=d*tan(theta*i)+a{(n+1)/2,(n+1)/2}(1,2);
   a{(n+1)/2-i,(n+1)/2}(1,1)=a{(n+1)/2,(n+1)/2}(1,1);
   a{(n+1)/2-i,(n+1)/2}(1,3)=a{(n+1)/2,(n+1)/2}(1,3);
   a{(n+1)/2,(n+1)/2+i}(1,1)=d*tan(theta*i)+a{(n+1)/2,(n+1)/2}(1,1);
   a{(n+1)/2,(n+1)/2+i}(1,2)=a{(n+1)/2,(n+1)/2}(1,2);
   a{(n+1)/2,(n+1)/2+i}(1,3)=a{(n+1)/2,(n+1)/2}(1,3);
end

for j=1:(n-1)/2
   for i=j:(n-1)/2
       for t=1:10
      x=a{(n+1)/2-j,(n+1)/2+i-1};
      y=a{(n+1)/2-j+1,(n+1)/2+i};
      a{(n+1)/2-j,(n+1)/2+i}=fsolve(@zuobiao,[(a{(n+1)/2-j,(n+1)/2+i-
1}(1,1)+a{(n+1)/2-j+1,(n+1)/2+i}(1,1))/2+t+d,(a{(n+1)/2-j,(n+1)/2+i-1}(1,2)+a{(n+1)/2-
j+1,(n+1)/2+i}(1,2))/2+t+d,d]);
      if a{(n+1)/2-j,(n+1)/2+i}(1,1)-(a{(n+1)/2-j,(n+1)/2+i-1}(1,1)+a{(n+1)/2-
j+1,(n+1)/2+i}(1,1))/2>0 && a{(n+1)/2-j,(n+1)/2+i}(1,2)-(a{(n+1)/2-j,(n+1)/2+i-
1}(1,2)+a{(n+1)/2-j+1,(n+1)/2+i}(1,2))/2>0
         a{(n+1)/2-j,(n+1)/2+i}=a{(n+1)/2-j,(n+1)/2+i};break;
      end
      end
   end
```

```
    for i=j:(n-1)/2
        for t=1:10
        x=a{(n+1)/2-i+1,(n+1)/2+j};
        y=a{(n+1)/2-i,(n+1)/2+j-1};
        a{(n+1)/2-i,(n+1)/2+j}=fsolve(@zuobiao,[(a{(n+1)/2-
i+1,(n+1)/2+j}(1,1)+a{(n+1)/2-i,(n+1)/2+j-1}(1,1))/2+t+d,(a{(n+1)/2-
i+1,(n+1)/2+j}(1,2)+a{(n+1)/2-i,(n+1)/2+j-1}(1,2))/2+t+d,d]);
       if a{(n+1)/2-i,(n+1)/2+j}(1,1)-(a{(n+1)/2-i+1,(n+1)/2+j}(1,1)+a{(n+1)/2-i,(n+1)/2+j-
1}(1,1))/2>0 &&a{(n+1)/2-i,(n+1)/2+j}(1,2)-(a{(n+1)/2-i+1,(n+1)/2+j}(1,1)+a{(n+1)/2-
i,(n+1)/2+j-1}(1,1))/2>0
           a{(n+1)/2-i,(n+1)/2+j}=a{(n+1)/2-i,(n+1)/2+j};break;
        end
        end
     end
end
for i=1:(n-1)/2
    for j=0:(n-1)/2
        a{(n+1)/2+i,(n+1)/2+j}(1,1)=a{(n+1)/2-i,(n+1)/2+j}(1,1);
         a{(n+1)/2+i,(n+1)/2+j}(1,2)=2*a{(n+1)/2,(n+1)/2}(1,2)-1*a{(n+1)/2-
i,(n+1)/2+j}(1,2);
         a{(n+1)/2+i,(n+1)/2+j}(1,3)=a{(n+1)/2-i,(n+1)/2+j}(1,3);
    end
end

for i=1:(n+1)/2
    for j=1:(n-1)/2
        a{i,(n-1)/2-j+1}(1,1)=2*a{(n+1)/2,(n+1)/2}(1,1)-1*a{i,(n+1)/2+j}(1,1);
         a{i,(n-1)/2-j+1}(1,2)=a{i,(n+1)/2+j}(1,2);
         a{i,(n-1)/2-j+1}(1,3)=a{i,(n+1)/2+j}(1,3);
    end
end
for i=(n+1)/2+1:n
    for j=1:(n-1)/2
        a{i,(n-1)/2-j+1}(1,1)=2*a{(n+1)/2,(n+1)/2}(1,1)-1*a{i,(n+1)/2+j}(1,1);
         a{i,(n-1)/2-j+1}(1,2)=a{i,(n+1)/2+j}(1,2);
         a{i,(n-1)/2-j+1}(1,3)=a{i,(n+1)/2+j}(1,3);
    end
end

m=zeros(n*n,3);

tt=cell2mat(a);

for i=1:n
    for j=1:n
        m(n*(i-1)+j,1:3)=tt(i,3*j-2:3*j);
```

```
    end
end
xaxis=m(:,1);
yaxis=m(:,2);

width=1000;
high=1000;
% pixel resolution: width*high
% set (gcf,'Position',[0 0 1000 1000]);
figure('position',[0,0,width,high]);
diameter=30; %pixel diameter=15pixel
scatter(xaxis,yaxis,(diameter/2).^2*9/16,'ok','markerfacecolor','r')
% color of spot
axis equal
set(gcf,'color','w');%background color
set(gca,'visible','off');
%axis([-0.72794,0.72794,-0.72794,0.72794]);
%axis off
box on
return
```